Universiteit Gent
Faculteit Wetenschappen
Vakgroep Vastestofwetenschappen

Modeling the reactive magnetron sputtering process

Koen Strijckmans

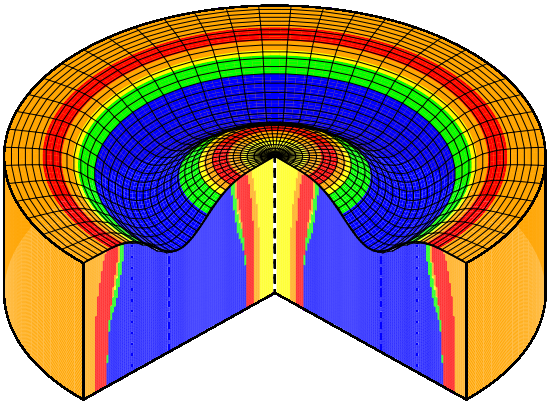

DRAFT

Proefschrift tot het behalen van de graad van
Doctor in de Wetenschappen: Fysica
Academiejaar 2014-2015

Universiteit Gent
Faculteit Wetenschappen
Vakgroep Vastestofwetenschappen

Modeling the reactive magnetron sputtering process

Koen Strijckmans

DRAFT

Proefschrift tot het behalen van de graad van
Doctor in de Wetenschappen: Fysica
Academiejaar 2014-2015

Universiteit Gent
Faculteit Wetenschappen
Vakgroep Vastestofwetenschappen

Promotor: Prof. Dr. D. Depla

Universiteit Gent
Faculteit Wetenschappen

Vakgroep Vastestofwetenschappen
Krijgslaan 281 (S1)
B-9000 Gent, België

☎ +32 9 264 43 42
✉ diederik.depla@ugent.be
🌐 http://www.draft.ugent.be

Leescommissie: Prof. Dr. Annemie Bogaerts
Dr. Andreas Pflug
Dr. Francis Boydens

Juryleden: Prof. Dr. Annemie Bogaerts (UAntwerpen)
Dr. Andreas Pflug (Fraunhöfer IST)
Dr. Francis Boydens (UGent)
Dr. Tomas Nyberg (Ångström laboratory)
Prof. Dr. Stefaan Cottenier (UGent)
Prof. Dr. Diederik Depla (UGent, promotor)
Prof. Dr. Maarten Baes (UGent, voorzitter)

Proefschrift tot het behalen van de graad van
Doctor in de Wetenschappen: Fysica
Academiejaar 2014-2015

The picture on the front page shows the target condition near the first critical point. It is a RSD2013 simulation of a planar, circular aluminum target with a $2\,\mathrm{inch}$ diameter which is reactively sputtered in an Ar/O_2 atmosphere. The color indicates the fraction of non-reacted metal where moving from blue (1-0.8) to red (0.2-0) this fraction decreases. The cross-section represents the in-depth oxidation profile which spans over a length of $3\,\mathrm{nm}$ given by center dashed line. The formed racetrack depth is amplified to become visual compared to the dimensions of the target.

Table of Contents

Table of Contents i

Dankwoord v

Nederlandse samenvatting vii

English summary xi

1 Reactive Magnetron Sputtering Deposition 1
1.1 Concept . . . 1
1.1.1 Sputtering . . . 2
1.1.2 Magnetron . . . 5
1.1.2.1 Diode sputtering . . . 5
1.1.2.2 Magnetron sputtering . . . 7
1.1.3 Deposition . . . 9
1.1.4 Reactive . . . 10
1.2 Magnetron types . . . 12
1.2.1 Target geometry . . . 12
1.2.2 Magnetic field . . . 15
1.2.3 Power characteristic . . . 15
1.3 Hysteresis . . . 18
1.3.1 Experiment . . . 19
1.3.1.1 Direct control . . . 20
1.3.1.2 Feedback control . . . 23
1.3.2 Relevance . . . 26
1.4 Modeling the technique . . . 27
1.4.1 Motivation . . . 27
1.4.2 Approach . . . 28
1.4.2.1 Atomistic . . . 29
1.4.2.2 Holistic . . . 31
1.5 Summary . . . 33
References . . . 35

2 First Models **41**
2.1 Pre-Berg models . . . 41
2.1.1 Heller model . . . 41
2.1.2 Abe model . . . 43
2.1.3 Shinoki model . . . 45
2.1.4 Steenbeck model . . . 47
2.1.5 Affinito model . . . 48
2.2 Berg model . . . 49
2.2.1 Original model . . . 50
2.2.2 Parameter dependencies . . . 55
2.2.2.1 Material properties . . . 56
2.2.2.2 Operation conditions . . . 57
2.2.3 Extended model . . . 60
2.2.3.1 Deposition profile . . . 60
2.2.3.2 Ion current profile . . . 65
2.2.3.3 Time dynamics . . . 67
2.3 Summary . . . 74
References . . . 76

3 RSD Model **79**
3.1 Relevance . . . 79
3.1.1 Limitations . . . 80
3.1.1.1 Compound thickness . . . 80
3.1.1.2 Influence inert gas pressure . . . 85
3.1.1.3 Influence pumping speed . . . 90
3.1.2 New mechanisms . . . 91
3.2 Original model . . . 93
3.2.1 Formulation . . . 93
3.2.1.1 Target . . . 93
3.2.1.2 Substrate . . . 96
3.2.1.3 Chamber . . . 97
3.2.2 Solution method . . . 98
3.3 Model parameters . . . 105
3.3.1 Experiments to fit . . . 105
3.3.2 Input parameters . . . 106
3.3.3 Model modifications . . . 109
3.3.4 Fit procedure . . . 111
3.3.5 Correlations . . . 116
3.3.5.1 One-cell model . . . 116
3.3.5.2 Multi-cell model . . . 120
3.4 Summary . . . 126
References . . . 128

4 New Model **133**
4.1 Introduction . . . 133
4.2 Redeposition . . . 135
4.2.1 Non-reactive . . . 135
4.2.2 Reactive . . . 138
4.3 RSD2013 . . . 139
4.3.1 Derivation . . . 140
4.3.1.1 Chamber . . . 140
4.3.1.2 Target . . . 141
4.3.1.3 Substrate . . . 150
4.3.2 Steady state solver . . . 153
4.3.2.1 Redeposition/one-cell target . . . 153
4.3.2.2 No redeposition/multi-cell target . . . 154
4.3.2.3 Redeposition/multi-cell target . . . 156
4.3.3 Implementation . . . 157
4.4 RSD2013 examples . . . 160
4.4.1 Target . . . 163
4.4.2 Substrate . . . 165
4.4.3 Redeposition . . . 166
4.4.4 Saturation limit . . . 168
4.5 Case study : redeposition fraction . . . 169
4.5.1 Reference system . . . 170
4.5.2 Target condition . . . 173
4.5.3 Hysteresis . . . 176
4.5.4 Racetrack profile . . . 177
4.5.5 Sputter profile . . . 182
4.6 Summary . . . 185
References . . . 187

5 Future models **191**

A Solutions Berg model **197**

B RSD2013: Steady state target solution **203**

C Publications and Conference contributions **207**

Dankwoord

Het bizarre aan een dankwoord is dat het proefschrift (en de lezer) er vaak mee start terwijl het voor de doctorandus het laatste is dat hij neerpent. Deze chronologie is te begrijpen. Een doctorandus wil van bij de start lezers die hebben bijgedragen tot zijn doctoraat een woordelijk bloemetje toewerpen. Anderzijds beseft hij misschien ook pas aan het einde wie allemaal heeft bijgedragen aan het verrijkende wetenschappelijk avontuur dat een doctoraat is. Dit is in mijn geval niet anders.

Bovenaan het lijstje staat natuurlijk mijn promotor Diederik. Zes jaar geleden opende hij voor mij de deur naar de wereld van reactief magnetron sputteren. Zijn gedrevenheid, oprechte interesse en niet aflatend optimisme vormde een fundamentele steun tijdens mijn onderzoek. Zijn deur stond letterlijk en figuurlijk altijd open, soms zelfs met de sleutels erop. Hij ging geen enkele wetenschappelijke discussie uit de weg hoeveel tijd die ook in beslag nam. Het heeft weinig gebotst tussen ons, maar één heikel punt is blijven bestaan: plot je nu de beste figuren met *Igor* of met *Gnuplot*? Hierover wil ik enkel nog kwijt dat geen enkele figuur in dit proefschrift met *Igor* werd gemaakt. Bedankt Diederik om mij zes jaar lang in alle vrijheid mijn ding te laten doen binnen het modelleren van reactief magnetron sputteren.

De volgorde van de rest van mijn bedanklijstje is wat minder duidelijk. Huidige en vroegere collega's binnen DRAFT en de vakgroep hebben elk op hun manier bijgedragen tot de fijne sfeer op S1. Bedankt Jerika, met wie ik vier jaar lang een bureau heb gedeeld. Bij elke snackpauze dacht ze ook aan mij. Zij heeft mij *condensed milk* leren appreciëren en mijn *english* op peil proberen te houden. Na Jerika kwam Roeland. Roeland is helemaal anders, hij eet nooit en is over het algemeen stil. Hem begeleiden als thesisstudent was voor mij verrijkend en boeiend. Zo stil hij achter zijn laptop kan zitten tokkelen, zo hevig zijn onze wetenschappelijk discussies tot op vandaag. Hij zorgde ervoor dat het wat minder eenzaam werd in mijn wereldje van modelleren. Verder wil ik ook nog Wouter bedanken voor de aangename babbels en zijn experimentele output. Francis, voor de LaTeX en morele ondersteuning tijdens de laatste maanden. Sigelinde, voor de rust en om mij enkele maanden in haar bureau op te vangen. Bert, Filip, Anna, Martha en Roger *The Gray* voor de leuke momenten binnen DRAFT.

Ook buiten de S1 ben ik dank verschuldigd. Thanks to dr. Teresa de los Arcos for my stay at the Ruhr-Universität Bochum. It was a pleasure to experience the

different work environment. I am also grateful for the effort and the time the committee has taken for the evaluation of this dissertation and for their interesting feedback.

Naast het overwegend professionele bedanklijstje bestaat er een minstens even belangrijk maar meer persoonlijk lijstje. Mijn voornamelijk Tieltse vriendengroep, die in de juiste mate vroegen waar ik mee bezig was en hoever ik stond. Bedankt om voor de broodnodige ontspanning te zorgen. Tom, voor al die toertjes rond de Watersportbaan waarbij ik de dingen in een ruimer perspectief kon plaatsen. Mijn ouders, Annemie en Karel, die over het grootste deel van mijn levenstraject en scholing hebben gewaakt. Korneel, mijn zoon die er altijd in slaagt om een glimlach op mijn gezicht te toveren. Maar bovenaan staat Merel, mijn vrouw. Het einde van dit doctoraat ging gepaard met een tweede zwangerschap, het zorgen voor Korneel, het bouwen van een huis en haar eigen doctoraat. Zonder haar niet aflatende liefde, steun en begrip was ik nooit tot deze laatste woorden gekomen.

Koen
Gent, augustus 2015

Nederlandse samenvatting –Summary in Dutch–

Reactief magnetron sputteren is een veelzijdige plasmatechniek om een dunne laag van een bepaalde chemische verbinding af te zetten op allerhande objecten. Het doel van deze dunne lagen is om een interessante eigenschap toe te voegen of een bestaande te versterken. De term "dun" dient geïnterpreteerd te worden als gaande van enkele nanometers tot verschillende micrometers. Deze techniek is industrieel relevant en wordt in talloze technologische producten toegepast gaande van ramen in flatgebouwen over auto-onderdelen en boorkoppen tot touchscreens in bijvoorbeeld smartphones. De basis van deze techniek is conceptueel simpel. Een metalen target of kathode wordt gebombardeerd met ionen uit een plasma van edelgas bij een lage druk. Deze ionen worden versneld door het aanleggen van een negatief potentiaal verschil tussen de kamer en de target. De gesputterde deeltjes condenseren op een oppervlak in de kamer en liefst op het voorwerpoppervlak dat van een dunne laag dient te worden voorzien. Om over te gaan van deze metaallaag naar een laag bestaande uit een complexere chemische verbinding wordt er één of meerdere reactieve gassen toegevoegd aan het proces. Dit reactieve gas reageert met het afgezette materiaal om zo de gewenste verbinding te vormen. De functie van een magnetron is om deze depositiemethode efficiënter te maken door het creëren van een magnetisch veld in de buurt van het targetoppervlak. Dit magneetveld versterkt lokaal de plasmadichtheid en de productie van ionen. Dit optimaliseert de depositieflux ten opzichte van het elektrisch vermogen dat in het proces wordt verbruikt.

In het eerste hoofdstuk wordt de techniek kwalitatief uitgelegd en de belangrijkste aspecten worden toegelicht. Sinds de toepassing van de techniek, zijn er verschillende types magnetrons ontworpen. Deze magnetrons kunnen verschillen in de targetgeometrie en de vorm van het magneetveld. Ook de overbrenging van het elektrische vermogen kan sterk uiteenlopen. De meest courante en de best gekende configuraties worden kort besproken. Kenmerkend voor reactief sputteren als depositietechniek zijn de hysteresisfenomenen die in de procescurves kunnen optreden. Zulke hysteresissen zorgen voor een niet unieke afhankelijkheid van de systeemconditie als functie van de instelbare parameters. De toestand van het systeem zal mede bepaald worden door zijn voorgeschiedenis. Deze hysteresissen kunnen enerzijds worden bestudeerd door direct gecontroleerde hysteresis experimenten en anderzijds door feedback gecontroleerde hysteresis experimenten. De twee types van experimenten verschillen in de manier hoe een operationeel punt in

de procescurve wordt ingesteld. Bij directe controle worden de instelbare parameters manueel aangepast ongeacht hoe het systeem zich zal gedragen. Bij feedback controle worden deze parameters automatisch aangepast op basis van de monitoring van het systeem met het oog op de realisatie van een welbepaalde toestand van het systeem. De technologische relevantie van deze hysteresisfenomenen ligt bij hun impact op de procesefficiëntie via de depositiesnelheid en op de operationele stabiliteit. Het modelleren van deze hysteresissen is interessant om hun oorsprong, hun afhankelijkheden en hun impact te kunnen begrijpen en voorspellen. Om deze doelstelling te bereiken kunnen twee modelleerbenaderingen worden onderscheiden. De eerste of "atomaire" benadering houdt in dat de verschillende fysische en chemische subprocessen waaruit de techniek bestaat, individueel worden gemodelleerd. Dit gebeurt met het oog op een grote kwantitatieve voorspellende kracht en met een grote zin voor een gedetailleerde beschrijving. Het combineren van deze individuele modellen zou dan resulteren in een sterk wapen om onnodige trial-and-error experimenten uit de weg te ruimen. Het doel van deze methodiek is heel ambitieus. Dit doel wordt echter gehinderd door de moeilijkheid om de sterk uiteenlopende schalen waarop de verschillende subprocessen zich afspelen, zowel ruimtelijk als in de tijd, te kunnen combineren. De tweede of "holistische" benadering start met het modelleren van deze techniek als zijnde één entiteit waarbij de realiteit sterk wordt vereenvoudigd. De primaire doelstelling van deze benadering is een eenvoudig kwalitatief begrip en model voor het volledige proces. Als secundaire doelstelling kan een echte kwantisatie naar voor worden geschoven. Het is deze tweede benadering, ook wel de top-bottom benadering genoemd, die in dit werk zal worden gevolgd. Dit is in tegenstelling tot de eerste "atomaire" of bottom-up benadering.

Het tweede hoofdstuk start met een historisch overzicht van de eenvoudige modellen die voor reactief sputteren werden geformuleerd. Zij vormen de prelude voor het originele Berg model. Het Berg model kan beschouwd worden als de voorvader van de Reactive Sputtering Deposition (RSD) modellen die erop volgen. De ontwikkeling van het Berg model past binnen de "holistische" benadering omdat het de essentie van de hysteresis tijdens reactief sputter depositie modelleert met een minimum aan complexiteit en parameters. De druk van het reactieve gas, een gemeten parameter, als functie van het reactieve gasdebiet, een instelbare parameter, kan zo'n hysteresis gedrag vertonen. Hoe deze hysteresis afhangt van het gebruikte materiaal en de procesparameters wordt bestudeerd met het Berg model. Uitgaande van het originele Berg model kunnen twee soorten van uitbreidingen worden geformuleerd. De eerste soort uitbreidingen omvat uitbreidingen die een nieuw fysisch mechanisme toevoegen aan het model of een bestaand fysisch mechanisme anders beschrijven. Een tweede soort verhogen de resolutie van het model ofwel ruimtelijk ofwel in de tijd. Hierbij verandert de essentie van het model niet. De doorgevoerde uitbreiding van het originele Berg model met een depositieprofiel (ruimtelijk), een ionenstroomdichtheid (ruimtelijk) en de tijdsafhankelijkheid (tijd) zijn van de eerste soort. Hierbij is de gemodelleerde tijdsafhankelijkheid vergeleken het experiment.

In hoofdstuk drie vormt de overgang van het originele Berg model naar het

RSD2007 model een uitbreiding van de tweede soort. Het nieuwe mechanisme dat het RSD2007 model introduceert is reactieve implantatie en chemische reactie van de geïmplanteerde reactieve atomen. Dit mechanisme lost grotendeels drie tekortkomingen op die het originele Berg model ondervindt bij confrontatie met experimenten. De keerzijde van de medaille is echter de introductie van extra modelparameters die slechts gedeeltelijk experimenteel bepaald zijn of uit andere modellen kunnen worden gehaald. De overige onbekende parameters worden afgeschat door twee RSD modellen te fitten aan gemeten experimentele hysteresissen tijdens het sputteren van een aluminium of yttrium target in een argon/zuurstof atmosfeer. Het ene RSD model dat een uniform stroomprofiel veronderstelt, is niet in staat om de correcte experimentele sputteropbrengsten voor de oxides te reproduceren. Het andere model dat wel een ruimtelijk stroomprofiel in rekening brengt, slaagt hier wel in. Het verband tussen de sputteropbrengsten en de reactiecoëfficiënt voor de geïmplanteerde reactieve atomen wordt onderzocht. De verhouding van de sputteropbrengsten tussen de twee materiaalsystemen blijkt constant te zijn en onafhankelijk van de modelkeuze.

Hoofdstuk drie stelt een nieuw RSD model voor, RSD2013. Een gedetailleerde beschrijving van het volledige model wordt gegeven. De implementatie van het model resulteert in een publiek toegankelijk en gebruiksvriendelijk software pakket dat eveneens RSD2013 is genoemd. Bijzondere aandacht is besteed om het model zowel in zijn tijdsafhankelijke als in zijn steady state vorm te implementeren. Ook werd de mogelijkheid voorzien om verschillende aspecten van het model uit te sluiten of mee te nemen in een simulatie. Dit wordt geïllustreerd met een serie van simulaties waar een referentiesysteem steeds met meer detail wordt gemodelleerd. De beste fysische verbetering aan het RSD model is de toevoeging van herdepositie. Herdepositie betekent de terugkeer van gesputterde materiaal naar het oppervlak van de target. Hoe herdepositie afhangt van de metaal-gas combinatie, de target-sample afstand, de hoekafhankelijke sputterdistributie en de gasdichtheid is bestudeerd met een Monte Carlo transport code SiMTra. De relevantie van herdepositie tijdens reactief sputterdepositie wordt toegelicht. Als case study wordt de invloed van de herdepositiefractie op het reactief sputter systeem onderzocht via RSD2013 simulaties. Meer specifiek wordt de invloed van de herdepositiefractie op de targetconditie, de hysteresis en de vormverandering van de erosiegroef en het sputterprofiel bestudeerd.

In het laatste hoofdstuk worden enkele suggesties gedaan voor toekomstige RSD modellen. Enkele van deze suggesties zijn actuele onderzoekspistes die vandaag binnen de onderzoeksgroep DRAFT worden uitgevoerd. Andere ideeën wachten wanhopig om aangepakt te worden.

English summary

Reactive magnetron sputtering is a versatile plasma technique to deposit thin layers of compound material on all kind of objects. The purpose of these thin films is to add or enhance interesting properties to the object. The term "thin" should here be interpreted as ranging from a few nanometers up till several microns. The technique is well appreciated in industry and found its application in numerous technological products ranging from big building glass windows, over car parts and drill chucks to the touch panel of smart phones. The basics of the technique are conceptually simple. A mostly metallic target is bombarded by the ions from a low-pressure noble gas plasma. These ions are accelerated over the applied negative voltage difference between the chamber and the target. The particles that are sputtered due to this bombardment, condense on surfaces within the vacuum chamber and ideally on the object to be coated. To modify this metallic layer into a compound layer, one or more reactive gases are added to the process. This reactive gas chemically reacts with the deposited material to form the desired compound. The purpose of the magnetron setup is to enhance this method by the creation of a magnetic field in the close neighborhood of the target surface. This magnetic field locally intensifies the plasma density and the ion production to optimize the deposition flux as function of the electrical power provided to the process.

In the first chapter the technique is qualitatively explained and the most important aspects are introduced. Over the decades that the technique has been used, several magnetron setups came to existence. These designs can differ in the target geometry, the shape of the magnetic field and the electrical operation characteristics. The more general known design decisions are touched on. Characteristic for reactive sputtering as deposition technique is the occurrence of hysteresis phenomena in the process curves. These hystereses cause that the operation conditions are not uniquely determined by their instantaneous operation parameters, but will be history dependent. These hystereses can be investigated by so called direct controlled or feedback controlled hysteresis experiments. They differ in the way how an operation point is established. For direct control, the operation parameters are manually set irrespective on how the system will behave. For feedback control these parameters are automatically adapted by system monitoring in order to realize a certain system state. The technological relevance of these hysteresis phenomena is the impact on the process efficiency through the deposition rate and on the operation stability. Modeling of these hystereses is then interesting to understand their origin, their dependencies and their impact. Two modeling approaches are here recognized to do this. The first "atomistic" approach individually models

in great detail and with high quantitative power the many physical and chemical subprocesses which are involved in the technique. Combining them would result in a strong predictive tool to cut away unnecessary trial-and-error experiments. The goal of this approach is very ambitious but is hampered by the big difference in temporal and spatial scales which have to be combined across the subprocesses. The second "holistic" approach starts to model the technique as a whole but in a way that strongly (over)simplifies the reality. Its primary goal is the basic qualitative understanding and modeling of the whole process and only in second order, the exact quantification of it. It is the second approach, also coined the top-bottom approach, which will be followed in this work. This contrasts with the former "atomistic" or bottom-up approach.

The second chapter sets off with a historical overview of simple reactive sputtering models which prelude the original Berg model. The Berg model can be viewed as the ancestor of the Reactive Sputtering Deposition (RSD) models which follow. The development of the Berg model fits the "holistic" approach as it models the essence of the hysteresis during reactive sputtering deposition with a minimum in model complexity and parameters. The dependency of the hysteresis in the reactive gas pressure (system observable), as function of the introduced reactive flow (operation parameter), is studied with respect to the material and the operation parameters within the Berg model. In the thesis, new solution strategies for the original Berg model are proposed which enables the simulation of the hysteresis as function of the pumping speed, for example. Starting from the original Berg model, two kinds of extensions can be formulated. The first kind embodies extensions which add physical mechanisms to the model or differently describe included mechanisms. The second kind of extensions add spatial or temporal resolution to the model without touching the essence of the model. For the original Berg model, the inclusion of a deposition profile (spatial), an ion current profile (spatial) and the time dynamics (temporal) are examples of second kind extensions. In this work, the modeled time dynamics are shown to qualitatively correspond with the experimental behavior.

In chapter three, a first kind extension of the original Berg model results in the RSD2007 model. The new mechanism that the original RSD2007 model introduces is reactive implantation and subsurface reaction. The derivation of this original RSD2007 model has here been investigated more thoroughly and lead to an analytical solution form of the subsurface implantation and reaction equations. For a uniform implantation profile an analytical closed form is achieved. In this work it is shown that these subsurface mechanisms can resolve at least three limitations of the original Berg model with experiments. The backside is the introduction of more model parameters which partially can be retrieved from experiments or other models. In this thesis, the remaining unknown parameters are estimated by fitting two RSD implementations to experimental hystereses of an aluminum and yttrium target sputtered in an argon/oxygen atmosphere. The first implemented RSD model which assumes an uniform current profile, is not able in reproducing the correct experimental oxide sputter yields. The second RSD implementation with a spatial resolved current profile however succeeds. The correlation between

these sputter yields and the subsurface reaction rate is investigated in this work and the sputter yield ratio between the two metal systems showed to be constant and independent of the chosen model.

Chapter four proposes a new formulated RSD2013 model elaborated within this thesis. The complete model is given in all its details together with the implementation of the model in a public available and user-friendly software package, equally called RSD2013. The major extensions over the previous version RSD2009 is the remodeling of redeposition, the addition of a second subsurface layer, a saturation limit for implanted reactive species and a complete equivalent steady state model for all model options including a multi-cell description and/or redeposition. Furthermore the option to include or exclude certain aspects of the model is been realized. The latter is illustrated with a series of simulations where the detail of the modeled system is gradually incremented. But the major physical enhancement to the RSD model is the remodeling of redeposition, the deposition of sputtered material back on the sputtering target surface. The dependency of redeposition on the metal-gas combination, the target-sample distance, the angular sputtering distribution and the gas density is examined with a Monte Carlo transport code SiMTra. The relevance of redeposition during reactive sputtering deposition is put forward. In a case study, the influence of the redeposition fraction on the reactive sputtering system is investigated by RSD2013 modeling. More specific, the influence on the target condition, the effect on the hysteresis and the shape modification of the racetrack and the sputter profile is examined.

In the final chapter some future suggestions for next generation RSD models are put forward. Some of these suggestions form contemporary research topics of the research group DRAFT while others are disparately waiting to be tackled.

"It's always possible to produce some kind of number,
but it's much harder to produce a meaningful number."

Gershenfeld in *The nature of mathematical modeling* (1998)

1 Reactive Magnetron Sputtering Deposition

1.1 Concept

Reactive magnetron sputtering deposition is a technique to cover the surface of an object with a thin layer of a certain compound. The aim of this thin film or coating is to add specific properties to the object (e.g. color) or to enhance present ones (e.g. hardness). The term "thin" should be interpreted as ranging from a few nanometer towards several microns. Particular for this technique is that the desired film is a chemical compound, it consists out of two or more different chemical elements with at least one metal (or metalloid) and one non-metal. The simplest of these chemical compounds is formed from two elements. In the process, the metal is mostly brought into a atomic vapor such that it can condense on the surface of the object to be coated. The non-metal is conversely introduced in the process under the form of a gas that can react with the condensed metal. The chemical reactivity between the two constituents defines then the possibility of compound formation.

The metal is brought into an atomic vapor state by sputtering. The metal is supplied to the process in a solid form, commonly called the target. This target is bombarded by energetic, positive ions which are extracted from a generated low pressure plasma. Due to the negative potential on the target compared to the vacuum chamber, these positive ions are accelerated towards the target, which acts as the cathode of the system. The energetic impact of these ions knocks off or sputters

metal atoms from the target into the vacuum chamber. These sputtered atoms get deposited on the surfaces they hit which is collectively called the substrate. The process of sputtering is described in more detail in the next section. The efficiency of the deposition technique is nowadays mostly enhanced by the generation of a strong magnetic field above the target surface. Such a setup is then called a magnetron. The mechanism of magnetron sputtering is discussed in section 1.1.2. In section 1.1.3, reactive magnetron sputter deposition will be oriented between other deposition techniques and its technological importance will be illustrated. In the last section 1.1.4, the reactive aspect of the process is been touched on.

1.1.1 Sputtering

Sputtering is the physical removal of particles from a target surface due to the energetic impact of bombarding particles. These bombarding particles may be ions, neutral atoms, neutrons, electrons or energetic photons.

Sputter phenomena can not only be found in technological applications or scientific experiments but are also directly observable in nature. For example, the surface of celestial bodies is sputtered by plasma particles of the solar wind changing the physical and chemical state of these bodies [1]. While in the technology of nuclear fusion, the high energetic neutron flux towards the vessel walls cause a contamination of the fusion plasma due to metal sputtering [2]. As scientific example, the cathode of an electric gas discharge will be sputtered by the ion current produced in the cathode fall or sheath, covering the glass walls of the discharge tube. It was this type of experiment where sputtering was first discovered more than 150 years ago [3]. Sputtering was longtime only an unwanted guest in many technological applications as a source of contamination. However nowadays it is an indispensable process in many modern technologies. The desire to understand the physics of sputtering is probably the most stimulated by its application in surface analysis [4], surface etching [5] and thin film deposition.

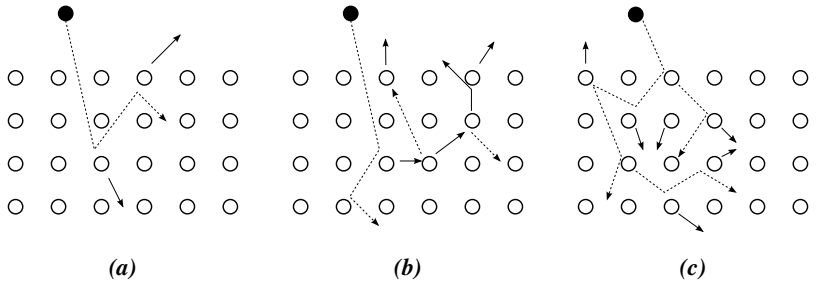

Figure 1.1: *Three regimes of collision cascade are defined the single knockon regime (a), the linear regime (b) and the spike regime (c).*

In the context of sputter deposition, the bombarding particles will be mainly inert gas ions like Ar^+ with energies in the sub-keV range. The emitted particles are mostly neutral, while generally less than $5\,\%$ are ionized [6]. Some atoms are sputtered in clusters. The sputtered atoms will typically originate from the nearest surface layers of the target [7]. They result out of the collision cascade which the bombarding ion initiates. In this collision cascade energy and momentum is transferred to the target atoms. When this energy transfer exceeds the binding energy of a target atom to its position, a primary recoil is created. If only primary recoils by the bombarding ion are generated, the collision cascade is in the single knock-on regime (Fig. 1.1a). If the initial hitting ion and the primary recoil on their turn create further recoils, respectively primary and secondary recoils which on their turn create possible further recoils (secondary and tertiary), the regime moves to the linear collision cascade (Fig. 1.1b). The density of recoils remains however small where higher order recoils receive less and less energy. The spike regime (Fig. 1.1c) is the situation of high recoil density where the majority of the target atoms in the neighborhood of the impact are in motion.

These collision cascades extend much deeper into the target then from where atoms are emitted. The depth of this region scales with the energy of the bombarding particles. If the bombarding particle are however light (like neutrons, electrons or light ions) and highly energetic ($E > 100\,\mathrm{keV}$), the interaction at the surface with the target will be low causing minimal sputtering. Higher mass particles at lower energies ($E < 100\,\mathrm{keV}$) will enhance the sputter effect, with a broad maximum in the energy region from 5 to $50\,\mathrm{keV}$. Sputtering of a target atom will then only occur when the energy component perpendicular to the surface exceeds the surface binding energy of that target atom. This surface binding energy is often approximated by the heat of sublimation. However sputtering is a highly non-thermal process, so it does fundamentally differ from evaporation.

Sputtering is not the only physical phenomena that is induced by ion bombardment. Several other processes can occur like ion implantation or backscattering, relocation of target atoms, dislocations, electron emission, photon emission and surface structure modification. The most relevant quantity for sputtering is the sputter yield Y which gives the mean number of sputtered atoms per incoming bombarding particle.

$$Y = \frac{\text{mean number of atoms}}{\text{number of bombarding particles}} \tag{1.1}$$

The sputter yield depends as well on the incoming particle energy and its mass (Fig. 1.2a) as on its incident angle (Fig. 1.2b). Also the properties of the target, namely the mass of the target atoms, their surface binding energy, the crystallinity of the target and its possible crystal orientation, do settle the value of the sputter yield. Sputter yields are however almost independent of temperature, unless a volatile compound is formed. Differential sputter yields are defined for describ-

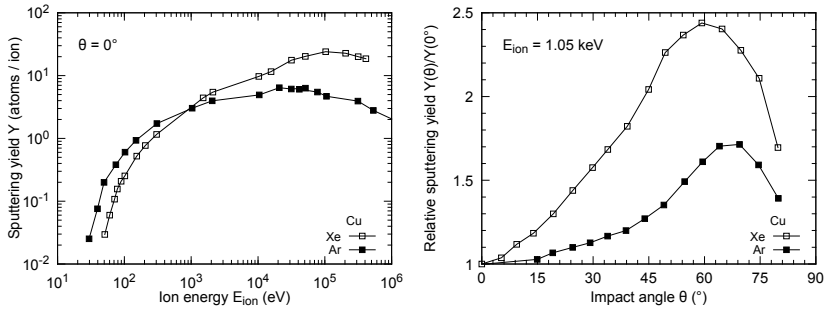

Figure 1.2: *The experimental sputter yield of Cu bombarded with Ar and Xe ions as function of (a) the energy [8] and (b) the incident angle [9].*

ing the energy (Fig. 1.3a) and the angular dependencies (Fig. 1.3b) as well as the state of the sputtered atoms. The maximum of this energy distribution is generally proportional with the surface binding energy of the target atoms. The higher energy tail typically decreases proportional to $1/E^2$. Its angular distribution strongly depends on the crystallinity of the target. For single crystals the distribution will show maximums in the close-packed directions, while for polycrystals the distribution will be a superposition of the different crystallites in the target. A cosine distribution is a good first approximation for the latter case when the energetic particles impinge on the target according the surface normal. This cosine distribution tends to become an under-cosine if the impinging particles become heavier and their energy gets lower. Conversely, a more over-cosine distribution is obtained with lighter impinging particles and higher energies.

Much work has been done in the quantification of the sputtering process. Analytical formulas can be derived from first-order asymptotic solution of the Boltzmann transport equation [12–18] and/or in combination with empirical data. A required condition for this approach is the validity of the binary collision approximation and the assumption of an amorphous target. The binary collision approximation is valid starting from energies above $\sim$ 100 eV. Polycrystalline targets can often be well approximated by an amorphous target if the crystallites are randomly oriented. Under the same conditions can sputtering be well described by Monte Carlo simulations [19–22]. But if the energies of the interacting particles drop below $\sim 100\,\mathrm{eV}$, a molecular dynamic model [23, 24] should be used. Let it be clear that the calculation time expense together with the physical resolution between the different approaches drastically increases from analytical over Monte Carlo to molecular dynamics.

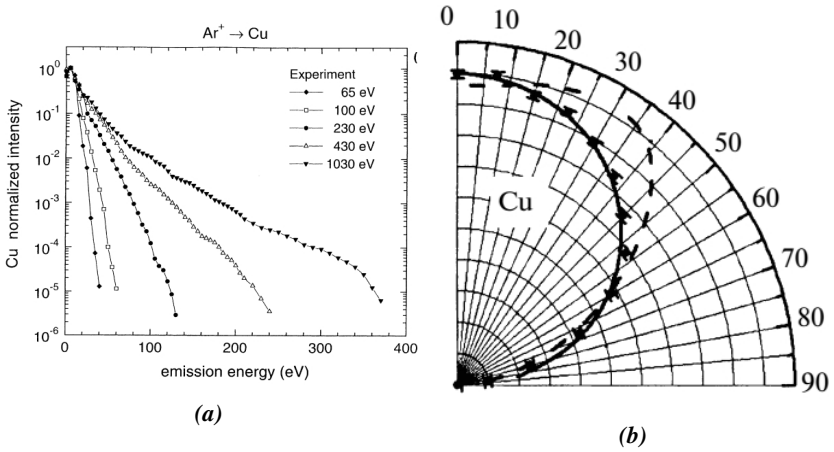

Figure 1.3: *Cu bombarded with Ar ions. (a) The energy distribution of the sputtered atoms for different Ar ion energies [10] and (b) the angular distribution of the sputtered Cu atoms for normal incident Ar ions with an energy of* $443\,\mathrm{eV}$ *[11].*

1.1.2 Magnetron

1.1.2.1 Diode sputtering

Although magnetron sputtering has today generally overruled diode sputtering, it is instructive to first consider diode sputtering before discussing magnetron sputtering. Diode sputtering is established by applying a high negative voltage (-2 to $-5\,\mathrm{kV}$ [6]) between two parallel electrodes in a vacuum cavity where a fixed pressure of inert gas, typically Ar, is set. If the right combination of voltage and gas pressure is applied, a discharge will ignite and a plasma can be maintained. For sputter deposition purposes, this discharge has to operate in the abnormal glow regime. In this regime the sputter rate is the highest as the discharge extends over the whole cathode and the ion current density varies as a positive power with the discharge voltage. The discharge can ignite by the presence of electrons generated by the background radiation and field emission. These electrons get accelerated in the electrical field and gain energy. As they acquired energy, they are able to excite the neutral Ar atoms. De-excitation of the energy levels between $1-3\,\mathrm{eV}$ emit photons in the visible spectrum and give the Ar plasma its purple glow. If the electrons reaches higher energies ($>15.76\,\mathrm{eV}$), they have the possibility to ionize the neutral Ar gas atoms. If this happens close enough to the cathode, these ions will be accelerated towards the cathode and by hitting the cathode, they sputter off the cathode material. This sputtering will not only be caused by ions but also high-energetic neutrals will have a substantial contribution during diode sputtering. As the accelerated electrons move in the opposite direction, they hit the anode and

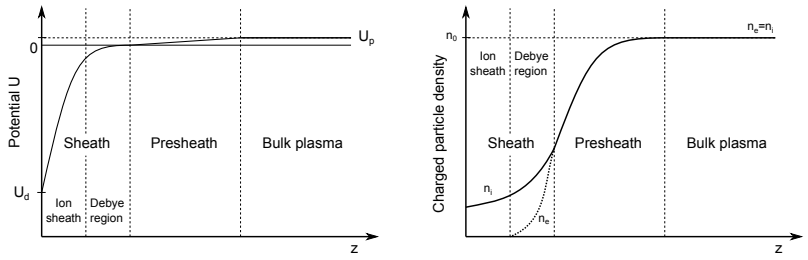

(a) ***(b)***

Figure 1.4: *Schematic representation of the potential distribution (a) and charge distribution (b) in a typical diode discharge in front of the cathode. Three regions can be distinguished: the sheath, the presheath and the bulk plasma. Figure is based on [25].*

are lost for further ionization. To maintain the discharge, new secondary electrons have to be introduced. These secondary electrons are emitted from the cathode due to ion impact. The average number of electrons that are emitted from the target surface per incoming ion without being recaptured is called the effective secondary electron emission yield Y_{SEE}. This value depends on the cathode material and on the ion energy. These electrons are accelerated away from the cathode gaining enough energy to ionize neutral Ar atoms which form the background gas. To establish then a self-sustaining discharge, the following condition should be met

$$Y_{SEE} N_{ion} > 1 \tag{1.2}$$

where N_{ion} is the mean number of effectively produced ions which hit the cathode for each emitted and non-recaptured secondary electron. A multiplication of the ionizing electrons can occur when the ionizations take place sufficiently close to the cathode surface. In this case the released electron can gain sufficient energy to ionize on their own. For diode sputtering the probability of electron recapture by the cathode is negligible. Depending on the operation conditions, the plasma can be spatially subdivided in several regions. A detailed description of these regions can be found in literature [26, 27]. Here only the most important aspects concerning the discharge will be mentioned (Fig. 1.4). The region right in front of the cathode is called the sheath where most of the potential drop U_d between the electrodes is located. It is in this region that the ions and electrons get the most of their energy. Right in front of the sheath is the presheath where a less steeper potential drop allows ions to move towards the sheath. Most of the plasma extends however in the quasi-neutral bulk region where an equipotential is maintained, the so called plasma potential U_p which is slightly positive compared to anode. Ions generated

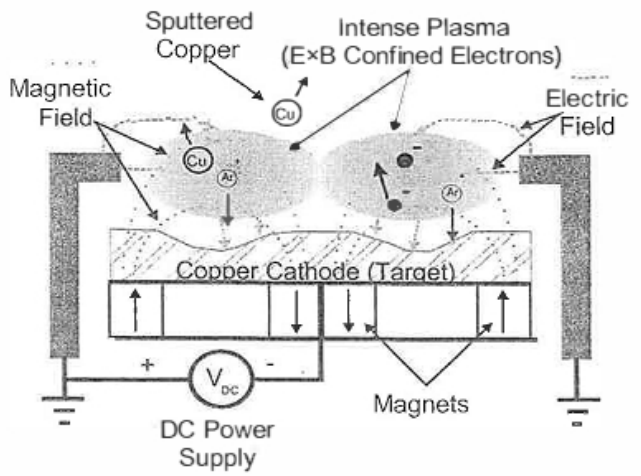

Figure 1.5: *A DC magnetron with a Cu target. Magnets are placed behind the target to have an intense plasma just above the target surface. Figure reproduced from [28].*

in this region do not feel the strong electrical field from the sheath and as such have a low probability to hit the cathode. Consequently the working pressure will have to be high enough such that sufficient ionizations can take place in the (pre)sheath regions. Typical operation pressures for diode sputter deposition range from 2 to 100 Pa. These high pressures limit however the deposition rate, while lowering the pressure would induce higher discharge voltages and an increasing minimal cathode-anode separation by the increase mean free path of the ionizing electrons. Although the cathode will be uniformly sputtered, the ion current densities are relatively low resulting in a low sputter rate. An additional disadvantage can be the substrate heating due to a high flux of electrons which minimally contribute to the ionization of the Ar gas but do strike the substrate with energies comparable with the discharge voltage.

1.1.2.2 Magnetron sputtering

A major advance compared to conventional diode sputter deposition was the introduction of a strong magnetic field in the close vicinity of the cathode. The role of the magnetic field is to confine the electrons in an intense plasma region near the cathode. The electron densities in this region can easily be 10 to 1000 times denser. The purpose of the magnetic field is to intensify the ionization of the working gas resulting in higher ion current densities (typically 10 to 100 times higher compared to diode sputtering [29]) at considerable lower operating pressures (order $0.1 - 1\,\mathrm{Pa}$). Ionization degrees for e.g. Ar can approach almost $5\,\%$ [6] whereas in a diode system ionization degrees are about $0.01\,\%$ [6, 30]. In this way as well

the sputter rate as the deposition rate is significantly increased compared to diode sputtering when similar discharge voltages are applied. The sputter rate is increased due to the higher ion current and due to a higher sputter yield. The sputter yield will increase as the lower pressure in magnetron sputtering reduces symmetric charge transfer between slow atoms and fast ions. This reduction causes more ions to be accelerated over the full potential compared to the diode case. The deposition rate is then directly increased by this higher sputter rate but also by the less scattering of the sputtered atoms with the working gas. This minimizes the randomization of the sputtered flux and conserves its directional character towards the substrate. The term magnetron originates from the confinement mechanism of the electrons by the interplay of the electrical and the magnetic field.

In order to ignite a magnetron plasma, a voltage between 200 and $1000\,\mathrm{V}$ is typically set between the cathode and anode of the system. The sources of ion and electron creation are similar as in the diode case, but now the trajectories of the electrons are bended by the magnetic field in such a way that they stay near the cathode. The electrons gyrate around these magnetic field lines and they will have a probability to be recaptured if these field lines cross the target surface. To prevent that, magnets (permanent or electromagnets) are positioned behind the cathode or target such that the largest fraction of the magnetic field lines run parallel with the target surface. Typical magnetic field strengths above the target range from around 100 to $1000\,\mathrm{G}$, but they do depend on the target material, the type of magnet and their mutual separation.

By the presence of the electrical $\mathbf{E}$ and the magnetic field $\mathbf{B}$ is the Lorentz force $\mathbf{F}_L$ acting on both ions and electrons

$$\mathbf{F}_L = q(\mathbf{E} + \mathbf{v} \times \mathbf{B}) \tag{1.3}$$

where q is the charge and $\mathbf{v}$ is the velocity of the species. Part of the magnetic component of the Lorentz force causes a circular motion of the charged species around its magnetic field line. The centripetal force F_c supporting this motion is given as

$$F_c = qv_\perp B = m\frac{v_\perp^2}{r_L} \tag{1.4}$$

where $v_\perp$ is the velocity component perpendicular to the magnetic field, m is the mass of the charged species and r_L is the orbital radius or Larmor radius. The Larmor radius r_L can then be expressed as

$$r_L = \sqrt{\frac{2mU}{qB^2}} \tag{1.5}$$

taking into account that the kinetic energy qU obtained by the charged species results from its position in the cathode potential U. Assuming kinetic energies of a

few eV to several $100\,\mathrm{eV}$ and magnetic field strengths of 100 to $1000\,\mathrm{G}$, typical Larmor radii for the electrons will range from 0.1 to $10\,\mathrm{mm}$. For Ar ions these will yet be in the range from 30 to $3000\,\mathrm{mm}$ due to their much greater mass. These radii are large compared to the confinement region. As such only the electrons are bound to the magnetic field lines, while the ions can be considered to be unaffected by the magnetic field. Ions will then only be influenced by the electrical component of the Lorentz force by which they are accelerated perpendicular towards the cathode surface. The flux of ions towards the target will be the most intense in regions where the magnetic field lines are nearly parallel.

The commonly used planar magnetrons do not have such parallel magnetic field above their entire target. Only in the center region between the magnets is the magnetic field nearly parallel with the target. Moving to the edges and the center of the target where the magnets are located, the field lines are bent into the target, increasing their normal component. This non uniformity of the magnetic field results in a non uniform ion flux which leads to non uniform sputtering. The erosion of the target will as such be more intense in between the magnets forming an erosion groove or racetrack in that case. This racetrack is economical unfavorable as only a limited portion ($30 - 50\,\%$) of the target can effectively been sputtered. Other types of magnetron are however designed to cope with this drawback, but they will be discussed in section 1.2.1.

Unlike the ions are the electrons near the cathode susceptible to both the electrical and magnetic field. That makes them undergoing the so called $\mathbf{E} \times \mathbf{B}$ or Hall drift. This Hall drift is oriented perpendicular to both electrical and magnetic field. This effect is important within every magnetron design. The design, especially the magnet configuration (section 1.2.1), should be such that the ionizing electrons drift along a closed trajectory above the cathode.

1.1.3 Deposition

From technological viewpoint, the major goal of reactive magnetron sputtering is the deposition of a thin film. The spectrum of possible technologies to grow thin films is huge and rapidly advancing. These technologies are also becoming more and more sophisticated. The reason is the never stopping demand of high-technological applications with increasing performance standards, desirably at a low production price. A list of areas where deposition technologies play a significant role is almost endless: the semiconductor industry, the fabrication of flat panel displays, all kind of optical applications, tribological coatings, photovoltaic cells, medical tools, packaging industry, etc. Even though reactive magnetron sputtering is already a long-lasting technique dating from the 1950s [6], it still occupies an important place in the world of thin film deposition. Technological advances and fundamental research in the reactive sputter technique is an ongoing business with

probably today reactive high power impulse magnetron sputtering (HiPIMS) as the most notable example.

With the huge diversity and the overlap in physical and chemical mechanisms, a classification of all deposition techniques is almost not feasible. However to give reactive magnetron sputtering a place among the other deposition techniques, a basic classification scheme proposed in [31] is here summarized. Four general categories are defined: particulate deposition, bulk coating, surface modification and atomistic deposition. The first category are the particulate deposition techniques which form their films by the solidification or sintering of molten or solid particles. The second category are bulk coatings where large amounts of material are deposited on a surface in a relatively short time. The third category is surface modification. Surface modification alters the surface composition or properties by ion, thermal, mechanical or chemical treatment. Reactive magnetron sputtering falls within the last category of atomic deposition. Here the film is formed by the condensation of atoms on the surface after which they migrate to nucleation and growth sites. The nucleation and growth mechanisms define the microstructure and the texture of the deposited film. Within the category of atomistic deposition, a subclass of physical vapor deposition PVD processes can be defined. The general definition of a PVD process is a method to deposit thin solid films by the condensation of a vaporized form of a solid material onto various surfaces involving the physical ejection of material as atoms or molecules. A PVD process can generally be divided into three steps: creation of the vapor, transport of the vapor from source to surface and film growth. Almost any PVD process can be described in these steps. Based on the vapor creation, three basic PVD processes can be coined: evaporation, sputtering and ion plating. From these basic processes, many more specialized PVD processes are derived. The present subject of interest, reactive magnetron sputtering, is an example of this. It is a reactive deposition process where the introduction of a chemical reactive gas into the sputtered vapor enables the formation of new compounds.

1.1.4 Reactive

The term reactive in reactive sputtering can be viewed in four ways [32]. From the viewpoint of thin film deposition (see section 1.1) where the objective is to deposit a compound layer on the substrate surface, two definitions can be given. Reactive sputtering can point to the deposition of a compound by sputtering of a compound target by inert gas ions, reactive gas ions or a mixture. As the electrical conductivity of compound targets is often (very) low, straightforward e.g. direct current (DC) sputtering will in many cases not be possible. However compound targets can be sputtered by radiofrequency (RF) sputter deposition (see section 1.2.3). The second definition of reactive sputtering is the deposition of a compound by

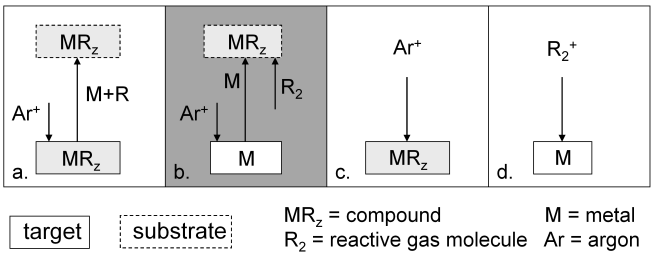

Figure 1.6: *Schematic representation of the different definitions which can be attributed to the term "reactive" in reactive sputtering [32]. Definition (a.) is the deposition with a compound target. Definition (b.) is the deposition with a metallic target in a reactive atmosphere to form compound. Definition (c.) and (d.) focus on the ion-solid interaction of respectively an ion with a compound and an reactive ion with a metal. Definition (b.) covers the best the term "reactive" in reactive magnetron sputtering deposition.*

sputtering of a metallic target where a reactive gas is added to the process. The reactive gas reacts then on the substrate with the deposited metal atoms to form the compound. As the target is here conductive, DC sputtering is a possible deposition technique.

When the focus is on the sputter process itself, viewed as an ion-solid interaction, two definitions along the previous two can be formulated. The first is the bombardment of a compound by inert ions and the second is the bombardment of a metal by reactive ions. An application of the first is the depth profiling of a compound, while an example of the second definition occurs during secondary ion mass spectrometry where a metallic sample e.g. silicon can be bombarded with reactive ions like oxygen to produce charged atoms or clusters.

Notwithstanding that reactive sputtering is here considered as film deposition by definition two, namely the sputtering of a metal target within a mixed inert/reactive gas atmosphere, do the details of the process also include the three other definitions. The compound is not only formed on the substrate but also on the target itself where it is subjected to sputtering. Sputtering and deposition of this target compound can then be classified under the first definition, while the interaction of this compound with the inert gas ions falls under the third definition. The last definition also applies as the metal target is not only bombard by inert gas ions but also by reactive gas ions which are formed in the plasma and interact with the target. In practice all sputtering depositions incorporate to a certain degree a reactive aspect as there will always be a residual reactive gas pressure in the chamber. However "reactive" in reactive magnetron sputtering deposition stands for the intended mixing of reactive gas(ses) with the inert working gas to produce the desired compound. This approach gives a real wealth in possible compounds.

Compounds	Reactive gases	Examples
Oxides	O_2	Al_2O_3, In_2O_3, SnO_2, SiO_2, Ta_2O_5
Nitrides	N_2	TaN, TiN, AlN, Si_3N_4, CNx
Carbides	CH_4, C_2H_2, C_3H_8	TiC, WC, SiC
Sulfides	H_2S	CdS, CuS, ZnS
Oxynitrides	O_2 and N_2	TiO_xN_y, TaO_xN_y, AlO_xN_y, SiO_xN_y
Oxycarbides	O_2 and CH_4, C_2H_2, C_3H_8	

Table 1.1: *The most common deposited compounds by reactive sputtering deposition, the used reactive gases and some examples [29].*

Table 1.1 lists the most common compounds deposited by reactive sputtering deposition and the used reactive gases.

1.2 Magnetron types

Magnetron setups can be subdivided according several criteria. A brief classification is made here based on three properties of the setup. A first property is the target geometry and how the magnets are oriented towards the target. The second property is the balance of the magnetic field, and the third property is the electrical powering characteristics of the magnetron.

1.2.1 Target geometry

The planar magnetron configuration (Fig. 1.7) is probably the most common geometry. The target is a circular or rectangular flat disk where permanent magnets (e.g. NdFeB) are placed behind. For the circular target, an annular magnet is used with its magnetic polarization perpendicular with the target surface. In the center of this ring magnet a button magnet is placed with a reversed polarization. In this way roughly half of the magnetic field lines stream from the north pole towards the south poles above the target surface. At the back a comparable stream of magnetic field lines exist. However, these field lines are spatial bounded by placing the magnets on a block of ferromagnetic iron. The electrons which are bounded to the arching magnetic field lines, influenced by a Hall drift and electrical accelerated and decelerated in the cathode sheath (see section 1.1.2.2), are forced to move in a circular hopping motion in between the concentric magnets. Their ionization rates are the highest where the magnetic field is parallel to the cathode surface and perpendicular to the electrical field. This is in the center between the magnets where a racetrack is formed.

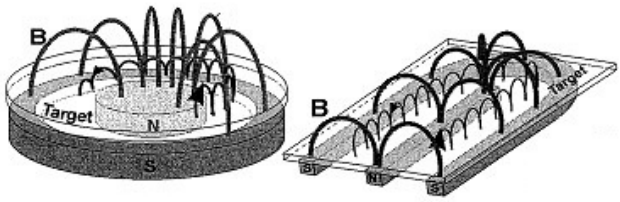

Figure 1.7: *Two types of planar magnetrons: a circular and a rectangular. Figure reproduced from [6].*

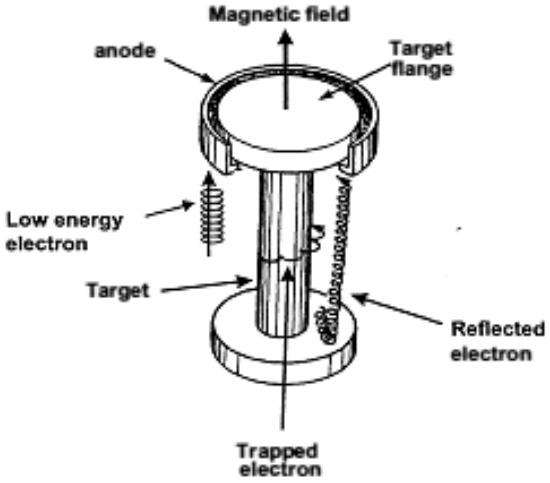

Figure 1.8: *A post-magnetron with a magnetic field coaxial with the system axis. Figure reproduced from [6].*

The planar rectangular target is similar. A rectangle of outer magnets encloses an inner bar magnet with reversed polarity under a planar rectangular target. In a well designed rectangular magnetron, the electrons will drift in ellipse shaped trajectories in between the magnets forming a racetrack of the same kind. The big disadvantage of planar configuration is the low target utilization (see section 1.1.2.2). To solve this magnetic field configurations are being optimized and sometimes the stationary magnets are replaced by magnets which move around under the target in a complex way.

In the cylindrical-post magnetron (Fig. 1.8) the target is a cylindrical tube. This cathode tube is surrounded by a cylindrical anode establishing a radial electrical field. A uniform magnetic field is applied which is parallel with the axial axis of

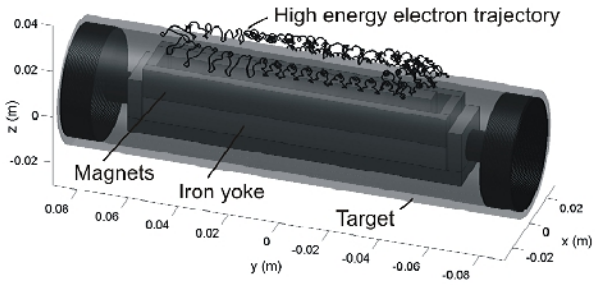

Figure 1.9: *A rotatable magnetron on lab scale with the trajectory of a high energetic electron. Figure reproduced from [32].*

the tube. This magnetic field can also be generated with permanent or electromagnets, however the cylindrical geometry allows here the use of a coaxial solenoid around the setup. In this way the electrical and magnetic field is everywhere perpendicular to each other maximizing the Hall drift which let the electrons orbit in a hopping way around the cylindrical target. This geometry results in an uniform gas ionization covering the whole cylindrical target surface. This essentially results in a uniform erosion of the target over a large extent of the target only deviating at the axial endings of the target. The electrons do not only orbit in a closed loop around target but also move along the magnetic field lines. Electron reflection surfaces at the magnetron ends where the magnetic lines crosses, prevent that the electrons get lost. These flanges are put on the same negative voltage as the cathode. The cylindrical-post magnetron has been commercially applied but the fabrication of cylindrical targets is more sophisticated and expensive compared with planar targets. The choice of target material is by this also more limited.

The rotating cylindrical magnetron (Fig. 1.9) which is for example used in the glass coating industry strongly improves the target utilization up to 85 %. The magnet design is similar with the planar rectangular magnetron, but now the target is a cylindrical tube which rotates around stationary magnets. As the racetrack moves over the target surface, the target is uniformly eroded. Nevertheless the target geometry is similar with the cylindrical-post magnetron, a possible advantage is that the sputter flux is directed to one side instead of being axial uniform. A second advantage is the better process stability during reactive magnetron sputtering. The compound formed on the target edges and outside the racetrack which can cause arcing due to charging, will rotate back into the sputter zone after each rotation. This compound is then sputtered making the target more metallic. On the other hand the rotating cylindrical magnetron shares his main disadvantage with the cylindrical-post magnetron: the more complex target fabrication. An overview of this type of magnetron can be found in [33].

1.2.2 Magnetic field

Planar and rotatable magnetrons can be classified according to the balance of their magnetic field. A magnetron is balanced when the total magnetic flux through the target surface of the outer pole equals the total flux of the inner pole (Fig. 1.10a). This means that a magnetic field line that crosses the target surface at the outer pole will cross the surface at the inner pole. The magnetron is type I unbalanced (Fig. 1.10b) when this magnetic flux is larger for the inner pole then for the outer pole and is type II unbalanced (Fig. 1.10c) when the reverse is true. The unbalance of a magnetron [34] is quantified by the coefficient K defined as

$$K = \frac{\int_{S_{out}} \mathbf{B}_{out} \cdot \mathrm{d}\mathbf{S}}{\int_{S_{in}} \mathbf{B}_{in} \cdot \mathrm{d}\mathbf{S}} \tag{1.6}$$

where the magnetic field $\mathbf{B}_{out}$ and $\mathbf{B}_{in}$ of the outer respectively the inner magnets are integrated over the area S_{out} and S_{in}. It is the area of the top surface of the corresponding magnet. A balanced magnetron has $K = 1$ while a type I unbalanced magnetron has $K < 1$ and a type II unbalanced has $K > 1$. The function of the magnetic field is the confinement of the electrons close to the target. When the magnetic field is balanced this confinement is maximal. In this case the high-energy secondary electrons emitted from the target are primarily lost to the bulk plasma after multiple ionizations when their energy drops below the threshold for ionization. Most electrons that reach the substrate will then be low energetic minimizing substrate heating. This situation is different from the typical situation for diode sputtering where substrate heating due to high-energy electrons is often substantial. Sometimes some level of substrate heating is desired. This can be controlled in magnetron sputtering by the balancing of the magnetic field. In an unbalanced magnetic field, the confinement of the electrons is relaxed. A portion of the field lines are now not closed but connect the target surface with the substrate or chamber walls. High-energy electrons gyrating around these field lines can now be transported towards the substrate depositing their energy and heating the substrate. Along their way they ionize gas atoms increasing also the ion flux towards the substrate. In this way the substrate heating becomes tunable as well as the ion-to-atom flux ratio.

1.2.3 Power characteristic

To apply sputter deposition electrical power has to be supplied to the process. This power is partially used to accelerate the ions to sputter of material but also to accelerate electrons to produce these ions. A big portion of the power is either used in excitation of the neutral gases which gives the plasma their typical glow. Different powering systems can be distinguished. The most common ones will be briefly touched on. These are direct current (DC), pulsed DC, alternating current (AC) at

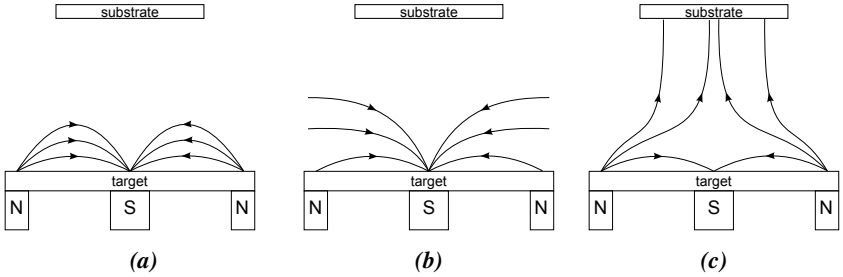

Figure 1.10: *Three types of magnetic configuration for a magnetron: balanced (a), unbalanced type I (b) and unbalanced type II (c). Figure reproduced from [35].*

radio frequencies (RF) and by high power impulses as in HiPIMS. Operating with a DC power supply is the simplest and cheapest way to operate a magnetron. The target is brought to a constant negative voltage relative to the chamber which sustains a discharge with a certain impedance that allows a constant current to flow. At the cathode the current is primarily carried by the bombarding ions but also partially by the emission of electrons due to this bombardment. The discharge current I_d can as such be related to the ion current I_{ion} as

$$I_d = I_{ion} + I_e = (1 + Y_{SEE})I_{ion} \tag{1.7}$$

where Y_{SEE} is the effective secondary electron emission yield as defined in section 1.1.2.1. Of particular importance for reactive magnetron sputtering is the inclusion of an arc suppression unit in the power supply. Arcing is a local high current discharge at a low voltage due to the build-up of charge. This can especially occur during reactive sputtering at the edges of the racetrack where a non-conducting compound is formed as its removal by sputtering is low at that place. The compound layer forms the dielectric of a charging capacitor which separates the surface charge on the compound layer with the underlying metallic target. When this "capacitor" reaches its breakdown voltage an arc takes place. Such an arc damages the target by locally melting it. This forms droplets which can hit the substrate. This negatively influences the quality of the deposited film. An arc suppression unit will prevent this arcing by monitoring the discharge current and voltage. A strong increase in current and/or a decrease in voltage indicates the development of an arc. The unit quenches this arc by briefly ($\sim \mu s$) switching off the power to discharge the built-up charge.

For pulsed DC sputtering the target is put on a comparable negative voltage as for normal DC sputtering after which the target is switch to a low positive voltage. During the negative voltage phase of the cycle the sputtering by ions takes place, while the shorter positive voltage phase is to attract electrons to the target. The purpose of the latter is to neutralize possible charging of the target during reactive

sputtering as discussed before. The asymmetry between the negative and the positive pulses is applied because of the higher electron mobility (short positive pulse) compared to the much heavier ions (long negative pulse). The typical working frequencies are application dependent but vary from 70-350 kHz [36]. This approach can also be adapted for two magnetrons in the mid-frequency AC mode (40-80 kHz). The negative and positive voltage alternates then between the two targets of the magnetrons. The first serves then as the cathode and sputtering source (negative voltage) in the first phase of a cycle while the second serves as the anode (positive voltage) of the system. During the second phase of a cycle the roles of the two targets are then reversed. This way of operating for reactive sputtering deposition does not only solve the charging problem but also the "disappearing anode" problem. This problem reveals when the anodes of the sputter system become covered by insulating compound due to the reactive deposition process. This is solved as the future anode is sputtered clean during its phase as cathode.

Radio frequency (RF) sputtering was historically the solution to deposit insulating films, also for reactive sputtering. A high-frequent (standard 13.56 MHz) electrical field is established between two electrodes. This high frequency causes only a response of the low-mass electrons to the rapid field changes while the high-mass ions only feel the field average. Because of this difference in mobility, the electrons are more easily collected by both electrodes which negatively charge. To maintain charge neutrality per cycle, the entire RF waveform is strongly biased to a negative DC voltage. The sustaining of a RF magnetron discharge is also somewhat different than with a DC magnetron discharge. The strength of the electron confinement alternates with the RF frequency due to the changing electrical field. This allows electrons to cross magnetic field lines away from the target reducing the ionization density in front of the target and the ion current. The so-called "in-phase" collisions however enhance the ionization density. These collisions occur when electrons reverse their speed direction by colliding just before the switching of the electrical field. After the switch their speed is already directed in the same direction as the accelerating field in which they gain energy. This results in a shift of the electron energy distribution to higher energies. A greater portion of the electron population will have now an energy above the ionization potential, enhancing the ionization density. However the deposition rate for RF sputtering is only half the deposition rate for DC sputtering when the same power is applied [37]. This makes RF sputtering not an attractive candidate for big scale industrial application. Additionally RF power supplies are far more complex in design and operation then DC power supplies, which further increase their expense.

HiPIMS can be considered as the most recent development in magnetron sputtering. Nowadays there is substantial scientific interest for studying and understanding this technique. In HiPIMS the power delivered to the sputter system is concentrated in short pulses ($50 - 500\ \mu s$) [38]. These pulses are generated in the

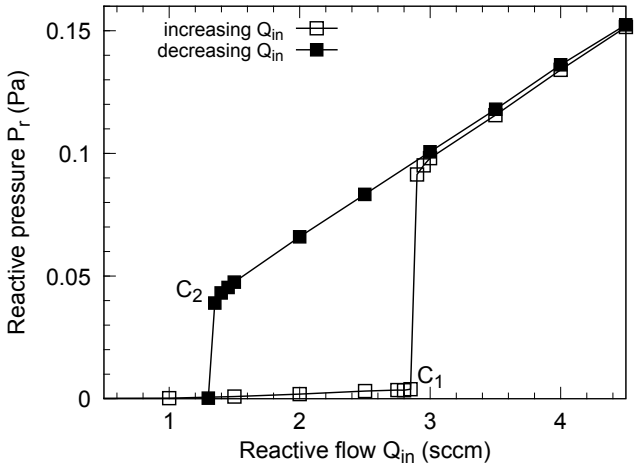

Figure 1.11: *Experimental measured $P_r - Q_{in}$ hysteresis of a* $2\,\mathrm{inch}$ *Al target sputtered in* $0.4\,\mathrm{Pa}$ *Ar with* O_2 *as reactive gas. The discharge current is* $0.5\,\mathrm{A}$ *and the pumping speed* $48\,\mathrm{Ls}^{-1}$*. The two critical points* C_1 *and* C_2 *are indicated.*

frequency range of a single pulse up to $500\,\mathrm{Hz}$ [38, 39]. During a pulse, power densities in the order of kW/cm^2 are delivered to the target. As only a minimal portion of the energy is transferred to the sputtered species during sputtering, most of the energy have to be drained off by the water cooling system. For this reason the duty cycle, which is the ratio between the on-time and the cycle time, will have to be low ($< 10\,\%$), such that the average power delivered to the target is comparable to a conventional (DC) sputtering system. The high power densities also substantially increase the plasma densities with a factor of 10^3 or even 10^4 compared with DC sputtering. A further consequence is the high ionization degree of the sputtered material, up to $70\,\%$. Combined with gas rarefaction, the initial gas discharge can even become a metal discharge where self-sputtering is the main sputtering mechanism. The high ionization degree of the sputtered material makes this technique useful for the deposition of dense layers or the coating of trenches by electrical biasing the substrate and attracting these metal ions.

1.3 Hysteresis

Contrary to non-reactive sputtering, reactive sputtering is often plagued by a hysteresis phenomenon. This hysteresis is almost inevitably connected to the reactive sputtering deposition of most compounds. It causes the deposition characteristics to be not only dependent on the present but also on previous operation conditions. As such the system response will not be unique for a given set of operation parame-

ters. The origin of this hysteresis phenomenon is the compound formation on the target during reactive sputtering deposition. A first necessary condition that some kind of hysteresis effect will emerge is then that the sputter yields of the elemental target material and the formed compound is substantially different [40]. The sputter yield of the deposited compounds like oxides, nitrides and carbides is usually much smaller than that of the elemental metal [41–43]. The second necessary condition is that the reactive gas consumption by the substrate and the target to form the compound is at least comparable with the pumping capacity of this gas by the vacuum system [44]. The level of gas consumption by the substrate and the target depends mainly on the intrinsic reactivity between the gas and the target material, and the availability of reaction sites. Section 1.3.1 illustrates how the hysteresis can be experimentally accessed. Section 1.3.1.1 qualitatively explains the mechanism behind its appearance and the three operation modes (metallic, transition and poisoned) will be defined. Section 1.3.1.2 describes the problem to access the transition mode, and shows possible solutions. In section 1.3.2 the relevance of studying the hysteresis effects in reactive sputtering deposition is been touched on.

1.3.1 Experiment

To illustrate the hysteresis effect during reactive sputtering, a typical experiment will be described. A $2\,\mathrm{inch}$ aluminum target is mounted on a circular planar magnetron. The target is DC powered while being reactively sputtered in an Ar/O_2 atmosphere. The intrinsic reactivity between oxygen and aluminum is high enough to observe a hysteresis. After pumping the chamber to a sufficiently low base pressure ($\sim 10^{-4}\,\mathrm{Pa}$) with the combination of a rotary vane and a turbomolecular pump, a constant flow of Ar gas ($10\,\mathrm{sccm}$) is introduced by means of a mass flow controller. The established Ar pressure ($0.4\,\mathrm{Pa}$) will be inversely proportional to the pumping capacity of the vacuum system for this fixed flow. This pumping speed ($48\,\mathrm{Ls}^{-1}$) should be chosen low enough to reveal the hysteresis. The DC power supply is switched on where the discharge voltage is determined by a limitation of the discharge current ($0.5\,\mathrm{A}$). For a sufficiently long time ($5\,\mathrm{min}$) the magnetron is operated in this non-reactive mode to sputter clean any surface contamination on the target and to cover the substrate with a metal layer. After process stabilization a reactive gas flow of oxygen is introduced in the chamber and stepwise increased. Between two steps, a sufficient long time interval ($2.5\,\mathrm{min}$) is present in order to reach steady state conditions. Several hysteresis quantities can be monitored in this way. In this example the reactive partial pressure is tracked and shown in Fig. 1.11. At low oxygen flows, the reactive partial pressure barely increases from the start but this slightly increases towards the first critical point C_1. This first critical point marks the oxygen flow after which the partial pressure abruptly increases. For higher oxygen flows than the first critical flow the partial

pressure will be proportional with the oxygen flow at a moderate rate. Stepwise lowering the oxygen flow after passing the first critical point will now exhibit the hysteresis. The partial pressure will now almost linearly decrease with the oxygen flow, it does not follow the initial process curve. An abrupt decrease in partial pressure occurs however just after the second critical point C_2. The corresponding oxygen flow and partial pressure is there distinctly lower than at the first critical point. The result is that for oxygen flows between the second and the first critical point two possible partial pressures exist. The actual measured pressure will depend on the process history. This kind of experiment is an example of a, here after called, hysteresis experiment under direct control. The basis of such hysteresis experiment is that the dependency of a hysteresis quantity like the reactive partial pressure is measured as function of the stepwise increase and decrease of an operation parameter like the reactive gas supply.

1.3.1.1 Direct control

The hysteresis experiment just described (section 1.3.1) can be viewed as an example of direct control. The process is governed by manually setting the operation parameters during the experiment. They are not dynamically adapted by any feedback mechanism based on monitoring of the system. It is the simplest way of controlling the reactive sputtering process. During a hysteresis experiment a single operation parameter is under direct control while all other remaining operation parameters are kept constant. In the example the reactive gas flow was directly controlled while keeping the operation parameters discharge current, pumping speed, argon flow, target and substrate area constant. This is the most common way of performing a hysteresis experiment but also direct control of the discharge power [45] or the pumping speed (while keeping other operation parameters constant) are possibilities. Figure 1.12 schematically shows a hysteresis behavior in the reactive partial pressure P_r when respectively the reactive flow Q_{in}, the discharge current I_d and the pumping speed S are stepwise increased and subsequently decreased. A qualitatively explanation of the observed hystereses goes as follows.

For the $P_r - Q_{in}$ hysteresis, the partial pressure before the first critical point C_1 slowly increases because almost all reactive gas is gettered by the substrate to form compound. Deposition of non-reacted target material on the substrate sustains this getter mechanism. Notwithstanding the target itself also getters reactive gas, most of the formed compound can be removed by sputtering. In approaching the first critical point C_1 some compound is formed on the target and the gettering capacity of the substrate gets saturated. This compound formation on the target is called target poisoning. As the gettering capacity decreases, the reactive pressure rises which severely poisons the target. As the sputtering yield of the compound is much lower than that of the elemental target, the getter capacity of the substrate is further lowered by the reduced sputter flux. This in turn further poisons the target, further

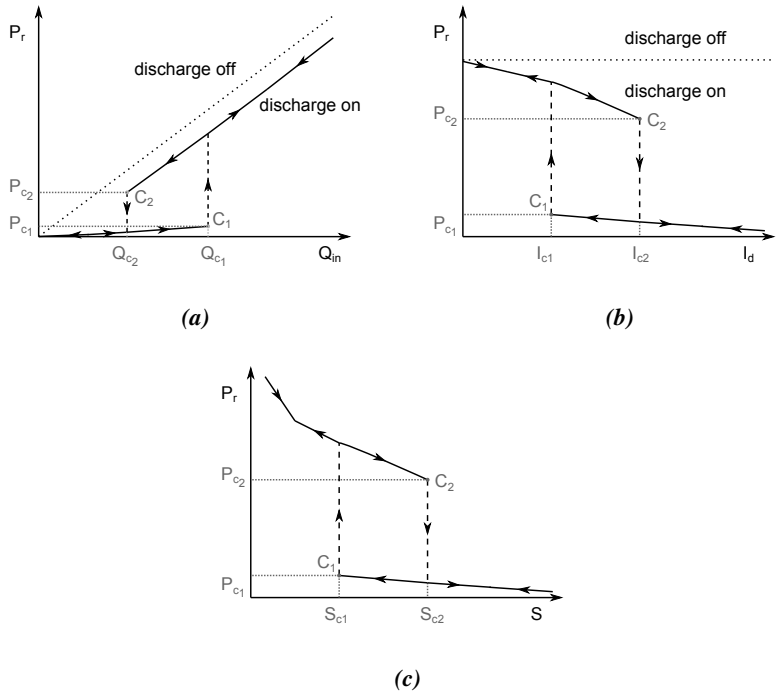

Figure 1.12: *Schematic direct controlled hystereses as function of the reactive flow Q_{in}, the discharge current I_d and the pumping speed S.*

reducing the getter capacity and a positive feedback loop arises. If the pumping speed can not take over this increasing loss in getter capacity of the system, the partial pressure will abruptly increase after this first critical point C_1. The regime before C_1 is called the metallic mode, while the regime after C_1 is called the poisoned mode. In poisoned mode the target and the substrate will both getter reactive gas at an almost constant rate independent of the reactive gas flow. The variation of P_r as function of Q_{in} will linearly change, proportional to the inverse pumping speed. The curve follows a lower line parallel with the $P_r - Q_{in}$ curve if the discharge would be switched off and only the pumping system would act. Subsequently lowering the reactive flow will deviate from the initial path when reaching the critical flow Q_{C_1}. The reactive gas gettering of the substrate was maximal just before Q_{C_1} in metallic mode due to an almost non-poisoned target. In returning towards Q_{C_1} the target is however highly poisoned. The reactive flow has first to be further reduced such that compound sputtering overcomes the compound formation on the target. This happens at the second critical point C_2 limiting the poisoned mode. There the sputter flux increases, which increases the

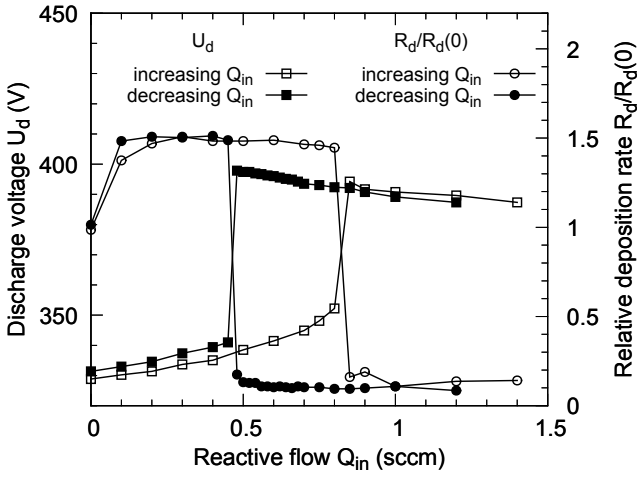

Figure 1.13: *Experimental hysteresis in discharge voltage U_d and deposition rate R_d of a Ti target sputtered in a Ar/O_2 atmosphere. A* $2\,\mathrm{inch}$ *target was mounted in a DC magnetron at a constant discharge current of* $0.3\,\mathrm{A}$*, Ar pressure of* $0.3\,\mathrm{Pa}$ *and pumping speed of* $30\,\mathrm{Ls}^{-1}$*. Data reproduced from [32]*

getter capacity of the substrate, further reducing the poisoning of the target and lowering the partial pressure. In this way the partial pressure abruptly drops and the system moves back into metallic mode. The difference between Q_{C_1} and Q_{C_2} is then called the hysteresis width.

For the $P_r - I_d$ hysteresis (Fig. 1.12b), similar mechanisms play, resulting in similar behavior. However the system is now in poisoned mode at a low discharge current. This reverses the transition as going from poisoned mode into metallic mode. The reactive flow which is now fixed should also be reasonable such that transition into metallic mode is possible at realistic discharge current. In the case of low discharge current, the target is poisoned due to a low sputtering limiting the getter capacity of the substrate. A high discharge current brings the system in metallic mode as it increases the getter capacity of the substrate by a higher sputter flux and diminishing the target poisoning. Around the critical points, similar positive feedback loops are at work as for the $P_r Q_{in}$ hysteresis. If the discharge current increases towards I_{C_1} more compound is removed from the target making it more metallic. Gradually more metal is sputtered. This increases the getter capacity of the substrate which further decreases the target poisoning and further increases the flux of sputtered metal. In this way the system abruptly shifts into metallic mode.

For the $P_r - S$ hysteresis (Fig. 1.12c), the behavior is similar as for the $P_r - I_d$

hysteresis. The system is in poisoned mode at a low pumping speed. Similarly, the reactive flow which is now fixed should be reasonable such that transition into metallic mode is possible at realistic pumping speeds. The target is now poisoned due to a high pressure which poisons the target and limits the substrate gettering rate. Of course towards the limit of no pumping the pressure will steeply increase. High pumping speed brings the system in metallic mode. A high pumping speed decreases the reactive gas available for gettering by substrate and target. Around the critical points similar positive feedback loops are at work as for the $P_r - Q_{in}$ hysteresis. For example, if the pumping speed increases towards S_{C_1} more reactive gas is extracted from the vacuum chamber, lowering the pressure and limiting the compound formation. Gradually more metal is sputtered. This increases the getter capacity of the substrate which further decreases the reactive pressure and further increases the flux of sputtered metal. In this way the system avalanches into metallic mode.

Up till now only the reactive partial pressure is pointed as hysteresis quantity. Also the discharge voltage (Fig. 1.13) is a possible hysteresis candidate when powering the magnetron with a constant current. This discharge voltage is mainly influenced by the changing reactive partial pressure and by the compound formation on the target [46, 47]. If the reactive partial pressure increases, the plasma density decreases. This is caused by the lower ionization cross section of the reactive gas molecules compared to the argon atoms and by the thermalization of the electron population due to higher cross sections for their vibrational excitations [48]. Maintaining the discharge current results then in a voltage increase. On the other hand, if the formed compound on the target has a significant higher Y_{SEE} then the elemental target, the discharge voltage will decrease as the degree of compound increases. A lower Y_{SEE} of the compound results in an increase of the voltage. The discharge voltage will exhibit a hysteresis behavior if one of the two effects dominate or when both effects amplify each other. The discharge voltage will indirectly give a measure of the reactive partial pressure or of the degree of target poisoning. Further measurable hysteresis quantities are the intensity of the optical emission line of the sputtered material quantifying the sputter rate, or the deposition rate (Fig. 1.13) which can be measured by a quartz microbalance.

1.3.1.2 Feedback control

The presence of a hysteresis causes not only history dependent deposition conditions between the critical points, but also certain deposition conditions seem not accessible. The composition of the deposited layer will primarily depend on the reactive partial pressure to which it is exposed and the deposition rate of metal. As can been seen in Fig. 1.11, the reactive partial pressure range between the first and the second critical pressures are however not reached under direct control. This is due to the positive feedback loop which develops when the critical points are

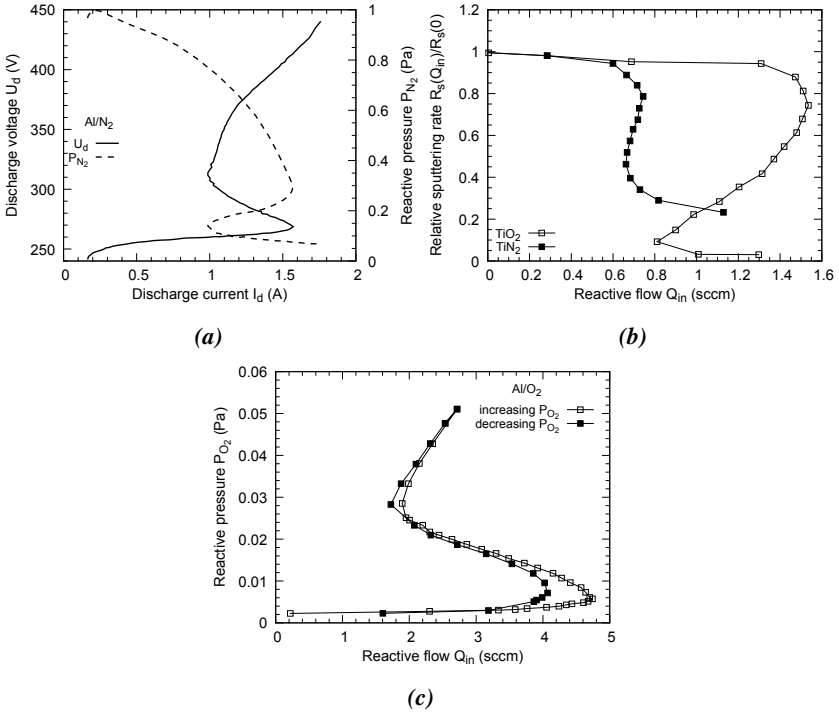

Figure 1.14: *Experimental hystereses under feedback control with as feedback signal (a) the discharge voltage [49], (b) the emission line of sputtered metal [50] and (c) the combination of the former two supplemented with mass spectroscopy [36].*

approached. To reach these seemingly inaccessible points, this positive feedback loop should be counteracted by an active feedback mechanism. By continuously monitoring a hysteresis quantity like the reactive partial pressure an independent operation parameter like the reactive gas flow can accordingly be adjusted in a way to correct the drifting of this hysteresis quantity. In this way the reactive sputter system is under feedback control. By feedback controlled operation, points in between the two critical pressures become accessible. This region of operations points embodies then the transition mode. For example, to reach a working pressure in transition mode by feedback control the system can be started from C_1 (see Fig. 1.12a). When the reactive flow is slightly increased, the reactive partial pressure will steeply increase. When the desired working pressure is reached, the feedback mechanism will strongly reduce the reactive flow to a value below Q_{C_1} to prevent a further rise of the pressure. As response, the monitored reactive pressure will drop below the desired value. The feedback mechanism will detect this and accordingly compensate by a flow adjustment. The feedback mechanism

will continuously correct the reactive flow in an attempt to converge to the desired pressure. This is necessary as these operation points are unstable in time. Even a small perturbation in the system conditions would push the system towards a stable operation point in the metallic or poisoned mode if there were no feedback adjustments. In this way the transition region becomes accessible and a subsequently increase of the controlling variable starting from C_1 towards C_2 results in the S-shaped curve as shown in Fig. 1.14.

The feasibility of feedback control was first demonstrated by Schiller et al. [51] and by Affinito et al. [49, 52]. Their feedback signal was respectively the intensity of the emission lines of the sputtered material as measured with an optical emission spectrometer, and the discharge voltage (or power). The spectral intensities decrease as the reactive partial pressure increase, while the discharge voltage is determined by the target poisoning. Figure 1.14a and Fig. 1.14b illustrate such kind of feedback controlled hysteresis measurements. Shortly after, Sproul et al. [53] used a mass spectrometer for directly monitoring the reactive partial pressure and generating a feedback signal. Affinito et al. [49] reported the successful use of the discharge voltage as feedback signal during reactive deposition of aluminum nitride (Fig. 1.14a). The time response of the feedback mechanism is an important parameter for a successful operation in the transition mode. This is the time between detecting the system change, e.g. a reactive pressure increase, generating and processing the feedback signal and finally response, e.g. a reactive flow decrease. If this time response is too long ($> 250\,\mathrm{ms}$), the hysteresis quantities will oscillate instead of converge to the desired value. This puts time restrictions as well on the hardware for generating the feedback signal as for the response. When using a mass spectrometer this can be problematic regarding the update time of the signal, while for the intensity of an emission line or a voltage measurement this is not a concern. These three feedback signals are nowadays still the most used, but all know their restrictions. Without the necessary corrections they can even turn out inappropriate feedback signals [36]. To overcome the shortcomings of one feedback signal compared with an other, modern feedback systems even combine multiple feedback signals. Figure 1.14c is the result of such feedback controlled hysteresis measurement. Also the response has to be fast enough. This response is typically a changing reactive flow [36, 45] but adapting the discharge current [45, 52] is also a possibility. In the case of a reactive flow response will most mass flow controllers be typically to slow ($\sim 1\,\mathrm{s}$). Directly controlled piezoelectric valves which regulate the reactive gas inlet showed to be fast enough [51, 53]. A hysteresis experiment under feedback control is than the stepwise increase and decrease of a hysteresis quantity that acts as the feedback signal where a variable operation parameter is used as response. This allows operating in the transition mode which connects the two critical points resulting in the S-shape of the hysteresis.

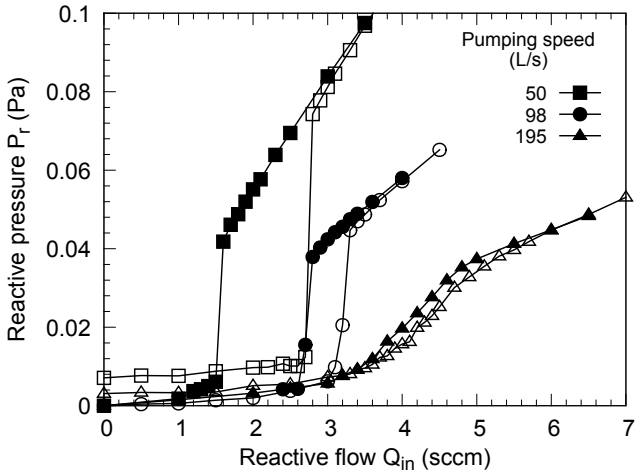

Figure 1.15: *Experimental hystereses under direct control of the reactive flow for increasing pumping speeds. The system was a* 2 inch *Al target sputtered in an Ar/O_2 atmosphere at a discharge current of* 0.5 A *and Ar pressure of* 0.4 Pa.

1.3.2 Relevance

The hysteresis phenomena during reactive sputtering are not just worth studying for the sake of scientific knowledge. The industrial relevance of understanding and mastering the hysteresis comes from the fact that the deposition rate follows the hysteresis behavior. The deposition rate is namely proportional to the average sputter yield of the target which depends on the degree of compound formation on the target. Operating in the metallic mode when the compound fraction on the target is low, results in high deposition rates due to the high sputter yield of the non-reacted metal. However the deposited films will have a typical understoichiometric composition. A full stoichiometric film is obtained in poisoned mode. Here the process is very stable and the film properties are easily reproduced. However operating in poisoned mode where a substantial amount of compound is formed on the target often results in drastically lower deposition rates (see Fig. 1.13). Also large quantities of the reactive gas are not consumed and lost to the vacuum pump. The optimum process conditions (stoichiometric composition and acceptable deposition rates) often lay in the transition mode. Operating in the transition mode is usually not easy and requires a feedback system as described in section 1.3.1.2. This nourishes the desire of industry to eliminate this hysteresis effect with a minimum in compromises, like operation cost or complexity. The disappearing of the hysteresis by increasing the pumping speed could be a solution as shown in Fig. 1.15. This effect was already demonstrated in 1983 by Serikawa and Okamoto [54, 55]. However for large industrial coaters the required pumping speeds are often un-

feasible high or come at a huge cost. As such the quest for other hysteresis free solutions is still ongoing.

1.4 Modeling the technique

During the last decades, experimental work and knowledge on all aspects of the (reactive) magnetron sputtering technique has been piling up. Experimental work alone can however not embody a complete understanding of the technique. From the smallest details up to some fundamental questions about the magnetron sputtering process are sometimes only accessible or solvable by a genuine model. The perfect model would not need any experiments as it would give the right predictions under any circumstances at maximum resolution. However on the never ending way towards such perfect model, experiments are badly needed. They are the only rightful judges to decide if a model holds or fails. As a perfect model is probably unreachable, experiments will decide the scope of validity of every proposed model. In this way modeling and experimental work are indispensable. First a more pragmatic motivation for modeling and simulating the reactive magnetron sputtering technique is given in section 1.4.1. As the reactive magnetron sputtering process encloses many different fields in physics and chemistry, the possible approaches in modeling will be almost as diverse. Section 1.4.2.1 briefly discuss the individual proposed models for each aspect of the process. In that way, the modeling of the reactive process is handled in an "atomistic" approach. In section 1.4.2.2, a "holistic" approach for modeling the reactive process as a whole, starting from the process itself, is argued.

1.4.1 Motivation

Modeling and simulating the reactive magnetron sputtering process can be motivated by the industrial importance of the technique. To obtain specific film properties, the deposition conditions will have to be just right. A genuine model would truly replace any trial-error experiment in the search for these optimal conditions. Also at the building stage of a deposition setup it would be interesting to predict the capabilities and the shortcomings of a certain design. The ability of simulating these designs would mean a huge cost reduction in manufacturing as the initial building of test setups can be minimized. The right film properties is one thing but doing this at a minimal production cost is an other. Model simulations can help to maximize the speed, the stability, the uniformity, the reproducibility or the duty cycle of the deposition. The ideal reactive magnetron sputtering simulator would have as input the wanted film properties (e.g. composition, morphology, microstructure, porosity) and the production limitations (e.g. deposition speed, energy consumption, maximal cost), and as output the necessary but optimal working

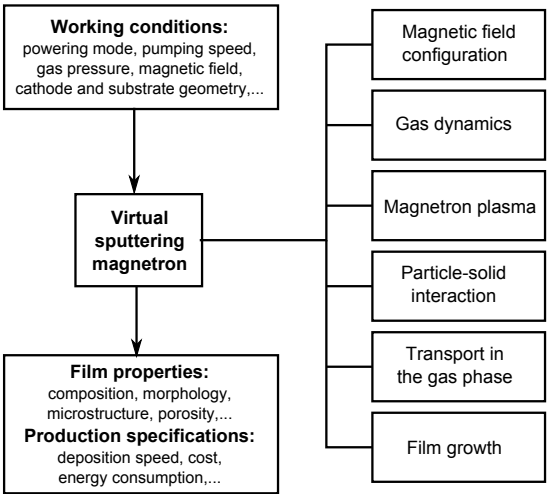

Figure 1.16: *Sketch of the virtual sputtering magnetron according the idea in [61].*

conditions (e.g. powering mode, pumping speed, gas pressure, magnetic field, substrate orientation, cathode shape). However, this kind of simulator is far from existing. A more realistic simulation model is one were in- and output are switched. Such a "virtual sputter magnetron" is the Holy Grail of the magnetron sputtering simulation community (Fig. 1.16). The inclusion of a reactive gas complicates the system to model, making this quest even harder. Some simulation projects [56–60] are working towards this goal but often the simulated pressures are quite high, the magnetic fields are at the weak side, the system sizes are small and they are mostly simulating non-reactive systems.

1.4.2 Approach

Section 1.4.2.1 gives a short overview of the current modeling and simulation approaches for the different processes during reactive magnetron sputtering deposition. Combining these different models together could then result in a global model for reactive sputtering. As the model of each individual process can already be quite complex and detailed, will the global model be even more complex. Quantitative predictions will benefit of this but the understanding of the underlying mechanisms for these predictions can become hard to retrieve. This approach could be viewed as a sort of bottom-up or "atomistic" approach where models of the individual subprocesses form the "atoms" or parts of a global model wherein they are combined. As such, the use of the term "atomistic" here does not imply that the individual models are necessarily atomistic on their own. An alternative approach is given in section 1.4.2.2 which can be viewed as a more top-bottom or

"holistic" approach where a minimal but global model is proposed and gradually extended.

1.4.2.1 Atomistic

The reactive sputtering process embodies many physical processes and as such many modeling approaches. Even an individual process can have a broad spectrum of modeling approaches to describe it reaching from simple to very complex [61, 62]. An example of the latter is the description of the magnetron discharge. Many different type of models have for this been proposed. These are analytical models [63], simplifications of the Boltzmann equation [64, 65], solutions of the fluid continuum equations [66], Monte Carlo models [67] and particle-in-cell Monte Carlo collision (PIC-MCC) models [68]. Partial combining of two or more of these approaches results in hybrid models [69]. Each model approach has its advantages but also some limitations. The benefits of analytical models is that they are very fast and often give in an easy way a good understanding of the mechanisms at play. However there quantitative validity and applicability is often limited. Solution of the full Boltzmann equation is very accurate but mostly hard to retrieve when the system is inherently two or three dimensional. Successful solving of the Boltzmann equation for the cylindrical post-magnetron (see section 1.2.1) has been performed due to the good one dimensional approximation of the system. The continuous fluid description for the plasma during magnetron sputtering is often questionable. The low pressure and high magnetic field undermine the assumption of a continuum fluid, the pure classical diffusion and the solvability of the magneto-hydrodynamic equations. Therefore it is only applicable at the boundaries of magnetron sputtering for high pressures and low magnetic fields. The PIC-MCC models compromise the least in physical description but have typical exuberant long computation times compared to alternatives. More simple Monte Carlo models alleviate this computation time at the cost of loosing self-consistency. Hybrid modeling tries to benefit from the strengths of several approaches to overcome some disadvantages of others.

The magnetron discharge is not the only physical process of importance during magnetron sputtering. At least five other important subprocesses or domains can distinguished (Fig. 1.16). These are the magnetic field configuration, the ion-solid interaction, the transport of sputtered particles, the gas dynamics and the film deposition or growth. The magnetic field can be analytically calculated if the magnet configuration remains relatively simple [70]. If more complex magnetic configuration have to be considered then the finite element method for the magnetostatic equations has to be applied [71]. High accuracy can be achieved on the condition that the spatial resolution of the mesh is small enough. This high accuracy is desirable if the calculated magnetic field is used to calculate the orbit of electrons in the plasma model.

The ion-solid interaction plays at the target where the most important effect is the sputtering of target atoms with as central quantity the sputter yield (eq. 1.1). Analytical expressions for the sputter yield as function of the ion energy [12] and the incident angle [72] exist as well as for the energy and the angular distribution of the sputtered atoms [17]. However most often this is simulated with a Monte Carlo model. In these Monte Carlo simulations the collision cascade is considered within the binary collision approximation. Within this class of MC models there are static [19, 22] and dynamic [20, 21] models. Static models do not change the state of the target due to the ion impact while dynamic models keep track of these changes. It is clear that the latter elongates the simulation time. If the energy of the involved particles becomes low ($< 100\,\mathrm{eV}$), the binary collision approximation starts to break down and more detailed molecular dynamic (MD) models [73] are necessary. A nice overview of the available simulation codes can be found in [74].

To some extent is the transport of sputtered particles through the gas phase similar with the ion-solid interaction. As such similar MC models do apply. Two main differences should however be pointed at. The energy of the transported particle is now much lower ($\sim 1\,\mathrm{eV}$) while moving through a much more rarefied medium of gas. For this combination the binary collision approximation holds out. Here a MC model [75, 76] is often followed up with a diffusion model when the followed particles thermalize. The largest uncertainty in this kind of simulations is the choice or the construction of a valid interatomic potential [77] as this directly defines the collisional behavior.

The gas dynamics of the sputter and the reactive gas are best described by a Direct Simulation Monte Carlo (DSMC) [78, 79] as rarefied gas flow conditions do apply (Knudsen number from 0.1 to 10). Industrial sputtering often happens in large vacuum chambers with multiple gas inlets, localized gas extraction by vacuum pumps and possible gas gettering by surfaces. This will inevitably result in pressure gradients even in steady state.

The last aspect is the film deposition and growth. This is probably the hardest part to model. For the prediction of the microstructure of the deposited films time expensive MD simulations [80] are needed. If however the deposition rate or the film thickness is only of interest, then this can almost be directly calculated from the arriving particle fluxes and given sticking probabilities. These sticking probabilities are however needed input parameters which can either experimentally be determined or by MD simulations.

A global detailed model for reactive magnetron sputtering can now be obtained by connecting the modeled subprocesses to each other (Fig. 1.17). One process is interconnected with an other forming one of their boundary conditions. For example the transport of the sputtered particles depends on the gas dynamics and on the ion-solid interaction. The gas dynamics describes the local gas density and as such the collision probability while the ion-solid interaction will predict the initial en-

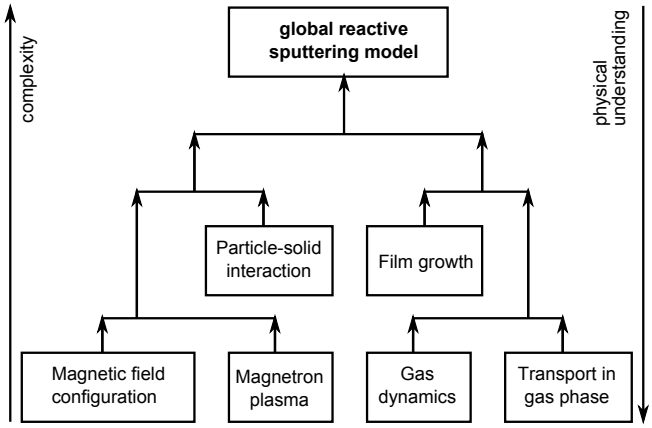

Figure 1.17: *Schematic representation of the atomistic or bottom-up modeling approach.*

ergy and starting direction of the sputtered particle determine its trajectory. In this way a bottom-up strategy for modeling is suggested, where the bottom is formed by the individual modeled subprocesses and the top is a complex multi-physics model of the complete technique, as represented in Fig. 1.17. The way to this top is however an unfinished journey with barriers of which some are hard to overcome. An important barrier is the time scale on which the different subprocesses evolve. They can differ many order of magnitude. An extreme example is the time scale of a PIC-MCC simulation which will be of the order of $10^{-11} - 10^{-12}\,\mathrm{s}$ reaching equilibrium after $\sim 10^{-5}\,\mathrm{s}$ [61] while the stabilization of the gas dynamics can be easily in the order of seconds and higher. This hampers an integrated model as the time to simulate a given snapshot of the real process will typically scale up as the minimal timescale becomes smaller. Also the spatial scale can trouble an integration. For example, the magnetic field has to be resolved at distances of $0.1\,\mathrm{mm}$ and even lower [61] while the vacuum chamber often has dimensions up to several meters. The danger also exists that this global model will only be as accurate as its weakest link. The modeling of one subprocess is more solid and well understood compared to another. Intermediate models which interconnect a subset of these processes are already presented [59, 81], but the "virtual sputter tool" is up till now not existing.

1.4.2.2 Holistic

As the main objective is the modeling and understanding of the hysteresis phenomena during reactive sputtering, a global model is desirable. These hysteresis

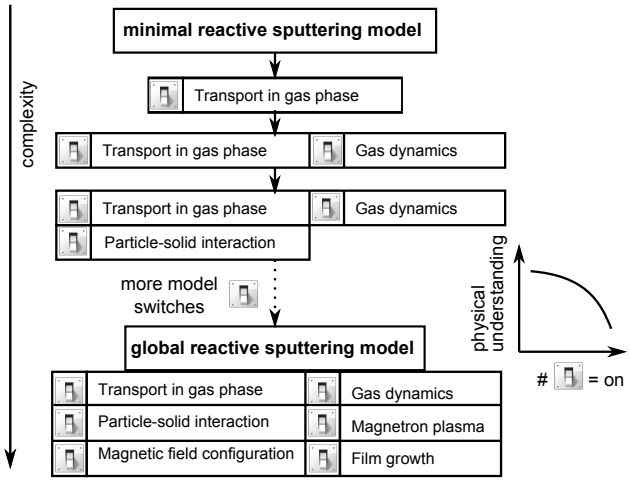

Figure 1.18: *Schematic representation of the holistic or top-bottom modeling approach.*

phenomena can be seen as a collective result of the reactive sputtering system. However proceeding to such model in a bottom-up approach as clarified in section 1.4.2.1 is not feasible. Therefore a kind of top-bottom strategy can be suggested to obtain a holistic model (Fig. 1.18). This means the formulation of an initial global but minimal model focusing on the basic understanding of reactive sputtering deposition. This simple model is then wisely extended with additional processes and details to examine their influences on the phenomena of interest or to widen its scope. Many aspects will be initially (over)simplified but this keeps the complexity low and benefits the physical insight of the system.

This way of modeling has of course also his drawbacks. A first drawback is that this kind of models will have a bunch of input parameters which have to be initially specified. Some will be straightforward operation parameters while other will be specific material dependent. A third class of parameters embodies simplifications of processes that influence the phenomena of interest but are not fully modeled. The second drawback is partially a consequence of the first. The quantitative accuracy of these holistic models will be poor without experimental fitting. However this dependency on experimental input will decrease as the model is more extended in moving from top to bottom. A good practice in developing such models is assuring the ability to return to simplified approaches of certain subprocesses. In Fig. 1.18 this is represented by model "switches". In this way the individual impact on the current research question of the different subprocesses can be studied better. Additionally proven dependencies with minor impact can be left out to speed up the simulation. To conclude neither of the proposed model strategies bottom-up or top-bottom is labeled here as more valuable. A choice

depends on the kind of questions you want to get answered and the time criticality in obtaining an answer.

1.5 Summary

Reactive magnetron sputtering deposition is a technique to cover the surface of an object with a thin film of a certain compound. The material to form this compound originates from sputtered material that reacts with a reactive gas. The physical mechanism of sputtering is widely occurring and is already studied for more than 150 years in all his forms. Within the thin film community this process is enhanced by the introduction of a magnetron compared to diode sputtering systems. A magnetic field bounds the ionizing electrons close to the sputtering surface to increase the bombarding ion flux which results in a higher sputter flux. Reactive magnetron sputtering can be classified as an atomic deposition technique and more specifically as a Physical Vapor Deposition (PVD) process. The reactive aspect in this technique covers a fourfold meaning with as most important the sputtering of a metal target within a mixed inert/reactive gas atmosphere.

The geometric designs of magnetrons is quite divers from rectangular and circular planar magnetrons over cylindrical post-magnetrons which are both stationary, towards large cylindrical rotatable magnetrons. The closure of the magnetic field is here a crucial property as it defines the bounding of the electrons to the target surface. More open magnetic field configuration allows an intenser electron flux towards the deposited film. Magnetrons are electrical powered in different ways, where the most common methods are direct current (DC), pulsed DC, alternating current (AC) at radio frequencies (RF) and high power impulses as in HiPIMS. The studied systems in this work will only consider a circular planar magnetron which is electrical DC powered.

Hysteresis phenomena are almost inevitably connected to reactive sputtering deposition of most compounds. This makes that process curves have no unique relation with their operation parameters, but are history dependent. Experimentally, these hysteresis phenomena are best illustrated by so-called hysteresis experiments. Two types are distinguished: direct controlled and feedback controlled hysteresis experiments. For the direct controlled experiment, a single operation parameter is manually stepwise changed, resulting in critical transition along the process curve of some system observables. For the feedback controlled experiment, this operation parameter is automatically adapted based on the feedback of one or more system observables which is now stepwise increased and decreased. The technological relevance of this hysteresis phenomena is their impact on the deposition rates and the consequences on the stability during process control.

The technique of reactive sputtering is widely applied and investigated as well experimentally as from modeling viewpoint. This work focuses on the modeling

side. Within the modeling world of this technique, two approaches can be formulated: an “atomistic” or bottom-up approach and a “holistic” or top-bottom approach. In the “atomistic” approach, the complex subprocesses are first separately modeled in great detail after which they are combined in a complex multi-physics model for reactive sputtering deposition. In the “holistic” approach, the set off is a global and (over)simplified model for reactive sputtering deposition which is gradually and modular extended. Both approaches have their value, strengths and weaknesses. The models discussed in the coming two chapters can all be classified in the later holistic or top-bottom strategy.

References

[1] Barghouty, A. F., Meyer, F. W., Harris, P. R., and Adams, J. H. *Nuclear Instruments & Methods in Physics Research Section B-Beam Interactions with Materials and Atoms* **269**(11), 1310–1315 (2011).

[2] Brooks, J. N., Allain, J. P., Doerner, R. P., Hassanein, A., Nygren, R., Rognlien, T. D., and Whyte, D. G. *Nuclear Fusion* **49**(3), 035007 (2009).

[3] Grove, W. R. *Philosophical Transactions of the Royal Society of London* **142**, 87–101 (1852).

[4] McPhail, D. S. *Journal of Materials Science* **41**(3), 873–903 (2006).

[5] Valbusa, U., Boragno, C., and de Mongeot, F. B. *Journal of Physics-Condensed Matter* **14**(35), 8153–8175 (2002).

[6] Westwood, W. *Sputter deposition*. AVS, (2003).

[7] Bordes, J. M. and Bauer, P. *Journal of Vacuum Science & Technology a-Vacuum Surfaces and Films* **19**(3), 812–819 (2001).

[8] Bohdansky, J. *Journal of Nuclear Materials* **9394, Part 1**, 44–60 (1980).

[9] Oechsner, H. *Zeitschrift Fur Physik* **261**(1), 37–58 (1973).

[10] Mousel, T., Eckstein, W., and Gnaser, H. *Nuclear Instruments & Methods in Physics Research Section B-Beam Interactions with Materials and Atoms* **152**(1), 36–48 (1999).

[11] Martynenko, Y. V., Rogov, A. V., and Shul'ga, V. I. *Technical Physics* **57**(4), 439–444 (2012).

[12] Sigmund, P. *Physical Review* **184**(2), 383–416 (1969).

[13] Thompson, M. W. *Physics Reports* **69**(4), 335–71 (1981).

[14] Thompson, M. W. *Vacuum* **66**(2), 99–114 (2002).

[15] Mahan, J. E. and Vantomme, A. *Journal of Vacuum Science & Technology a-Vacuum Surfaces and Films* **15**(4), 1976–1989 (1997).

[16] Mahan, J. E. and Vantomme, A. *Physical Review B* **61**(12), 8516–8525 (2000).

[17] Stepanova, M. and Dew, S. K. *Journal of Vacuum Science & Technology a-Vacuum Surfaces and Films* **19**(6), 2805–2816 (2001).

[18] Stepanova, M. and Dew, S. K. *Journal of Applied Physics* **92**(3), 1699–1708 (2002).

[19] Takeuchi, W. and Yamamura, Y. *Radiation Effects and Defects in Solids* **71**(1-2), 53–64 (1983).

[20] Moller, W., Eckstein, W., and Biersack, J. P. *Computer Physics Communications* **51**(3), 355–368 (1988).

[21] Mutzke, A., Schneide, R., Eckstein, W., and Dohmen, R. *SDTrimSP Version 5.00 : Report IPP 12/8*. Technical report, (2011).

[22] Ziegler J.F., Biersack J.P., Z. M. *SRIM - The Stopping and Range of Ions in Matter*. www.srim.org. (2012).

[23] Urbassek, H. M. *Nuclear Instruments & Methods in Physics Research Section B-Beam Interactions with Materials and Atoms* **122**(3), 427–441 (1997).

[24] Smith, R. *Atomic and ion collisions in solids and at surfaces theory, simulation and applications*. Cambridge University Press, (1997).

[25] Buyle, G. *Simplified model for the d.c. planar magnetron discharge*. PhD thesis, (2005).

[26] Chapman, B. *Glow Discharge Processes: Sputtering and Plasma Etching*. Wiley, (1980).

[27] Lieberman, M. and Lichtenberg, A. *Principles of Plasma Discharges and Materials Processing*. Wiley, (2005).

[28] Barnat, E. and Lu, T. *Pulsed and Pulsed Bias Sputtering: Principles and Applications*. Kluwer Academic Publishers, (2003).

[29] Ohring, M. *Materials science of thin films Deposition & structure*, chapter 5, 203–275. Academic Press (2002).

[30] Ball, D. J. *Journal of Applied Physics* **43**(7), 3047–& (1972).

[31] Martin, P. M. *Handbook of Deposition Technologies for Films and Coatings*, chapter 1, 1–31. William Andrew Publishing, 3rd edition (2010).

[32] Depla, D. *Magnetrons, reactive gases and sputtering*. Lulu.com, 2nd edition, (2014).

[33] De Gryse, R., Haemers, J., Leroy, W. P., and Depla, D. *Thin Solid Films* **520**(18), 5833–5845 (2012).

[34] Svadkovski, I. V., Golosov, D. A., and Zavatskiy, S. M. *Vacuum* **68**(4), 283–290 (2002).

[35] Boydens, F. *Key aspects of sputter ing illustrated by the use of multi-element powder mixtures*. PhD thesis, (2013).

[36] Sproul, W. D., Christie, D. J., and Carter, D. C. *Thin Solid Films* **491**(1-2), 1–17 (2005).

[37] Este, G. and Westwood, W. D. *Journal of Vacuum Science & Technology a-Vacuum Surfaces and Films* **6**(3), 1845–1848 (1988).

[38] Helmersson, U., Lattemann, M., Bohlmark, J., Ehiasarian, A. P., and Gudmundsson, J. T. *Thin Solid Films* **513**(1-2), 1–24 (2006).

[39] Depla, D., Mahieu, S., and Greene, J. E. *Handbook of Deposition Technologies for Films and Coatings*, 253–296. William Andrew Publishing, 3rd edition (2010).

[40] Hollands, E. and Campbell, D. S. *Journal of Materials Science* **3**(5), 544–552 (1968).

[41] Behrisch, R. and Andersen, H. H. *Sputtering by particle bombardment II*. Springer-Verlag, (1983).

[42] Gntherschulze, A. and Betz, H. *Zeitschrift fr Physik* **108**(11-12), 780–785 (1938).

[43] Schirrwitz, H. *Beitrge aus der Plasmaphysik* **2**(3), 188–204 (1962).

[44] Kadlec, S., Musil, J., and Vyskocil, H. *Journal of Physics D-Applied Physics* **19**(9), L187–L190 (1986).

[45] Malkomes, N. and Vergohl, M. *Journal of Applied Physics* **89**(1), 732–739 (2001).

[46] Lewis, M. A., Glocker, D. A., and Jorne, J. *Journal of Vacuum Science & Technology a-Vacuum Surfaces and Films* **7**(3), 1019–1024 (1989).

[47] Goranchev, B., Orlinov, V., and Popova, V. *Thin Solid Films* **33**(2), 173–183 (1976).

[48] Eltoukhy, A. H., Natarajan, B. R., Greene, J. E., and Barr, T. L. *Thin Solid Films* **69**(2), 229–235 (1980).

[49] Affinito, J. and Parsons, R. R. *Journal of Vacuum Science & Technology A* **2**(3), 1275–1284 (1984).

[50] Moradi, M., Nender, C., Blom, H. O., and Berg, S. *Vacuum* **41**(7-9), 1974–1976 (1990).

[51] Schiller, S., Heisig, U., Steinfelder, K., Strümpfel, J., Voigt, R., Fendler, R., and Teschner, G. *Thin Solid Films* **96**(3), 235–240 (1982).

[52] McMahon, R., Affinito, J., and Parsons, R. R. *Journal of Vacuum Science & Technology* **20**(3), 376–378 (1982).

[53] Sproul, W. and Tomashek, J. *Initiation by bombardment of target with ionized inert gas*. US4428811 A. (1984).

[54] Serikawa, T. and Okamoto, A. *Thin Solid Films* **101**(1), 1–6 (1983).

[55] Okamoto, A. and Serikawa, T. *Thin Solid Films* **137**(1), 143–151 (1986).

[56] Serikov, V. V., Kawamoto, S., and Nanbu, K. *Plasma Science, IEEE Transactions on* **27**(5), 1389–1398 (1999).

[57] Vyas, V. and Kushner, M. J. *Journal of Vacuum Science & Technology A* **24**(5), 1955–1969 (2006).

[58] Kolev, I. and Bogaerts, A. *Plasma Science, IEEE Transactions on* **34**(3), 886–894 (2006).

[59] Jimenez, F. J. and Dew, S. K. *Journal of Vacuum Science & Technology A* **30**(4), 041302 (2012).

[60] Jimenez, F. J., Dew, S. K., and Field, D. J. *Journal of Vacuum Science & Technology A* **32**(6), 061301 (2014).

[61] Bogaerts, A., Kolev, I., and Buyle, G. *Reactive Sputter Deposition*, chapter 3, 61–130. Springer Berlin Heidelberg (2008).

[62] Bogaerts, A., Bultinck, E., Kolev, I., Schwaederle, L., Van Aeken, K., Buyle, G., and Depla, D. *Journal of Physics D-Applied Physics* **42**(19), 194018 (2009).

[63] Bradley, J. W. *Plasma Sources Science and Technology* **7**(4), 572–580 (1998).

[64] Porokhova, I. A., Golubovskii, Y. B., and Behnke, J. F. *Physical Review E* **71**(6), 066406 (2005).

[65] Porokhova, I. A., Golubovskii, Y. B., and Behnke, J. F. *Physical Review E* **71**(6), 066407 (2005).

[66] Surzhikov, S. T. and Shang, J. S. *Journal of Computational Physics* **199**(2), 437–464 (2004).

[67] Sheridan, T. E., Goeckner, M. J., and Goree, J. *Journal of Vacuum Science & Technology a-Vacuum Surfaces and Films* **8**(1), 30–37 (1990).

[68] Kolev, I. and Bogaerts, A. *Journal of Vacuum Science & Technology A* **27**(1), 20–28 (2009).

[69] Kolev, I. and Bogaerts, A. *Contributions to Plasma Physics* **44**(7-8), 582–588 (2004).

[70] Ravaud, R., Lemarquand, G., Lemarquand, V., and Depollier, C. *Ieee Transactions on Magnetics* **44**(8), 1982–1989 (2008).

[71] Meeker, D. *FEMM*. http://www.femm.info. (2013).

[72] Eckstein, W. and Preuss, R. *Journal of Nuclear Materials* **320**(3), 209–213 (2003).

[73] Yorizane, K., Muramoto, T., and Yamamura, Y. *Nuclear Instruments & Methods in Physics Research Section B-Beam Interactions with Materials and Atoms* **153**(1-4), 292–297 (1999).

[74] Ono, T., Kenmotsu, T., and Muramoto, T. *Reactive Sputter Deposition*, chapter 1, 1–42. Springer Berlin Heidelberg (2008).

[75] Macak, K., Macak, P., and Helmersson, U. *Computer Physics Communications* **120**(2-3), 238–254 (1999).

[76] Van Aeken, K., Mahieu, S., and Depla, D. *Journal of Physics D-Applied Physics* **41**(20), 205307 (2008).

[77] Kuwata, K. T., Erickson, R. I., and Doyle, J. R. *Nuclear Instruments & Methods in Physics Research Section B-Beam Interactions with Materials and Atoms* **201**(4), 566–570 (2003).

[78] Shen, C. *Rarefied Gas Dynamics*, chapter 8, 275–315. Springer Berlin Heidelberg (2005).

[79] Pflug, A., Siemers, M., and Szyszka, B. *Recent Advances in Parallel Virtual Machine and Message Passing Interface*, 383–390. (2006).

[80] Georgieva, V., Saraiva, M., Jehanathan, N., Lebelev, O. I., Depla, D., and Bogaerts, A. *Journal of Physics D-Applied Physics* **42**(6), 065107 (2009).

[81] Pflug, A., Szyszka, B., and Niemann, J. *Thin Solid Films* **442**(1-2), 21–26 (2003).

2 First Models

2.1 Pre-Berg models

Berg et al. [1] proposed their analytical model for reactive sputtering in 1987. The Berg model is able to produce the hysteresis phenomena. Analytical modeling of reactive sputtering in the sense of thin film deposition sets off much earlier with a model by Heller [2] (section 2.1.1). More quantitative models followed which were formulated by Abe [3] (section 2.1.2) and Shinoki [4] (section 2.1.3). These simple models are however not able to describe a hysteresis as they focus on the abrupt decrease in deposition and sputtering rate at a critical reactive partial pressure as observed in experiments [5, 6]. This was attributed to the poisoning of the target as the compound has a typically much lower sputtering yield. Only the model proposed by Steenbeck [7] (section 2.1.4) was the first pre-Berg model that enables the reproduction of the hysteresis. Modeling by Affinito [8] (section 2.1.5) recognized as first reactive ion implantation as possible compound forming mechanism besides chemisorption.

2.1.1 Heller model

Heller [2] gave an explanation with his model for the decrease of the sputtering rate observed during DC and RF sputtering in an Ar/O_2 atmosphere. Experiments with varying reactive pressure but fixed total pressure showed that this decrease started at a critical pressure P_c of the reactive gas. He distinguished two situations, one where this decrease sets off smoothly and a second where this decrease was

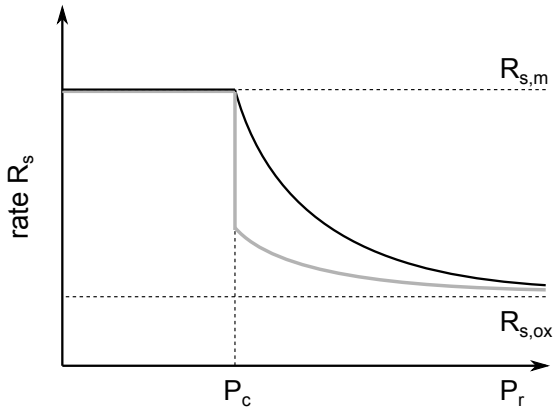

Figure 2.1: *Abrupt (grey) and smooth (black) transition of the sputter rate at the critical reactive pressure P_c.*

abrupt. Figure 2.1 schematically illustrates the two situations. For pressures below P_c the sputtering rate R_s is almost constant and equals the sputtering rate of the metal $R_{s,m}$. The more the pressures exceeds P_c, the more it converges towards the (lower) sputtering rate of the oxide $R_{s,ox}$. Heller explained this by a changing balance between the oxidation and the sputtering rate which both depend on the oxide thickness x at the target surface. For the oxidation rate he also assumed a dependency on the reactive pressure P_r. Heller defined the oxidation rate R_{ox} as

$$R_{ox}(x, P_r) = \rho \frac{\mathrm{d}x}{\mathrm{d}t} = A(P_r) e^{-\frac{x}{B}} \tag{2.1}$$

where ρ is the mass density of the oxide, $A(P_r)$ a function increasing with increasing P_r and B a characteristic thickness limiting the oxidation rate. The sputtering rate $R_s(x)$ has the form

$$R_s(x) = R_{s,ox} + (R_{s,m} - R_{s,ox}) e^{-\frac{x}{C}} \tag{2.2}$$

with $R_{s,ox}$ and $R_{s,m}$ respectively the sputtering rate of the oxide and the metal, and C a constant characterizing the depth from where particles are sputtered. The oxide thickness x and the sputtering rate R_s are then determined by the ratio of R_s and R_{ox}. The high metallic sputtering rate is obtained when $R_s(0) > R_{ox}(0, P_r)$ for $P_r < P_c$. The critical pressure P_c is defined by the condition that $R_s(0) = R_{ox}(0, P_c)$. The sputtering rate is lowered if $R_s(0) < R_{ox}(0, P_r)$ for $P_r > P_c$. The oxide thickness and sputtering rate is then defined by the condition $R_s(x_{ox}) = R_{ox}(x_{ox}, P_r)$. The abruptness of the transition from the high to the

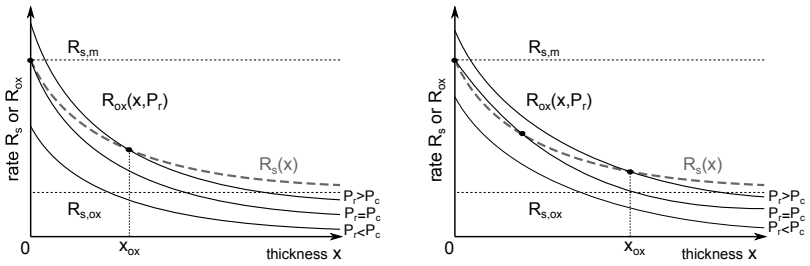

Figure 2.2: *The balance between the oxidation rate R_{ox} and the sputtering rate R_s with the corresponding oxide thickness x_{ox} as function of the reactive pressure P_r for a smooth transition (a) and for an abrupt transition (b).*

low sputtering rate depends on how the functions $R_s(x)$ and $R_{ox}(x, P_r)$ change as function of P_r. Figure 2.2 illustrates the two situations of a smooth and an abrupt transition. For the smooth transition (Fig. 2.2a) there is only a single intersection of $R_s(x)$ and $R_{ox}(x, P_r)$ when $P_r > P_c$. For the abrupt transition (Fig. 2.2b) there exist two intersection points at $P_r = P_c$. In the latter case, if P_r becomes greater then P_c the first intersection disappears at $x = 0$ and the system jumps towards the second intersection with a thicker oxide layer x_{ox} and a substantial lower sputtering rate. In the smooth case the intersection point runs smoothly along the $R_s(x)$ with increasing P_r starting at $x = 0$ for $P_r = P_c$.

This model only considers the compound formation at the target side. The role of the substrate is not incorporated. Heller also did not quantify any of the model parameters by experiments for example. Nevertheless he modeled a mechanism describing the observed sputtering rate decreases by a balance between compound (oxide) formation and removal.

2.1.2 Abe model

Abe and Yamashina [3] also formulated a model to explain the steep decrease in sputtering rate around a critical reactive pressure. Similar to Heller's model does this model only describe a balance at the target side with the reactive pressure as independent variable. They derived a formula for the sputtering rate R_s depending on the reactive pressure P_r. They stated that R_s, by definition, is a linear combination of the metallic sputtering rate $R_{s,m}$ and the compound sputtering rate $R_{s,ox}$ as

$$R_s(\theta_t) = R_{s,m}(1 - \theta_t) + R_{s,ox}\theta_t \tag{2.3}$$

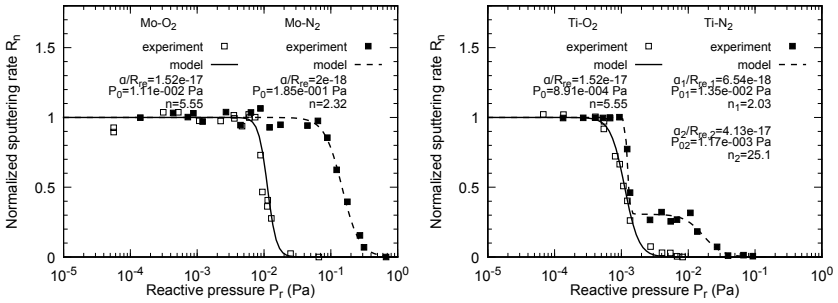

Figure 2.3: *Normalized sputtering rate (eq. 2.5) as function of the reactive pressure for (a) a Mo-O_2 and a Mo-N_2 system and for (b) a Ti-O_2 and a Ti-N_2 system. For the Ti-N_2 system a two term linear combination of eq. 2.5 is used for fitting with weights $b_1 = 0.307$ and $b_2 = 0.693$. Experimental data reproduced from [3].*

where θ_t is the fractional coverage of the target by adsorbed reactive gas atoms. The variation with time of this fraction θ_t is given by

$$n_t \frac{\mathrm{d}\theta_t}{\mathrm{d}t} = \alpha \left(\frac{P_r}{P_0}\right)^n F_r(P_r)(1-\theta_t) - R_{re}\theta_t \tag{2.4}$$

where n_t is the total number of absorption sites, $\alpha(\frac{P_r}{P_0})^n$ the specific sticking probability at P_r, $F_r(P_r)$ the flux of reactive gas atoms by kinetic gas theory and R_{re} the re-emission rate of reactive gas atoms when all absorption sites are occupied. The parameter P_0 is the saturation pressure introduced by the Brunauer-Emmett-Teller (BET) theory [9] and n the order of reaction. The steady state condition for eq. 2.4 yields an expression for θ_t. Substitution in eq. 2.3 and following normalization gives

$$R_n(P_r) = \frac{R_s(P_r) - R_{s,ox}}{R_{s,m} - R_{s,ox}} = 1 - \frac{(\alpha/R_{re})(P_r/P_0)^n F_r(P_r)}{1 + (\alpha/R_{re})(P_r/P_0)^n F_r(P_r)} \tag{2.5}$$

expressing the sputtering rate as function of the reactive pressure. This equation was well fitted to deposition rate measurements instead of the sputtering rate, which are modeled, for Mo/O_2, Mo/N_2 (Fig. 2.3a) and Ti/O_2 (Fig. 2.3b) systems with α/R_{re}, n and P_0 as fitting parameters. However for compounds with several co-existing stoichiometries like TiN and Ti_2N, they argued that a linear combination of eq. 2.5 with different parameters sets $(\alpha/R_{re})_i$, n_i and $P_{0,i}$ is justified to accurately fit these experiments.

Hrbek [10] formulated this same model two year later but sets the reaction number $n = 0$. He also fitted this model to experiments but now with sputter rate measurements instead of deposition measurements like Abe. The parameter R_{re}

is determined as $R_{re} = \alpha F_r(P_r^*)$ where P_r^* is the reactive pressure at $\theta_t = 1/2$ or the pressure corresponding with the normalized sputtering rate $R_n(P_r^*) = 1/2$ retrieved from the experiment. This reduces the fitting parameters to only α if the sputtering rates $R_{s,m}$ and $R_{s,ox}$ are know. As this model did not satisfactorily described the measurements for Mo$-$O$_2$ and Ta$-$N$_2$, he proposed to adapt the sputtering rate as

$$R_s^{mol}(\theta_t) = R_{s,m}(1 - \theta_t^2) + R_{s,ox}\theta_t^2 \tag{2.6}$$

which expresses a sputtering rate of molecules compared to the atomic sputtering rate of eq. 2.3.

Castellano [11] used the full Abe-Yamashina model for their experiments and showed that the saturation pressure P_0 in the model could be determined as

$$P_0 = 3.0 \times 10^{-5} \frac{D_m}{\Delta G^\circ} \tag{2.7}$$

where D_m is the deposition rate of pure metal (Å per minute) and ΔG° is the standard free energy of compound formation (cal per mole).

2.1.3 Shinoki model

The model of Shinoki and Itoh [4] is a modification of Abe model with the extension of including reactive gas gettering by the deposited metal particles. The focus remains however on the description of the decrease in sputtering rate as function of the reactive pressure. The expression for the time variation of the fractional coverage θ_t of the target is given as

$$n_t \frac{\mathrm{d}\theta_t}{\mathrm{d}t} = \alpha F_r(P_r)(1 - \theta_t) - Y_c \frac{J_{ion}}{e}\theta_t \tag{2.8}$$

where n_t is the total number of absorption sites, α is the sticking probability, $F_r(P_r)$ the flux of reactive gas atoms by kinetic gas theory, Y_c the sputtering yield of the compound, J_{ion} the ion current density and e the elementary charge. This corresponds with eq. 2.4 taking the reaction parameter $n = 0$ and identifying the re-emission rate $R_{re} = Y_c J_{ion}/e$. Shinoki and Itoh now included an expression for the reactive pressure P_r as the effective reactive pressure during the process. They stated that

$$P_r S = P_{r,in} S - \gamma \frac{Y_m J_{ion} A_t}{e}(1 - \theta_t) \tag{2.9}$$

where $P_{r,in}$ is the reactive pressure if the discharge is off, γ is a conversion factor of sputtered atoms to the gas adsorption rate, S is the pumping speed, Y_m is the sputtering yield of metal and A_t is the sputtering area on the target. Equation 2.9 gives an expression for the balance in gas consumptions. The LHS is the flow of reactive gas pumped away, while the second term of the RHS is the flow Q_s

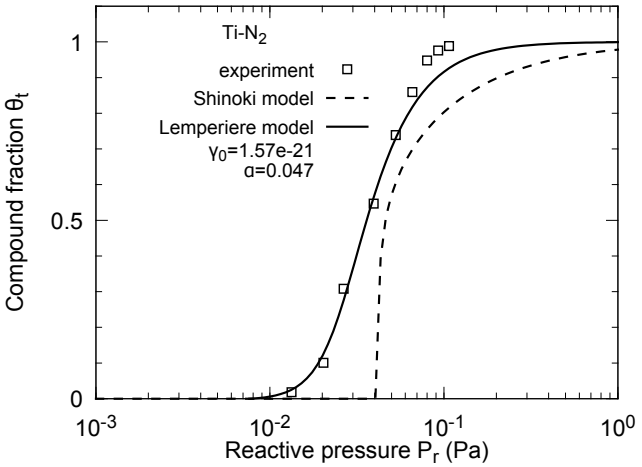

Figure 2.4: *The model of Lemperiere fitted to a Ti-N_2 system with γ_0 (eq. 2.10) and α (eq. 2.4) as fitting parameters. This is compared with the model of Shinoki applying the same parameters. Experimental data and remaining system parameters reproduced from [12].*

of reactive gas incorporated in the deposited film on the substrate. The first term of the LHS is then the flow $Q_{in}(= P_{r,in}S)$ of reactive gas introduced into the process. This remark is interesting as eq. 2.9 gives the relation between reactive gas flow Q_{in} and the effective reactive pressure P_r after substitution of eq. 2.8. This enables a possible description of a hysteresis behavior between these two variables. However the authors proceeded differently. Elimination of P_r between eq. 2.8 and eq. 2.9 gives a quadratic equation $f(\theta_t^2, \theta_t)$. Its solution is substituted into the expression of the sputtering rate R_s (eq. 2.3) which becomes a function of $P_{r,in}$.

The decrease of the sputtering rate as function of the reactive pressure which sets off from a critical pressure P_c could be reproduced as follows. The discriminant $D(P_{r,in})$ of the quadratic equation $f(\theta_t^2, \theta_t)$ sets a condition for P_c by $D(P_c) = 0$. The high sputtering rate $R_{s,m}$ is then obtained by the condition $D(P_{r,in}) < 0$ for $P_{r,in} < P_c$ and the only solution for θ_t is $\theta_t = 0$. While a decreasing sputtering rate $(R_{s,m} \rightarrow R_{s,r})$ is then defined by the condition $D(P_{r,in}) > 0$ for $P_{r,in} > P_c$ with a solution for $\theta_t > 0$.

Lemperiere and Poitevin [12] took over the model Shinoki with two modifications. They set the reaction number $n = 1$ in the original equation of Abe (eq. 2.4) and the conversion factor γ in eq. 2.9 was made pressure dependent as

$$\gamma(P_r) = \gamma_0 \frac{P_r}{P_r + P_0} \tag{2.10}$$

with P_0 the previous defined saturation pressure. These modifications gave a smoother behavior of θ_t near the critical pressure. A fit of the Lemperiere model to a Ti-N_2 system is shown in Fig. 2.4 where it is compared with the model of Shinoki applying the same parameters.

2.1.4 Steenbeck model

Steenbeck et al. [7] were the first to formulate a model that was able to describe the hysteresis phenomena. The essence of the model is the one of Shinoki (eq. 2.8) and eq. 2.9), where they made the gettering of reactive gas by sputtered metal dependent on the fractional oxidation θ_s of the gettering surfaces (= substrate). Their model takes the non uniform ion current on the target into account, but to easily compare it with previous and further models, the uniform formulation will be treated here. They modified the original eq. 2.9 of Shinoki to

$$P_r S = P_{r,in} S - \theta_s R_{s,m}(1 - \theta_t) \tag{2.11}$$

where the second term of the RHS is identified as the reactive flow Q_s consumed by the substrate and the sputtering rate $R_{s,m}$ of the metal is defined as

$$R_{s,m} = \frac{Y_m J_{ion} A_t}{e} \tag{2.12}$$

Necessarily they added a relation for the oxidation fraction θ_s as

$$2R_{s,m}\theta_s = \alpha_s F_r(P_r)(1 - \theta_s)A_s \tag{2.13}$$

where A_s is the gettering surface area and the sticking coefficient α_s for the substrate, like α for the target, was set to 1.

This model was used by the authors to describe the hysteresis in the IV characteristics of a reactive sputter process by solving the equations (eq. 2.8, eq. 2.11 and eq. 2.13) towards the ion current $I_{ion}(\theta_t) = J_{ion}(\theta_t)A_t$ and assuming the relation

$$V(\theta, I_{ion}) = V' \left(\frac{I_{ion}}{C A_t} \right)^{1/(\nu + \beta\theta)} \tag{2.14}$$

between the discharge voltage V and the ion current I_{ion}, where V', C, $\nu > 4$ and β are constants fitted to IV characteristics of fully metallic and fully poisoned targets. In this way they were able to qualitatively produce the observed hysteric IV characteristics within a given range of reactive flows. Interesting is that the model also reproduce other hystereses like the reactive pressure $P_r(Q_{in})$ with $Q_{in} = P_{r,in}S$ the reactive flow or the compound coverage $\theta_t(I_{ion})$. This is illustrated in Fig. 2.5 where the model of Steenbeck is compared with the original Berg model (see section 2.2.1).

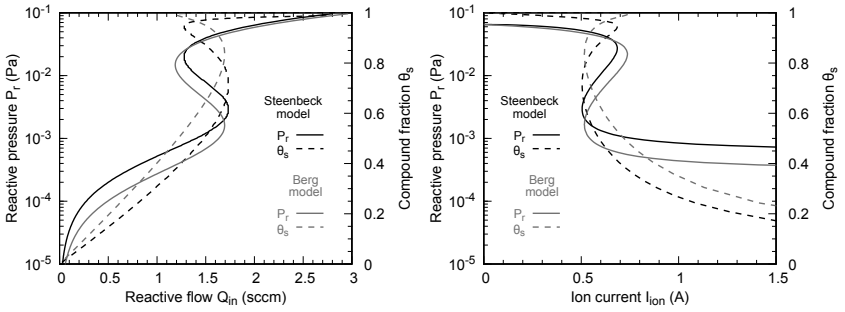

Figure 2.5: *Calculated hysteresis curve for (a) the Q_{in} and for (b) the I_{ion} dependency ($Q_{in} = 1.75\,\mathrm{sccm}$). The reactive pressure P_r and the compound fraction θ_s on the substrate are compared between the model of Steenbeck (black lines) and the original Berg model (gray lines). The Berg model is treated in section 2.2.1. The model parameters are taken from Table 2.1.*

2.1.5 Affinito model

Affinito and Parsons [8] were the first to include compound formation on the target due to the implantation of reactive gas ions. They experimentally considered two metal-gas combinations in their DC sputter system: Al−O_2 and Al−N_2. While the chemisorption of O_2 on Al is strong, this is for the Al−N_2 system very weak. Therefore they suggested that reactive ion plating to the target should be the dominating poisoning mechanism in the latter case. To prove this, an implantation term was added to the rate equation for the target coverage θ_t, which is stated as

$$n_t \frac{\mathrm{d}\theta_t}{\mathrm{d}t} = \alpha(\theta_t) P_r + \left[f\left(\frac{P_r}{P_{tot}}\right) \epsilon(\theta_t) - Y_c(\theta_t) \right] \frac{I_{tot}}{e(1 + Y_{SEE}(\theta_t))} \qquad (2.15)$$

where P_{tot} is the total pressure, $\epsilon(\theta_t)$ is a reaction probability for the implanted reactive gas ions, $f(P_r/P_{tot})$ is the fraction of the ion current that is reactive and I_{tot} is the total discharge current.

Based on experimental data [13–15] they postulate for the Al−O_2 system a decreasing linear dependency of the reactive ion fraction f on the reactive mole fraction P_r/P_{tot} for $P_r/P_{tot} < 0.15$ and for the Al−N_2 system an increasing linear dependency over the full range. The explicit dependencies on θ_t of the parameters α, ϵ, Y_{SEE} and Y_c are not given. But by limiting the analysis of eq. 2.15 to the case of a fully poisoned ($\theta_t = 1$) target together with the proposed forms of $f(P_r/P_{tot})$, they were able to explain the almost non-existing chemisorption of N_2 on Al compared to O_2. A linear dependency of P_r/P_{tot} as function of P_r/I_{tot} was obtained for the Al−O_2 combination, while P_r/P_{tot} was constant for the Al−N_2 combination, both in agreement with their experimental results.

Aiming the prediction of the film composition, the authors also expressed equations for the balance of the reactive gas flows as

$$SP_r = Q_{in} - Q_s \tag{2.16}$$

They distinguished between the metallic mode where the reactive gas supply is limited and the poisoned mode where the reactive gas is overabundant. In the first case they assume that the gettering of the reactive gas by the substrate will be proportional to the reactive pressure and the flux of sputtered metal as

$$SP_r = Q_{in} - \beta P_r R_{s,m} \tag{2.17}$$

where β is a proportionality constant. The sputtered metal flux $R_{s,m}$ was correlated proportional to the measured intensity I_{Al} of the optical emission line of neutral Al. In the model it is defined as

$$R_{s,m} = \frac{Y_m(\theta_t) I_{ion}}{(1 + Y_{SEE}(\theta_t))e} = \delta I_{\mathrm{Al}} \tag{2.18}$$

For the poisoned case the substrate gettering rate is identified with $R_{s,m}$, resulting in

$$SP_r = Q_{in} - \frac{1}{2} R_{s,m} \tag{2.19}$$

for the reacitve gas balance. The factor $1/2$ is under the assumption of a diatomic reactive gas and compound molecule. These two balance equations (eq. 2.17 and eq. 2.19) nicely modeled the experimental $P_r(I_{\mathrm{Al}})$ correlation in respectively the metallic and the poisoned mode with δ and β as fitting parameters. The term $z = 2\beta P_r$ gives then a measure of the stoichiometry z of the formed compound MR_z in the metallic mode.

2.2 Berg model

As the process control of reactive sputtering deposition is often plagued by some hysteresis phenomena, a worthy reactive sputtering model should at least be able to describe these effects. A second valuable property of a reactive sputtering model should be that the process can be described as a function of the operation parameters like the reactive gas supply and predicting deposition and process conditions like film composition and reactive partial pressure. This would allow an easier fine tuning of automated production systems limiting the initial experimental setup phase with trial-and-error experiments. Berg et al. [1] were the first to setup such model really taking those values into account. This model is known in literature as the “Berg” model. Notwithstanding the analytical and rather simple nature of this model, it offers already a broad understanding of the non-linear mechanism of

reactive sputtering as function of several operation conditions and material properties. It tries to model the essence of reactive sputtering in a compact analytical description.

Section 2.2.1 motivates the basic equations of the Berg model with their approximations. The dependencies of the model on the operation and material parameters is investigated in section 2.2.2. Some interesting extensions on the model without changing its basic physics are presented in section 2.2.3.

2.2.1 Original model

In the Berg model it is recognized that the reactive gas kinetics especially at the substrate surface (sample and chamber walls) are of prime importance in modeling the hysteresis. Earlier models often did not considered reactive gas gettering by the substrate surface [2, 3, 10, 11]. Other models [4, 8, 12] proposed a gettering mechanism of the deposited material but the model did not give any hysteresis phenomena in its variables. Only Steenbeck et al. [7] (see section 2.1.4) formulated a model which produces hysteresis phenomena. This was realized by making the substrate gettering dependent on its composition (eq. 2.11). However, their focus was on the modeling of the IV-characteristics during reactive sputtering which could exhibit a hysteresis as experimentally measured.

A critical or saturation pressure as model parameter like in eq. 2.4 or eq. 2.10 is rejected in the Berg model as being of a semi-empirical nature. They concluded that it is the reactive mass flow that greatly characterizes the process instead of the pressure [16]. Furthermore does the model only contain simple accepted physical mechanisms which are linked to form a consistent model. The model makes no attempt in a fully detailed description of any of these mechanisms but aims to keep it as simple as possible with a maximum in predictive power and understanding, like in the philosophy of the holistic approach (section 1.4.2.2).

The original model assumptions and equations are the following. It describes the reactive sputtering process of a single uniformly sputtered metallic target which uniformly deposits a thin film on a substrate surface. Besides the inert sputtering gas is a single reactive gas deliberately introduced to the vacuum chamber quantified by the reactive flow Q_{in}. This reactive gas can leave the vacuum chamber by three pathways as illustrated in Fig. 2.6a. A fraction of the reactive gas is pumped out of the system by the vacuum pump, represented by the flow Q_p. This flow is proportional to the volumetric pumping speed S and the reactive partial pressure P_r as

$$Q_p = \frac{P_r S}{k_B T} \tag{2.20}$$

where k_B is the Boltzmann constant and T is the temperature of the reactive gas. Another fraction of reactive gas is consumed by gettering at the substrate surface with area A_s where sputtered material is deposited, reacts and forms compound.

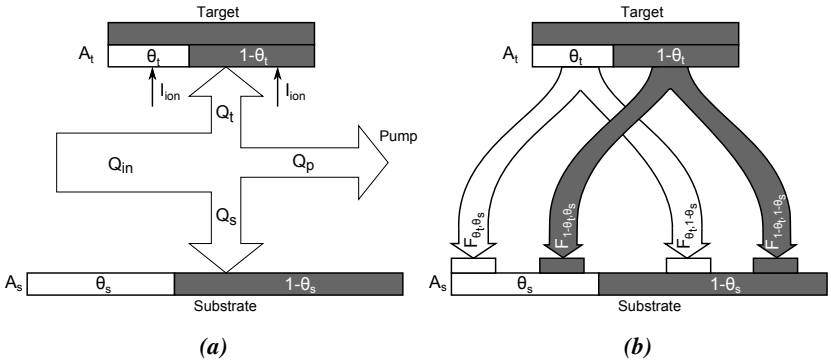

Figure 2.6: *Schematic representation of the original Berg model. (a) The balance in reactive flow consumption and (b) the sputtered material fluxes.*

The substrate consumes as such a reactive flow Q_s. A final fraction reactive gas with flow Q_t is consumed by the target with area A_t causing compound formation and poisoning. This results in a balance equation of the reactive flow as

$$Q_{in} = Q_p + Q_s + Q_t \tag{2.21}$$

Recall that similar balance equations (eq. 2.9, eq. 2.11, eq. 2.17 and eq. 2.19) were proposed in earlier models, but they all omitted a contribution Q_t by the target. The reactive flows consumed by substrate and target depend on the non-occupied chemisorption sites. This is quantified in the model by a fractional surface coverage θ_t on the target and θ_s on the substrate of stoichiometric formed compound M_xR_y. A non-occupied chemisorption site corresponds then with a surface site of a single metal atom M, while an occupied site corresponds with a surface site of a virtual compound molecule MR_z with $z = y/x$. These fractional coverages θ_s and θ_t determine the gettering rate of reactive gas of the corresponding surfaces as

$$Q_s = \alpha_s F_r (1 - \theta_s) A_s \tag{2.22}$$

$$Q_t = \alpha_t F_r (1 - \theta_t) A_t \tag{2.23}$$

where F_r is the impinging flux of the diatomic reactive gas molecules on the surface and α_s (α_t) its sticking probability on a non-occupied sit on the substrate (target). Sticking of reactive gas on the compound fractions θ_t and θ_s is neglected. Assuming an uniform pressure P_r and temperature T over the whole vacuum chamber, the flux F_r will be given by kinetic gas theory as

$$F_r = \frac{P_r}{\sqrt{2\pi m_r k_B T}} \tag{2.24}$$

with m_r the mass of the diatomic reactive gas molecule. The fraction θ_s and θ_t are governed by the balance of essentially four sputtered material fluxes from the

target towards the substrate and the defined reactive flux F_r. This is schematically illustrated in Fig. 2.6b. The first material flux F_{θ_t,θ_s} is sputtered compound deposited on already deposited compound, given by

$$F_{\theta_t,\theta_s} = J_{ion} A_t Y_c \theta_t \theta_s \tag{2.25}$$

where Y_c is the sputtering yield of compound by inert gas ions and J_{ion} is the ion current density. The sputtering due to reactive gas ions is neglected as its mole fraction is typical low compared to the inert gas ions. This flux does not change the θ_s fraction, but decreases the compound fraction θ_t on the target as the compound molecule is removed from the surface replaced by an underlaying metal atom. This makes the chemisorption site back available. Remark that the sputtering of compound is considered in entities of MR_z molecules. Depending on the binding energy between the metal and the reactive atom in the compound, the contribution of atomically or molecularly sputtering of the compound will shift [17]. To simplify, the model assumes molecular sputtering and deposition of the compound. The second flux $F_{1-\theta_t,\theta_s}$ is sputtered elemental metal from the $1-\theta_t$ fraction of the target which is deposited on already deposited compound of the substrate and is given by

$$F_{1-\theta_t,\theta_s} = J_{ion} A_t Y_m (1-\theta_t) \theta_s \tag{2.26}$$

where Y_m is the sputtering yield of elemental metal. As compound will be covered by metal at the substrate, the fraction θ_s will be reduced. The metal fraction $1-\theta_t$ will remain unaffected. The third flux $F_{\theta_t,1-\theta_s}$ is compound sputtered of the target deposited on the metallic fraction $1-\theta_s$ of the substrate and is given by

$$F_{\theta_t,1-\theta_s} = J_{ion} A_t Y_c \theta_t (1-\theta_s) \tag{2.27}$$

This increases the compound fraction θ_s and decreases θ_t. The fourth flux $F_{1-\theta_t,1-\theta_s}$ is sputtered metal from the target deposited on the metallic fraction $1-\theta_s$ of the substrate, defined by

$$F_{1-\theta_t,1-\theta_s} = J_{ion} A_t Y_m (1-\theta_t)(1-\theta_s) \tag{2.28}$$

This leaves the θ_s and θ_t fractions unchanged. Finally, the reactive flux F_r will increase the fractions θ_t and θ_s by chemisorption on the metallic fractions, decreasing the latter. The balance of these fluxes now define the steady state fractions θ_s and θ_t. For the target compound fraction θ_t is the balance between the compound formation by the reactive flux F_r and the compound removal by the sputtering flux $F_{\theta_t,\theta_s} + F_{\theta_t,1-\theta_s}$ which gives

$$\frac{2}{z} \alpha_t F_r A_t (1-\theta_t) = J_{ion} A_t Y_c \theta_t \tag{2.29}$$

where the factor 2 parameterizes the contribution of two reactive atoms to the compound formation and the factor z the stoichiometry of the compound. The balance for the substrate compound fraction θ_s is an increase by compound formation due to the reactive flux F_r and by the compound deposition flux $F_{\theta_t,1-\theta_s}$ on the metallic fraction, which is balanced by the metal deposition flux $F_{1-\theta_t,\theta_s}$ on the compound fraction. This gives the balance equation

$$\frac{2}{z}\alpha_s F_r A_s(1-\theta_s) + J_{ion}A_t Y_c \theta_t(1-\theta_s) = J_{ion}A_t Y_m(1-\theta_t)\theta_s \tag{2.30}$$

defining the fraction θ_s.

The original Berg model summarizes as seven equations solving seven quantities out of nineteen involved variables. The remaining twelve variables will have to be specified as constants. Traditionally this model is solved to produce the hysteresis in the $P_r - Q_{in}$ processing curve. To this end the constant variables are the material properties Y_m, Y_c, α_t, α_s, z and m_r, and the operation and process conditions J_{ion}, S, A_t, A_s and T. By taking P_r as independent variable, the model is solved towards the dependent variable Q_{in} which result in the $P_r - Q_{in}$ process curve. The sequence of solving the seven equations eq. 2.21 for Q_{in}, eq. 2.20 for Q_p, eq. 2.22 for Q_s, eq. 2.23 for Q_t, eq. 2.24 for F_r, eq. 2.29 for θ_t and eq. 2.30 for θ_s is as follows

$$F_r = \frac{P_r}{\sqrt{2\pi m_r k_B T}} \tag{2.31a}$$

$$\theta_t = \frac{\frac{2}{z}\alpha_t F_r}{\frac{2}{z}\alpha_t F_r + J_{ion}Y_c} \tag{2.31b}$$

$$\theta_s = \frac{\frac{2}{z}\alpha_s F_r A_s + J_{ion}A_t Y_c \theta_t}{J_{ion}A_t Y_m(1-\theta_t) + \frac{2}{z}\alpha_s F_r A_s + J_{ion}A_t Y_c \theta_t} \tag{2.31c}$$

$$Q_s = \alpha_s F_r(1-\theta_s)A_s \tag{2.31d}$$

$$Q_t = \alpha_t F_r(1-\theta_t)A_t \tag{2.31e}$$

$$Q_p = \frac{P_r S}{k_B T} \tag{2.31f}$$

$$Q_{in} = Q_p + Q_s + Q_t \tag{2.31g}$$

This solution scheme results in an one-to-one relation between the process conditions P_r, θ_t and θ_s and the operation parameter Q_{in}. Similar one-to-one solution procedures can be formulated for the dependent operation parameters J_{ion}, S, A_s and A_t for a constant Q_{in} which are given in detail in Appendix A.

To illustrate one of these alternative solution procedures, the solution of the original Berg model as function of the pumping speed S is given in Fig. 2.7 for different introduced reactive gas flows Q_{in}. At sufficiently low pumping speeds, the reactive pressure will be substantial ($> 0.1\,\mathrm{Pa}$) and even further lowering the

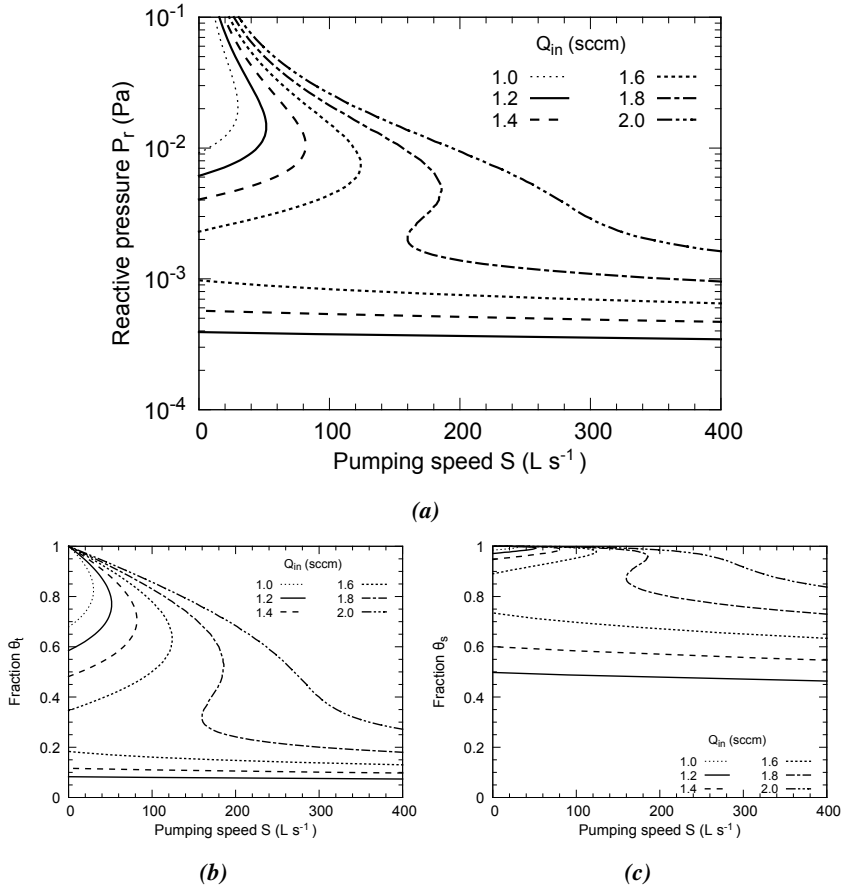

Figure 2.7: *Solution of the original Berg model of (a) the reactive pressure, (b) the compound fraction on the target and (c) the compound fraction on the substrate as function of the pumping speed S. Model parameters are taken from Table 2.1.*

pumping speed will diverge the reactive pressure if not all reactive gas can be incorporated into the compound film. If the pumping speed is increased and the reactive flow $1.6\,\mathrm{sccm} < Q_{in} \leq 1.8\,\mathrm{sccm}$, a hysteresis exists as explained in section 1.3.1.1. However if the reactive flow $Q_{in} \leq 1.6\,\mathrm{sccm}$ and the first critical point is passed, by subsequently decreasing the pumping speed it seems not possible anymore to access the poisoned mode without switching off the magnetron discharge. When the pumping speed reaches to zero, all the introduced reactive gas will be incorporated in the substrate and target. Of course it has to be realized that also an inert sputtering gas is present in the chamber. Changing the pumping speed will influence this inert pressure and although it is not an explicit parameter

Material properties		
$\mathrm{Y_m}\,(\mathrm{M\,ion^{-1}})$	0.5	sputter yield metal M
$\mathrm{Y_c}\,(\mathrm{MR_z\,ion^{-1}})$	0.05	sputter yield compound MR_z
α_t	1	sticking probability reactive gas target
α_s	1	sticking probability reactive gas substrate
z	1.5	stoichiometric coefficient compound (MR_z)
$\mathrm{MM_r}\,(\mathrm{g\,mol^{-1}})$	32	molar mass reactive gas
Operation conditions		
$\mathrm{I_{ion}}\,(\mathrm{A})$	0.5	ion current
$\mathrm{S}\,(\mathrm{l\,s^{-1}})$	50	volumetric pumping speed
$\mathrm{A_t}\,(\mathrm{cm^2})$	10	sputtering area (target)
$\mathrm{A_s}\,(\mathrm{cm^2})$	1000	deposition area (substrate)
$\mathrm{T}\,(\mathrm{K})$	300	gas temperature

Table 2.1: *Set of parameters for the Berg model of the standard reactive sputter system with O_2 as reactive gas.*

in the original Berg model, this will implicitly influence other model parameters like sputter yields, deposition area and ion current density. An experimental option could be, in order to keep the inert gas pressure constant along the hysteresis, to increase (decrease) the inert gas flow accordingly the increasing (decreasing) pumping speed.

2.2.2 Parameter dependencies

In this section the dependency of the hysteresis on the parameters from the original Berg model are presented. To have a good reference for comparison, a standard reactive sputter system is defined for the model. The parameters are chosen such that a well pronounced hysteresis is reproduced. The reactive gas is assumed to be O_2 and the metal can be for example Al forming Al_2O_3. The solution scheme of eq. 2.31 is used to produce the process curves as function of the reactive gas flow Q_{in}. The set of parameters for this standard system is listed in Table 2.1. The parameters are grouped in material properties and operation conditions. The first are basically defined by the choice of metal-gas combination while the operation conditions are more or less tunable towards optimal deposition conditions. Section 2.2.2.1 shows the dependency of the hysteresis on the material properties, as section 2.2.2.2 investigates the dependency of the operation conditions.

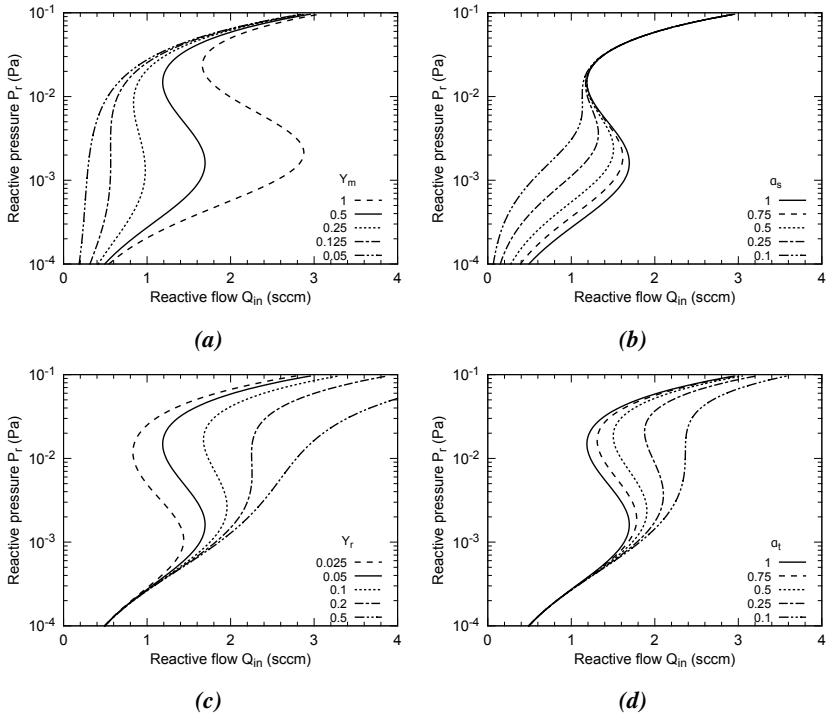

Figure 2.8: *Hysteresis curves of the standard "Berg" system (Table 2.1) with a variation of the material parameters (a) Y_m, (b) α_s, (c) Y_c and (d) α_t. The solid line represents the standard system. Corresponding line styles in (a) and (c) indicate a similar ratio Y_m/Y_c.*

2.2.2.1 Material properties

The Berg model describes the metal-reactive gas system with the sputter yields of the metal Y_m and the compound Y_c, and with sticking probabilities between a reactive gas molecule and elemental metal for the target α_t and for the substrate α_s. Figure 2.8 shows how the $P_r - Q_{in}$ hysteresis curve changes as function of these material parameters compared to the standard "Berg" system (Table 2.1), given by the solid line. Comparing Fig. 2.8a and Fig. 2.8c clearly shows that a less pronounced hysteresis is obtained if the ratio Y_m/Y_c becomes smaller. If Y_m and Y_c become similar the hysteresis eventually vanishes. In Fig. 2.8a this is done by lowering the Y_m which shifts faster the first critical point of the hysteresis to lower reactive flows than the second critical point. In Fig. 2.8c the same ratios of Y_m/Y_c are presented but now by increasing Y_c. The hysteresis also vanishes but in this case the shift of the second critical point towards higher reactive flows is faster than for the first critical point. This observation learns that the metallic

sputter yield Y_m is a more decisive parameter for the first critical point compared to the compound sputter yield Y_c. The latter is then of greater importance for the position of the second critical point. These effects can qualitatively be understood. The first critical point is determined by the gettering capacity of the substrate. This gettering capacity depends on the supply of deposited metal which mainly depends on the metallic sputter yield at constant ion current. A higher metallic sputter yield increases this gettering capacity by which more reactive gas can be incorporated in a compound film, and this shifts the first critical point to a higher reactive flow. The second critical point is determined by the de-poisoning of the target surface. Along the increase of the compound sputter yield will the removal rate of compound increase. The target will then become back metallic at a higher critical reactive flow as the compound formation rate, proportional to the reactive flow, balancing this removal rate has to have a similar increase.

The Fig. 2.8b and Fig. 2.8d investigate the influence of the sticking probability α_s and α_t on the hysteresis. As they are probabilities, their possible value ranges from 0 to 1. The standard "Berg" system takes the maximum sticking probability 1 for both target and substrate. As α_t is decreased, both critical points shift to higher reactive flows. As the second critical point shifts faster, the hysteresis is reduced and even vanishes if α_t becomes an order of magnitude lower. A resembling qualitatively explanation for this shift can be given as for the case of the increasing Y_c (Fig. 2.8c). Now the compound formation rate on the target is decreased by the lower sticking probability. To compensate the almost unaffected critical removal rate of the compound, a higher reactive flow will be necessary. A reduction of α_s shifts the first critical point towards a lower reactive flow, while the second critical point remains fixed. This causes again a disappearing hysteresis for a sufficiently low α_s. Similar arguments as for the decreasing metallic sputter yield (Fig. 2.8a), explain the shift of the first critical point. Now the lower sticking probability gives a reduction in the gettering capacity of the substrate resulting in a lower first critical flow.

2.2.2.2 Operation conditions

While the material parameters are basically settled by the desired film, the operation parameters are by definition more tunable. The original Berg model has the sputtering area of the target A_t and the deposition area of the substrate A_s as operation parameters, besides the pumping speed S and the ion current I_{ion}. The sputtering area A_t can directly be changed by the choice of the target size or indirectly by changing the magnetic configuration. The deposition area A_s is tuned by the size of the vacuum chamber and the target-substrate distance. The target-substrate distance determines the deposition area as this area will become smaller the closer the substrate (sample) is positioned to the target. The sputtered flux becomes then more concentrated on this substrate. Moreover, it will act as

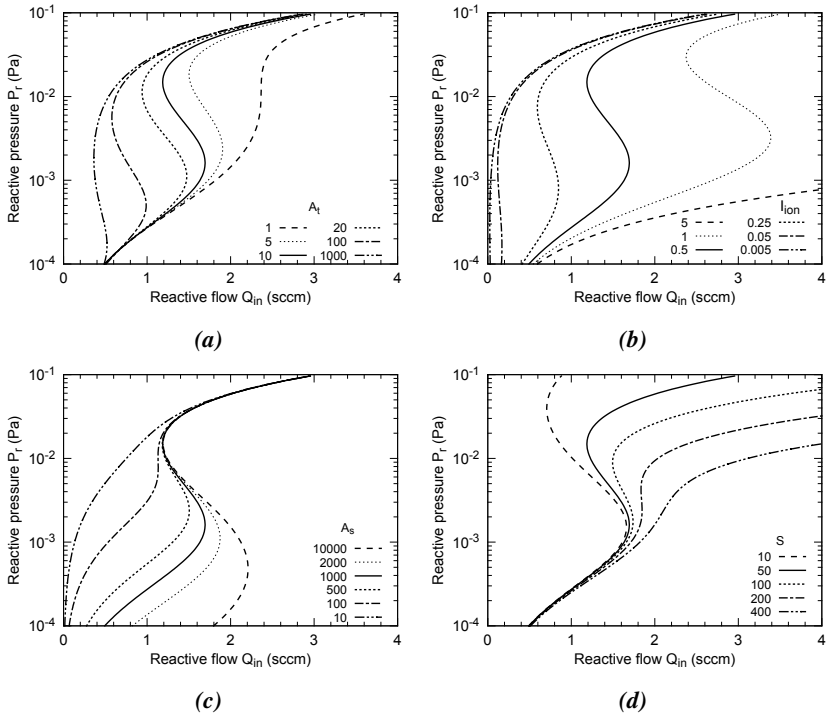

Figure 2.9: *Hysteresis curve of the standard "Berg" system (Table 2.1) with a variation of the operation parameters (a) A_t, (b) I_{ion}, (c) A_s and (d) S. The solid line represents the standard system. Corresponding line styles in (a) and (c) indicate a similar ratio A_t/A_s, while similar line styles between (a) and (b) correspond to the same ion current density J_{ion}.*

an increasing blocking of the sputter flux which becomes less spread out over the vacuum chamber. The ion current I_{ion} can be fixed by the power supply by establishing an appropriate discharge current. The latter will influence the sputter yields Y_m and Y_c as they depend on the energy of the sputtering ion. In this sense, the sputter yields are somehow controllable. The pumping speed S will depend on the used pumping system defining an upper limit.

Figure 2.9a shows the influence of the target sputtering area A_t on the hysteresis, while Fig. 2.9b shows the influence of the ion current I_{ion}. Similar line styles in Fig. 2.9a and Fig. 2.9b correspond with the same ion current density J_{ion}. In this way it is clear that a changing J_{ion} behaves differently if I_{ion} is increased or if A_t is decreased to obtain the same J_{ion}. In the first case the hysteresis becomes more pronounced (Fig. 2.9b) with increasing I_{ion}, entirely shifting it to higher reactive flows. More material is sputtered so the getter capacity is increased shifting up the first critical point. The intenser ion current at the second critical point results in a

larger removal rate of compound, increasing the second critical flow. Even how, at very low ion currents the hysteresis disappears. Practically this is not very interesting as the deposition rate scales with the ion current. In the case of a sufficiently decreasing A_t keeping the I_{ion} unchanged, the hysteresis vanishes. This finding results in a hysteresis free operation without compromising in deposition rate or power consumption. Nyberg et al. [18] were the first to recognize this effect. They exploited this in a patented magnetron design [19]. In their design a fast moving magnet causes an intense sputtering spot on the target, minimizing the sputtering area A_t. The movement of this spot has two advantages: it causes a more uniform erosion of the target and it distributes the sputtering energy preventing cooling problems.

Figure 2.9c illustrates the effect of a changing substrate deposition area A_s. Similar line styles between Fig. 2.9a and Fig. 2.9c indicate the same ratio A_t/A_s. This learns that the vanishing hysteresis for decreasing A_t is not caused by this ratio decrease. When A_s increases, the first critical point shifts to higher reactive flows as the gettering capacity is increased. Decreasing A_s towards a value in the order of A_t, eliminates the hysteresis as the first critical flow gets lowered while the second critical flow remains almost fixed. Reducing the hysteresis by reducing the effective deposition area has been performed in so called triode magnetron sputtering (TMS) systems [20]. By the introduciton of a movable grid between target and substrate, the width of the hysteresis can be controlled. As the grid is brought closer to the target, the effective A_s is decreased, narrowing the hysteresis. Remark that the hysteresis behavior for an decreasing α_s (Fig. 2.8b) is comparable with that for a decreasing A_s (Fig. 2.9c). In the same way is the behavior for a decreasing α_t (Fig. 2.8d) comparable with that for a decreasing A_t (Fig. 2.9a). The influence of the pumping speed S is shown in Fig. 2.9d. With increasing S the hysteresis fades away. The shift of the first critical point to higher reactive flows is small. The second critical flow however drastically increases, surpassing the first critical flow and eliminating the hysteresis. An increase in pumping speed means that a larger reactive flow has to introduced to obtain similar partial reactive gas pressures. That the impact on the second critical point is more invasive stems from the fact that the reactive gas consumption of the pumping system Q_p is proportional with the gas pressure P_r (eq. 2.20). As this pressure is higher at the second critical point compared to the first critical point can this explain the stronger impact. The effect of an increasing pumping speed to eliminate the hysteresis is an already long known experimental fact [21]. Practical this effect can serve as a method for hysteresis free operation, but it comes at a price. The necessary pumping speeds are often unacceptable high and the power consumption scales with the desired pumping speed.

2.2.3 Extended model

The original Berg model presented in section 2.2.1 is beautiful in the way that it grasps many essential features of the reactive sputtering process by a limited number of analytical equations. Since its formulation [1] up till now [22] researchers in the field use the model to explain experimental observed trends. Over the years many extensions on the original model of Berg have been formulated. These extensions could be subdivided in two categories. A first category embodies extensions where essential physical processes are added besides the sputtering and the chemisorption process, or where an existing process is differently modeled. The second category are extensions which resolve an aspect of the modeled system in space or time, without touching the essence of the model. In this section some extensions of the second category are presented. The next chapter, chapter 3, can be seen as an extension of the first category, while in chapter 4 extensions of both categories are formulated. A first spatial extension of the Berg model is the inclusion of a deposition profile as in section 2.2.3.1, instead of the assumed uniform deposition. A second spatial extension in section 2.2.3.2 is considering a non-uniform current distribution over the target. Finally in section 2.2.3.3 a dynamic time dependent Berg model is presented where the dynamic of the poisoning and depoisoning of the reactive system is investigated.

2.2.3.1 Deposition profile

The uniform deposition in the original Berg model can be replaced with a deposition profile which spatially resolves the deposition area of the system. This is sensible if a more realistic simulation of the actual deposition is needed. For simple geometric configurations there have been analytical models proposed to calculate the deposition profile [23]. For more complex configurations the need for Monte Carlo based transport codes [24–27] will quickly emerge. In this work the Monte Carlo code SiMTra (Simulation of Metal Transport) [27, 28] developed within the research group DRAFT will be used. SiMTra simulates the trajectory of sputtered metal particles through the gas phase towards its deposition place. SiMTra allows the definition of quite complex chamber and substrate configurations where the area of each deposition surface is meshed in equal sized cells. The deposition profile of a surface is then obtained from SiMTra as a 2-dimensional matrix. A matrix element N_i is the number of test particles that arrive within the area $A_{s,i}$ of the cell i. A deposition fraction $\varepsilon_{s,i}$ can be defined as

$$\varepsilon_{s,i} = \frac{N_i}{N_{tot}} \tag{2.32}$$

where N_{tot} is the total number of simulated test particles.

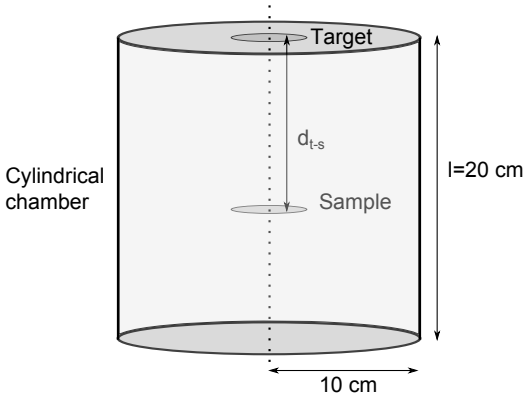

Figure 2.10: *Sketch of the simulated geometric setup wherefore a deposition profile is simulated.*

The metallic deposition flux $F_{m,i}$ and the compound deposition flux $F_{c,i}$ on a cell i is then given as

$$F_{m,i} = \frac{\varepsilon_{s,i}}{A_{s,i}} I_{ion} Y_m (1 - \theta_t) \tag{2.33a}$$

$$F_{c,i} = \frac{\varepsilon_{s,i}}{A_{s,i}} I_{ion} Y_c \theta_t \tag{2.33b}$$

The same deposition profile for the sputtered metal as the compound is assumed to prevent changes in the simulation results due to a simultaneous variation of two deposition profiles. Equation 2.30 which defines a single fraction θ_s for the whole substrate, will become

$$\frac{2}{z}\alpha_s F_r A_{s,i}(1 - \theta_{s,i}) + \varepsilon_{s,i} I_{ion} Y_c \theta_t (1 - \theta_{s,i}) = \varepsilon_{s,i} I_{ion} Y_m (1 - \theta_t)\theta_{s,i} \tag{2.34}$$

which attributes a compound fraction $\theta_{s,i}$ to every deposition cell. Similarly will eq. 2.22 be transformed into

$$Q_{s,i} = \alpha_s F_r (1 - \theta_{s,i}) A_{s,i} \tag{2.35}$$

This connects to every cell i a rate of reactive gas consumption to form compound. The total flow Q_s consumed by the substrate is then the sum of eq. 2.35 over all cells.

To illustrate the effect of a deposition profile on the hysteresis, a cylindrical vacuum chamber is defined with a sample placed in front of a Al target (Fig. 2.10). The vacuum chamber has a radius $r = 10\,\mathrm{cm}$ and a length $l = 20\,\mathrm{cm}$. A circular planar target with radius $2.5\,\mathrm{cm}$ is mounted on the top of this chamber. A

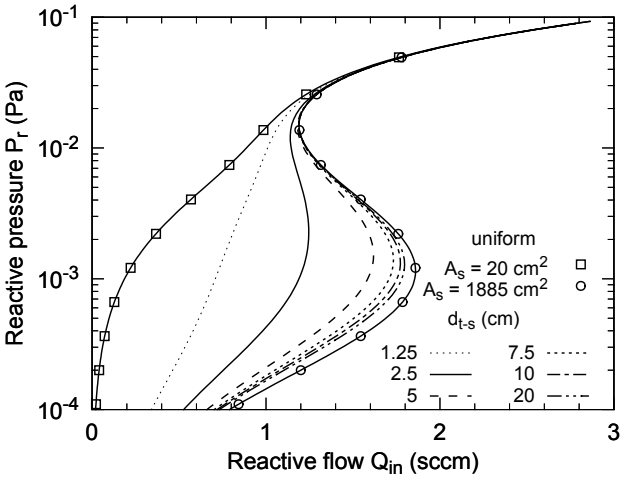

Figure 2.11: *Hysteresis curves for a cylindrical vacuum chamber ($r = 10\,\mathrm{cm}, h = 20\,\mathrm{cm}$) with a circular sample ($20\,\mathrm{cm}^2$) coaxially placed at a distance d_{t-s} from the target. The deposition area of the chamber itself is $1885\,\mathrm{cm}^2$. Other parameters are taken from Table 2.1.*

circular sample with similar size as the target is placed at a distance d_{t-s} from the target. Target and sample are positioned coaxial with the cylinder axis. The deposition profiles for this configuration are simulated with SiMTra where the deposition on the chamber walls and the sample surface facing the target are collected. The transported element is Al through an Ar gas of $0.4\,\mathrm{Pa}$ at $300\,\mathrm{K}$ with a Molière interaction potential. The angular distribution of the sputtered atoms is a cosine distribution with starting energies drawn from a Thompson distribution limited at $400\,\mathrm{eV}$. The emission positions are distributed as the included "Gent" erosion racetrack [1] from SiMTra. The target-sample distance is varied from 1.25 to $20\,\mathrm{cm}$ within the SiMTra simulations. When d_{t-s} is small, a big portion of the sputtered atoms will be deposited on the similar sized sample just in front of the target. By increasing d_{t-s}, more sputtered atoms will be deposited at the chamber walls. Also a larger fraction of the chamber surface area will become reachable for the sputtered atoms by the diminishing blocking due to the sample. In the upper limit the sample is placed at the back end of the chamber ($d_{t-s} = 20\,\mathrm{cm}$). This makes the deposition profile broader as the sputtered atoms are more spread out over the available deposition surfaces. The effect of this changing deposition profile on the hysteresis is shown in Fig. 2.11. The same model parameters as for the standard Berg system Table 2.1 are used replacing the substrate area A_s with the corresponding deposition profile. As the d_{t-s} increases and the deposition profile

[1] This erosion racetrack was measured by contact profilometry where an axial symmetry is assumed.

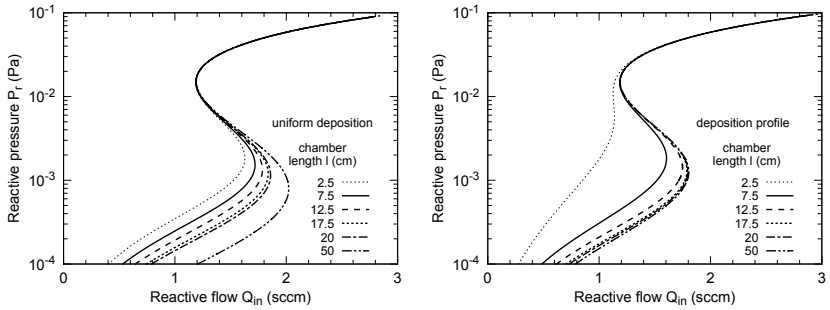

Figure 2.12: *Hysteresis curves for a cylindrical vacuum chamber with radius* $10\,\mathrm{cm}$*. The hystereses simulated with (a) uniform deposition and (b) a deposition profile are compared for different chamber lengths. Other parameters are taken from Table 2.1.*

becomes broader, the first critical point shifts to higher oxygen flows. This trend is comparable with the original Berg model if the substrate area A_s is increased. Indeed effective deposition areas could be defined for the cases with a deposition profile ranging from the sample area (small d_{t-s}) up to the entire chamber surface area (maximum d_{t-s}). In Fig. 2.11 the hysteresis for uniform deposition with these two extreme effective deposition areas are given. The hysteresis for maximum d_{t-s} approaches well the hysteresis simulated with the maximum effective area from the left. Here the deposition profile is well approximated by a uniform profile over the entire chamber surface. The hysteresis with minimum d_{t-s} approaches the hysteresis with an effective area equaling the sample area, from the right. The deviation between the two hystereses remains large. This indicates that this effective area is too small and that the deposition flux is spread out over a larger area than only over the sample surface. To summarize, the deposition profile of each configuration can be approximated by a different effective deposition area laying within the expected boundaries namely the sample area and the area of the entire chamber.

It is interesting now to consider the cylindrical vacuum chamber without the sample and to look at the hysteresis behavior as function of the chamber length l. This is shown in Fig. 2.12. Without the sample in the chamber, their is no element blocking the sputtered metal flux. The effect of elongating the chamber on the first critical point is investigated for the case of uniform deposition and for the case with a deposition profile. As Fig. 2.13 shows, the first critical flow shifts in both cases towards higher values. This is understandable as the deposition area equally increases. However an initial steeper increase for the deposition profile is noted which completely flattens at large chamber length ($> 20\,\mathrm{cm}$). In the

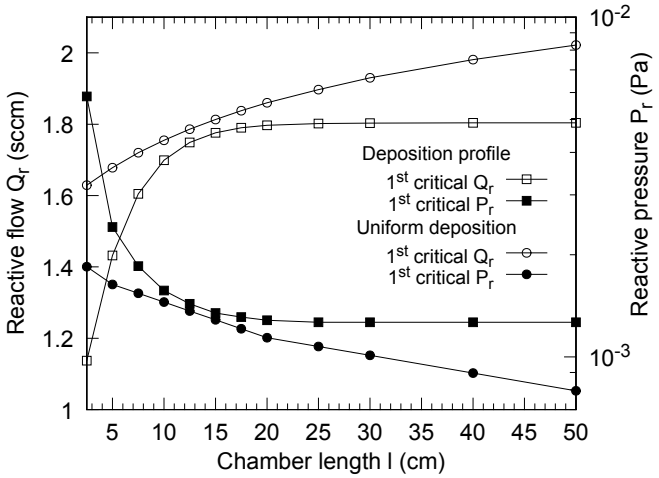

Figure 2.13: *Simulation of the first critical flow (left axis) and pressure (right axis) depending on the length of the chamber (without sample). The case with a deposition profile is compared with the case assuming a uniform deposition.*

case of uniform deposition the initial increase is more moderate, but it continues to increase even for large chamber length. The initial steeper increase for the deposition profile is caused by not only an increasing deposition area but also by a broadening of the profile. Indeed, the deposition intensity on the chamber bottom will diminish and spread out. At larger lengths, this increase stops because sputtered atoms can not be deposited at arbitrarily far places. Starting from a certain critical chamber length, there will be almost no deposition on the bottom of the chamber and as such this surface hardly getters reactive gas. The effective gettering area and deposition profile will converge as will the first critical point. Fig. 2.13 shows this convergence as well in flow as in pressure. In the case of a uniform deposition this convergence is absent and the critical flow continues to increase while the critical pressure continues to decrease, say it less steeper. The deposition flux is smeared more and more out over the entire chamber as its length increases. In this model it is allowed to distribute the deposited atoms in a layer thickness lower then one monolayer, which is unphysical. This shows a breakdown of the uniform deposition approach in the original Berg model. Besides this, their is also a physical limit on how much reactive gas can be gettered. This limit is proportional to the metal sputter flux as the reactive gas is gettered by reaction with this metal to form a compound film. In the case of uniform deposition this limit is not respected. This illustrates that the choice of the deposition area A_s is sometimes not straight forward and that including a deposition profile resolves such issue besides giving a more detailed description.

2.2.3.2 Ion current profile

The uniform current density over the target which is assumed in the original Berg model is in reality only valid for a DC diode sputtering system. The presence of a non uniform magnetic field above the target surface in a magnetron sputtering setup causes a non uniform current profile across the target. In a similar way as for the deposition profile on the substrate, the original Berg model can be extended to incorporate this spatial resolved current density. The ion current profile forms then an extra input. This input can at least be estimated from simulations, direct measurements [29] or by measuring the erosion racetrack. For a circular planar target, the shape of the erosion racetrack is axial symmetric and can be well approximated by a two-dimensional (r, θ) Gaussian distribution $G(r; \mu, \sigma)$ with a mean μ and a deviation σ normalized over the target surface. The target can then be partitioned in N concentric surface cells with radial dimension Δr_i. To each surface cell i a compound fraction $\theta_{t,i}$ and a local ion current $I_{ion,i}$ can be assigned. Based on eq. 2.29, the governing equation for $\theta_{t,i}$ becomes

$$\frac{2}{z}\alpha_t F_r A_{t,i}(1-\theta_{t,i}) = I_{ion,i} Y_c \theta_{t,i} \tag{2.36}$$

where $A_{t,i}$ is the surface area of the i^{th} concentric surface cell, and $I_{ion,i}$ is the local ion current calculated as

$$I_{ion,i} = 2\pi I_{ion} \int_{\Delta r_i} G(r) r \mathrm{d}r \tag{2.37}$$

The reactive gas consumption $Q_{t,i}$ of each surface cell is now given by

$$Q_{t,i} = \alpha_t F_r (1-\theta_{t,i}) A_{t,i} \tag{2.38}$$

and the sum of all $Q_{t,i}$ gives the total gas consumption by the target. As the deposition flux depends on the metallic and compound fractions of the target, the equation governing the compound fraction on the substrate also needs an update. The target coverage θ_t in eq. 2.30 (or eq. 2.34) has to be replaced by a current weighted average $\overline{\theta_t}$ defined as

$$\overline{\theta_t} = \frac{1}{I_{ion}} \sum_i I_{ion,i} \theta_{t,i} \tag{2.39}$$

to account for the correct sputter flux of metal and compound.

The influence of the current profile on the hysteresis behavior is investigated. An Al circular planar target with diameter of $5\,\mathrm{cm}$ is radially partitioned in 100 concentric cells. Each cell has the same radial dimension of $\Delta r = 0.025\,\mathrm{cm}$. A Gaussian current profile is assumed with $\mu = 1.25\,\mathrm{cm}$ and $\sigma = 0.25\,\mathrm{cm}$. Apart from the current profile and the target size ($20\,\mathrm{cm}^2$) are the remaining parameters

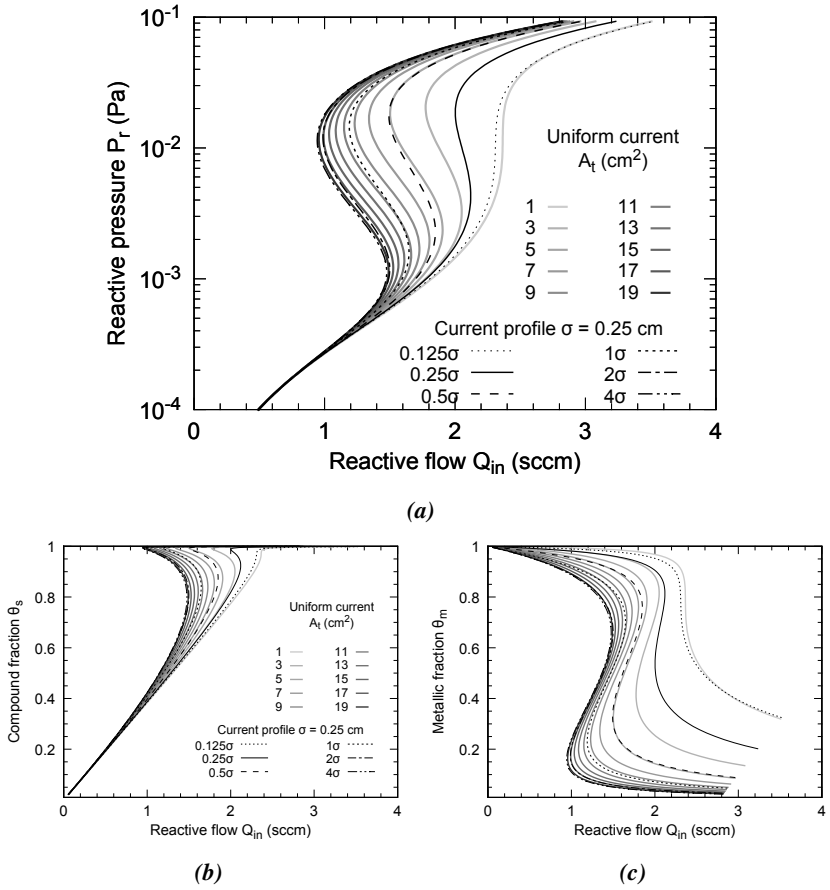

Figure 2.14: *Simulated hysteresis curves of (a) the reactive pressure, (b) the compound fraction on the substrate and (c) the metal fraciton on the target for different target areas which are uniformly sputtered. This is compared with the hysteresis curves for a fixed target area of* $20\,\mathrm{cm}^2$ *where a Gaussian sputter profile is used varied in width.*

taken from Table 2.1. The width of the current profile is varied by subsequently doubling or halving the deviation σ of the Gaussian profile. Figure 2.14 shows the impact of this variation on the hysteresis of the reactive pressure P_r, the average target metal fraction $\overline{\theta_m}$ and the average substrate compound fraction $\overline{\theta_s}$. A decreasing sigma narrows the current profile which shifts the hysteresis towards higher reactive flows and decreases its width. This behavior resembles the effect of a decreasing target area in the original Berg model (see also Fig. 2.9a). Again an effective target area can be connected to each current profile. To give an idea with which effective area a given current profile corresponds, hystereses simulated

with a uniform current but with the target size varied up to the full target size are added to Fig. 2.14. If the current profile is widened by increasing the deviation, the hysteresis converges towards the hysteresis of uniform current with $A_t = 20\,\mathrm{cm}^2$ as expected. An upper limit for the effective target area is thus the full target area, while the effective area decreases as the current profile narrows. Figure 2.14c learns that the $\overline{\theta_m}$ hysteresis is more metallic when the current profile is narrowed. Remark that Fig. 2.14c presents the current weighted metal fraction (see eq. 2.39) which is proportional to the sputter flux. This results in higher deposition rates just before the first critical point of a compound film which tends to be more and more full stoichiometric as shown in Fig. 2.14b. This result is an additional advantage besides the disappearing of the hysteresis when the erosion area is reduced in a reactive sputtering system.

2.2.3.3 Time dynamics

Up till now the Berg model is formulated to describe the steady state conditions of a reactive sputtering system. The extensions of the Berg model in section 2.2.3.1 and section 2.2.3.2 spatially resolve the substrate respectively the target. However the dynamics of the reactive sputtering system can currently not be studied with this kind of models. For this a time dependent model is needed which not only allows to describe the evolution to steady state but also additional time dependent features of the system.

The original Berg model, and its spatial extensions can easily be transformed into a dynamic time dependent form. Here the dynamic version of the original Berg model is given. Its steady state formulation is based on three balance equations for the target condition (eq. 2.29), the substrate condition (eq. 2.30) and the reactive gas consumption (eq. 2.21). The imbalance of these equations drives then the rate in change of the compound fraction on the target and the substrate, and of the reactive partial pressure. This results in three coupled ordinary differential equations (ODE's) with the time t as independent variable. The ODE for the target condition $\theta_t(t)$ is obtained from eq. 2.29 by subtracting the compound removal term (RHS) from the compound formation term (LHS) which gives

$$n_{0,s}\frac{\mathrm{d}\theta_t(t)}{\mathrm{d}t} = \frac{2}{z}\alpha_t F_r(t) A_t(1-\theta_t(t)) - J_{ion} A_t Y_c \theta_t(t) \tag{2.40}$$

where the time dependency of the coupled variables is explicitly shown and $n_{0,s}$ is the maximum surface density of reaction places. This surface density can be identified with the atomic surface density of the target material. The ODE for the compound fraction $\theta_s(t)$ on the substrate is similarly obtained from eq. 2.30. Subtraction of the metallic covering term (RHS) from the compound formation

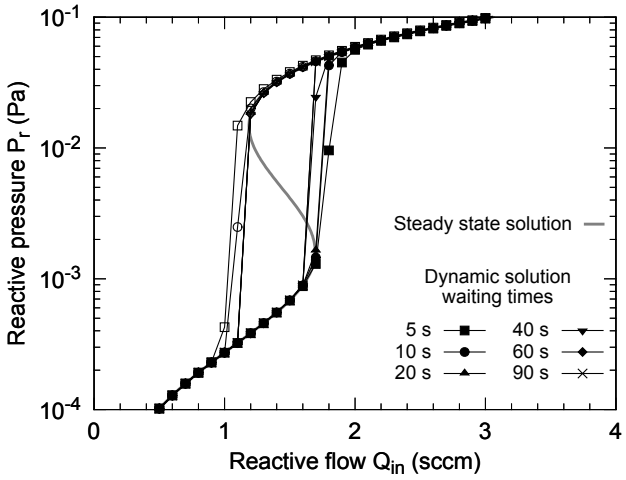

Figure 2.15: *Influence of the waiting time between successive flow increments (closed markers) and flow decrements (open markers) on the hysteresis. The simulation parameters are taken from Table 2.1 with a chamber volume of* $0.125\,\mathrm{m}^3$.

term and the compound covering term gives

$$n_{0,s}\frac{\mathrm{d}\theta_s(t)}{\mathrm{d}t} = \frac{2}{z}\alpha_s F_r(t) A_s(1-\theta_s(t)) + J_{ion} A_t Y_c \theta_t(t)(1-\theta_s(t)) - J_{ion} A_t Y_m (1-\theta_t(t))\theta_s(t) \tag{2.41}$$

The same surface density $n_{0,s}$ as for the target is assumed. The last ODE closing this system is the rate of change in the reactive partial pressure $P_r(t)$ or proportionally (see eq. 2.24) the reactive gas flux $F_r(t)$. The imbalance of eq. 2.21 produces this ODE. Subtraction of the gas consumptions by the target (eq. 2.23), the substrate (eq. 2.22) and the pump (eq. 2.20) from the introduced gas flow $Q_{in}(t)$ gives

$$\frac{\mathrm{d}P_r(t)}{\mathrm{d}t} = \frac{k_B T}{V_c}(Q_{in}(t) - Q_p(t) - Q_s(t) - Q_t(t)) \tag{2.42}$$

where V_c is the volume occupied by the reactive gas in the vacuum chamber. The gas flow $Q_{in}(t)$ is independently applied as a time dependent boundary condition.

The time dependent Berg model has no analytical solution and needs to be numerically solved. An explicit 4^{th} order Runge-Kutta integration scheme has here been applied with a fixed integration step of $1\,\mathrm{ms}$. In contrast to the steady state model were a solution can be obtained as function of the reactive pressure P_r, is the independent variable in the dynamic model the introduced reactive gas flow $Q_{in}(t)$. In this way the steady state model mimics the stabilized points of a feedback controlled hysteresis experiment (section 1.3.1.2) while the time dependent

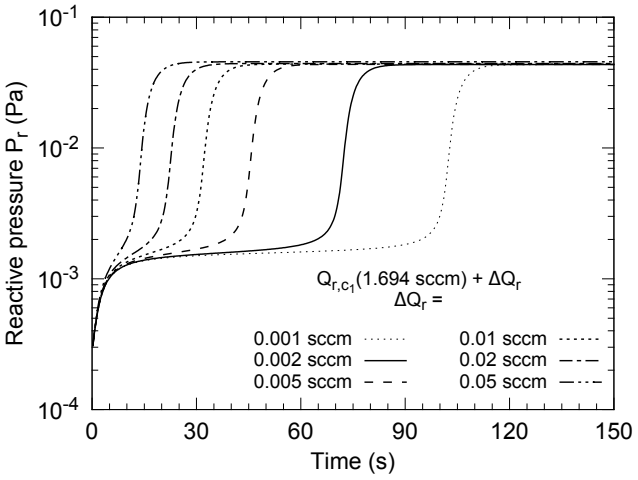

Figure 2.16: *The elongation of the stabilization time when approaching the first critical flow from the higher flow side. The simulation parameters are taken from Table 2.1 with a chamber volume of* $0.125\,\mathrm{m}^3$.

model enables the description of the dynamics of a hysteresis experiment under direct flow control (section 1.3.1.1). These steady state points can be obtained by stepwise increasing and decreasing the reactive flow with a sufficient long stabilization time in between every two consecutive steps. That this stabilization time depends on the position within the hysteresis is illustrated in Fig. 2.15. The steady state solution is compared with the time dependent solution for different stabilization times. The simulation parameters are taken from Table 2.1 with the volume $V_c = 0.125\,\mathrm{m}^3$. The transition mode is not accessed by the time solution. The metallic and the poisoned mode however do coincidence if the stabilization time is chosen long enough ($> 60\,\mathrm{s}$). It are the steady state points near the critical points which ask the longest stabilization times.

This is made even more explicit in Fig. 2.16. For the same system, the reactive flow is immediately increased from $0\,\mathrm{sccm}$ (metallic mode) to a reactive flow $Q_{r,c_1} + \Delta Q_r$ (poisoned mode) just above the first critical flow Q_{r,c_1}. Figure 2.16 reveals three things. Firstly the stabilization time elongates when ΔQ_r decreases. Secondly the rise of the reactive pressure happens in basically three steps: an initial fast but limited pressure increase, an intermediate quasi pressure plateau and a final fast and large pressure increase. Thirdly this intermediate pressure plateau vanishes when the stabilization time shortens. A similar behavior is obtained when moving from fully poisoned mode towards a reactive flow $Q_{r,c_2} - \Delta Q_r$ just under the second critical flow Q_{r,c_2}. Of course a pressure decrease instead of a pressure increase is now observed. This dynamic behavior from poisoned to metallic mode

was already investigated by Jonsson et al. [30] with a multi-layered Berg model.

To get a better insight in this dynamical behavior near the critical points, Fig. 2.17 represents the change in target and substrate condition accompanying the pressure change when moving into poisoning and returning from poisoned mode. The simulation went as followed Q_{in} was set for 60 s to $Q_{r,c_2} - \Delta Q_r$ with $\Delta Q_r = 0.01\,\mathrm{sccm}$ operating in metallic mode. Then Q_{in} was abruptly increased to $Q_{r,c_1} + \Delta Q_r$ with a stabilization time of 120 s moving it into poisoned mode. In the last step Q_{in} was back decreased to $Q_{r,c_2} - \Delta Q_r$ transcending into metallic mode. The compound fractions θ_s on the substrate and θ_t on the target show a similar dynamic as the reactive pressure. The inset of Fig. 2.17a shows the second steep decrease when moving back to metallic mode. This inset already indicates that the change of these three variables is not always completely simultaneous. In analyzing their time sequence, the normalized first derivatives are plotted in Fig. 2.17b. The normalization of these first derivatives $\mathrm{d}X(t)/\mathrm{d}t$ with $X = \theta_t, \theta_s, P_r$ is performed as

$$\frac{\mathrm{d}X^*}{\mathrm{d}t} = \frac{1}{X_{max} - X_{min}} \left| \frac{\mathrm{d}X(t)}{\mathrm{d}t} \right| \tag{2.43}$$

where X_{max} is the maximum steady state value in poisoned mode while X_{min} is the minimum steady state value in metallic mode. In essence these are the RHS's of the ODE's (eq. 2.40, eq. 2.41 and eq. 2.42) governing the model. Figure 2.17b shows in the first figure the first steep increase before the "plateau" and in the second figure the second steep increase after the plateau when moving from metallic to poisoned mode. The third and fourth figure show the same when mowing from poisoned to metallic mode. Now the dynamics that play can be understood. When the reactive flow is initially increase at time $t = 60\,\mathrm{s}$, the pressure rise is limited as most reactive gas is gettered by the substrate, increasing θ_s. Also the target getters some gas, increasing θ_t but to a smaller degree then the substrate as sputtering has a cleaning effect on it. The second steep pressure rise ($t = 91\,\mathrm{s}$) is preceded by a steep poisoning of the target ($t = 89.5\,\mathrm{s}$) which is slightly preceded by a steep poisoning of the substrate ($t = 89\,\mathrm{s}$). This can be interpreted as the gettering of the substrate that reduces first after which the target poisons and finally the reactive pressure quickly rises to it new steady state value. The return to metallic mode shows a somehow reversed behavior. At $t = 180\,\mathrm{s}$ the reactive flow is lowered which initially only decreases the pressure substantially. The second steep decrease of compound fraction on the substrate ($t = 238\,\mathrm{s}$) is preceded by a decrease of compound on the target ($t = 237\,\mathrm{s}$) which is slightly preceded by a decrease in pressure ($t = 236.5\,\mathrm{s}$). The following interpretation makes sense. The decrease in pressure limits the compound forming on the target which becomes back more metallic due to sputtering. The latter supplies the substrate of more metal not only increasing its gettering capacity but at the same time also decreasing its compound fraction.

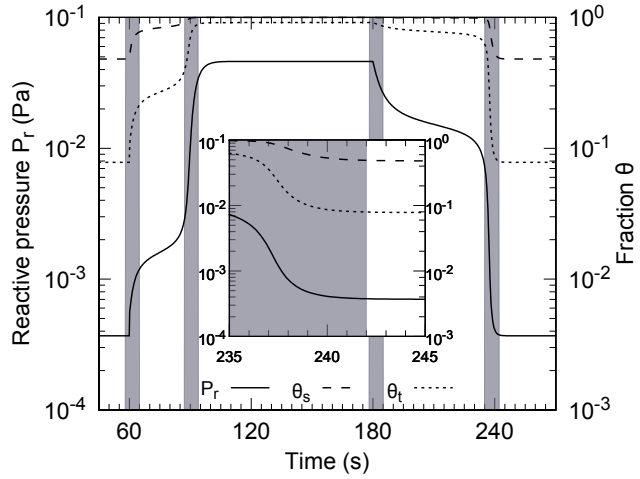

(a)

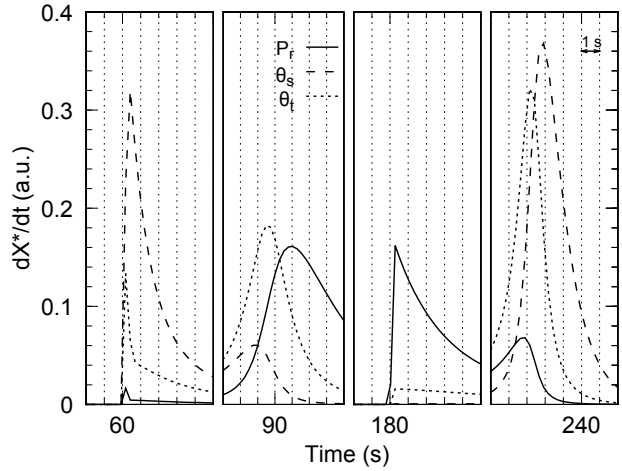

(b)

Figure 2.17: *Time evolution of the reactive pressure, the compound fraction on the substrate and the compound fraction on the target when increasing the reactive flow from just below the second critical flow to just above the first critical flow at time* 60 s *and decrease it in the same way at time* 180 s*. The evolution of (a) the variables and of (b) their normalized first derivatives (see eq. 2.43) is shown. The highlighted zones in (a) corresponds with the figures in (b).*

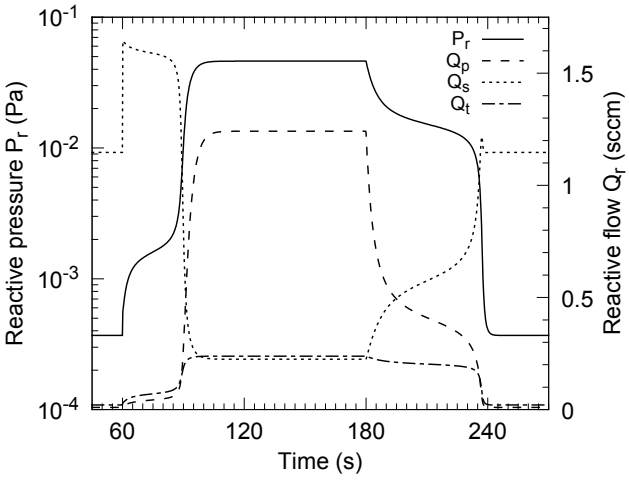

Figure 2.18: *Time evolution of the reactive pressure and the gas consumptions by the pump, the substrate and the target when increasing the reactive flow from just below the second critical flow to just above the first critical flow at time* $60\,\mathrm{s}$ *and decrease it in the same way at time* $180\,\mathrm{s}$.

Figure 2.18 shows the gas consumptions by the target, the substrate and the vacuum pump. It supports the higher given interpretations. Additionally it clearly shows that when moving from metallic towards poisoned mode, the substrate consumes at the beginning of the transition the largest portion reactive gas. At the end of the transition the substrate hands over this role to the vacuum pump. The return from poisoned mode to metallic mode sets off with a strong reduction in reactive gas consumption by the pump, while the substrate dominantly takes over the gas consumption towards the end of this transition.

This behavior qualitatively corresponds with experimental findings. To prove this, the time dynamics of the poisoning of an Al $2\,\mathrm{inch}$ target in an $\mathrm{Ar/O_2}$ atmosphere is measured by recording the total pressure and the discharge voltage. As the experiment is performed with a constant Ar flow $(10\,\mathrm{sccm})$ which results in a pressure of $0.34\,\mathrm{Pa}$, the pumping speed equals $49\,\mathrm{Ls^{-1}}$. The reactive pressure is obtained by subtracting the total pressure with the Ar pressure when operating non reactive. The measured limited discharge current was $0.5\,\mathrm{A}$. The recorded discharge voltage is primarily determined by the state of the target and can as such be viewed as a measure for the compound fraction. The experiment went as follows. The reactive flow was initially set to $0.5\,\mathrm{sccm}$ operating in metallic mode for $200\,\mathrm{s}$. Subsequently the reactive flow was in one step increased to $3.0\,\mathrm{sccm}$. This operation point lays in the order of $0.1\,\mathrm{sccm}$ above the first critical flow. After $200\,\mathrm{s}$ operating in poisoned mode the reactive flow is back decreased to the

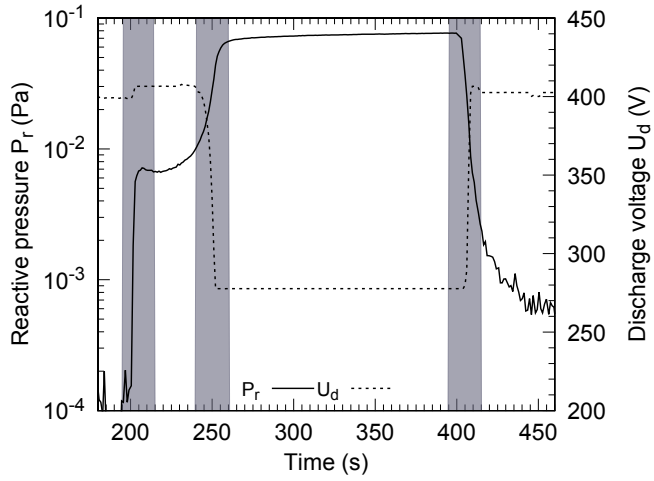

(a)

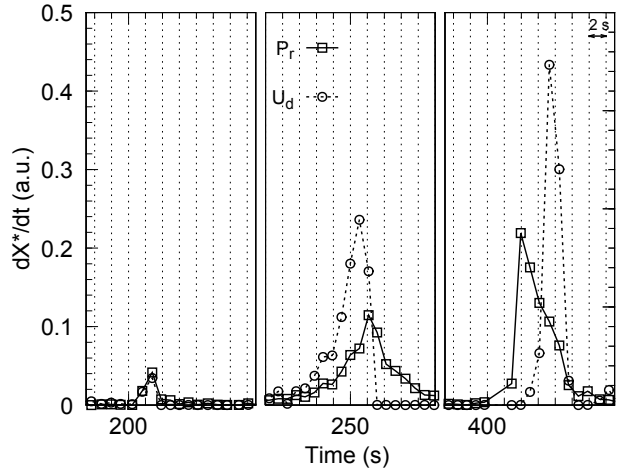

(b)

Figure 2.19: *Experimental time evolution of the reactive pressure and the discharge voltage when the reactive oxygen flow is increased from* $0.5\,\mathrm{sccm}$ *to* $3\,\mathrm{sccm}$ *at* $t = 200\,\mathrm{s}$ *and decreased back to* $0.5\,\mathrm{sccm}$ *at* $t = 400\,\mathrm{s}$*. The evolution of (a) the variables and of (b) their normalized first derivatives (see eq. 2.43) is shown. The highlighted zones in (a) corresponds with the figures in (b).*

initial $0.5\,\mathrm{sccm}$ for $200\,\mathrm{s}$. The recording rate for both the voltage and the pressure was $1\,\mathrm{Hz}$. When moving from metallic mode into poisoned mode, the experimental pressure behavior (Fig. 2.19a) qualitatively corresponds with the simulated behavior (Fig. 2.17a). Indeed, the two steep pressure increases are separated by a quasi-plateau. The first pressure increase coincidence with the first voltage increase at $203\,\mathrm{s}$. The second pressure increase follows $\sim 1\,\mathrm{s}$ after the steep voltage decrease at $251\,\mathrm{s}$. As this time separation approaches the experimental resolution, this experiment is repeated for different reactive flows that poisons the target. This time separation of $\sim 1\,\mathrm{s}$ was reproducible for each experiment. The fact that the voltage first slightly increases and in the second step decreases indicates that an intermediate state of the target is accessed before full poisoning. This can be attributed to the formation of a dominating chemisorbed fraction in the first step and in the second step of stoichiometric oxide. This can however not be explained within the Berg model as only one type of compound is modeled. Nevertheless is the voltage change each time a consequence of some kind of compound formation or removal.

When moving from poisoned to metallic mode at $400\,\mathrm{s}$ only one steep change in pressure and voltage is noted in contrast to the simulation (Fig. 2.17a). The intermediate quasi plateau disappeared as the working flow of $0.5\,\mathrm{sccm}$ in the metallic mode lays much lower then the second critical flow. Because of this, the two transitions are not separated in time. This effect is already implicitly illustrated for the Berg model by Fig. 2.16. However the increase in pressure at $404\,\mathrm{s}$ now precedes the increase in voltage with almost $4\,\mathrm{s}$ (Fig. 2.19b). This is in qualitative agreement with the simulation (Fig. 2.17b) where the time separation is yet much smaller. The reactive pressure in the experiment when moving from poisoned to metallic mode gradually decreases back to the start pressure after the steep transition at $404\,\mathrm{s}$.

2.3 Summary

The original Berg model from 1987 was not the first model for reactive sputtering. Analytical models describing the abrupt transition in deposition rate at a critical pressure set off with Heller in 1973. As the original Berg model, most models did only considered sticking of reactive gas to the surface as poisoning mechanism. Up till Steenbeck (1982) none of these models was able to reproduce a hysteresis as described in section 1.3. It was the inclusion of a gettering mechanism depending on the state of the substrate which made this possible. Affinito (1984) was the first to recognize that chemisorption could not be the only poisoning mechanism of importance for some reactive sputtering systems and included this in his model equations. These pioneers paved the way for the godfather of the reactive sputtering model: S. Berg.

The original Berg model can be considered as a first milestone in modeling reactive sputtering deposition. The prime importance of gas kinetics at the substrate was recognized by successfully reproducing a hysteresis. The model is analytical and simple with a minimum in parameters. Nevertheless the model is able to reproduce many qualitative trends concerning the hysteresis and towards operation optimization. The dependency of the original model on the material and the operation parameters are investigated. Their trends can be qualitatively understood. A manifold of extensions based on this model exist and can be subdivided in two categories: extensions which add or change essential physical mechanisms, and extensions which improve the spatial or temporally resolution of the model. Three extensions of the last category are implemented: a deposition profile (spatial), a ion current profile (spatial) and a time dependent model (temporally). A deposition profile results not only in a more detailed description but also resolves the problem of choosing a correct effective substrate area if the original model is used. A current profile that is narrowed, confirms that the hysteresis will decrease and even vanish. Finally a time dependent Berg model is implemented, the time dynamics of poisoning and depoisoning of the system are simulated and compared with experiment. The time sequence of first target poisoning followed by a reactive pressure rise when moving from metallic to poisoned mode, and the reversed sequence when moving from poisoned to metallic mode are in agreement.

References

[1] Berg, S., Blom, H. O., Larsson, T., and Nender, C. *Journal of Vacuum Science & Technology a-Vacuum Surfaces and Films* **5**(2), 202–207 (1987).

[2] Heller, J. *Thin Solid Films* **7**(2), 163–176 (1973).

[3] Abe, T. and Yamashina, T. *Thin Solid Films* **30**(1), 19–27 (1975).

[4] Shinoki, F. and Itoh, A. *Journal of Applied Physics* **46**(8), 3381–3384 (1975).

[5] Hollands, E. and Campbell, D. S. *Journal of Materials Science* **3**(5), 544–552 (1968).

[6] Stirling, A. J. and Westwood, W. D. *Thin Solid Films* **7**(1), 1–10 (1971).

[7] Steenbeck, K., Steinbeiss, E., and Ufert, K. D. *Thin Solid Films* **92**(4), 371–380 (1982).

[8] Affinito, J. and Parsons, R. R. *Journal of Vacuum Science & Technology A* **2**(3), 1275–1284 (1984).

[9] Brunauer, S., Emmett, P. H., and Teller, E. *Journal of the American Chemical Society* **60**(2), 309–319 (1938).

[10] Hrbek, J. *Thin Solid Films* **42**(2), 185–191 (1977).

[11] Castellano, R. N. *Thin Solid Films* **46**(2), 213–221 (1977).

[12] Lemperiere, G. and Poitevin, J. M. *Thin Solid Films* **111**(4), 339–349 (1984).

[13] Lounsbury, J. *Journal of Vacuum Science & Technology* **6**(5), 838–842 (1969).

[14] Karulkar, P. C. and Nordman, J. E. *Journal of Applied Physics* **50**(11), 7051–7059 (1979).

[15] Aita, C. R. and Marhic, M. E. *Journal of Applied Physics* **52**(11), 6584–6587 (1981).

[16] Blom, H. O., Berg, S., and Larsson, T. *Thin Solid Films* **130**(3-4), 307–313 (1985).

[17] Coburn, J. W., Taglauer, E., and Kay, E. *Japanese Journal of Applied Physics* **13**(S1), 501–504 (1974).

[18] Nyberg, T., Berg, S., Helmersson, U., and Hartig, K. *Applied Physics Letters* **86**(16), 164106 (2005).

[19] Nyberg, T. and Berg, S. *A method for reactive sputtering deposition*. WO2003006703 A1. (2003).

[20] Sagas, J. C., Duarte, D. A., Irala, D. R., Fontana, L. C., and Rosa, T. R. *Surface & Coatings Technology* **206**(7), 1765–1770 (2011).

[21] Okamoto, A. and Serikawa, T. *Thin Solid Films* **137**(1), 143–151 (1986).

[22] Hsieh, J. H., Li, C., and Liu, S. J. *Materials Chemistry and Physics* **141**(2-3), 869–873 (2013).

[23] Kadlec, S., Musil, J., and Vyskocil, J. *Journal of Vacuum Science & Technology a-Vacuum Surfaces and Films* **8**(3), 1560–1565 (1990).

[24] Somekh, R. E. *Journal of Vacuum Science & Technology a-Vacuum Surfaces and Films* **2**(3), 1285–1291 (1984).

[25] Motohiro, T. *Journal of Vacuum Science & Technology a-Vacuum Surfaces and Films* **4**(2), 189–195 (1986).

[26] Macak, K., Macak, P., and Helmersson, U. *Computer Physics Communications* **120**(2-3), 238–254 (1999).

[27] Van Aeken, K., Mahieu, S., and Depla, D. *Journal of Physics D-Applied Physics* **41**(20), 205307 (2008).

[28] Depla, D. and Leroy, W. P. *Thin Solid Films* **520**(20), 6337–6354 (2012).

[29] Clarke, G. C. B., Kelly, P. J., and Bradley, J. W. *Surface and Coatings Technology* **200**(56), 1341–1345 (2005).

[30] Jonsson, L. B., Nyberg, T., and Berg, S. *Journal of Vacuum Science & Technology a-Vacuum Surfaces and Films* **18**(2), 503–508 (2000).

3 RSD Model

A successor of the Berg model treated in the previous chapter is the so-called RSD model or Reactive Sputter Deposition model. It is a first category extension (see section 2.2.3) of the original Berg model where the physical process of direct reactive ion implantation and reactive knock-on implantation is added. This model extension is able to resolve some limitations of the original Berg model. The relevance of the RSD model is demonstrated in section 3.1 as the original Berg model fails in predicting some experimental findings. Also the pre-RSD models including the process of reactive implantation as additional poisoning mechanism are mentioned. The original RSD model [1] is formulated in section 3.2 with some new views on the theoretical base and solving of the implantation and reaction in the subsurface. The analytical solution for the uniform implantation profile is one of the achievements here. As the quantification of the model parameters is usually incomplete, their will exist some freedom in parameter choice. Within this work, the parameter freedom is investigated by fitting two versions of the RSD model to experimental hystereses in section 3.3.2. Some new interesting correlation between parameters have be retrieved.

3.1 Relevance

The original Berg model already explains most of the basic concepts in reactive sputtering deposition. However, as almost every model, it has its limitations. In section 3.1.1 it is shown that the original Berg model at least fails in three exper-

imental observations: the formed compound thickness on the target, the influence of the inert gas pressure and the influence of the pumping speed. These three limitations can be related to the missing mechanism of reactive implantation as poisoning process in the original Berg model. Section 3.1.2 gives a chronological overview of the introduction of this mechanism in reactive sputter models up to the original RSD model.

3.1.1 Limitations

3.1.1.1 Compound thickness

The original Berg model is inherently a one-layer surface model with chemisorption as only compound forming mechanism. On the target side this implicitly means that only one monolayer of compound can be formed. However this seems experimentally not the case. This can be demonstrated in a target sputter cleaning experiment as in [2]. Such experiment proceeds as follows. After removing any contamination on the target by sputtering in pure Ar gas, the system is operated in pure reactive gas to ensure a complete poisoning of the target surface. In a following step, the discharge is switched off and the reactive gas is pumped away. This ensure that no reaction takes place during the last step. For this last step, inert gas is introduced into the chamber. After stabilization, the discharge is switched on and the discharge voltage as function of time is measured. The discharge voltage is mainly influenced by the effective secondary electron emission yield Y_{SEE} of the target surface. This Y_{SEE} depends on the composition of the target surface or said differently on the compound fraction on the target surface. Assuming a linear dependency of the Y_{SEE} on the compound fraction θ_c between a fully poisoned surface and a pure metal surface [3] gives

$$Y_{SEE} = Y_{SEE,m}(1 - \theta_c) + Y_{SEE,c}\theta_c \tag{3.1}$$

with $Y_{SEE,m}$ and $Y_{SEE,c}$ respectively the effective secondary electron emission yield of pure metal and of pure compound. The discharge voltage can be related to the Y_{SEE} by a relation proposed by Thorton [4] and modified by Buyle [5]. He states that the minimum discharge voltage U_{min} for a magnetron discharge as function of the Y_{SEE} is given by

$$U_{min} = \frac{W_i}{E(P)Y_{SEE}\varepsilon_i\varepsilon_e} \tag{3.2}$$

where W_i is the effective ionization energy of Ar, $E(P)$ is the effective gas ionization probability depending on the pressure P, ε_i is the ion collection efficiency and ε_e is the average ion fraction generated by a single emitted electron out of the V_{min}/W_i ions that maximally can be generated. For constant pressure and assuming that only Y_{SEE} is material dependent while the other parameters in eq. 3.2

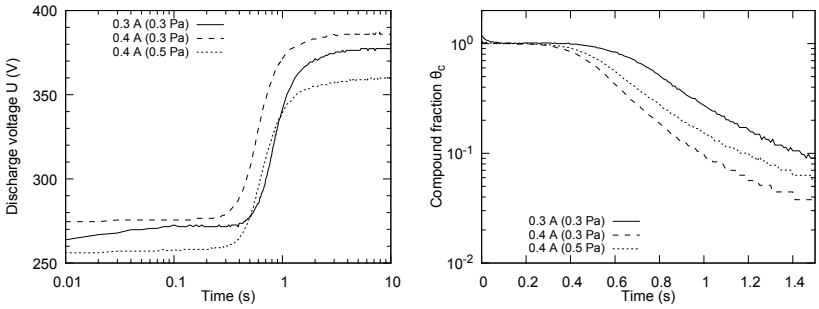

Figure 3.1: *Sputter cleaning experiment of a sputter oxidized* $2\,\mathrm{inch}$ *Al target for different discharge currents and different Ar pressures. The target is first sputtered in pure* O_2 *to fully oxidize and afterwards sputtered clean in pure Ar. (a) The recorded discharge voltage and (b) the calculated compound fraction based on eq. 3.4. Data taken from Depla et al. [2].*

have a weak dependency on the material and/or voltage, the Y_{SEE} of a material will be inversely proportional to the discharge voltage [6]. In this way eq. 3.1 can be rewritten as

$$\frac{1}{U} = \frac{1}{U_m}(1-\theta_c) + \frac{1}{U_c}\theta_c \tag{3.3}$$

in terms of the discharge voltage for a metal U_m and a compound U_c surface. The time evolution in voltage $U(t)$ can now be linked to the compound fraction $\theta_c(t)$ of the target surface as

$$\theta_c(t) = \frac{1/U(t) - 1/U_m}{1/U_c - 1/U_m} \tag{3.4}$$

Such target sputter cleaning experiments [2] of an Al target oxidized in pure oxygen and sputter cleaned in Ar at the same conditions are shown in Fig. 3.1. The discharge voltage behavior for a current of $0.3\,\mathrm{A}$ and $0.4\,\mathrm{A}$ at an argon pressure of $0.3\,\mathrm{Pa}$ and at $0.5\,\mathrm{Pa}$ for the current $0.4\,\mathrm{A}$. The compound fraction as calculated according eq. 3.4 is shown in Fig. 3.1b. The discharge voltage U_c of the compound is identified with $U(30\,\mathrm{ms})$ as this is the minimal ramp time of the power supply. The discharge voltage U_m of the metal is the stabilized voltage $U(10\,\mathrm{s})$ when the target is completely clean again. At the same pressure $(0.3\,\mathrm{Pa})$ the entire voltage curve of the high current $(0.4\,\mathrm{A})$ lays above the low current $(0.3\,\mathrm{A})$ as may be expected from typical IU-characteristics. Similarly the voltage curve at low pressure $(0.3\,\mathrm{Pa})$ lays above the high pressure $(0.5\,\mathrm{Pa})$ voltage curve for the same current $(0.4\,\mathrm{A})$. A greater potential difference has to be applied to obtain the same current when the pressure drops as the impedance of the plasma increases. Figure 3.1b clearly shows that their seems some delay in the cleaning or the compound re-

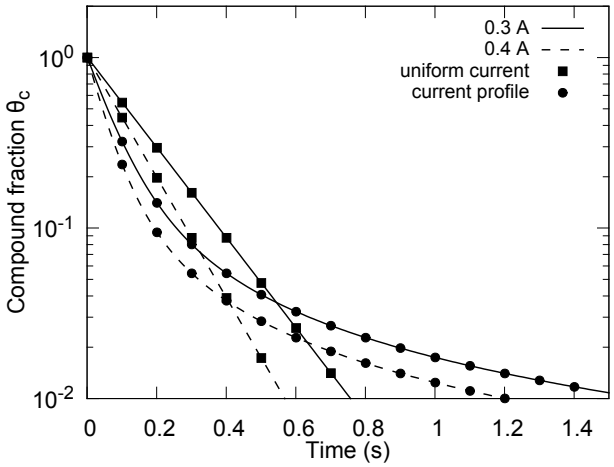

Figure 3.2: *The sputter cleaning time dynamics following a Berg model with a uniform current (■) and with a current profile (●) for two different discharge currents.*

moval of the target surface. This delay becomes longer if the current is decreased or if the pressure is increased.

If the time dependent Berg model (section 2.2.3.3) is applied to the time dynamic of this sputter cleaning step, the compound formation term due to the reactive gas in eq. 2.40 falls out and becomes

$$n_{0,s}\frac{\mathrm{d}\theta_t(t)}{\mathrm{d}t} = -I_{ion}Y_c\theta_t(t) \tag{3.5}$$

This allows a straightforward solution of the time dependency of θ_c which is

$$\theta_c = e^{-\frac{I_{ion}Y_c}{n_{0,s}}t} \tag{3.6}$$

This exponential behavior of θ_c for the current $0.3\,\mathrm{A}$ and $0.4\,\mathrm{A}$ is given in Fig. 3.2. Their is of course a faster cleaning at higher current as in the experiment but the direct exponential decrease in compound fraction is experimentally not observed. The assumption of an uniform current is maybe to crude here. The time dependent Berg model is extended with the inclusion of an ion current profile as in section 2.2.3.2. Equation 3.6 becomes

$$\theta_{c,i} = e^{-\frac{I_{ion,i}Y_c}{n_{0,s}}t} \tag{3.7}$$

by subdividing the target in cells with label i and assigning an ion current $I_{ion,i}$ and a compound fraction $\theta_{c,i}$ to it. The compound fraction θ_c is then defined as a current weighted average of the fractions $\theta_{c,i}$. The same Gaussian current profile

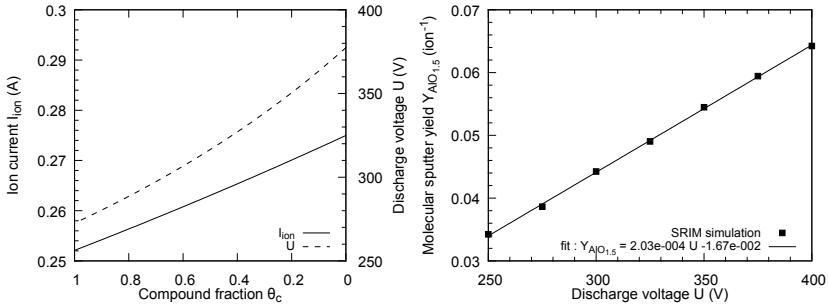

Figure 3.3: *(a) The calculated dependency of the ion current (eq. 3.8) and the discharge voltage (eq. 3.9) on the compound fraction. (b) SRIM simulated voltage dependency of the sputter yield for $AlO_{1.5}$ molecules with surface binding energies taken from [7].*

as in section 2.2.3.2 is used. This seems to improve at some point the match with the experiments. Notwithstanding the initial decrease in θ_c is even steeper then in the uniform case, this decrease becomes less and less steeper at later times. When the current profile is included, the simulated compound fraction after $1.5\,\mathrm{s}$ differs"only" one order of magnitude while this is for the uniform current many orders. This deviation could in principle be fixed by optimization of the used parameters I_{ion}, Y_c, $n_{0,s}$ and the current profile. However in the simulations of Fig. 3.2 the maximum decrease is observed at the start of the cleaning process while the experiment shows its maximum decrease at a much later time ($\sim 1\,\mathrm{s}$). This can not be fixed by parameter optimization but indicates a wrong functional dependency.

Two additional improvements in the functional dependency of eq. 3.5 are still possible without changing the basic assumption of the Berg model. For the moment there is assumed that the ion current equals the discharge current. This is not fully true. The ion current I_{ion} and the discharge current I_d are related to each other according eq. 1.7 with the secondary electron emission yield. Taking this Y_{SEE} constant during the sputter cleaning would just mean a parameter optimization. However the Y_{SEE} changes due to the change in compound fraction as in eq. 3.1. This means that the ion current I_{ion} depends on the compound fraction θ_c as

$$I_{ion}(\theta_c) = \frac{I_d}{1 + Y_{SEE,m}(1-\theta_c) + Y_{SEE,c}\theta_c} \tag{3.8}$$

This dependency is shown in Fig. 3.3a with $Y_{SEE,m} = 0.091$ and $Y_{SEE,c} = 0.19$ [2] for the discharge current of $0.3\,\mathrm{A}$. This relationship can be considered as almost linear.

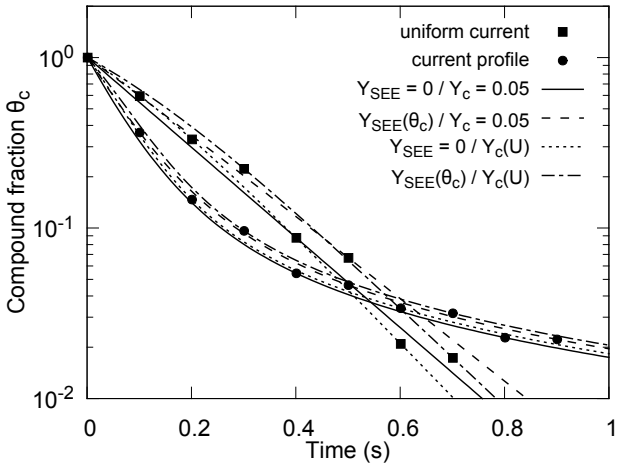

Figure 3.4: *The sputter cleaning time dynamics following a Berg model with a uniform current (■) and with a current profile (●) for a discharge current of* 0.3 A*. The influence of the compound sputter yield $Y_c(U)$ and of the effective secondary electron emission yield $Y_{SEE}(\theta_c)$ on the dynamics is taken into account separately and combined.*

A second improvement is taking into account the energy dependency of the sputter yield Y_c of the compound. For simplicity it is here assumed that the energy of an Ar^+ ion hitting the target equals the full discharge voltage. Rewriting eq. 3.4 as a function of θ_c gives

$$U = \frac{U_m U_c}{U_c(1-\theta_c) + U_m \theta_c} \tag{3.9}$$

This relationship between θ_c and U is added to Fig. 3.3a. The dependency of the sputter yield on the ion energy for Al_2O_3 is simulated with SRIM [8]. The most important parameter in the SRIM simulation for determining sputter yields is the surface binding energy (SBE) of the constituents. Kubart et al. [7] fitted SBE's for Al_2O_3 with TRIDYN [9], a similar simulation package as SRIM, to experimental data. He found satisfactory results with SBE(Al)=12 eV and SBE(O)=9 eV. A linear fit to the SRIM simulation results was obtained and is shown in Fig. 3.3b. Note that using packages as SRIM or TRIDYN to simulate sputter yields of compounds is questionable. However the goal here is not to quantify this relation into detail, but just to have a reasonable estimate. The relation between the compound fraction θ_c and the sputter yield Y_c of the Al_2O_3 becomes in this case

$$Y_c(\theta_c) = \left(\frac{0.0203 U_m U_c}{U_c(1-\theta_c) + U_m \theta_c} - 1.67 \right) \times 10^{-2} \tag{3.10}$$

Substitution of eq. 3.8 and eq. 3.10 into the eq. 3.5 gives a new functional dependency of the compound fraction as function of time. The impact of these two adjustments is shown in Fig. 3.4 for the original Berg model with uniform current and the extended model with a current profile. The separate and the combined modifications are compared with the initial model. The impact on the functional dependency of the compound fraction is yet minimal within each model. Even more important is that the maximal removal rate remains close to the start of the sputter cleaning and that no delay in compound removal is observed. For the uniform case the decrease in compound fraction seems a little bit decelerated in the beginning, but not sufficient to match the experiments. This indicates that the observed starting delay in sputter removal can not be explained by adding more detail to the existing processes.

3.1.1.2 Influence inert gas pressure

A second limitation of the original Berg model is observed when the influence of the inert gas pressure on the hysteresis is studied. Hystereses of an Al target were measured in an Ar/O_2 atmosphere were the Ar pressure was varied between $0.4 - 3.06\,\mathrm{Pa}$. The reactive pressure as function of the oxygen flow are shown in Fig. 3.5. These experiments were performed with a fixed current of $0.4\,\mathrm{A}$ and pumping speed of $65\,\mathrm{Ls}^{-1}$ in a cylindrical tube. This tube was closed at the top with a circular lid where a cut-away is foreseen to introduce the magnetron. It appears that with an increase of Ar pressure the hysteresis width decreases and even vanishes as shown in Fig. 3.6b. This hysteresis width is defined as the difference between the first critical oxygen flow $Q_{c,1}$ and the second $Q_{c,2}$. As the transitions between metallic and poisoned mode also become less abrupt with increasing Ar pressure, the critical flows become, especially at the highest Ar pressures, not trivial to determine. To uniquely quantify these critical points for all hystereses a Gaussian is fitted to the first derivative $\mathrm{d}P_r/\mathrm{d}Q_{in}$ of the increasing and the decreasing branches of the hysteresis. The mean of each Gaussian is identified as a critical flow. The dependency on the Ar pressure of these critical flows is given in Fig. 3.6a. Both critical oxygen flows shift to higher values, but because $Q_{c,2}$ shifts faster as function of P_{Ar}. The hysteresis disappears around $P_{Ar} = 3\,\mathrm{Pa}$.

An explanation of this trend with the Berg model is not evident as the inert gas pressure is not an explicit parameter of the model. However the inert gas pressure can implicitly be included as it influences other model parameters. These are:

- the sputter yields of compound and metal by a changing discharge voltage
- the effective substrate area or deposition profile
- the effective target area or ion current profile by a changing racetrack width

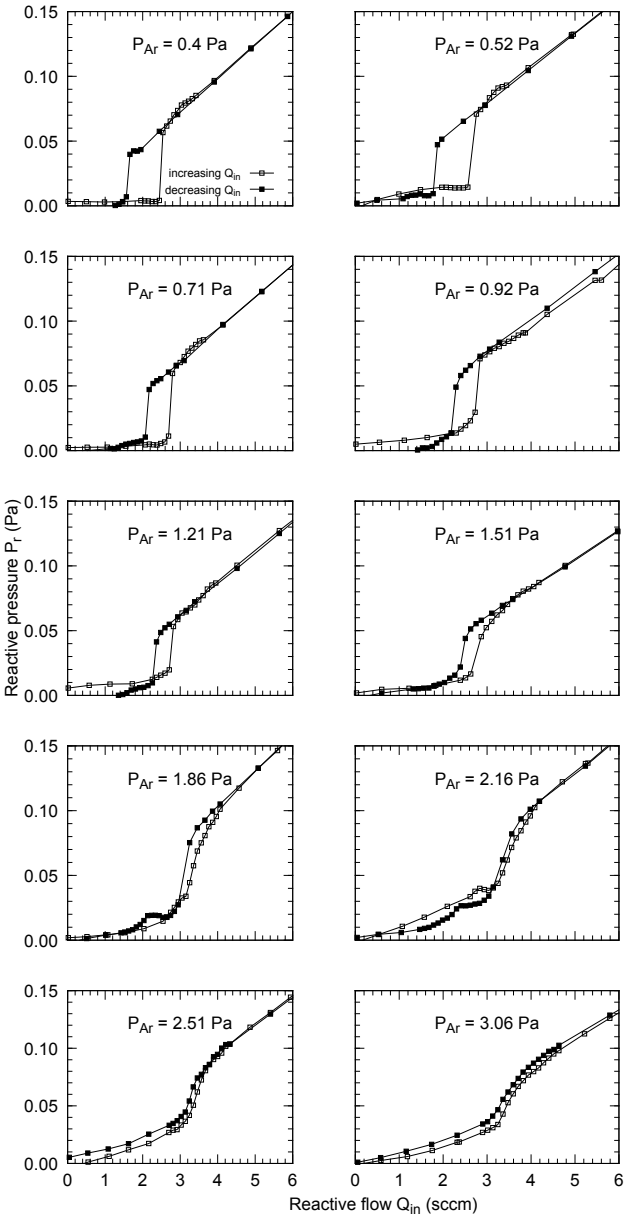

Figure 3.5: *Influence of the Ar pressure on the hysteresis for a* $2\,\mathrm{inch}$ *Al target sputtered in a cylindrical tube under an Ar/O_2 atmosphere at a discharge current of* $0.4\,\mathrm{A}$ *and pumping speed of* $65\,\mathrm{Ls}^{-1}$*. Unpublished data provided by D. Depla.*

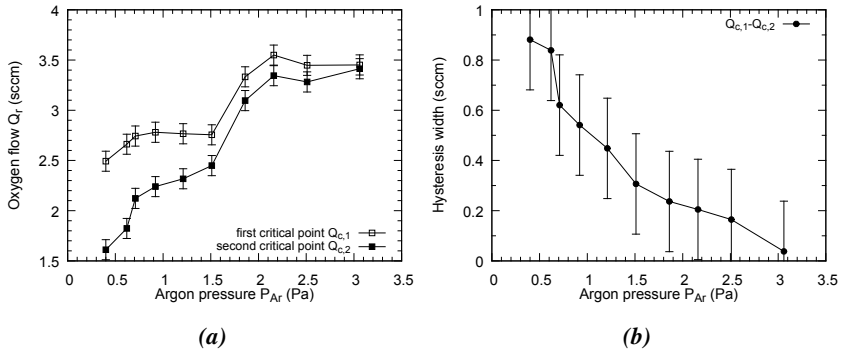

(a) ***(b)***

Figure 3.6: *(a) The critical points of the hystereses of Fig. 3.5 determined as the mean of a Gaussian fitted to the first derivative $\mathrm{d}P_r/\mathrm{d}Q_{in}$. (b) The hysteresis width defined as the difference between the first and the second critical point from (a). Unpublished data provided by D. Depla.*

The inert gas pressure influences the discharge voltage and as such the sputter yields. The influence of the sputter yields on the Berg model were already shown in Fig. 2.8a and Fig. 2.8c. A voltage dependency on the Ar pressure is shown in Fig. 3.7a for an Al $2\,\mathrm{inch}$ target operating in non-reactive mode at a constant current of $0.25\,\mathrm{A}$. The target erosion across this measurements was limited. In the relevant pressure range ($> 0.4\,\mathrm{Pa}$) the voltage decrease is already quite flat. To match closer with the experiments the average voltage at start and end of every hysteresis experiment is also shown in Fig. 3.7a for the current of $0.4\,\mathrm{A}$. This voltage dependency is not only influenced by the working pressure but also by target erosion. As the experiments were performed sequentially with the same target for the pressure range $0.4 - 1.51\,\mathrm{Pa}$ the target erosion increases in parallel with the working pressure. Increasing the working pressure and a deeper target erosion both lower the discharge voltage explaining the somewhat steeper decrease in this case. The latter voltage dependency is used to determine the sputter yields of the metal and the compound in the Berg model. The previous fitted relation based on SRIM simulations in Fig. 3.3b is used for the $\mathrm{AlO}_{1.5}$ sputter yield while the Al sputter yield is based on a linear fit to experimental sputter yields [10] as

$$Y_m(U_d) = (1.91U_d - 111) \times 10^{-3} \tag{3.11}$$

Also the deposition profile is strongly dependent on the gas pressure. This means that the effective substrate area will reduce as the working pressure increases due to an increased scattering of sputtered particles with the gas. This dependency on the hysteresis for the Berg model was shown in Fig. 2.9c. In this way the sputtered material will be deposited within a more restricted area. A further consequence is that more material will return back to the target resulting in a

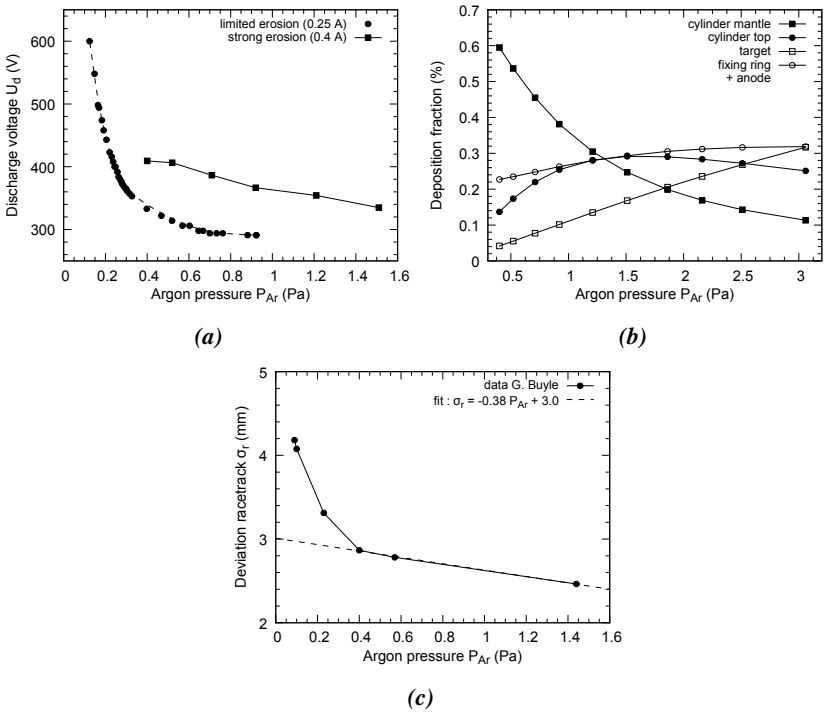

Figure 3.7: *The implicit effect of the Ar pressure on (a) the discharge voltage, (b) the deposition fractions and (c) the width of the racetrack. Unpublished data taken from G. Buyle.*

further decrease of the effective sputter yields. The deposition profile on the cylindrical tube, the closing lid and the magnetron were simulated with SiMTra for the pressures of the hysteresis experiments. Figure 3.7b shows how the fraction of particles that are deposited on the cylindrical tube decreases while the fraction on the magnetron (target, fixing ring and anode) increases with higher Ar pressures. The fraction on the closing lid initially increases but eventually also decreases at pressures above 1.5 Pa.

Finally the target racetrack is also to some extent determined by the gas pressure which translates to a changing effective target area in the Berg model which was already illustrated in Fig. 2.9a. The influence of the Ar pressure on the racetrack width was measured and explained by Buyle et al. [11]. These racetrack measurements were fitted with a Gaussian where the deviation of the Gaussian quantifies the width. These results are given in Fig. 3.7c where a narrowing of the racetrack with increasing pressure is noted. However the strongest change is observed at pressures lower then used in the hysteresis experiments. A linear fit to the

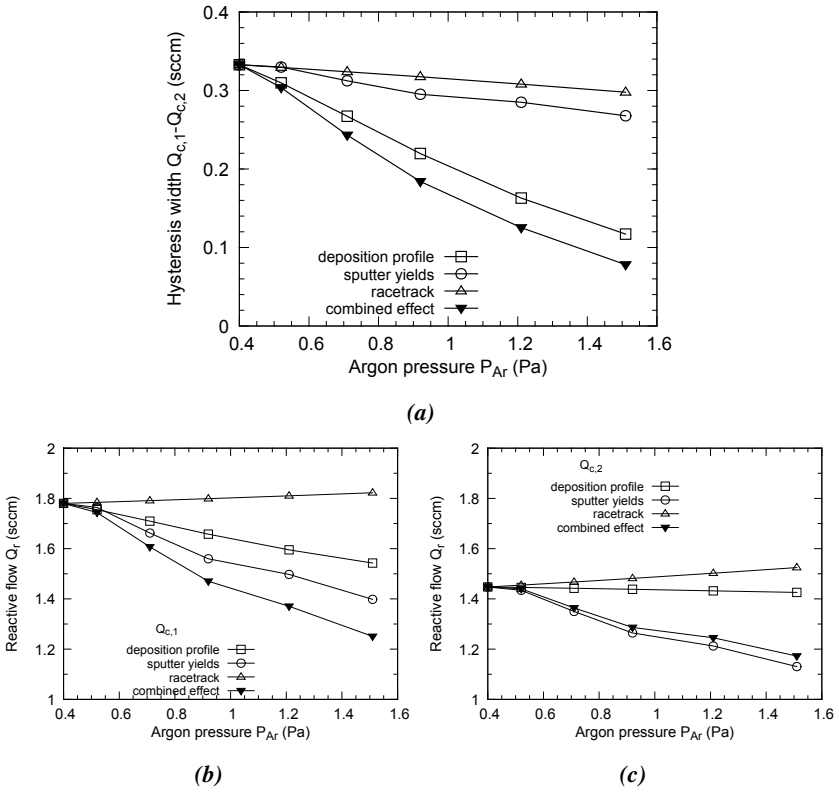

Figure 3.8: *The implicit influence of the Ar pressure on the hystereses modelled by a Berg model with a deposition profile and a current profile. The hysteresis is quantified by (a) the hysteresis width which is the difference between (b) the first critical flow and (c) the second critical flow.*

three pressures within the range of the hysteresis experiments has been performed to quantify the narrowing of the hysteresis.

Armed with these estimates for the functional dependencies of the sputter yields, the deposition profile and the current profile on the working pressure, the influence on the hysteresis is simulated with an extended Berg model. This spatial extended Berg model includes both a deposition profile as in section 2.2.3.1 and a ion current profile as in section 2.2.3.2. The simulations are performed for the pressure range $0.4 - 1.51\,\mathrm{Pa}$ where the individual influence and the combined influence of the parameters on the hysteresis width (Fig. 3.8a) and on the two critical points (Fig. 3.8b and Fig. 3.8c) are shown. As well the combined as the individual parameter variation result in a decrease of the hysteresis width conform with the experiments. However outside the simulation range, the hysteresis seems

to completely vanish at even higher pressures. Notwithstanding this qualitative resemblance between the Berg model and the experiments for the decreasing hysteresis width, do the critical flows in the simulations shift to lower oxygen flows in contrast to the experimental findings. Only the impact of the racetrack narrowing reproduces the expected trend. However as this narrowing is comparably small, it only slightly increases both critical flows. A second qualitative difference can be observed. While for the hysteresis experiments the shift of $Q_{c,2}$ is stronger then the shift of $Q_{c,1}$, this is in the simulations reversed. This stronger shift of $Q_{c,1}$ compared to $Q_{c,2}$ in the simulations is most prominently present for the influence of the deposition profile.

To conclude, the changes in deposition profile, sputter yields and racetrack by the working pressure can not qualitatively explain in a correct way the experimental observed disappearing of the hysteresis for Al sputtered in an Ar/O_2 atmosphere. It seems that an additional process depending on the reactive mole fraction is missing in the description. As the Ar pressure does not influence the oxygen partial pressure should the chemisorption process be left unaffected by the Ar pressure increase. However the mole fraction of oxygen will decrease which hints that a process mainly depending on this mole fraction is missing in the model. A first candidate that depends on this mole fraction is the composition of the ion current hitting the target which will be mainly composed out of Ar^+ and $O_2{}^+$.

3.1.1.3 Influence pumping speed

The influence of the pumping speed on the hysteresis has already been mentioned before. Experimental evidence for the sputtering of Al in an Ar/O_2 atmosphere was already shown in Fig. 1.15. By increasing the pumping speed the hysteresis narrows and eventually vanishes. The Berg model is able to reproduce this behavior. This was shown before in Fig. 2.9d for the original Berg model. However the experiments disagree with the simulations at some point. In the experiments the entire hysteresis shifts to higher reactive flows with increasing pumping speed, notwithstanding that the second critical flow shifts faster to eliminate the hysteresis. In the simulations only the second critical flow seems to substantially shift in order to remove the hysteresis.

The corresponding hystereses of Fig. 1.15 in discharge voltage are shown in Fig. 3.9. This voltage behavior is interesting as it is hard to explain with the Berg model. The discharge voltage seems to increase before the first critical point after which it decreases by going to poisoned mode. The pressure rise before the first critical point is small, as such will changes in the plasma composition probably not be the main cause. It seems more likely that the state of target surface through the Y_{SEE} defines this voltage behavior. Besides the metal state and the compound state as defined in the Berg model, their seems a third state possible with a lower Y_{SEE} then metal.

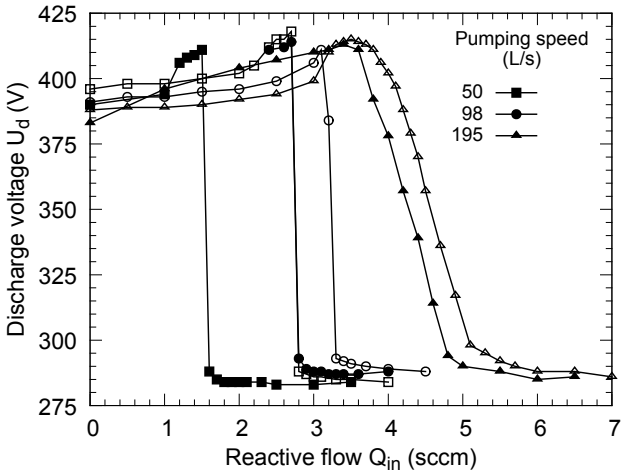

Figure 3.9: *Experimental hystereses of the discharge voltage U_d under direct control of the reactive flow for increasing pumping speeds. The system was a* 2 inch *Al target sputtered in an Ar/O_2 atmosphere at a discharge current of* 0.5 A *and Ar pressure of* 0.4 Pa*. Unpublished data provided by W. Leroy.*

3.1.2 New mechanisms

A mechanism that can resolve the above mentioned limitations of the Berg model is reactive ion implantation. Indeed the sputter atmosphere consists out of inert gas atoms and reactive gas molecules. Both species can be ionized and will contribute to the ion current bombarding the target. This means that reactive gas species will be implanted into the target after which they can react to form compound. This is called direct reactive ion implantation. On the other hand it is possible that chemisorbed reactive gas atoms on the target surface are hit by an energetic ion and be knocked into the target. This is called reactive knock-on implantation. Briefly it is explained how these mechanisms could resolve some of the limitations of section 3.1.1. As reactive species get implanted by direct and knock-on implantation beyond the first surface layer, the compound formation range will reach up to the implantation depth. This will result in a compound thickness of the same order. While this not necessarily needs both implantation mechanisms to explain, as only knock-on implantation could be sufficient, this is not the case for the influence of the inert gas pressure. Increasing the inert gas pressure, decreases the mole fraction of the reactive gas in the ion current towards the target. This would mean that the contribution of directly implanted reactive gas ions is diminished. In the case that direct reactive implantation is the dominating poisoning mechanism compared to chemisorption, poisoning of the target becomes harder with increasing inert gas pressure. The lower supply of reactive species in the target diminishes the hystere-

sis.

Historically Affinito et al. [12] were the first to include reactive ion implantation into a reactive sputter model as demonstrated in section 2.1.5. This was even before Berg formulated his first model. Affinito et al. argued that for the system Al$-$N$_2$ chemisorption is very small and cannot (alone) account for the observed poisoning of the Al target. They also showed that voltage controlled operation would only be possible if chemisorption is almost absent. As shown in eq. 2.15 they included a direct reactive ion implantation term with a reaction probability depending on the available reaction sites, which depends on the mole fraction of the reactive gas. Even how, their model remained a one-layer model without mentioning any layer thickness. They termed the compound formation by reactive ion implantation also as an ion plating process.

Sobe [13, 14] even proposed a model where ion plating was the only compound forming mechanism as chemisorption of neutral reactive gas for their system is non existing. The system they investigated was the sputtering of CrSi in CH_4, N_2 or CO_2. He also assumed a reactive ion current which is proportional with the mole fraction of the reactive gas in the chamber and found that the proportionality constant was even close to one for the N_2 gas. Again the model describes the target surface as a single layer.

Depla et al. studied in [15] the voltage behavior of a Al target and in [3] the voltage behavior of a Si target sputtered in an Ar/N_2 atmosphere. In the later it is possible to separate the influence of the plasma condition and the target surface condition on the discharge voltage. Based on their results they argued that chemisorption could not explain the observed phenomena and suggested direct reactive ion implantation as additional poisoning mechanism. This changes the target surface condition resulting in a changing Y_{SEE} and as such a changing voltage. Also they measured N_2 desorption of the Si target after reactive sputtering, which would indicate that not all implanted nitrogen is consumed in compound formation. The presence of non-reacted nitrogen after the sputtering of Cu was also measured with XPS [16]. A first quantitative analytical model for this direct reactive ion implantation was posted in [17]. It predicts avalanches and possible hysteresis of the target condition around critical reactive mole fractions, which are absent in the reactive pressure for conditions of high pumping speed and low ion current. This initial analytical model is a two layer model with a surface layer and a subsurface layer where implantation and consecutive reaction takes place based on a reaction probability and available reaction sites. An alternative reactive ion implantation model was formulated in [18] which calculates the compound fraction, the concentration of implanted reactive ions and the concentration of non-reacted reactive gas ions at the surface in time. This single layered model for the target was integrated in a time dependent Berg model in [19]. A simplification of the latter model was given in [20] to predict the critical mole fractions of existing ex-

perimental data where a fair agreement was found. The importance of direct ion implantation for the hysteresis increases when the pumping speed becomes high and/or the ion current low.

Rosen et al. [21] demonstrated with TRIDYN simulations the impact of both direct and knock-on implantation on the target poisoning. Kubart et al. [22] was the first to include this knock-on reactive implantation into a model of reactive sputtering deposition. The model he proposed was a time dependent Berg model with a multi layer description of the target. A threefold poisoning mechanism of the target was included: chemisorption, direct reactive ion implantation and knock-on reactive implantation. Notwithstanding the multi layer approach of the target, the implantation of reactive species only occurs in the bottom layer proportional to free reaction sites which makes the model more a two layer model. The compound formation after implantation was also assumed immediate.

In [1], Depla et al. proposed the steady state RSD model which incorporates the poisoning mechanisms of direct and knock-on reactive implantation into a Berg-like model. This model is on target level truly multi layered provided with a implantation profile and a reaction mechanism. The formulation of this RSD model forms the core of the next section.

3.2 Original model

3.2.1 Formulation

In the steady state RSD model, the reactive sputter process is divided in three parts: the target, the substrate and the vacuum chamber. For each part, balance equations have been formulated to conserve the relevant quantities, as in the original Berg model (see section 2.2.1). Besides this, direct and knock-on implantation are included together with a subsurface second order reaction mechanism for the compound formation between the implanted reactive gas species and the metallic target material. This section summarizes the equations and the variables governing each part of the steady state RSD model.

3.2.1.1 Target

The target is subdivided in two regions, the surface region with thickness s from where sputtering occurs and the underlying subsurface region with thickness D where reactive ions are implanted and react with the target material. While s is the thickness of one monolayer, D is defined by the implantation depth of reactive ions. For the target, three fractions are considered θ_m, θ_r and θ_c. The fractions θ_m and θ_r represent the fraction of non-reacted and of reacted target atoms in the surface layer of the target, while θ_c is the fraction of target atoms that has chemisorbed reactive gas molecules. The reacted fraction θ_r accounts for compound

molecules formed in subsurface regions by implanted reactive ions, after which they are transported to the surface by sputtering. The sputter yield of the target will be defined as

$$Y_s = Y_m\theta_m + Y_r\theta_r + Y_c\theta_c \tag{3.12}$$

with Y_m, Y_r, and Y_c the corresponding sputter yields of the different fractions. As in [1], it will be assumed that the compounds formed by chemisorption or by subsurface reaction are identical, so it can be stated that $Y_r = Y_c$. The speed v_s with which the surface recedes due to sputtering, is defined as

$$v_s = \frac{J_{ion}Y_s}{n_0} \tag{3.13}$$

where J_{ion} is the ion current density and n_0 is the atomic metal density of the target surface. Because of the receding surface, subsurface compound molecules are transported to the surface region. As the fraction θ_r remains in steady state constant, the following continuity equation is valid,

$$v_s\theta_b n_0 = J_{ion}Y_r\theta_r \tag{3.14}$$

Here θ_b represents the fraction of reacted compound molecules at the interface between the surface and the subsurface region. θ_b can be calculated from the concentration of non-reacted target atoms $n_M(s)$ at the subsurface-surface interface located at s, as

$$\theta_b = 1 - \frac{n_M(s)}{n_0} \tag{3.15}$$

The concentration profile $n_M(x)$ in the subsurface region is determined by a chemical reaction mechanism between implanted reactive ions and target atoms. For this, a second order reaction is proposed by Vancauwenberghe et al. [23, 24], with the introduction of a reaction rate coefficient k. The reaction rate for the non-reacted target atoms can be stated as

$$\frac{\mathrm{d}n_M(x[x',t])}{\mathrm{d}t} = -kn_R(x[x',t])n_M(x[x',t]) \tag{3.16}$$

in a coordinate frame x moving along with the receding target surface, illustrated in Fig. 3.10. The origin is positioned at the target surface. The coordinate frame x' is the fixed laboratory frame. The two coordinate frames are related to each other as

$$x = x' - v_s t \tag{3.17}$$

Working out the total time derivative in the LHS of eq. 3.16 with eq. 3.17 results in

$$\frac{\partial n_M(x)}{\partial t} - v_s\frac{\partial n_M(x)}{\partial x} \tag{3.18}$$

The steady state condition is obtained by setting the partial time derivative to zero. Hence, the change of the concentration profile $n_M(x)$ within the moving coordinate frame x where the coordinate x corresponds to the depth, can be written as

$$-v_s \frac{\mathrm{d}n_M(x)}{\mathrm{d}x} = -kn_R(x)n_M(x) \tag{3.19}$$

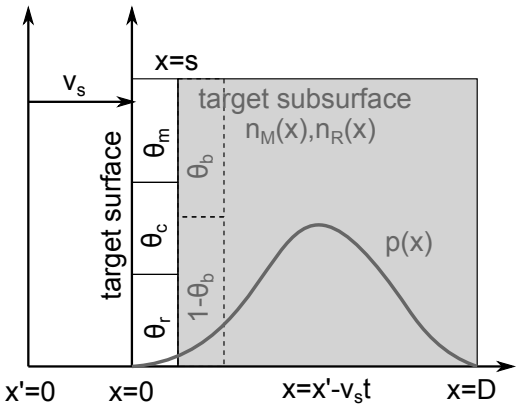

Figure 3.10: *Schematically representation of the modeled target illustrating how the moving reference frame x is connected with the fixed laboratory frame x' by the erosion speed v_s. The fractions (θ_m, θ_r, θ_c,θ_b) and the concentrations ($n_M(x)$,$n_R(x)$) which the model solves, are mentioned together with the implantation profile $p(x)$.*

The minus sign in front of the spatial derivative originates from the directional choice of the x-axis pointing into the target. Typically will the problem be numerically solved by setting boundary conditions at the maximum implantation depth. The origin of the x-frame is then chosen at the maximum implantation depth with an axis pointing in the opposite direction. This choice results then in eq. 3.19 without the minus sign in the LHS. The change of $n_M(x)$ is also depending on the concentration of implanted reactive ions $n_R(x)$, wherefore a similar rate equation can be derived as

$$-v_s \frac{\mathrm{d}n_R(x)}{\mathrm{d}x} = -kzn_R(x)n_M(x) + J_{ion}(2f + \beta\theta_c)p(x) \tag{3.20}$$

with the inclusion of an implantation term. This implantation term includes two contributions: one of direct ion implantation and one of knock-on implantation. For the direct ion implantation term, f is the ratio between the reactive ions and

the total number of incoming ions. In a first approach f is set equal to the reactive mole fraction of the used gases:

$$f = \frac{P_r}{P_r + P_{Ar}} \tag{3.21}$$

where P_{Ar} is the Ar gas pressure. This is a reasonable assumption supported by the results from a Monte-Carlo plasma code [25] and a simple analytical plasma model [26]. For the knock-on implantation, only chemisorbed reactive atoms at the surface are considered to be knocked into the subsurface region by ions. β is then the yield at which chemisorbed atoms are knocked on per incoming ion. Furthermore, the same implantation profile $p(x)$ for both implantation mechanisms is assumed. The stoichiometry of the formed compound molecules is defined by the number z, i.e. MR_z (e.g. for Al_2O_3, $z = 3/2$). The steady state fraction θ_c is maintained by the formation of compound molecules by chemisorption and their removal by sputtering and by knock-on implantation. This results in the following balance

$$2F_r\alpha_t\theta_m = zY_cJ_{ion}\theta_c + \beta\theta_cJ_{ion} \tag{3.22}$$

with F the flux of reactive molecules toward the target and α_t the sticking coefficient of reactive molecules on the target surface. This neutral reactive flux F_r is then given by

$$F_r = \frac{P_r}{\sqrt{2\pi m_r k_B T}} \tag{3.23}$$

P_r represents the reactive gas partial pressure, m_r the molecular mass, k_B the Boltzmann constant and T the temperature of the gas species. A similar equation as eq. 3.22 can be given for the fraction θ_m, the steady-state fraction of unreacted target material in the surface region, namely

$$\frac{J_{ion}}{z}\beta\theta_c + J_{ion}Y_s(1-\theta_b) = Y_m\theta_m J_{ion} + \frac{2}{z}F_r\alpha_t\theta_m \tag{3.24}$$

The first term of the LHS accounts for the removal of chemisorbed atoms by knock-on, while the second term represents the transport of non-reacted target material from the subsurface region to the surface region. On the RHS there is the sputtering of non-compound atoms and the transformation of target material into compound molecules by chemisorption.

3.2.1.2 Substrate

In analogy with the extended Berg model (section 2.2.3.1), the same balance equations for the substrate can be obtained which are repeated for completeness. The substrate is defined as the whole of surfaces where sputtered material is deposited, except the target. The sputtered material is deposited on this substrate according to a certain deposition profile. Knowledge of a deposition profile allows to treat the

substrate in a multi-cell approach [27]. Hereby the substrate is subdivided in N cells with each an area $A_{s,i}$ according to the resolution of the deposition profile. To each cell, a compound fraction $\theta_{s,i}$ and a weighting factor ε_i are connected. The weighting factor ε_i of cell i is defined by the deposition profile, and corresponds to the fraction of the sputtered material that is deposited in this cell. The forming of compound molecules is due to chemisorption of the reactive molecules and is governed by a sticking coefficient α_s. It is assumed that these compound molecules have the same stoichiometric factor z as the one on the target. The process is described in the same way as chemisorption at the target level, but a different sticking coefficient, α_s, is used. The following balance equation can be written for each cell i,

$$J_{ion}A_tY_m\theta_m\theta_{s,i}\varepsilon_i = \frac{2}{z}\alpha_sF_r(1-\theta_{s,i})A_{s,i} + J_{ion}A_t(Y_c\theta_c + Y_r\theta_r)(1-\theta_{s,i})\varepsilon_i \quad (3.25)$$

where A_t is the racetrack area. This equation allows to calculate the full substrate condition, described by the individual fractions $\theta_{s,i}$.

3.2.1.3 Chamber

During reactive sputtering a given flow rate Q_{in} (molecules per second) of reactive gas is introduced in the vacuum chamber. This reactive gas flow can be consumed in three ways: by reaction on the target Q_t, by reaction on the substrate Q_s or by the action of the vacuum pump Q_p. The steady state condition requires then that

$$Q_{in} = Q_t + Q_s + Q_p \quad (3.26)$$

The gas consumption by the target, Q_t, and by the substrate, Q_s, depends on the target and the substrate condition, respectively, as explained in the sections above. The consumption by the vacuum pump is defined by

$$Q_p = \frac{P_rS}{k_BT} \quad (3.27)$$

with S as the pumping speed (in m^3s^{-1}). For the flow toward the substrate in the multi-cell approach, it is given by

$$Q_s = \sum_i Q_{s,i} \quad (3.28)$$

where

$$Q_{s,i} = \alpha_sF_r(1-\theta_{s,i})A_{s,i} \quad (3.29)$$

Reactive gas is assumed to only react with already deposited target material by chemisorption. The calculation of the flow toward the target consists of three

terms, and states that

$$Q_t = \alpha_t F_r \theta_m A_t + \frac{z}{2} J_{ion} Y_r \theta_r A_t - \frac{\beta}{2} J_{ion} \theta_c A_t \tag{3.30}$$

The first term is the amount which is consumed by chemisorption. The second term is the contribution of reactive gas that is implanted. The final term subtracts the double counted contribution of knocked in chemisorbed gas atoms by the first two terms.

3.2.2 Solution method

The solution of the RSD model proceeds in first solving the target state (eq. 3.12 to eq. 3.24) as this can be solved independently of the substrate and the chamber. Secondly the state of the substrate can be solved by eq. 3.25 with the knowledge of the target solution. Finally based on the reactive flow consumptions (eq. 3.27 to eq. 3.30) and its balance (eq. 3.26) the reactive flow introduced into the chamber which is compatible with the state of target, substrate and the reactive pressure is calculated.

This lays in the same line as the solution method for the Berg model. However the solution procedure for the target is not as straightforward in the RSD model. The non-linearity in the RSD equations for the target can not be removed. This is in contrast to the Berg model where choosing P_r or θ_t as independent solution variable removes the non-linearity. Either choice of independent variable like P_r or θ_b in the RSD model can not remove all non-linearities. Additionally the balance equations for the surface fractions are coupled to the ODE's which govern the subsurface region, by the subsurface fraction θ_b.

The most attractive solution procedure for the target is taking θ_b as independent variable and give an initial guess for P_r or equivalently f. This enables to solve eq. 3.24, eq. 3.14 and eq. 3.22 for the three surface fractions as

$$\theta_m = \frac{1}{N}(1-\theta_b)(zJ_{ion}Y_rY_c + \beta J_{ion}Y_r) \tag{3.31a}$$

$$\theta_r = \frac{1}{N}\theta_b(zJ_{ion}Y_mY_c + \beta J_{ion}Y_m + 2\alpha_t F_r Y_c) \tag{3.31b}$$

$$\theta_c = \frac{1}{N}(1-\theta_b)2\alpha_t F_r Y_r \tag{3.31c}$$

with

$$\begin{aligned} N = {} & (1-\theta_b)(zJ_{ion}Y_rY_c + \beta J_{ion}Y_r + 2\alpha_t F_r Y_r) + \\ & \theta_b(zJ_{ion}Y_mY_c + \beta J_{ion}Y_m + 2\alpha_t F_r Y_c) \end{aligned} \tag{3.32a}$$

This completely specifies the ODE's (eq. 3.19 and eq. 3.20) governing the subsurface region. Solution of these ODE's gives a non-reacted metal concentration

$n'_M(s)$ at the surface-subsurface interface which defines by eq. 3.15 a θ'_b which not equals θ_b if the initial guess for f (or P_r) was not correct. A solution of the system will be found for a given θ_b if f satisfies

$$\theta_b - \theta'_b(f, \theta_b) = 0 \tag{3.33}$$

which is a non-linear root finding problem as function of f. This problem is easily numerically solved with a standard root finding algorithm like the Brent algorithm [28] if there is a unique root. This is from physical viewpoint likely as $\theta'_b(f, \theta_b)$ will be a monotonic increasing function in f. The reason for this is that the contribution of direct implanted reactive gas ions will increase as f increases which enhances subsurface compound formation. A higher reactive pressure will also enhance the degree of chemisorption resulting in more available chemisorbed gas atom to be knock-on and in a decrease of the erosion speed giving implanted reactive atoms more time to form compound.

The coupled ODE's (eq. 3.19 and eq. 3.20) can be numerically solved with for example a Runge-Kutta integrator to define the function $\theta'_b(\theta_b, f)$ which is standard practice. However an analytical expression for the solution of these ODE's was discovered and as such an analytical definition for $\theta'_b(\theta_b, f)$. These coupled ODE's can be written as a single ODE in the variable $n_M(x)$ or $n_R(x)$. Only the derivation of this single ODE in the variable $n_M(x)$ is given but for $n_R(x)$ the derivation is quite analog. To shorten notation the coupled ODE's are restated as

$$\frac{\mathrm{d}n_M(x)}{\mathrm{d}x} = -k_v n_R(x) n_M(x) \tag{3.34a}$$

$$\frac{\mathrm{d}n_R(x)}{\mathrm{d}x} = -k_v z n_R(x) n_M(x) + p_v(x) \tag{3.34b}$$

where

$$k_v = k/v_s \tag{3.35a}$$

$$\begin{aligned} p_v(x) &= p_v p(x) \\ &= \frac{J_{ion}}{v_s}(2f + \beta\theta_c)p(x) \end{aligned} \tag{3.35b}$$

in a moving reference frame x with the origin at the maximum implantation depth D and the axis pointing towards the target surface. Dividing eq. 3.34a by $n_M(x)$ and take the derivative to x at both sides gives

$$\frac{\mathrm{d}}{\mathrm{d}x}\left(\frac{1}{n_M(x)}\frac{\mathrm{d}n_M(x)}{\mathrm{d}x}\right) = -k_v \frac{\mathrm{d}n_R(x)}{\mathrm{d}x} \tag{3.36}$$

If $-k_v n_R(x) n_M(x)$ is eliminated between eq. 3.34a and eq. 3.34b, this gives

$$\frac{\mathrm{d}n_R(x)}{\mathrm{d}x} = z\frac{\mathrm{d}n_M(x)}{\mathrm{d}x} + p_v(x) \tag{3.37}$$

Substitution of eq. 3.37 in eq. 3.36 and integration over x results in

$$\frac{1}{n_M(x)}\frac{\mathrm{d}n_M(x)}{\mathrm{d}x} = -zk_v n_M(x) - k_v \int p_v(x)\mathrm{d}x + C_0 \tag{3.38}$$

where C_0 is an integration constant. Multiplying both sides with $\theta_M = n_M(x)/n_0$ and writting in the variable θ_M finally gives

$$\frac{\mathrm{d}\theta_M(x)}{\mathrm{d}x} + zk_v n_0 \theta_M^2(x) + \left(k_v \int p_v(x)\mathrm{d}x - C_0\right)\theta_M(x) = 0 \tag{3.39}$$

This is a single ODE which has the form of the Bernoulli differential equation

$$\frac{\mathrm{d}y}{\mathrm{d}x} + P(x)y = Q(x)y^n \tag{3.40}$$

with $n = 2$. The general solution of the Bernoulli differential equation for $n \neq 1$ is

$$y(x) = \left[\frac{(1-n)\int e^{(1-n)\int P(x)\mathrm{d}x}Q(x)\mathrm{d}x + C_1}{e^{(1-n)\int P(x)\mathrm{d}x}}\right]^{1/(1-n)} \tag{3.41}$$

with C_1 an integration constant. So the general solution of eq. 3.39 is

$$\theta_M(x) = \frac{e^{-\int P(x)\mathrm{d}x}}{C_1 - Q\int e^{-\int P(x)\mathrm{d}x}\mathrm{d}x} \tag{3.42}$$

where

$$P(x) = k_v \int p_v(x)\mathrm{d}x - C_0 \tag{3.43a}$$

$$Q = -zk_v n_0 \tag{3.43b}$$

The constant C_0 can be determined from eq. 3.39 with boundary conditions on $n_M(x = 0)$ and $n_R(x = 0)$. As the implantation occurs over a limited depth in the target, the origin of the coordinate system will be located at a depth D where reactive implantation becomes zero (and stays zero). The positive x-direction is pointed to the target surface and the coordinate system equally moves with the erosion speed. As by definition no reactive implantation occurs at $x = 0$, the concentration $n_R(0) = 0$ while $n_M(0) = n_0$ or $\theta = 1$. Evaluation of eq. 3.34a at $x = 0$ gives then

$$\left.\frac{\mathrm{d}n_M(x)}{\mathrm{d}x}\right|_{x=0} = \left.\frac{\mathrm{d}\theta_M(x)}{\mathrm{d}x}\right|_{x=0} = 0 \tag{3.44}$$

If these boundary conditions are applied to eq. 3.39 the constant C_0 reads

$$C_0 = zk_v n_0 \tag{3.45}$$

The second constant C_1 is determined by applying the boundary condition $\theta_M(x = 0) = 1$ to eq. 3.42 which results in

$$C_1 = 1 \tag{3.46}$$

independent of the exact form of $P(x)$ as the integrals cancel out.

The integrals in the general solution eq. 3.42 can analytically be solved for an uniform implantation profile ranging from $x = 0$ to $x = D$. In that case the implantation profile is $p_v(x) = p_v/D$ such that

$$\int_0^D p(x)\mathrm{d}x = p_v \tag{3.47}$$

The argument $-\int P(x)\mathrm{d}x$ of the exponentials in eq. 3.42 is obtained after twice integrating $p_v(x)$ which results in

$$-\int P(x)\mathrm{d}x = \frac{k_v p_v x^2}{2D} - zk_v n_0 x + C_2 \tag{3.48a}$$

$$= -\left[ax^2 + 2bx + c\right] \tag{3.48b}$$

where $C_0 = zk_v n_0$ (eq. 3.45) has been used, C_2 is a new integration constant and the following identifications have been used

$$a = \frac{k_v p_v}{2D} \tag{3.49a}$$

$$b = -\frac{1}{2} zk_v n_0 \tag{3.49b}$$

$$c = C_2 \tag{3.49c}$$

The remaining integral of eq. 3.42 has an analytical solution [29], namely

$$\int e^{-\left[ax^2+2bx+c\right]}\mathrm{d}x = \frac{1}{2}\sqrt{\frac{\pi}{a}} e^{\frac{b^2}{a}-c} \mathrm{erf}\left(\sqrt{a}x + \frac{b}{\sqrt{a}}\right) + C_3 \tag{3.50}$$

with C_3 another integration constant. Substitution of eq. 3.48 and eq. 3.50 in eq. 3.42, and clustering the constants c, C_3 and $e^{b^2/a}$ into C_4, gives as solution $\theta_{M,u}(x)$ for uniform implantation

$$\theta_{M,u}(x) = \frac{e^{-\left[\sqrt{a}x + \frac{b}{\sqrt{a}}\right]^2}}{C_4 - \sqrt{\pi}\frac{b}{\sqrt{a}}\mathrm{erf}\left(\sqrt{a}x + \frac{b}{\sqrt{a}}\right)} \tag{3.51}$$

where the $Q = 2b$ (eq. 3.43b) is used. The constant C_4 is obtained by applying the boundary condition $\theta_{M,u}(x = 0) = 1$ to eq. 3.51 which results in

$$C_4 = e^{-\frac{b^2}{a}} + \sqrt{\pi}\frac{b}{\sqrt{a}}\mathrm{erf}\left(\frac{b}{\sqrt{a}}\right) \tag{3.52}$$

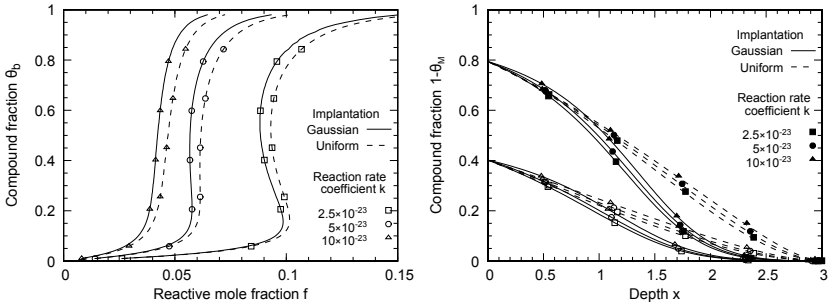

Figure 3.11: *(a) Influence of the implantation profile $p(x)$ and the reaction rate k on the solution of eq. 3.33, only including direct implantation. (b) The in-depth compound profiles corresponding with the solutions for the subsurface compound fraction $\theta_b = 0.4$ and $\theta_b = 0.8$ from (a). The target surface is located at $x = 0$. Simulations parameters are given in Table 3.1.*

The final analytical solution for simultaneous reaction and uniform implantation becomes then

$$\theta_{M,u}(x) = \frac{e^{-\left[\sqrt{a}x+\frac{b}{\sqrt{a}}\right]^2}}{e^{-\frac{b^2}{a}} + \sqrt{\pi}\frac{b}{\sqrt{a}}\left[\mathrm{erf}\left(\frac{b}{\sqrt{a}}\right) - \mathrm{erf}\left(\sqrt{a}x + \frac{b}{\sqrt{a}}\right)\right]} \tag{3.53}$$

If this solution is evaluated at $x = D$ then $\theta_b'(f, \theta_b)$ of eq. 3.33 becomes for uniform implantation

$$\theta_b'(f, \theta_b) = 1 - \theta_{M,u}(D; f, \theta_b) \tag{3.54}$$

where the relation eq. 3.15 is used and the parameters a and b of $\theta_{M,u}(D)$ (eq. 3.53) contain the f and θ_b dependencies.

An uniform implantation profile is a rather crude approximation. A Gaussian implantation profile is typical used within the RSD model as this corresponds better with reality. When a Gaussian implantation profile is used, the general solution of eq. 3.39 is not straightforward calculable. The integral in the denominator of eq. 3.42 will need a numerical evaluation. For this reason there is no real preference in either numerical evaluating eq. 3.42 or numerical integrating the single ODE of eq. 3.39 or the coupled ODE's of eq. 3.34. The latter approach is used for the latter results of this chapter.

The solution of eq. 3.33 for the target is illustrated for a uniform and a Gaussian implantation profile in Fig. 3.11a. The used parameters are given in Table 3.1 which indicate that only direct reactive implantation is included, omitting chemisorption and knock-on implantation as poisoning mechanism. This kind of system where direct implantation dominates, can be identified with the systems

$CrSi/N_2$, CH_4, CO_2 studied by Sobe [13, 14] or the system Si/N_2 studied by Depla et al. [3]. To compare the two implantation profiles, the same maximum implantation depth D is used, where for the Gaussian

$$D = R_p + 3\Delta R_p \tag{3.55}$$

with R_p the mean implantation depth and ΔR_p the deviation of the Gaussian implantation profile. The influence of the reaction rate k on the solution for both implantation profiles is shown in Fig. 3.11a. For the same k and reactive mole fraction f, the system with the Gaussian profile is more poisoned compared to the uniform profile. However the dependency on k is similar for both implantation profiles. The transition from quasi metallic to poisoned is quite steep and if k is even sufficiently low, even a hysteresis could emerge. This steep transition was experimentally shown in [3] for the Si/N_2 system, but a real hysteresis is up till now not experimentally proven. If a similar variation of J_{ion} or D on the solution (f, θ_b) is studied by either halving and doubling their value, exactly the same figure as Fig. 3.11a is obtained. This can for the uniform profile directly be understood from its analytical solution eq. 3.53. The solution $\theta_b = 1 - \theta_{M,u}(D)$ only depends on the parameters aD^2 and b^2/a which read in the original parameters as

$$aD^2 = \frac{f}{Y_s^2}\frac{kn_0^2 D}{J_{ion}} \tag{3.56a}$$

$$\frac{b^2}{a} = \frac{z^2}{4f}\frac{kn_0^2 D}{J_{ion}} \tag{3.56b}$$

This explains that multiplying k with a factor is equivalent with multiplying D or dividing J_{ion} with that same factor, and even multiplying n_0 with the square root of that factor. Remarkable is now that this relationship also exactly holds for the Gaussian profile where only a numerical solution is obtained. The maximum implantation depth D is here doubled or halved by respectively doubling or halving both R_p as ΔR_p. As such the solution for the Gaussian profile will also solely depend on these parameters by the ratio $kn_0^2 D/J_{ion}$. This result lays in the same line as an analytical solution obtained in the Appendix of [27]. There it was supposed that the reaction could be spatially separated from the implantation. Their solution also depends on this same parameter ratio.

In order to obtain more physical understanding on the parametric dependency of the subsurface fraction θ_b, the parameters aD^2 and b^2/a can be written as

$$aD^2 = \frac{1}{2}kn_{R,max}\Delta t_{max} \tag{3.57a}$$

$$\frac{b^2}{a} = \frac{1}{2}k\frac{zn_0}{n_{R,max}}zn_0\Delta t_{max} \tag{3.57b}$$

Parameters		Implantation profile	
$\mathrm{Y_m}\,(\mathrm{M\,ion^{-1}})$	0.5	*Uniform*	
$\mathrm{Y_c}\,(\mathrm{MR_z\,ion^{-1}})$	0.05	$\mathrm{D}\,(\mathrm{nm})$	3
$\mathrm{J_{ion}}\,(\mathrm{A\,cm^{-2}})$	0.05	*Gaussian*	
z	1.5	$\mathrm{R_p}\,(\mathrm{nm})$	1.5
$\mathrm{n_0}\,(\mathrm{at\,cm^{-3}})$	6.03×10^{23}	$\Delta\mathrm{R_p}\,(\mathrm{nm})$	0.5
$\mathrm{k}\,(\mathrm{cm^3 at^{-1} s^{-1}})$	$2.5/5/10 \times 10^{-23}$	$\mathrm{D}\,(\mathrm{nm})$	$R_p + 3\Delta R_p$
α_t	0		
β	0		

Table 3.1: *Overview of the RSD simulation parameters for the solution of the target considering only direct reactive implantation. The solutions are shown in Fig. 3.11.*

where $\Delta t_{max} = D/v_s$ is the maximum reaction time an implanted reactive atom can get and $n_{R,max} = 2fJ_{ion}/v_s$ is the maximum concentration of bounded and unbounded implanted reactive atoms. The parameter b^2/a seems to dependent on the ratio $zn_0/n_{R,max}$ which is the ratio between the maximum concentration of reactive atoms zn_0 that can be incorporated in the compound to the maximum concentration of implanted reactive atoms $n_{R,max}$. This represents that the subsurface compound formation is determined by three interpretable parameters: a material dependent reaction rate coefficient k, the maximum reaction time Δt_{max} and the maximum implanted concentration reactive gas $n_{R,max}$. Indeed the formation of compound will be enhanced if the reaction rate is higher, more time for reaction is given and a bigger supply of reactive atoms is provided. On the other hand will the formation be limited by the steadily decreasing metal concentration available to form compound.

A special case is when $n_{R,max} = zn_0$. In that case, the solution for $\theta_b = 1-\theta_{M,u}(D)$ only depends on $b^2/a = kzn_0\Delta t_{max}/2$ as the difference of eq. 3.57a and eq. 3.57b then equals zero and cancels out in eq. 3.53, realizing that the negative square root of b^2/a should be considered.

Finally, the in-depth compound profiles corresponding to the solutions $\theta_b = 0.4$ and 0.8 of Fig. 3.11a are shown in Fig. 3.11b. The influence of the implantation profile can be observed. For a Gaussian profile a steeper in-depth transition between the compound and the metallic bulk is noted. The variation of k (or equivalent J_{ion}, D or n_0) for similar (sub)surface compound fractions seems to have a small impact on how the in-depth compound profile looks like.

3.3 Model parameters

Although the RSD model further enhances the understanding of reactive magnetron sputtering by including reactive implantation as new process, it also introduces the extra parameters k, β, $p(x)$ and P_{Ar}. This can be regarded as one of the drawbacks of this model as compared to the Berg model. More parameters, and the fact that some of these parameters are experimentally or theoretically hard to retrieve, result in more "flexibility" to fit experimental trends. Therefore, in the last years, the research group DRAFT has investigated the reactive sputtering process in detail to retrieve more experimental data [10, 30, 31] to quantify these parameters. These quantified parameters will be used to reduce the fit freedom of well conditioned direct controlled hysteresis experiments of Al and Y in an Ar/O_2 atmosphere as published in [32]. These experimental conditions are given in section 3.3.1. The quantification of these parameters that are not fitting parameters is elucidated in section 3.3.2. To do the fitting, two more elaborated RSD models are used in an attempt to optimize the use of the experimental data and to obtain a higher degree in quantification of the fitting parameters. The modifications are explained in section 3.3.3. The fitting procedure and the search algorithm to find good fits between experiments and the models are described in section 3.3.4. The good fits give more insight in the reactive sputter process because some parameters show interesting correlations, given in section 3.3.5. Furthermore, the two different metal/oxygen systems will be quantitatively compared.

3.3.1 Experiments to fit

The experiments were performed in a varied O_2/Ar atmosphere. The homemade vacuum chamber was each time pumped to a background pressure in the order of 10^{-4} Pa, before setting the appropriate constant Ar flow. The gas pressure was measured by a capacitance gauge, while the residual gas pressure was measured with a Penning gauge. The vacuum pumping system consisted of a turbomolecular pump, backed up by a rotary vane pump. Standard planar targets of 2 inch diameter with a purity of 99.99 % (K.J. Lesker) were mounted on the conventional DC magnetron. The DC power generator (Hüttinger 1500 DC) limited the current. Nevertheless the current showed a stepwise jump when shifting from the metallic to the poisoned mode and vice versa. This increase was although limited to $\sim 5\,\%$. To establish a well-defined deposition area, the substrate consisted of a cylindrical steel container which completely enclosed the target, as shown in Fig. 3.12. The magnetron was inserted at the top of this cylinder. The direct controlled (see section 1.3.1.1) hystereses of two metal targets aluminum (Al) and yttrium (Y) were measured. This direct controlled hysteresis experiment consisted in a stepwise increase and decrease of the O_2 flow. The waiting time between two successive steps was such that a steady state value of the discharge voltage and the total pressure

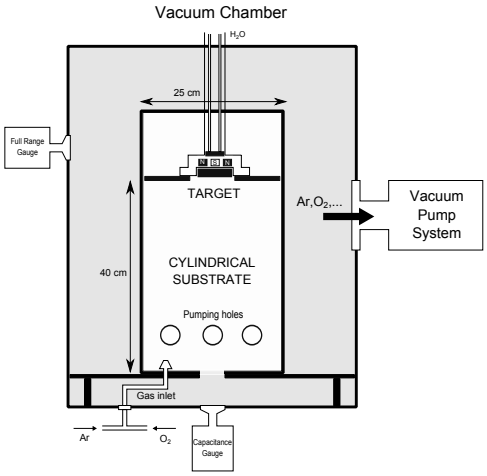

Figure 3.12: *The experimental setup for the measurement of direct controlled hystereses where a cylindrical tube is placed within the vacuum chamber.*

was obtained. The O_2 flow step size has been adapted during an experiment such that the two critical points are defined within a resolution of 0.1sccm.

For both Al and Y, three separate hystereses were measured, where only the current limitations has been changed from $0.45\,\mathrm{A}$ to $0.55\,\mathrm{A}$ to $0.65\,\mathrm{A}$. During an experiment the total pressure, the discharge voltage and the discharge current were measured. For the Al case, the Ar flow was fixed at $10\,\mathrm{sccm}$ while the pumping speed was reduced to obtain a pressure of $0.45\,\mathrm{Pa}$. In the Y case, the Ar flow was set to $20\,\mathrm{sccm}$ and the pumping speed reduced such that a pressure of $0.37\,\mathrm{Pa}$ was measured. Here the pumping speed is defined as the slope of the hysteresis curve in poisoned mode. For the Al case this resulted in a pumping speed of $55\,\mathrm{Ls}^{-1}$ while for Y $112\,\mathrm{Ls}^{-1}$ was measured. These operating conditions were chosen to obtain well-pronounced hysteresis curves and consequently well-defined critical points.

3.3.2 Input parameters

Some a priori known parameters are needed when the RSD model is solved: the input parameters. The quantitative reliability of RSD's output is strongly dependent on the accuracy of those input parameters. The scheme in Fig. 3.13 summarizes those parameters for the RSD2007 model. There are essentially three sources where input parameters can be retrieved from. The first source of input parameters are the operating conditions such as pumping speed and discharge current.

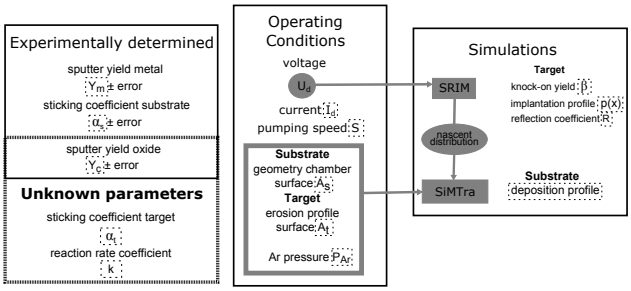

Figure 3.13: *A schematical representation of the input parameters (dashed boxes) of the steady state RSD model.*

The second source of input parameters is data retrieved from simulation software. The SRIM package [8] is used to model the ion-target interactions and provides the implantation profile $p(x)$ of incident reactive ions, the knock-on yield β of chemisorbed oxygen, the reflection coefficient R of reactive ions and a nascent distribution of sputtered material. The knock-on yield for oxygen on Y has a value of 0.18 and for oxygen on Al a value of 0.29 was found. This was simulated with SRIM by defining a monolayer of oxygen on the pure metal. After Ar ion bombardment of this layer, the number of oxygen implanted in the metal divided by the ion dose results in an estimate for the knock-on yield. The obtained nascent distribution of the sputtered atoms in SRIM defines energies and directions that serves as an input for SiMTra [33]. This simulation package gives as output a deposition profile of the sputtered material in the chamber, which is used in the multi-cell approach of the substrate description.

The last source of input parameters are the experimentally determined parameters. Experimental determination of the sputter yield of the metal and the sticking coefficient of oxygen on the substrate have been performed in [10, 30, 31]. The sticking coefficient has there been determined as the ratio of the amount of arriving oxygen at the substrate surface to the amount of incorporated oxygen in the substrate layer [30, 31]. In determining the sputter yield of the metal, a weighting method has been adopted in order to find a relation between the sputter yield and the applied voltage [10], which is linear over the considered voltage range. The same method has been applied to retrieve the sputter yield of the oxides with a voltage measured in poisoned mode. Both target materials were sputtered in full poisoned mode. After sputtering for a sufficiently long time, the target mass loss was used to calculate the sputter yield of the metal. As the target is fully poisoned this agrees with the partial sputter yield of the metal atoms from the oxide target as needed in the RSD model. In [32], a misinterpretation of these obtained sputter

yields happened as they were multiplied by a factor 2.5 which results in the total atomic sputter yield of the oxide. As such the simulations were compared with the wrong experimental sputter yields. However this honest mistake is here acknowledged and a corrigendum [34] is published based on the results in this work.

Leroy et al. obtained a partial metal sputter yield of 0.0206 ± 0.002 for Al and 0.0061 ± 0.002 for Y. These are partial metal sputter yields measured during reactive sputtering in an Ar/O_2 plasma which can not be easily compared with partial metal sputter yields of oxides bombarded with only Ar^+ ions in a pure Ar atmosphere. The latter partial sputter yield will be typically higher because when an oxide molecule which has lost an oxygen atom by sputtering will have no opportunity to restore this loss by replacement of another oxygen atom from the plasma. This mechanism does play if oxygen is available in the plasma as in the reactive sputter case [35, 36]. This will lower the partial sputter yield of the metal while increasing the partial sputter yield of the oxygen. This can explain the possible discrepancy between the sputter yields of oxides obtained here by Leroy et al. with the sputter yields obtained from the sputter cleaning experiments as in [2]. As the precise nature and strength of this oxygen replacement for Al and Y is not well understood, it does not form a part of the model. However the additional injection of atomic oxygen due to this mechanism will be reflected into the used experimental sticking coefficient of oxygen on the substrate. This sticking coefficient does not distinguish between atomic or molecular oxygen similarly as the model.

The compound sputter yield Y_c in the model is thus assumed as a molecular sputter yield that sputters the compound according to the stoichiometry of the formed compound. This means that for a stoichiometric compound MR_z, it is assumed that on average with every sputtered metal M, there are also z reactive atoms R sputtered. Notwithstanding the sputtering of compound molecules is to large extend of an atomic nature, the molecular sputter yield is used in the model. However, this simplification showed to only slightly influence the simulated hysteresis [37] for congruently, non-reducing sputtering oxides [2] which are at hand. Although only two parameters are really unknown i.e. k and α_t, the sputtering yield of the formed oxide is added as unknown parameter. In this way the compound sputter yield Y_c will serve as an internal check for the used approach in finding the unknown parameters.

As presented in Fig. 3.13, two other input parameters remain unknown . Firstly, there is the second order reaction rate coefficient k which controls the formation rate of oxide in the subsurface region of the target. There is no experimental or simulated value known for this. Secondly, there is the sticking coefficient of molecular oxygen on the target α_t. Experimental values for α_t exist [38], but are not measured in real reactive sputter conditions and seem not applicable. This summarizes to the three unknown model parameters Y_c, k and α_t .

3.3.3 Model modifications

Some of the known input parameters change during a hysteresis experiment, mainly because of the target composition variation. First there is the discharge voltage which abruptly drops between metallic and poisoned mode due to the changing effective secondary electron emission yield Y_{SEE} of the target [39]. There is also a smaller variation between and within each experiment. This can be attributed to the changing magnetic field above the target due to target erosion [6, 40] and the fraction of chemisorbed oxygen [2]. Consequently this varying discharge voltage affects the metallic sputter yield Y_m. Besides this, the voltage variation also changes the energy by which reactive ions are implanted in the target. Also the target composition, in which the reactive ion is decelerated, is not constant. Those two effects result in a modifying implantation profile of the reactive ions during the experiment. A second effect of the evolving target composition is a changing ion current. The ion current I_{ion} is connected to the discharge current I_d by the effective Y_{SEE} as

$$I_{ion} = \frac{I_d}{1 + Y_{SEE}} \tag{3.58}$$

This Y_{SEE} changes due to the changing surface composition, and will similarly as in eq. 3.8 be defined as

$$Y_{SEE} = Y_{SEE,m}\theta_m + Y_{SEE,c}(1 - \theta_m) \tag{3.59}$$

where $Y_{SEE,m}$ is the effective secondary electron emission yield for the metal [2] and $Y_{SEE,c}$ for the compound [41]. Although the experiments are limited in current, there is also a small increase in the measured current when going in the poisoned mode.

Implantation profiles of reactive ions are retrieved from SRIM. For the SRIM simulations it is assumed that the reactive oxygen molecule gets ionized and subsequently accelerated over $80\,\%$ of the discharge voltage [42, 43]. Only oxygen molecular ions are considered. Arriving at the target surface the molecular ions dissociate and each atomic oxygen enters the target with $40\,\%$ of the discharge voltage. The implantation profiles are well fitted by a skew Gaussian

$$p(x) = \frac{1}{\sqrt{2\pi\omega^2}} e^{-\left(\frac{x-\varepsilon}{\sqrt{2\pi\omega^2}}\right)} \left[1 + \operatorname{erf}\left(\alpha \frac{x-\varepsilon}{\sqrt{2\pi\omega^2}}\right)\right] \tag{3.60}$$

A lookup table of the fit parameters ε, ω and α is constructed. These parameters can be looked up as function of the impinging energy of the ions and of the target composition. The impinging energy is retrieved from the measured discharge voltage while the target composition is predicted by the model. The RSD model gives for each $P_r - Q_{in}$ couple an oxidation depth profile of the target. This oxidation profile will be approximated by a uniform profile with an average oxidation

fraction $\overline{\theta_b}$ defined as

$$\overline{\theta_b} = \int_0^D P(x)\theta_b(x)\mathrm{d}x \tag{3.61a}$$

$$P(x) = \frac{1}{N}\int_D^x p(x')\mathrm{d}x' \tag{3.61b}$$

The $\theta_b(x) = 1 - n_M(x)/n_0$ is the oxidation depth profile calculated by RSD, $p(x')$ is the reactive implantation profile defined in eq. 3.60 and $D = R_p + \Delta R_p$ is the maximum implantation depth with R_p the average implantation depth and ΔR_p the deviation of the implantation profile. $P(x)\mathrm{d}x$ represents a probability distribution for an incoming ion to pass the depth x. The factor N normalizes this distribution to one which is defined as

$$N = \int_D^0 p(x')\mathrm{d}x' \tag{3.62}$$

$P(x)$ is then used as a weighting factor for calculating the average oxidation fraction $\overline{\theta_b}$. Also the reflection of reactive ions at the target surface is taken into account. The SRIM simulations of the implantation profiles, also predict the fraction of the ions that will be reflected as function of of the impinging energy and the surface composition. This effect was included in eq. 3.20 by multiplying the direct implantation term by a factor $1 - R$, representing the non-reflected fraction of the arriving ions. The oxidation grade at the surface served as a lookup value for the interpolation table. The interpolation table was constructed with a resolution of $5\,\mathrm{eV}$ for the incident energies and a resolution of $1\,\%$ for the oxidation grade, ranging from pure metal to stoichiometric oxide.

The calculation procedure goes as follows. The above mentioned evolution in metallic sputter yield, ion current and implantation profile has been taken into account in the simulated pressure-flow ($P_r - Q_{in}$) relations. The hysteresis experiments provide steady state values of the discharge voltage and the current in function of the oxygen flow. Hereby the calculation of the $P_r - Q_{in}$ relation has been limited to the experimental part in order to use this data. As such the calculation of $P_r - Q_{in}$ is split into two parts: starting from a pure metallic target and starting from a fully oxidized target. While stepwise increasing (decreasing) the oxidation grade of the target, the corresponding $P_r - Q_{in}$ couples are determined by the RSD model. This advances until the first (second) critical point is reached. These critical flows are determined as the inflection values of the calculated Q_{in}. As the P_r and Q_{in} values are not a priori known and determination is based on the oxidation state of the target, the evolving input parameters are linearly interpolated based on the previous calculated Q_{in} value. This approach is satisfactory if the resulting Q_{in} resolution is small enough. This is obtained by a well chosen distribution of the independent solution variable θ_b.

In a first instance, these model modifications were implemented in the RSD2007 model (section 3.2.1) where the results of [32] were based on. In a latter stage, when the misinterpretation of the sputter yields was realized, they were implemented for the steady state multi-cell target solution of the RSD2013 model (section 4.3.2.2). Section 4.3 discusses in full length the exact details of this latter model. For now it is just interesting to know that this model includes a spatial resolved current profile on the target. As such it is called in this section the multi-cell model, while for the RSD2007 model a uniform profile is assumed, calling it the one-cell model. The results of the two model approaches will be discussed in section 3.3.5.

3.3.4 Fit procedure

The values of three input parameters are not easily retrieved, neither experimentally nor from simulations. These three parameters are the sticking coefficient of oxygen onto the target α_t, the reaction rate coefficient k and the compound sputter yield Y_c. To complete the set of input parameters for our two models, the modified RSD models (section 3.3.3) is fitted to the hysteresis experiments (section 3.3.1). It is expected that these three fit parameters will not be uniquely defined by fitting. The goal is to find all combinations of fit parameters that result in good fits. For this purpose a searching algorithm is developed which gives all the parameter combinations within a connected region that fit the hystereses. The development of this algorithm is based on general ideas from mathematical optimization [44]. The algorithm contains an evaluation component, the fitting procedure, which evaluates parameter sets on their goodness-of-fit, and a parameter-selecting component.

The parameter-selecting component is responsible for creating new parameter sets that need to be checked with the experiments. The evaluation component will perform the confrontation of those created parameter sets with the experiments and decides if the parameter set is accepted or rejected. The parameter-selecting component is illustrated for a 2-D parameter space (X, Y) in Fig. 3.14. The selected and evaluated parameter sets will be stored in one of the following three ordered lists: the finished accepted list (F, chessboard pattern), the unfinished accepted list (U, wavy pattern) and the rejected list (R, uniform pattern). An element in such a list is represented by an (X, Y) combination together with two direction markers for each dimension. The two direction markers represent the increasing and the decreasing directions of their corresponding dimension. The algorithm works as follows. The algorithm starts with a parameter set (x_S, y_S) that is accepted by the evaluation component. The direction markers of (x_S, y_S) are initially set to zero. (x_S, y_S) is placed as a single element in the list U, while lists F and R are empty. Now the algorithm will generate a parameter set (x_{S-1}, y_S) that is one of the four closest neighbors of (x_S, y_S), defined by a resolution $(\Delta x, \Delta y)$. Hereby

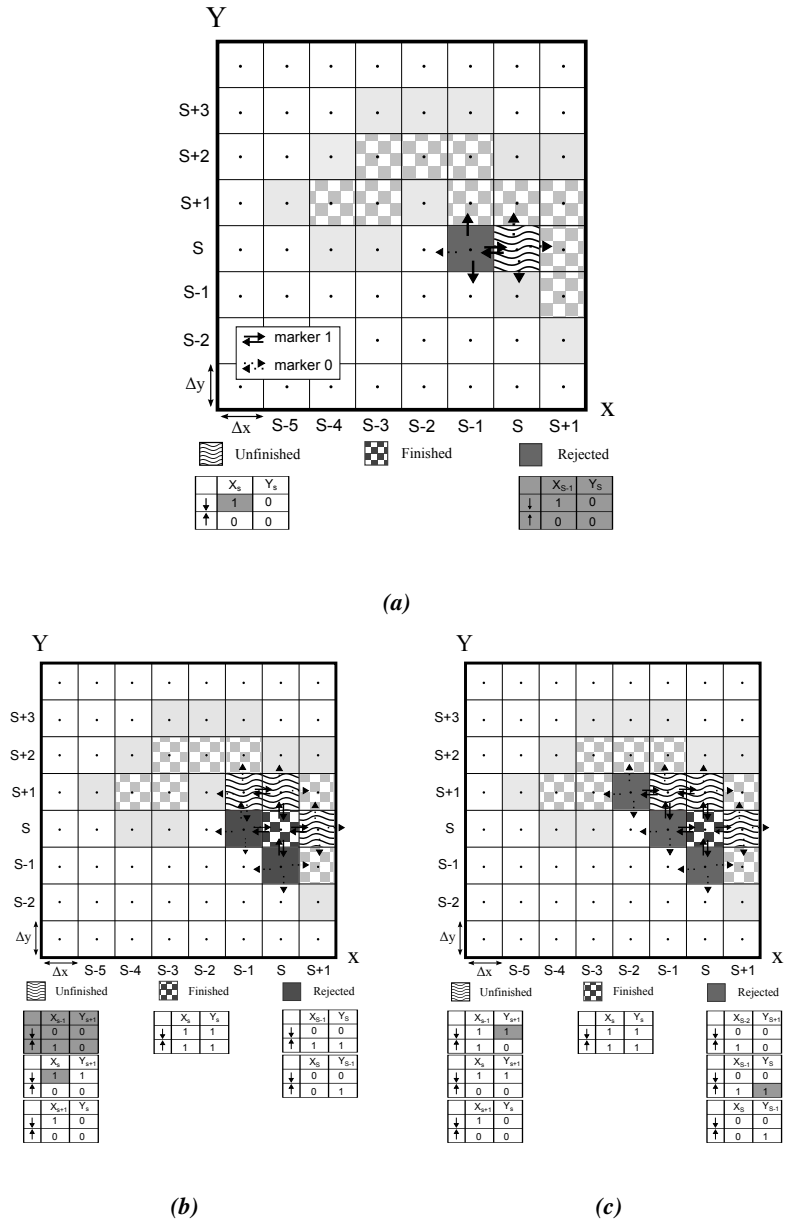

Figure 3.14: *A 2-D illustration of the parameter selecting component of the searching algorithm. The lighter coloring indicates the final listings of F(inished) and R(ejected). The darker coloring indicates an intermediate listing of F, R and U(nfinished). The couple* (x_S, y_S) *represents the starting point and* $(\Delta x, \Delta y)$ *the step resolution. (a) The creation of a non-existing couple* (x_{S1}, y_S) *that after evaluation is rejected and placed in list R. (b) The creation of a non-existing couple* (x_{S1}, y_{S+1}) *that after evaluation is accepted, but not yet fully marked and placed in list U. (c) The creation of an existing couple* (x_{S1}, y_S) *that already is evaluated and where only the appropriate direction markers are set.*

the direction marker of (x_S, y_S) in the direction of (x_{S-1}, y_S) and the direction marker of (x_{S-1}, y_S) in the direction of (x_S, y_S) is set equal to one. Each newly selected parameter sets (x_i, y_i) is first crosschecked with list U or R. If it does not appear in either list, the (x_i, y_i) is evaluated and accordingly placed in an ordered way in list R (Fig. 3.14a) or U (Fig. 3.14b), depending on the rejection or the acceptance of (x_i, y_i). If it does appear in the U or the R list, the element is updated by setting the appropriate direction marker to one and no evaluation takes place (Fig. 3.14c). In this way the algorithm is filling the list U with (x, y)'s wherefore not all the direction markers are set. The algorithm creates new (x, y), based on this list U, by moving in directions that are not yet marked. When an element of the list U is fully marked, it is moved to list F. The algorithm finishes if the list U becomes empty. The end result of the algorithm is the list F of all parameter combinations (x_i, y_i) in a connected region that models the experiments well. Additionally there is the list R of all rejected parameter combinations which exactly forms the boundary of this connected region. Now there is the issue of finding an accepted (x_S, y_S) that will form the start of the above explained algorithm. This starting point (x_S, y_S) is found by a slightly modified version of the algorithm, called the minimization algorithm. Starting from a randomly selected point, all elements encountered are selected and evaluated. These elements are sorted in list U according to the evaluation result of the parameter combination they represent. This results in a selection of (x, y)'s that are potentially better than the best element of list U. This minimization algorithm will end when it detects the (x_S, y_S) for which the evaluation result is below a predefined acceptance tolerance. This searching algorithm knows some limitations. As already mentioned, it will only find those combinations that lay within a connected region. This is the same as stating that the evaluation result $E(X, Y)$ has to have a global minimal region. This also includes the second limitation, namely that $E(X, Y)$ has to be nearly smooth. Small roughness in $E(X, Y)$ could be overcome by increasing the acceptance tolerance of the evaluation component. The disadvantage of the latter is the increase of performed evaluations, and hence of rejected parameter combinations. Apart from that, the usefulness of this algorithm will be determined by the computational intensity of the (model) evaluation component. Besides this, the increase of the dimensionality of the parameter space and the size of the final accepted region are also adverse for this approach. Nevertheless, a well-chosen step size $(\Delta x, \Delta y)$ and acceptance tolerance in the algorithm can partially overcome some of these problems.

The above mentioned searching algorithm contains an evaluation component. It is the component where the model is evaluated for a chosen set of input parameters and the output is confronted to the experimental data. In the case of the RSD models, one of the outputs is the pressure-flow $(P_r - Q_{in})$ relation of the reactive gas. It is this simulated $(P_r - Q_{in})$ relation that will be confronted to the

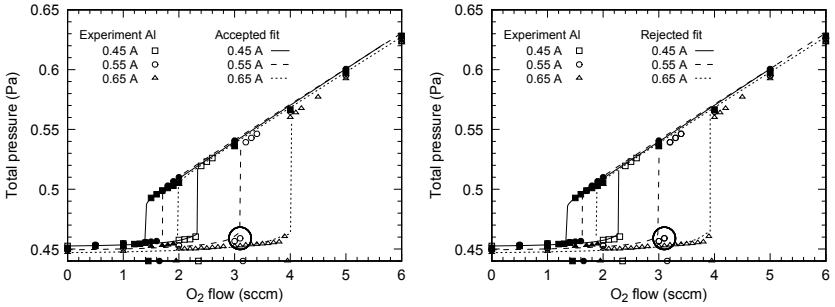

Figure 3.15: *The three measured hystereses (markers), only varied in discharge current, combined with the simulated Al curves (lines) for the one-cell model. The used parameter set only differs in the reaction rate coefficient k. (a) An accepted fit ($f_a = 1.16$) with $k = 5.4 \times 10^{-23}$. (b) A rejected fit ($f_a = 3.3$) with $k = 6.0 \times 10^{-23}$. The circles indicate the critical points which were decisive in the rejection or acceptation of the set of simulated curves. On the horizontal axis the position of the experimental critical points is indicated. Open markers represent an increasing oxygen flow, while full markers represent a decreasing flow.*

experimental hysteresis curves. To decide how well the $(P_r - Q_{in})$ relation fits the experimental data, the deviation of the simulated with the experimental critical points is examined. A simulated critical point will be accepted if it falls within the experimental resolution of the measured critical point. This criterion for acceptation can be relaxed by defining an acceptance tolerance f_a. With $f_a > 1$ the acceptance interval around the measured critical point is increased. The purpose of increasing f_a is to avoid the exclusion of accepted regions caused by small roughness in the parameter space. The acceptation criteria is implemented as

$$\max\left[\left(\frac{Q_{S,1} - Q_{E,1}}{f_a \frac{\Delta Q_E}{2}}\right)^2, \ldots, \left(\frac{Q_{S,6} - Q_{E,6}}{f_a \frac{\Delta Q_E}{2}}\right)^2\right] < 1 \qquad (3.63)$$

where $Q_{S,i}$ is the i$^{\text{th}}$ simulated critical flow, $Q_{E,i}$ is the corresponding experimental critical flow and ΔQ_E is the experimental resolution. The six critical flows values $Q_{S,i}$ (or $Q_{E,i}$) represent the first and second critical points for each discharge current out of three. Equation 3.63 selects the worst fit as criterion for acceptation or rejection. The acceptation tolerance f_a will be set to 1.5 for the one-cell model and to 3 for the multi-cell model. This difference follows from the higher observed roughness in the parameter space for the latter model. The experimental resolution of the critical points is $0.1\,\text{sccm}$. Figure 3.15 shows two fits with different evaluation values for the one-cell model, resulting in an accepted fit

(Fig. 3.15a) and a rejected fit (Fig. 3.15b).

Fit parameter	Boundaries	Step resolution
Aluminum		
Y_m	$(1.91 \times U_d - 111) \times 10^{-3} \pm 10\%$	5×10^{-3}
α_s	$0.075 - 0.139$	5×10^{-3}
α_t	$0 - 1$	5×10^{-3}
Y_c	$0 - 0.1$	5×10^{-4}
k	$0 - 40 \times 10^{-23}$	5×10^{-25}
Yttrium		
Y_m	$(0.785 \times U_d - 260) \times 10^{-3} \pm 10\%$	1×10^{-2}
α_s	$0.187 - 0.273$	1×10^{-2}
α_t	$0 - 1$	1×10^{-2}
Y_c	$0 - 0.1$	2.5×10^{-5}
	$0 - 0.1$	1×10^{-4}
k	$0 - 0.465 \times 10^{-23}$	2.5×10^{-26}
	$(0.32 - 40) \times 10^{-23}$	1×10^{-25}

Table 3.2: *The boundaries and step size of the search algorithm for the one-cell RSD model.*

Fit parameter	Boundaries	Step resolution
Aluminum		
Y_m	$(1.91 \times U_d - 111) \times 10^{-3} \pm 10\%$	10^{-2}
α_s	$0.075 - 0.139$	10^{-2}
α_t	$0 - 1$	10^{-3}
Y_c	$0 - 0.1$	10^{-3}
k	$0 - 7.5 \times 10^{-23}$	10^{-24}
Yttrium		
Y_m	$(0.785 \times U_d - 260) \times 10^{-3} \pm 10\%$	10^{-2}
α_s	$0.187 - 0.273$	2×10^{-2}
α_t	$0 - 1$	5×10^{-2}
Y_c	$0 - 0.1$	10^{-4}
k	$0 - 7.5 \times 10^{-23}$	10^{-24}

Table 3.3: *The boundaries and step size of the search algorithm for the multi-cell RSD2013 model.*

The search algorithm and the RSD models are implemented in C++ within the MPI framework [45] for parallel execution on the High Performance Computing (HPC) system of the Ghent University. The parallel implementation of the search algorithm principally speeds up the number of simultaneous evaluations to

the number of used cores minus one. This one master core is responsible for the generation of new parameter sets and the maintenance of the parameter lists. As the items in the lists are increasing, the creation time of a new parameter set increases, which for big lists gradually bottlenecks the linear performance gain. This implementation has been used to find the freedom in the so called three unknown parameters. This results in a 3-D parameter space which is extended to a 5-D parameter space by including variations in the two other experimental determined parameters, the sputter yield of the metal Y_m and the sticking coefficient of molecular oxygen on the substrate α_s. Their variations were restricted to their error intervals, while for the three unknowns reasonably wide intervals are selected. As the experimental errors on the operating conditions are much smaller compared to the errors on the experimental values, they are not explicitly included. The errors on the simulated values (SRIM and SiMTra) are hard to establish. These simulation packages are then considered as an integral part of the model for reactive sputtering. A summary of the five varied parameters, the used boundaries and step sizes for the search algorithm are given in Table 3.2 for the one-cell model and in Table 3.3 for the multi-cell model. With these algorithm settings, the number of evaluated, accepted and rejected, parameter sets ran up to $\sim 4 \times 10^6$ for the one-cell model, while it reached $\sim 1 \times 10^6$ for the multi-cell model.

3.3.5 Correlations

3.3.5.1 One-cell model

The results of the parameter search with the one-cell RSD model for Al and Y are summarized in Fig. 3.16 and Fig. 3.17. Each figure shows couples of the unknown parameters that fit the experimental critical points with an acceptance tolerance $f_a \leq 1.5$. In this way, the graphs represent 2-D projections of the 5-D parameter space. The acceptance tolerance connected to each couple is determined as the optimal choice of the three remaining parameters (Y_m, α_s, α_t) for Fig. 3.16, (Y_m, α_s, Y_c) for Fig. 3.17a and (Y_m, α_s, k) for Fig. 3.17b. When looking at the (Y_c, k) map (Fig. 3.16), a comparable relation is noticed for both Al and Y. For an increasing sputter yield of the oxide, a higher value for the reaction rate coefficient is found. This is qualitatively understandable. When Y_c increases not only more surface oxide gets removed, but also the reaction time in the bulk to form oxide gets shorter by a faster receding surface. To obtain the same surface composition in the simulation, more oxide molecules from the bulk should be provided, hence an increased reaction rate k is necessary. One could reason that the increasing removal of the oxide molecules can be balanced by the role of chemisorption (by increasing the value of α_t). Nevertheless, the impact of the oxide sputter yield will especially be important when returning from the poisoned mode to the metallic mode. In this regime chemisorption is of less importance because the sticking

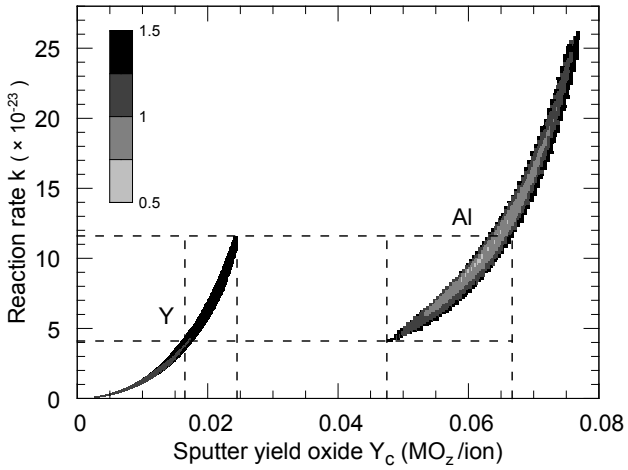

Figure 3.16: *The parameter couples (Y_c, k) that result in an accepted fit with an acceptance tolerance lower than 1.5. The acceptance tolerance (gray scale) is based on the best choice of the remaining three parameters $(Y_m, \alpha_s, \alpha_t)$. The dashed lines delimit the (Y_c, k) zone wherefore accepted fits are found with an equal k for both material systems, namely Y and Al.*

coefficient of oxygen molecules on the compound fraction will be low. In the model this is even assumed to be not existing.

When comparing the $k - Y_c$ relations for the Al and the Y case it is noted that they are not equal for both materials, indicating a unique relationship for each material. This is at first sight somewhat surprising as the material dependency was not included in the reasoning discussed above to explain this $k - Y_c$ relation. The observed shift in the $k - Y_c$ relation toward lower Y_c values for yttrium is mainly caused by a difference in the elemental target density n_0 for Y and Al. The reasoning goes as follows. The elemental target density defines the erosion speed of the target as stated in eq. 3.13. A lower density results in a higher erosion speed, and a lower supply of metal per volume unit to form oxide molecules. Both of these effects reduce the amount of formed oxide molecules in the subsurface region. Therefore, at the same k value, a material with a lower elemental target density, needs a lower sputter yield of the oxide to obtain the same target oxidation state as a material with a higher elemental target density. If the elemental target density of Y ($3.03 \times 10^{22}\,\mathrm{atoms/cm^3}$) is compared with the Al density ($6.03 \times 10^{22}\,\mathrm{atoms/cm^3}$), their is a difference of a factor 2. This explains the shift of the $k - Y_c$ relation toward lower Y_c values for the yttrium case. The (α_t,k) and (α_t,Y_c) maps, shown in Fig. 3.17, have a less pronounced correlation between the two parameters. These maps show a bigger freedom in choosing an α_t compared

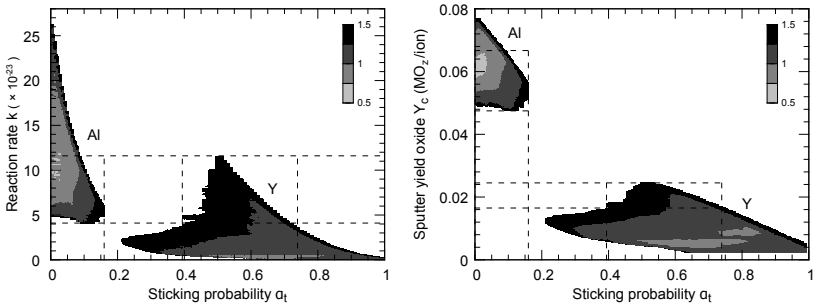

Figure 3.17: *Comparable figure as Fig. 3.16, for the couples (a) (α_t, k) and (b) (α_t, Y_c). The dashed lines correspond with those of Fig. 3.16. Here they determine a separate scope of α_t for Al and Y, assuming a comparable k.*

to k or Y_c. However if a k or Y_c is chosen, the maps define an upper boundary for the sticking probability α_t, where choosing an α_t of course results in an upper boundary for k and Y_c. These upper boundaries decreases if the initial chosen α_t increases in order to maintain some maximum reactivity represented by the parameters k and α_t.

In an attempt to narrow the value range of the fitted parameters for each material, the same reaction rate coefficient k for both metals is assumed. This hypothesis is based on the high reactivity of the implanted oxygen atom. Due to this high reactivity, the chemical reactivity of the metal is of minor importance. Or stated differently, from a physicochemical point of view, the hypothesis of a comparable reaction rate coefficient for both Y and Al can be put forward. This hypothesis is further supported by the observation that the sticking coefficient for atomic oxygen is generally assumed to be one, independent of the material surface. Indeed, sticking coefficients of 0.9 and larger have been reported for atomic oxygen on Ni [46], Si [47], and Ag [48]. Even more, studies of the impact of hyperthermal atomic oxygen on different metals used for space craft applications show the same reactivity [49]. Applying this hypothesis to Fig. 3.16, a range of possible reaction rates can be delimited to $(4.1 - 11.6) \times 10^{-23}\,\mathrm{cm^3 at^{-1} s^{-1}}$. It is the k range (see Fig. 3.16) wherefore accepted fits are found for both Y as for Al. This range defines, by the high correlated $Y_c - k$ relation, an interval for the oxide sputter yield Y_c of each metal. The oxide sputter yield for Al lays in the range $0.048 - 0.067$ while for Y the range $0.017 - 0.02$ is found. This is not compatible with the experimental values of 0.0206 for the Al case and 0.0061 for Y case mentioned in section 3.3.2, which are almost a factor three lower. By the misinterpretation of these sputter yields in [32] by multiplying the experimental yields with a factor 2.5, a seemingly quantitative agreement was found. The agreement with the published

oxide sputter yields in the case of Al [50] gave then confidence as the mechanism of oxygen replacement as discussed in section 3.3.2 during reactive sputtering was overlooked. However the ratio $r = Y_c^{Al}/Y_c^{Y}$ between the experimental sputter yields ($r = 3.4$) and the fitted sputter yields ($r = 3.1$) seems comparable. This is logic as the sputter yields were wrongly multiplied by the same factor which does not change this ratio. So as preliminary conclusion about the sputter yields, one can state that the fitted oxide sputter yields quantitatively do not match with the experimental sputter yields, but that the fits result in a quasi similar ratio. In this way the one-cell model is insufficient to reproduce the correct oxide sputter yields. But as the next section will show and explain, the multi-cell model largely improves the agreement between the fitted and the experimental sputter yields

Finally the $k - \alpha_t$ and $Y_c - \alpha_t$ relations (Fig. 3.17) show that the critical points are only weakly dependent on chemisorption. Especially for the Y case, the freedom in the sticking coefficient α_t is wide. This directly contrasts with the restrictive choice of the parameters k and Y_c, who control the subsurface oxide formation. Nevertheless, in the former assumption of a similar reactivity, a higher molecular oxygen sticking coefficient for Y than for Al is yielded by the one-cell model. This is in agreement with how the experimental sticking coefficients α_s of molecular oxygen on the substrate compare to each other (see Table 3.2). With the range of valid sticking coefficients limited under the assumption of a similar reaction rate k, a sticking coefficient α_t in the range $0 - 0.16$ for Al, and in the range $0.39 - 0.74$ for Y are retrieved for this one-cell model. Reported sticking coefficients of molecular oxygen on Al at room temperature are ranging from 0.005 to 0.03 [38, 51]. The higher values of the sticking coefficients for Al, both on the target as on the substrate [30], can be explained by the presence of atomic oxygen and of hyperthermal oxygen with sticking approaching unity [38, 51]. A simple plasma model [26] indicates that the atomic oxygen flux towards the target amounts to $\sim 10\%$ of the molecular oxygen flux. Also the activation of the target surface by ion bombardment will probably enhance this sticking coefficient. As such the obtained sticking coefficients α_t and α_s should be seen as an effective oxygen sticking coefficients during reactive magnetron sputtering.

In qualitatively explaining the higher sticking on Y compared to Al and the opposite for the compound sputter yield, the surface binding energies U_s of the constituents can be considered. Malherbe et al. [52] proposed a model for calculating these U_s based on the bonding energies and the electron negativity differences of the constituents. When applying his model, values of $U_{s,\mathrm{Al}} = 5.03\,\mathrm{eV}$ and $U_{s,\mathrm{O}} = 6.89\,\mathrm{eV}$ are found for Al_2O_3, while $U_{s,\mathrm{Y}} = 6.7\,\mathrm{eV}$ and $U_{s,\mathrm{O}} = 8.55\,\mathrm{eV}$ are found for Y_2O_3. This calculation shows higher surface bindings energies in the Y case, explaining a smaller compound sputter yield for Y_2O_3. These surface binding energies can also be seen as a measure for the affinity of a metallic surface to form compound molecules by chemisorption, and as such for the sticking coef-

ficients. In addition, Leroy et al. [30] reported substantial higher concentrations of atomic oxygen in the plasma for the Y case compared with Al, further sustaining the higher observed effective sticking on Y.

3.3.5.2 Multi-cell model

The discrepancy of the oxide sputter yields for Al and Y obtained in the fits with the one-cell model compared to the experimental determined yields shows the shortcoming of the one-cell model. A latter developed RSD model, RSD2013, is in a second stage used to fit the experiments. This model forms the core of chapter 4. It is not necessary right now to understand the exact details of this model as the extension to the one-cell model which is previously used is limited. The inclusion of a non-uniform current profile for the target is the only real difference. This extension is similar with the extension to the original Berg model in section 2.2.3.2. Moving to a multi-cell model where the uniform current on the target is replaced by an axial symmetric Gaussian current profile (mean $1.03\,\mathrm{cm}$, deviation $0.28\,\mathrm{cm}$) resolves a large portion of this discrepancy. The second critical point is mainly defined by the parameters Y_c and k as chemisorption of oxygen on oxide is neglectable. The sputter yield Y_c parametrizes the removal of oxide while the reaction coefficient k parametrizes the production of oxide at that point. The second critical point occurs if the oxide removal overrules its production and more metal is sputtered which avalanches the system to metallic mode. By the introduction of a Gaussian current profile which approximates the experimental racetrack, the center of the racetrack will have a larger ion current density compared to the average current density over the entire target, as in the one-cell model. This has a significant impact on the second critical point. The racetrack center will become easier metallic when moving to the second critical point from poisoned mode by decreasing the oxygen flow. This makes that more metal is deposited which can getter oxygen at a higher oxygen flow which decreases the oxygen supply to the target for oxide formation. In this way the second critical point will shift to higher oxygen flows. That this impact is substantial proves Fig. 3.18 which is the same figure as Fig. 4.13a. For now it is only important to know that simulation A is a one-cell target while simulation B is a multi-cell target. This can explain the almost three times higher oxide sputter yields for the fits with the one-cell model. To fit the experiments where this non-uniform current plays, the higher oxide sputter yield compensates in the model for this effect. A higher oxide sputter yield shifts the second critical point to higher oxygen flows. The shift in the first critical point to a higher oxygen flow is on the other hand much less pronounced.

The steady state target solution of the RSD2013 model for a multi-cell target (details, see section 4.3.2.2) is implemented in the evaluation component of the parameter scan algorithm. The target is spatial resolved in 100 radial cells exploiting the axial symmetry of the circular target and racetrack. A similar scan as

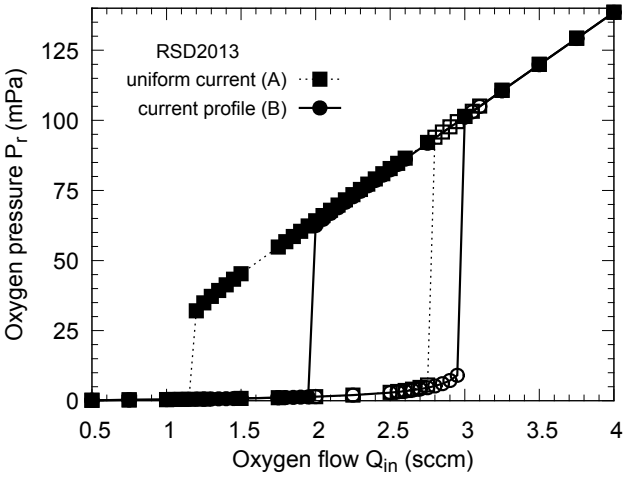

Figure 3.18: *Difference in critical points between a simulation A which is modeled with a one-cell target while simulation B is modeled with a multi-cell target. For more details on these two RSD2013 simulations, see section 4.4.*

for the one-cell model was performed with parameter boundaries and step resolutions given by Table 3.3. As this model is much more computational intensive the boundaries and the resolution are much more restrict. It was also noticed that the parameter space where good fits exist is less smooth compared to the one-cell model. To compensate for both these effects the acceptance tolerance f_a was doubled to 3.

The relations between the three fit parameters α_t, k and Y_c for the multi-cell model are given in Fig. 3.19 and Fig. 3.20. The strong correlation between k and Y_c (Fig. 3.19) remains notwithstanding the doubled acceptance tolerance f_a from 1.5 to 3. If the hypothesis of a similar reaction rate k for both metals is again picked up, the corresponding ranges in oxide sputter yield for both metals will be large, namely $0.0043 - 0.0145$ for yttrium and $0.0186 - 0.0386$ for aluminum. However the experimental sputter yields with their error fall within these range, while this was not the case for the one-cell model. The two experimental yields each delimit a range of valid k's where a good fit is found. This is represented on Fig. 3.19 by the horizontal lines while the vertical lines represent the error range on the experimental sputter yields. The two ranges for k do overlap. As such the hypothesis of a similar k for both metals has not to be rejected based on this result.

The conclusions based on the one-cell model about the sticking coefficient of oxygen on the target for both metals remain valid. The sticking coefficient for yttrium is larger compared with the sticking coefficient for aluminum. The fitting with the multi-cell model and the doubled acceptance tolerance have even further

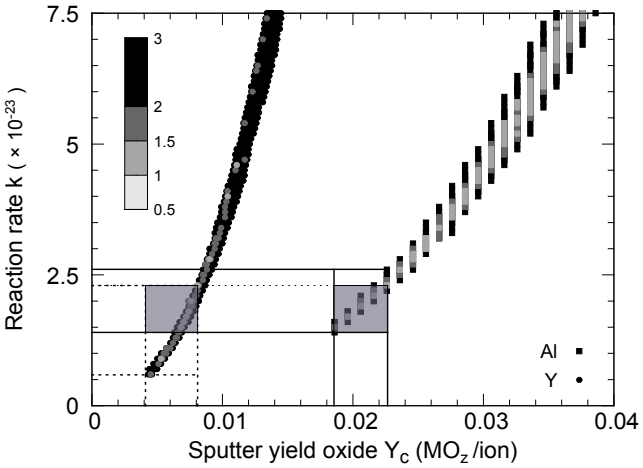

Figure 3.19: *The parameter couples (Y_c, k) that result in an accepted fit with an acceptance tolerance f_a lower than 3. The acceptance tolerance (gray scale) is based on the best choice of the remaining three parameters $(Y_m, \alpha_s, \alpha_t)$. The dashed lines delimit the experimental Y_c for Yttrium and the corresponding k range where valid fits were found. The solid lines doe the same for the aluminum system. The gray rectangle indicates then the overlap wherefore the k is equal for both material systems.*

widened the spread in their values, which is especially the case for yttrium. The sticking coefficient for aluminum should lay between 0 and 0.219 and for yttrium between 0.237 and 1 if a similar reaction rate k is assumed. In Fig. 3.20 these ranges are indicated by the gray rectangles which correspond to the gray rectangles in Fig. 3.19. These ranges reach at their opposite extrema almost towards each other. This gives it a small chance of being comparable. However if an average for these sticking coefficients is calculated, weighted with the inverse of their acceptance tolerance, a clear distinction is obtained. This gives a value of 0.080 for aluminum and 0.53 for yttrium. This lays in the same line as for the one-cell model.

The strong correlation between the reaction rate k and the oxide sputter yield Y_c for each material and for both models is remarkable. It is interesting to have a closer look at their exact functional dependency. These four correlations can all be well fitted with the power law

$$Y_c = b' k^a \tag{3.64}$$

These fits are given in Fig. 3.21 and are obtained by using a least square method with the linear fit function

$$-\ln(Y_c) = -a\ln(k) + b \tag{3.65}$$

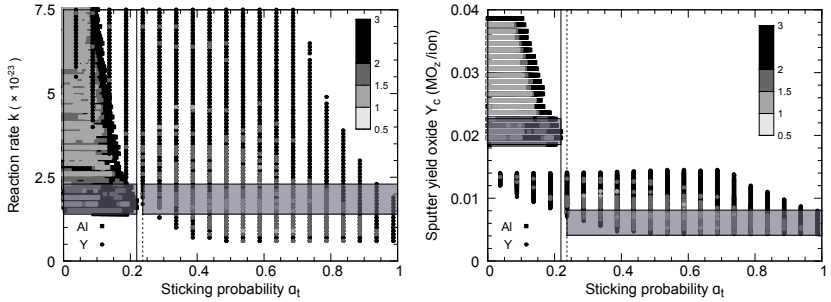

(a) *(b)*

Figure 3.20: *Comparable figure as Fig. 3.19, for the couples (a) (α_t, k) and (b) (α_t, Y_c). The gray rectangles correspond with those of Fig. 3.19. They determine a separate scope of α_t for Al and Y, assuming a comparable k.*

Metal	# cells	f_a	$a \pm$ stnd error	$b \pm$ stnd error
Al	1	1.5	0.249 ± 0.001	-9.85 ± 0.05
Al	100	1.5	0.428 ± 0.004	-18.5 ± 0.2
Y	1	1.5	0.3485 ± 0.0005	-13.90 ± 0.03
Y	100	1.5	0.440 ± 0.003	-18.1 ± 0.2
Al	100	3	0.423 ± 0.005	-18.28 ± 0.03
Y	100	3	0.448 ± 0.002	-18.6 ± 0.1

Table 3.4: *Fit parameters for the relation $-ln(Y_c) = -aln(k) + b$ which are fitted to the data of Fig. 3.16 and Fig. 3.19. The fits with $f_a = 1.5$ are represented in Fig. 3.21.*

on the data in Fig. 3.16 for the one-cell model and Fig. 3.19 for the multi-cell model. For the multi-cell model only the couples below an acceptance tolerance of 1.5 are selected for the fits in Fig. 3.21. However increasing this acceptance tolerance to 3 for the multi-cell model has no major impact on the outcome of the fitted relation. The obtained fit parameters with their standard errors are given in Table 3.4.

Recall that, notwithstanding the absolute values of the oxide sputter yields for both metals did not match the experimental values in the one-cell model, their ratio Y_c^{Al}/Y_c^{Y} did. The multi-cell model is an indispensable quantitative improvement as a match in these absolute values between the fitted and the experimental sputter yields for both metals is obtained. Logically the ratio of the sputter yields should also match. These sputter yields were mutually compared under the hypothesis of a similar reaction rate k. The ratio of the fitted relations eq. 3.64 between the two metals can be calculated per model which is represented in Fig. 3.22. This

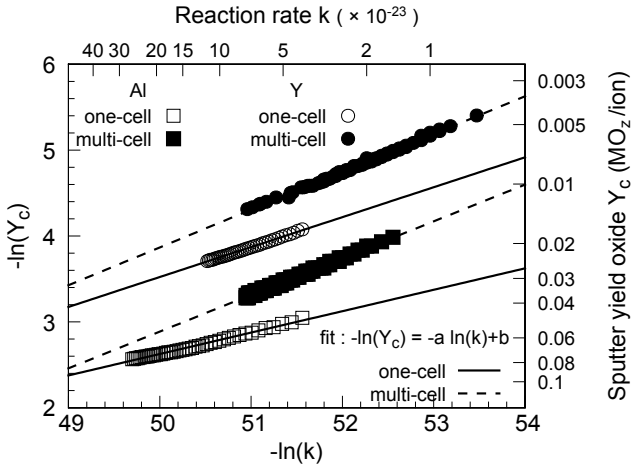

Figure 3.21: *The relations between Y_c and k found with the one-cell and the multi-cell model are fitted with a power law (eq. 3.64) using a least square method. All fitted data has an acceptance tolerance f_a of* 1.5.

ratio is for both models the same within their error when comparing the k ranges where accepted fits are found for both metal systems. This is remarkable as this means that the geometry of the current profile on the target, which is the essential difference between the two models, does not influence how the oxide sputter yields of the two systems are in proportion to each other. If the experimental ratio of the sputter yields is placed besides these fitted ratio as in Fig. 3.22, then these ratios are in agreement with each other accounting for the errors. Of course, the errors are large, especially on the experimental ratio, but aware of the low complexity of the used models, this is already a fair agreement. If these results are transferable to other metal systems, it allows with the knowledge of one compound sputter yield the prediction of other compound sputter yields, even if the simplest model of the two is used.

This tight relation between the reaction rate coefficient k and the oxide sputter yield Y_c follows out of their importance in defining the second critical point. In poisoned mode and towards this second critical point, the state of the target is almost only determined by these two parameters. Chemisorption does not play as their are hardly metallic sites available. Consequently also knock-on implantation of chemisorbed atoms can almost be excluded. The only mechanisms that are significant are the creation of oxide by the direct implantation of reactive ions which react, form oxide and are transported to the surface, and the removal of the oxide by sputtering. The second critical point occurs if the removal of oxide surpasses the creation of it. To sustain this claim about these obtained parameter relation, the

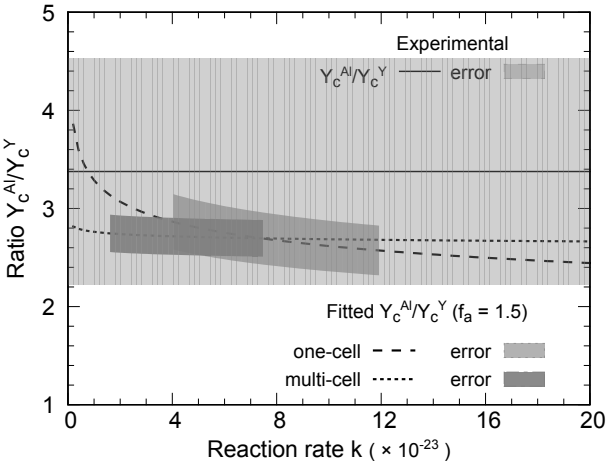

Figure 3.22: *The ratio Y_c^{Al}/Y_c^{Y} as function of k obtained from the fitted relations in Fig. 3.21 with their error interval, compared with the experimental ratio. The errors are defined as three times the standard error.*

analytical solution eq. 3.53 for the target which was derived in section 3.2.2 for an uniform implantation profile is considered. This analytical expression describes the oxide fraction $\theta_b = 1 - \theta_{M,u}(D)$ at the surface-subsurface interface for only the just mentioned mechanisms : direct reactive implantation, subsurface reaction and sputtering. It can now be checked if this power law relation between k and Y_c also can be obtained from this expression. In doing so, the following strategy is used.

The fits with the multi-cell model show that at the second critical point the surface is almost fully oxidized. This means that the oxide sputter yield only determines the erosion speed with no surface dependency. These fits also show that the subsurface metal fraction $\theta_{M,u}(D)(= 1 - \theta_b)$ amounts 0.15 ± 0.05 across all fits. These two statements are valid independent of the chosen metal. If now the (k, Y_c) couples are calculated wherefore $\theta_{M,u}(D) = 0.15$, these couples will then define the target state at the second critical point. These calculations are executed for the Al and Y case ($I_d = 0.55\,\mathrm{A}$) with as experimental input the average ion current density J_{ion} and the reactive mole fraction f on the second critical point. The implantation depth D is estimated as $2\,\mathrm{nm}$ for both metals. Again a correlation between k and Y_c, similar as in Fig. 3.21, is found for both metals. The same power law (eq. 3.64) is fitted to these relations which are shown in Fig. 3.23. The fits are performed over a k range running from 10^{-24} to 2×10^{-22}. Not only the mutual position of these relations for the two metals matches with the earlier fits of the more complex models, but also the fitting coefficients closely match with

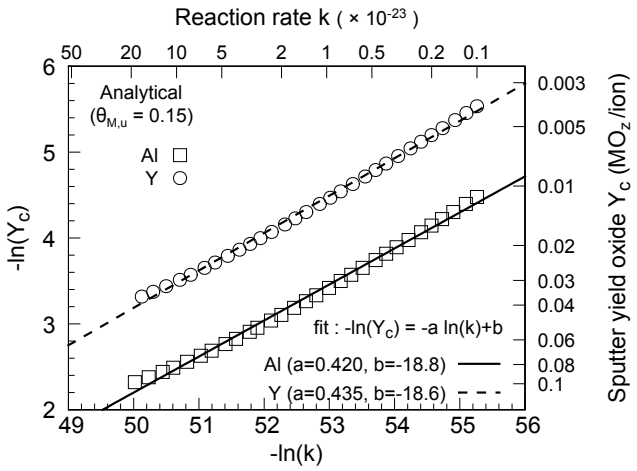

Figure 3.23: *The relation between Y_c and k obtained with the analytical solution eq. 3.53 where a uniform implantation profile is assumed. The $\theta_{M,u}$ is fixed at* 0.15*. The relations for Al and Y are fitted with a power law (eq. 3.64) using a least square method.*

those in Table 3.4. This proves that the mechanism of direct reactive implantation, subsurface reaction and compound sputtering which are only modeled by this analytical simplification are the decisive processes that fix the second critical point.

3.4 Summary

A successor of the Berg model is the RSD model by D. Depla. This model can be classified as an first category extension of the Berg model. It includes direct and knock-on reactive implantation as additional poisoning mechanism. This mechanism can resolve three observed limitations in the Berg model: the compound thickness on the target, the influence of the inert gas pressure and the influence of the pumping speed. The original RSD model is derived, and the solution method is explained. In the case of an uniform implantation profile, the solution can be written in an analytical closed form. As the RSD model has some hard to quantify parameters, dedicated fitting of the model with experiments has been performed. It showed a larger target sticking coefficient for oxygen on yttrium compared to oxygen on aluminum during reactive sputtering. However, a RSD model with a uniform current profile is not able to reproduce the correct experimental oxide sputter yield for the Al/O_2 and the Y/O_2 system. However the correct ratio between those two oxide sputter yields was retrieved. Moving to an extended RSD model by including a Gaussian current profile largely fixed this mismatch between

model and experiment. Furthermore the fitting results for both models showed that this ratio in oxide sputter yield between the two metals is almost independent from the used current profile and from the exact value for the reaction rate between the implanted reactive atoms and the non-reacted metal. These conclusions were made under the reasonable assumption of a similar effective reaction rate for both metals. Finally it is shown that the tight relation between the oxide sputter yield and the reaction rate originates from their prime importance in the determination of the second critical point. This is proven by applying the analytical solution with uniform implantation which only accounts for direct reactive implantation, subsurface reaction and sputtering.

References

[1] Depla, D., Heirwegh, S., Mahieu, S., and De Gryse, R. *Journal of Physics D-Applied Physics* **40**(7), 1957–1965 (2007).

[2] Depla, D., Heirwegh, S., Mahieu, S., Haemers, J., and De Gryse, R. *Journal of Applied Physics* **101**(1), 013301 (2007).

[3] Depla, D. and De Gryse, R. *Journal of Vacuum Science & Technology a-Vacuum Surfaces and Films* **20**(2), 521–525 (2002).

[4] Thornton, J. A. *Journal of Vacuum Science & Technology* **11**(4), 666–670 (1974).

[5] Buyle, G. *Simplified model for the d.c. planar magnetron discharge*. PhD thesis, (2005).

[6] Depla, D., Haemers, J., and De Gryse, R. *Thin Solid Films* **515**(2), 468–471 (2006).

[7] Kubart, T., Nyberg, T., and Berg, S. *Journal of Physics D-Applied Physics* **43**(20), 205204 (2010).

[8] Ziegler J.F., Biersack J.P., Z. M. *SRIM - The Stopping and Range of Ions in Matter*. www.srim.org. (2012).

[9] Moller, W., Eckstein, W., and Biersack, J. P. *Computer Physics Communications* **51**(3), 355–368 (1988).

[10] Saraiva, M., Georgieva, V., Mahieu, S., Van Aeken, K., Bogaerts, A., and Depla, D. *Journal of Applied Physics* **107**(3), 034902 (2010).

[11] Buyle, G., Depla, D., Eufinger, K., Haemers, J., De Gryse, R., and De Bosscher, W. *Journal of Vacuum Science & Technology A* **21**(4), 1218–1224 (2003).

[12] Affinito, J. and Parsons, R. R. *Journal of Vacuum Science & Technology A* **2**(3), 1275–1284 (1984).

[13] Sobe, G., Neelmeijer, A., Weise, G., and Heinrich, A. *Thin Solid Films* **201**(1), 109–122 (1991).

[14] Sobe, G. *Contributions to Plasma Physics* **34**(1), 81–97 (1994).

[15] Depla, D. and De Gryse, R. *Plasma Sources Science & Technology* **10**(4), 547–555 (2001).

[16] Depla, D., Haemers, J., and De Gryse, R. *Plasma Sources Science & Technology* **11**(1), 91–96 (2002).

[17] Depla, D. and De Gryse, R. *Surface & Coatings Technology* **183**(2-3), 184–189 (2004).

[18] Depla, D., Chen, Z. Y., Bogaerts, A., Ignatova, V., De Gryse, R., and Gijbels, R. *Journal of Vacuum Science & Technology A* **22**(4), 1524–1529 (2004).

[19] Depla, D. and De Gryse, R. *Surface & Coatings Technology* **183**(2-3), 190–195 (2004).

[20] Depla, D. and De Gryse, R. *Surface & Coatings Technology* **183**(2-3), 196–203 (2004).

[21] Rosen, D., Katardjlev, I., Berg, S., and Moller, W. *Nuclear Instruments & Methods in Physics Research Section B-Beam Interactions with Materials and Atoms* **228**, 193–197 (2005).

[22] Kubart, T., Kappertz, O., Nyberg, T., and Berg, S. *Thin Solid Films* **515**(2), 421–424 (2006).

[23] Vancauwenberghe, O., Herbots, N., and Hellman, O. C. *Journal of Vacuum Science & Technology a-Vacuum Surfaces and Films* **10**(4), 713–718 (1992).

[24] Rabalais, J. W. *Low energy ion-surface interactions*. Wiley, 1st edition, (1994).

[25] Schelfhout, R. *Monte Carlo simulatie van elektron-gasinteracties in een reactief magnetron plasma*. Master's thesis, (2014).

[26] Depla, D. *Magnetrons, reactive gases and sputtering*. Lulu.com, 3rd edition, (2015).

[27] Depla, D., Mahieu, S., and De Gryse, R. *Reactive Sputter Deposition*, chapter 5, 153–197. Springer Berlin Heidelberg (2008).

[28] Press, W. H., Teukolsky, S. A., Vetterling, W. T., and Flannery, B. P. *Numerical Recipes: The Art of Scientific Computing*. Cambridge University Press, 3rd edition, (2007).

[29] Abramowitz, M. and Stegun, I. A. *Handbook of Mathematical Functions with Formulas, Graphs, and Mathematical Tables*. Dover, (1964).

[30] Leroy, W. P., Mahieu, S., Persoons, R., and Depla, D. *Thin Solid Films* **518**(5), 1527–1531 (2009).

[31] Leroy, W. P., Mahieu, S., Persoons, R., and Depla, D. *Plasma Processes and Polymers* **6**, S342–S346 (2009).

[32] Strijckmans, K., Leroy, W. P., De Gryse, R., and Depla, D. *Surface & Coatings Technology* **206**(17), 3666–3675 (2012).

[33] Van Aeken, K., Mahieu, S., and Depla, D. *Journal of Physics D-Applied Physics* **41**(20), 205307 (2008).

[34] Strijckmans, K., Leroy, W. P., De Gryse, R., and Depla, D. *Surface and Coatings Technology* **278**, 126 (2015).

[35] Tian, C. and Vandervorst, W. *Journal of Vacuum Science & Technology a-Vacuum Surfaces and Films* **15**(3), 452–459 (1997).

[36] Serrano, J. J., Blanco, J. M., Guzman, B., De Witte, H., and Vandervorst, W. *Journal of Applied Physics* **90**(9), 4456–4466 (2001).

[37] Berg, S. and Nyberg, T. *Thin Solid Films* **476**(2), 215–230 (2005).

[38] Kuschel, T. and von Keudell, A. *Journal of Applied Physics* **107**(10), 103302 (2010).

[39] Depla, D., Mahieu, S., and De Gryse, R. *Thin Solid Films* **517**(9), 2825–2839 (2009).

[40] Depla, D., Strijckmans, K., and De Gryse, R. *Surface & Coatings Technology* **258**, 1011–1015 (2014).

[41] Depla, D., Li, X. Y., Mahieu, S., and De Gryse, R. *Journal of Physics D-Applied Physics* **41**(20), 202003 (2008).

[42] Czekaj, D., Goranchev, B., Hollmann, E. K., Volpyas, V. A., and Zaytsev, A. G. *Vacuum* **42**(1-2), 43–45 (1991).

[43] Czekaj, D., Hollman, E. K., Volpyas, V. A., Zaitsev, A. G., Chernakova, A., and Goranchev, B. *Bulgarian Journal of Physics* **18**(1), 63–67 (1991).

[44] Chong, E. and Zak, S. *An Introduction to Optimization*. Wiley, 2nd edition, (2001).

[45] Dongarra, J., Walker, D., and Lusk, E. *International Journal of Supercomputer Applications and High Performance Computing* **8**(3-4), 167–414 (1994).

[46] Slezak, J. A., Zion, B. D., and Sibener, S. J. *Surface Science* **442**(1), L983–L988 (1999).

[47] Gomez, S., Steen, P. G., and Graham, W. G. *Applied Physics Letters* **81**(1), 19–21 (2002).

[48] Kaspar, T. C., Droubay, T. C., and Chambers, S. A. *Thin Solid Films* **519**(2), 635–640 (2010).

[49] Reddy, M. R. *Journal of Materials Science* **30**(2), 281–307 (1995).

[50] Depla, D., Buyle, G., Haemers, J., and De Gryse, R. *Surface & Coatings Technology* **200**(14-15), 4329–4338 (2006).

[51] Osterlund, L., Zoric, I., and Kasemo, B. *Physical Review B* **55**(23), 15452–15455 (1997).

[52] Malherbe, J. B., Hofmann, S., and Sanz, J. M. *Applied Surface Science* **27**(3), 355–365 (1986).

4 New model

4.1 Introduction

In the previous chapter, it was shown that the first models for reactive sputter systems already date back to the 1970's [1–5] and focused on an abrupt transition in erosion rate at a critical pressure (section 2.1). The original Berg model [6] was based on these earlier ideas and explains the observed hysteresis behavior during reactive sputtering (section 2.2). Bergs original model gives already a good understanding of the origin of the hysteresis in reactive sputtering. It describes the hysteresis under steady state conditions, and is based on balance equations. For a given reactive pressure, the corresponding flow can be calculated, together with the target and substrate state and the different gas consumptions. As such the hysteresis is simulated in a feedback-controlled way which enables modeling the three working regimes of the hysteresis. This simple model is able to successfully describe several qualitative trends of the reactive sputter process [7].

The major drawback of the Berg model and most of its ancestors, is that they only account for the process of chemisorption for the compound forming on the target. The addition of reactive implantation as poisoning mechanism for the target in a reactive sputtering model was first proposed by Affinito et al. (section 2.1.5) [8]. However more mature models for reactive sputtering including reactive implantation mechanisms were formulated by Kubart et al. [9] and Depla et al. [10]. They both accounted for two possible pathways of reactive implantation. A reactive ion is directly implanted [11] or a chemisorbed atom is knocked-on [12]

by an ion. The models [10, 13–16] of Depla et al., which are generic called RSD (Reactive Sputtering Deposition) models, are the most developed over time. With the RSD2007 model (section 3.2) [10], an attempt to quantify the model parameters by dedicated fitting has been performed (section 3.3) [17]. A further step on the way towards a genuine RSD model was the addition of a description of the deposition profile on the substrate [18]. A spatially resolved current profile on the target and the process of redeposition was for the first time included in the RSD2009 model [19]. This redeposition stands for the deposition of sputtered material back on to the target. The RSD2009 model was used to elucidate the importance of redeposition for a rotatable cylindrical DC magnetron. This model has a time dependent and a steady state version. However the steady state version can only be used without a current profile and/or redeposition.

In this chapter an updated model RSD2013 is presented. It forms a critical revision of the RSD2009 model including all the aforementioned target processes and extending the solution possibilities. The focus of this new model shifted to stationary planar targets. The implementation of the RSD2013 model happened from scratch aiming at an user-friendly, publicly available software package, equally called RSD2013, for simulating the reactive sputtering deposition in DC mode. The RSD2009 model suffered from some scientific, and computational shortcomings. In a nutshell, three main scientific adaptations were needed: the unrealistic high number of non-reacted implanted atoms, the inappropriate description of the redeposition process for planar targets and the solution of the steady state equations. Moreover, the implementation of the RSD2009 model was not suited for the work presented in this chapter. As it is a primary goal of the DRAFT research group to make the developed software available for third party users, the user-friendliness of the RSD2009 software was completely redesigned. The latter allows other users not only to perform simulations but also to verify the results presented in this work. The most notable modifications and improvements compared to the RSD2009 model and its implementation are

- All options are available to time dependent and steady state solver (multicell and redeposition)
- Restating the equations for the physical mechanism of redeposition
- Adding a second discrete subsurface layer for a physical more correct description of redeposition
- Adding a saturation limit on the implantation of reactive gas
- Improvements in numerical solving and stability
- Object oriented programming in C++ (compared to Visual Basic)

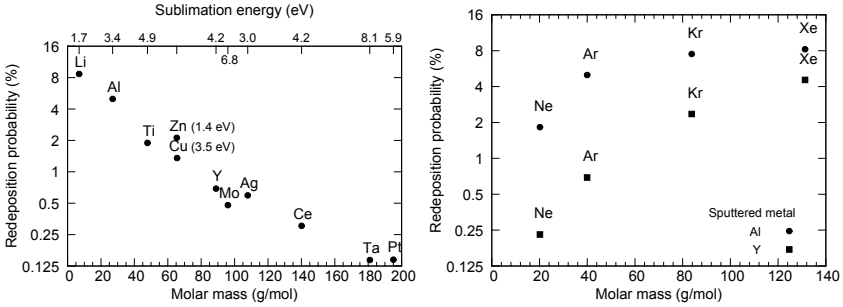

Figure 4.1: *(a) The dependency of the redeposition probability (given on a ^2log scale) on the sputtered element in $0.4\,\mathrm{Pa}$ Ar. Lower axis shows the mass of the element while the top axis the sublimation energy. Note that the top axis is not continuous. (b) The influence of the inert sputter gas ($0.4\,\mathrm{Pa}$) on the redeposition probability for aluminum and yttrium.*

- New graphical user interface (GUI) with parameter scan functionality
- User manual is now provided
- Improved text based output facilities
- GUI binary is completely separated from simulation binary which allows command line execution on Windows and Linux platforms

Central during the development of this new model was the mechanism of redeposition. Redeposition is introduced in section 4.2 for the non-reactive and the reactive case.

Section 4.3 will present the RSD2013 software with the derivation of the new model in all its detail and some necessary model extensions. Some comments on the numerical implementation and the software structure will be elucidated. A reference system is defined in section 4.4 for which several simulation configurations are formulated. These configurations differ in how detailed the system is modeled. Results for the different simulations are compared. In Section 4.5 a case study with the RSD2013 model is performed. The influence of the redeposition fraction on the hysteresis, the racetrack and the sputter profile are investigated.

4.2 Redeposition

4.2.1 Non-reactive

Besides the desired deposition of material on the substrate surface to be coated, deposition will also occur on the chamber walls and back on the target. The lat-

ter phenomenon is commonly called redeposition [20]. This redeposited material is then available to be sputtered, but evidently this phenomenon reduces the efficiency of the sputter process. Additionally the redeposited material flux is to some degree redistributed over the target surface. This means that the racetrack shape will be partially determined by this process and not only by the ion current profile.

A measure for redeposition is the probability for a sputtered particle to return to the sputtered surface. This is here called the redeposition probability. Several parameters will influence this redeposition probability and to get a better notion of their individual impact, their dependencies are studied by SiMTra simulations. Indeed, SiMTra does not only calculate the deposition on the substrate and the chamber walls but also gives a deposition profile on the sputtering surface, the target. To have a good reference to compare with, the chamber defined in section 2.2.3.1 is retaken. It is a cylindrical chamber of $20\,\mathrm{cm}$ length and diameter. A planar, circular Al $2\,\mathrm{inch}$ target is placed on top where a sample of the same size is coaxially positioned at a distance $d_{t-s} = 10\,\mathrm{cm}$ (Fig. 2.10). The reference simulation is in an Ar atmosphere of $0.4\,\mathrm{Pa}$ at $300\,\mathrm{K}$. The angular sputtering distribution is a cosine distribution and the energy sputtering distribution is a Thompson distribution where the surface binding energy is approximated with the sublimation energy of the sputtered metal. The maximum energy a sputtered metal atom can obtain is $400\,\mathrm{eV}$.

The focus is on the two metals, aluminum and yttrium, of the previous chapter. But first the dependency of some common sputtered metals on the redeposition probability is been examined. Two properties, their mass and their sublimation energy, influence this quantity. Recall that this sublimation energy is identified with the surface binding energy U_s. It corresponds to twice the most probable energy, $U_s/2$, a sputtered atom will have when assuming a Thompson energy distribution. Figure 4.1a learns that the redeposition probability is mainly determined by the mass of the metal and only in second order by the surface binding energy. Redeposition will become more important for lighter metals as Al and for a lower surface binding energy. The latter is best illustrated by comparing Zn and Cu in Fig. 4.1a which have almost equal molar masses. That heavier metals have a lower return probability is understandable as their deflection angle when scattering with the sputter gas decreases as function of their mass. More precise to say is that the mass ratio between the gas element and the metal element scale with this deflection angle and as such with the redeposition probability. This is illustrated in Fig. 4.1b for the metals Al and Y and the noble gases Ne, Ar, Kr and Xe. Indeed, metal-gas combination like Al-Ar and Y-Xe with similar mass ratios will have comparable redeposition probabilities.

The influence of the target-sample distance in the reference system is depicted in Fig. 4.2a for Al and Y. The closer the sample is placed, the less probable a sputtered particle will return. This seems reasonable as the initial sputter direction

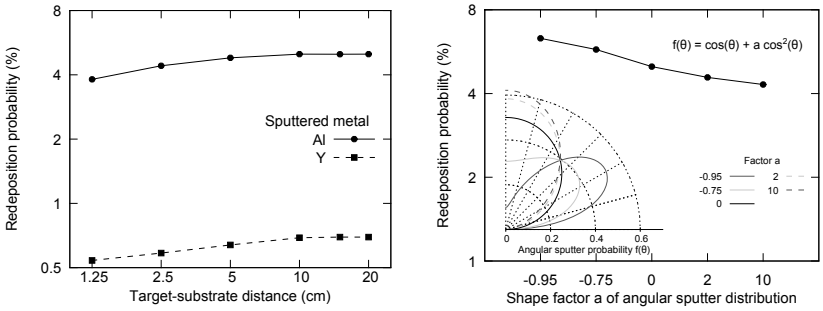

Figure 4.2: *(a) Simulated redeposition probability as function of the target-sample distance d_{t-s} on a $^2log\,-^2$ log scale for the Al/Ar system defined in Fig. 2.10. (b) The dependency of the redeposition probability on the angular sputter distribution (shown in the inset) characterized by the shape factor a for the Al/Ar system.*

has to be reversed to be redeposited. Therefore multiple collisions have to take place. But if the particle encounters a surface before a sufficient amount of collisions have occurred, it cannot return. However, as Fig. 4.2a shows, the impact of this effect is limited for the given pressure.

Also the angle under which a metal is sputtered can influence the redeposition probability. This is quantified by the angular sputter distribution. This distribution depends on many parameters, like the metal type, the target roughness and the racetrack shape [21]. These distributions can often be well approximated by a power series in $\cos(\theta)$ as in SiMTra where θ is the emission angle compared to the surface normal. Here the cosine distribution of the reference system is compared with two over-cosine distributions and two under-cosine distributions (see inset Fig. 4.2). These distributions $f(\theta)$ are parametrized as

$$f(\theta) = \cos(\theta) + a\cos^2(\theta) \tag{4.1}$$

where an over-cosine is obtained for $a > 0$ and an under-cosine for $-1 < a < 0$. In this way the factor a defines the shape of the angular sputter distribution. The impact on the redeposition probability is even how rather limited considering the extreme shape differences. The more under-cosine this distribution is, the larger the redeposition probability. This is understandable as more particles will be sputtered under larger angles compared with the surface normal. This means that the deflection angle needed to return will decrease. For the over-cosine distribution the opposite is true.

Finally the effect of the inert gas pressure on the redeposition probability is simulated for Al an Y (Fig. 4.3). Apart from the mass ratio between the gas and the sputtered element, this impact is the strongest. An almost linear relation for Al

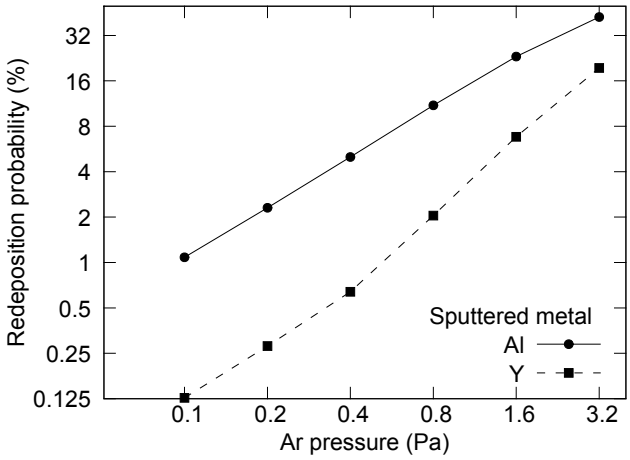

Figure 4.3: *Simulated redeposition probability as function of the Ar pressure for aluminum and yttrium on a* $^2log\ -^2\ log$ *scale.*

and even a superlinear relation for Y are obtained for pressures below $3.2\,\mathrm{Pa}$. The pressure defines the gas particle density through the ideal gas law. Higher pressures result in higher densities, which means that the mean free path of sputtered particles will decrease. As such more collisions over a shorter distance will occur which can deflect the sputter particle in the direction of the target. In this way, a decreased gas temperature will have the same effect as it increases the gas density.

4.2.2 Reactive

In non-reactive sputter deposition, the redeposited material on the target is the same as the initial target material. When moving to reactive sputter deposition where a reactive gas is added, the picture changes. The purpose of the reactive gas is to deposit a compound film on the substrate. However compound formation also occurs on the target itself, where it is subject to sputtering. As such the (re)deposition flux will be a mixture of compound constituents and original target material. In this way the effect of redeposition also defines the level of compound formation on the target. Considering redeposition in reactive sputter systems is then of technological importance as it influences the arcing behavior and the racetrack formation. Segers et al. [22] argued that arcing seriously intensifies when a certain critical compound thickness is reached. The spots of arcing are then located at the racetrack rim where porous, non-stoichiometric compound is formed. The growth of this compound layer is due to redeposition.

Also the racetrack formation will be altered due to redeposition. Redeposition

will non-uniformly reduce the erosion rate of the target, as it plays a role in the compound formation and as it returns sputtered material. Studies of the influence of the redeposition fraction on the reactive sputter process are limited [19, 23]. Here, this influence will be studied by simulating the process with a new RSD model and it will be shown what the impact is on the racetrack and the sputter profile in section 4.5. The redeposition fraction as function of the Ar pressure and its distribution over the target will be an input for this RSD model. As illustrated in the previous section, this redeposition fraction can be calculated by the Monte Carlo program SiMTra [24, 25]. Combining this new RSD2013 model and SiMTra enables then the study of the redeposition fraction on the process.

4.3 RSD2013

This new model is entitled RSD2013 and describes the reactive sputtering process for a direct current (DC) regime. The model forms a critical revision and extension of the RSD2009 model. The focus is on the description of planar magnetrons, while the extension to rotatable magnetron is quite straightforward. For completeness and to allow a reader to understand the model irrespective of reading previous chapters, the model is fully described in section 4.3.1. Note however that the extensions and changes in the model equations basically apply to the target description. Analogical as the previous RSD model, the modeled system is divided into three entities: the vacuum chamber, the target and the substrate surface. Except for the vacuum chamber, these entities are further subdivided into multiple surface cells. In this way a spatially resolved surface model of the reactive sputter process is established. Moreover, the RSD2013 model will be derived in its time dependent formulation in section 4.3.1 compared to the steady state version of RSD2007 in section 3.2. In essence this time dependent model solves first-order time dependent ordinary differential equations (ODEs) for the three mentioned entities. For the target these ODEs are coupled to first-order partial differential equations (PDEs) of time and of one space coordinate, describing the subsurface region. This subsurface region is then spatially resolved by subdividing it in multiple volume or subsurface cells. These ODEs and PDEs express the continuity of the resolved quantities in each entity. A steady state formulation of the model is obtained by setting the time derivatives in these equations to zero. These modified equations express then the balance of incoming and outgoing species. The solution of this steady state formulation, excluding redeposition and in a one-cell approach for the target, has been treated in section 3.2. The equations for a multiple surface cell target become highly non-linear and coupled when considering redeposition, their direct steady state solutions are as such not easily obtained. However a solution strategy for the steady state RSD2013 model is proposed in section 4.3.2. The RSD2013 model is implemented in the RSD2013 software provided with a

GUI (Graphical User Interface). The global software structure and some numeric implementation details are given in section 4.3.3. Finally, the possibilities and flexibility of the RSD2013 software is illustrated by the simulation of an example system where gradually a more detailed description is used.

4.3.1 Derivation

4.3.1.1 Chamber

The vacuum chamber is considered as a separate entity of which the description is zero-dimensional in space. The chamber embodies the partial ionized inert (e.g. Ar) and reactive (e.g. O_2) gases besides the vacuum pumping system. This pumping system is characterized by a constant volumetric flow rate or pumping speed S (in $cm^3\ s^{-1}$) which determines the rate of gas extracted out of the chamber. The gases are specified by their state variables temperature T , volume V , number of particles n and pressure P. Because of the typical low pressures ($\sim 0.01 - 1\,\mathrm{Pa}$), these gases can be considered as ideal gases for which the equation of state (ideal gas law)

$$PV = nk_BT \tag{4.2}$$

links their state variables. The ideal gases occupy the same constant volume V which corresponds to the volume of the vacuum chamber. Furthermore their temperature T is assumed to be equal and constant during the whole process. For the inert gas, its pressure P_i and its number of particles n_i are in a steady state, while for the reactive gas n_r (and consequently P_r) will be time dependent. Differentiating equation eq. 4.2 with respect to time for the reactive gas gives

$$\frac{\mathrm{d}P_r}{\mathrm{d}t} = \frac{k_BT}{V}\frac{\mathrm{d}n_r}{\mathrm{d}t} \tag{4.3}$$

This expresses the reactive pressure change due to the in- or outflow of gas particles in the chamber. This gas flow Q_r $(= \mathrm{d}n_r/\mathrm{d}t)$ is given by

$$Q_r = Q_{in} - Q_p - Q_t - Q_s \tag{4.4}$$

Q_{in} is the reactive gas flow introduced in the chamber by a mass flow controller. This reactive gas can flow out of the chamber's volume by three pathways: by being pumped out Q_p, by reaction with the substrate surface Q_s or by reaction with the target Q_t. The gas flows towards the substrate Q_s and the target Q_t depend on their state, and will be described later in this section. The gas flow towards the pumping system is defined by its pumping speed S and the state of the gas [26], as

$$Q_p = \frac{P_rS}{k_BT} \tag{4.5}$$

The flux of reactive gas molecules F_r towards the boundaries of the chamber (e.g. target and substrate) is proportional to the reactive gas pressure when assuming it as an ideal gas. In that case it is given by

$$F_r = \frac{P_r}{\sqrt{2\pi m_r k_B T}} \tag{4.6}$$

with m_r the mass of the reactive gas particle. In the magnetron plasma, part of the inert and the reactive gas particles are ionized. These fractions of ionization can be calculated by a wealth of different types of plasma models [27]. In this model it is assumed as a first approximation that the fraction of reactive ions f is proportional to the fraction of reactive gas which, accounting for eq. 4.2, is given by

$$f = \frac{P_r}{P_i + P_r} \tag{4.7}$$

This assumption is a rather satisfying approximation of what state-of-the-art plasma models predict for typical magnetron conditions [28]. This model further assumes that the target is then proportionally bombarded by this fraction of reactive ions compared to the ions of the inert gas. Berg models coupled with analytical plasma models do exist [29, 30], but the additionally introduced uncertainty in hard-to-retrieve parameters for these plasma models is often unwanted as the plasma itself is not the focus of the model.

4.3.1.2 Target

The target forms one of the boundaries of the vacuum chamber. It is defined as the entity that acts as the cathode in the sputtering system and from where target material can be sputtered. Initially it consists of pure metal. Its description is generally three-dimensional in space with a spatially resolved surface and subsurface region. This spatial resolving of the target surface is necessary to account for the non-uniform ion current distribution and the non-uniform redeposition profile on the target. In order to model this, the target is subdivided in surface cells. Each surface cell describes its surface state by three particle fractions: the metal fraction θ_m, the chemisorbed fraction θ_c and the compound fraction θ_r. The metal fraction θ_m is the metallic (non-reacted) portion of the surface cell, while the chemisorbed θ_c and the compound θ_r fraction are the reacted portions of the surface cell. For the reacted fraction metal is bounded to reactive gas atoms respectively by chemisorption of reactive gas on the metallic surface and due to the reactive implantation (direct and knock-on) of reactive gas atoms. For the fractions θ_r and θ_c, the same stoichiometric factor z is assumed. A reacted particle is then defined as MR_z with M a metal atom and R a reactive atom. A reacted particle can then be a chemisorbed particle or a compound particle depending on its formation. The distinction between θ_r and θ_c can be important as, for example, oxygen chemisorbed on aluminum affects the electron emission yield in a different way than a

fully oxidized compound formed by oxygen implantation [31]. A metal particle M is evidently just a metal atom which is unbounded. Reacted MR_z and metal M particles are collectively called particles in the following, while an unbounded reactive species R will be called a reactive atom. For simplicity, each particles is assumed to occupy the same volume, namely $1/n_0$ where n_0 is the bulk particle density of the metal. In this way their is no difference between defining the fractions θ as a particle ratio, a volume ratio or a surface ratio.

The particle fraction $\overline{\theta}$ weighted by the local ion current averaged over the whole target surface will be useful latter on. These average fractions will be denoted with an over bar to distinguish them from local particle fractions θ^i defined for each surface cell i. Such an averaged fraction is then defined as

$$\overline{\theta} = \frac{1}{I_{ion}} \sum_i I^i \theta^i \tag{4.8}$$

with I_{ion} the total ion current towards the target and I_i the local ion current towards a surface cell i. The label i connected to local quantities will be skipped in the remainder of this section in order to avoid cluttered notation, and will only be used when ambiguity arises. An overview of the used parameters is given in Table 4.1.

The state of a target surface cell is modified by the following processes which the model accounts for:

- Sputtering of the surface by the bombardment of ions, which removes the material of the target surface and reveals the underlying material.
- Chemisorption of reactive gas with surface metal particles, modifying them to chemisorbed particles.
- Deposition of already sputtered material back on to the surface of the cell, effectively transporting the underlying material into the subsurface region.
- Knock-on implantation of reactive atoms into the subsurface region bounded in a chemisorbed particle. This modifies a chemisorbed particle into a metal particle.
- Direct implantation of reactive ions into the subsurface region, supplying it with reactive atoms.

The reactive implantation into the subsurface region is accounted for by defining for each surface cell a depth profile. This depth profile is resolved by subdividing the implantation range in subsurface (or volume) cells. This implantation range typically extends up to a few nanometres below the surface but depends on the energy and type of the implanted reactive ion [32]. Each subsurface cell will then describe the concentration of implanted reactive atoms, of metal particles and of compound particles. These concentrations are altered due to the reaction between

Global parameters	Description
$\mathrm{Y_m, Y_c, Y_r\,(M[R_z]\,ion^{-1})}$	sputter yield of metal particles M, compound paritlces MR_z, chemisorbed particles MR_z
α_t, α_s	sticking probability of reactive gas on metal for the target, substrate surface
$\mathrm{k\,(cm^3 s^{-1} R^{-1})}$	2^{nd} order reaction rate coefficient of implanted reactive atoms with metal particles
$\beta\,\mathrm{(R\,ion^{-1})}$	knock-on yield of chemisorbed reactive atoms
$\mathrm{p(x)\,(cm^{-1})}$	implantation profile of reactive atoms
$s(n_M, n_R)$	saturation function for implantation of reactive atoms
$\mathrm{n_0\,(M[R_z]cm^{-3})}$	particle density
$\mathrm{n_{0,s}\,(M[R_z])cm^{-3}}$	particle surface density
$\mathrm{\Delta x\,(cm)}$	monolayer thickness
z	stoichiometric factor
$\mathrm{I_{ion}\,(ion\,s^{-1})}$	ion current
$\mathrm{P_i\,(Pa)}$	inert gas pressure
$\mathrm{T\,(K)}$	gas temperature
$\mathrm{V\,(cm^3)}$	volume of vacuum chamber
$\mathrm{S\,(cm^3 s^{-1})}$	pumping speed
Local parameters	
$\mathrm{j\,(ion\,cm^{-2} s^{-1})}$	ion current density on target cell
$\mathrm{I\,(ion\,s^{-1})}$	ion current to target cell
$\varepsilon_t, \varepsilon_s$	deposition fraction on target, substrate cell
$\mathrm{A_t, A_s\,(cm^2)}$	area of target, substrate cell

Table 4.1: *Overview of the global and local (=cell dependent) parameters in the model.*

metal particles and implanted reactive atoms, the continuous implantation of reactive atoms and the target surface movement. The erosion will transport subsurface material to the surface, while growth (due to redeposition) will transport surface material to the subsurface region

Surface As mentioned at the start of section 4.3, the state of each surface cell is defined by its corresponding ODEs. Before deriving these ODEs (eq. 4.12), the definition of some characteristic quantities is useful. Firstly, an average sputter yield Y_{av} can be given for each surface cell as

$$Y_{av} = Y_m\theta_m + Y_c\theta_c + Y_r\theta_r \tag{4.9}$$

It is a particle-weighted average of the sputter yield Y_m of metal particles, the sputter yield Y_c of chemisorbed particles and the sputter yield Y_r of compound

particles. It defines the number of particles, in units of particles (e.g. M and MR_z), that are ejected from a target surface cell per incoming ion. Secondly, a redeposition metal F_m and compound F_c flux can be defined for each surface cell. They represent the fluxes of redeposited material on the surface cell with area A_t. These fluxes are given by

$$F_m = \varepsilon_t \frac{I_{ion}}{A_t} Y_m \overline{\theta_m} \tag{4.10a}$$

$$F_c = \varepsilon_t \frac{I_{ion}}{A_t} (Y_r \overline{\theta_r} + Y_c \overline{\theta_c}) \tag{4.10b}$$

They depend on the total metal (eq. 4.10a) and reacted (eq. 4.10b) particle flux sputtered from the target surface. The averaged particle fractions $\overline{\theta_m}$, $\overline{\theta_r}$ and $\overline{\theta_c}$ have already been defined in eq. 4.8. The fraction ε_t determines which portion of these particle fluxes are deposited on the surface of the target cell. This redeposition fraction is considered independent of the particle type for the moment. The definitions (eq. 4.10a and eq. 4.10b) show that redeposition of chemisorbed particles contribute to the compound fraction. The reasoning behind this, is that reacted particles (=chemisorbed and compound) are assumed to be molecularly sputtered in the model as a MR_z particle. This is a simplification of reality as sputtering is mainly an atomistic mechanism. Nevertheless, it has been shown that this simplification has little impact on the outcome of this kind of models [7]. The ODEs are coupled with the PDEs by the surface fractions θ_m, θ_r and θ_c and by the subsurface fraction θ_b. This θ_b is the fraction of compound particles in the subsurface cell, just underneath its corresponding surface cell, and is related to the subsurface metal particle concentration $n_M(x)$ as

$$\theta_b = 1 - \frac{n_M(0)}{n_0} \tag{4.11}$$

with $n_M(0)$ the concentration in the boundary subsurface cell labeled as 0 (see further, eq. 4.21) and n_0 the initial metal particle concentration (=atomic density) before reaction. The ODEs are stated as

$$\begin{aligned} n_{0,s} \frac{\mathrm{d}\theta_m(t)}{\mathrm{d}t} &= -jY_m\theta_m + jY_{av}(1-\theta_b) + F_m \\ &\quad -(F_m + F_c)\theta_m + j\frac{\beta}{z}\theta_c - \frac{2}{z}\alpha_t F_r \theta_m \end{aligned} \tag{4.12a}$$

$$\begin{aligned} n_{0,s} \frac{\mathrm{d}\theta_r(t)}{\mathrm{d}t} &= -jY_r\theta_r + jY_{av}\theta_b + F_c \\ &\quad -(F_m + F_c)\theta_r \end{aligned} \tag{4.12b}$$

$$\begin{aligned} n_{0,s} \frac{\mathrm{d}\theta_c(t)}{\mathrm{d}t} &= -jY_c\theta_c \\ &\quad -(F_m + F_c)\theta_c - j\frac{\beta}{z}\theta_c + \frac{2}{z}\alpha_t F_r \theta_m \end{aligned} \tag{4.12c}$$

where F_m and F_c represent the redeposition fluxes (eq. 4.10), Y_{av} the average sputter yield (eq. 4.9) and F_r the flux of reactive gas particles (eq. 4.6). The time dependencies of the RHS terms are not explicitly written for compactness. These surface fractions are based on the in- and outflow of the relevant particle species. These particles are transported to the vacuum chamber (subsurface region) due to sputtering (redeposition). Additionally chemisorption and knock-on implantation convert particle species on the surface.

Figure 4.4 assists in the derivation of these ODEs (eq. 4.12) of a surface cell, while Table 4.1 summarizes the parameters involved. For example, the first term of eq. 4.12a is the sputtering of surface metal into the chamber which decreases the metal fraction. On Fig. 4.4, this is given by the sum of the top and bottom outflow arrow on the θ_m block, namely

$$jY_m\theta_m(1-\theta_b) + jY_m\theta_m\theta_b = jY_m\theta_m \tag{4.13}$$

The metal fraction is increased due to the removal of surface material, revealing underneath subsurface metal. This is the second term in eq. 4.12a and is denoted on Fig. 4.4 as the sum of the three inflow arrows at the top of each block representing the three fractions, namely

$$\begin{aligned} &jY_m\theta_m(1-\theta_b) + jY_r\theta_r(1-\theta_b) + jY_c\theta_c(1-\theta_b) \\ &\quad = j(Y_m\theta_m + Y_r\theta_r + Y_c\theta_c)(1-\theta_b) \\ &\quad = jY_{av}(1-\theta_b) \end{aligned} \tag{4.14}$$

The third term of eq. 4.12a is the gain of surface metal due to the redeposition of metal on the surface. In Fig. 4.4 this is shown as the sum of the second inflow arrow on each block, namely

$$\begin{aligned} &F_m\theta_m + F_m\theta_r + F_m\theta_c \\ &\quad = F_m(\theta_m + \theta_r + \theta_c) \\ &\quad = F_m \end{aligned} \tag{4.15}$$

Fourth term of eq. 4.12a is the transport of surface metal into the subsurface due to covering by redeposition. This decreases the surface metal fraction. The top and bottom outflow arrows pointing into the subsurface on the θ_m block in Fig. 4.4 represent this as

$$F_m\theta_m + F_c\theta_m = (F_m + F_c)\theta_m \tag{4.16}$$

The fifth and sixth terms of eq. 4.12a are conversions. The fifth term represents the knock-on of reactive atoms into the subsurface, converting the chemisorbed particle into a metal particle. The knock-on efficiency is determined by the knock-on yield β, defined as a yield in units of reactive atoms per incoming ion. On Fig. 4.4, the knock-on is represented by the curled arrow on the θ_c block. The sixth term

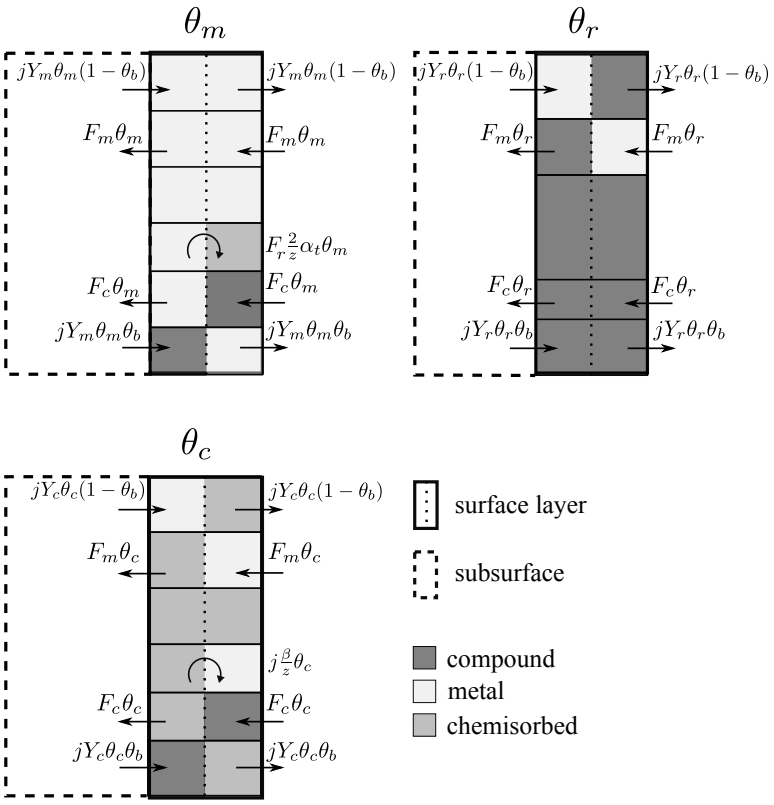

Figure 4.4: *A schematic representation of the modeling of a target surface cell. The three gray levels represent the three particle fractions θ_m (light gray), θ_r (dark gray) and θ_c (gray) of a single surface cell. The dashed contour attached to each block represents the boundary cell of the subsurface. This subsurface cell is specified by the particle fraction θ_b (not shown). The dotted line separates the initial species from the replacing species due to particle transport (straight arrows) or conversion (curled arrows) in the surface cell. Straight arrows pointing out of the surface cell specify transport of the initial species out of the cell, while the arrows pointing inwards specify transport of the replacing species into the cell. Transport of particles can go into the boundary subsurface cell (left) or into the vacuum (right). The transport arrows are paired (in- and outward transport) to guarantee the conservation of the number of particles in the surface cell. The curled arrows indicate conversions of the species in the surface cell, keeping the number of particles unmodified. The variables defining these transport terms and conversions are defined in the text and in Table 4.1.*

of eq. 4.12a is the chemisorption of reactive gas on metal converting it into chemisorbed particles, decreasing the metal fraction. The affinity for chemisorption is characterized by the sticking probability α_t where a diatomic reactive gas R_2 is assumed, explaining the factor two. This chemisorption conversion is stated on Fig. 4.4 as the curled arrow on the θ_m block. In a same way the eq. 4.12b and eq. 4.12c can be derived from Fig. 4.4.

The compound fraction θ_r (eq. 4.12b) is decreased due to the sputtering of compound particles (first term of eq. 4.12b). On the other hand it is increased due to the removal of surface particles revealing underneath compound particles (second term in eq. 4.12b). The redeposition of reacted particles however, increases the compound fraction at the surface (third term in eq. 4.12b). The transport of compound particles to the subsurface region by redeposition finally decreases the compound fraction (fourth term in eq. 4.12b).

The chemisorbed fraction θ_c (eq. 4.12c) is decreased due to the sputtering of chemisorbed particles (first term in eq. 4.12c), due to transport to the subsurface region (second term in eq. 4.12c) and due to its modification into metal particles by the knock-on implantation (third term in eq. 4.12c). It is only increased due to the chemisorption of reactive gas with metal particles (fourth term in eq. 4.12c). Recall that chemisorbed particles transported to the subsurface region are modified into compound particles as in the subsurface region only those compound particles are described.

Subsurface The subsurface region of every surface cell is spatially resolved by partitioning it in subsurface (or volume) cells. A subsurface cell specifies the concentration of implanted reactive atoms $n_R(x)$ and of metal particles $n_M(x)$ at a certain depth x in the target. The concentration of compound particles is by definition obtained as $n_0 - n_M(x)$ with n_0 the initial metal concentration. The concentrations $n_M(x)$ and $n_R(x)$ have a spatial (=depth) and time dependency, and are described by two coupled PDEs as

$$\frac{\partial}{\partial t} n_M(x,t) = v_s(t) \frac{\partial}{\partial x} n_M(x,t) - k n_M(x,t) n_R(x,t) \tag{4.17a}$$

$$\frac{\partial}{\partial t} n_R(x,t) = v_s(t) \frac{\partial}{\partial x} n_R(x,t) - z k n_M(x,t) n_R(x,t) + j[2f(t) + \beta\theta_c(t)] p(x) s(n_M, n_R) \tag{4.17b}$$

These PDEs are defined in a coordinate system moving at a speed $v_s(t)$ with the origin attached to the target surface and the positive direction pointing into the target. The mathematical derivation is analog to eq. 3.19 keeping the explicit time dependency of the concentrations. These PDEs each contain a transport term (first term eq. 4.17) which accounts for the transversal transport of the particle species due to effective erosion ($v_s > 0$) or growth ($v_s < 0$) of the corresponding surface

cell. In this context the definition of an effective surface speed v_s of a target cell is appropriate, given as

$$v_s = v_e - v_r \tag{4.18}$$

where the erosion speed v_e and the redeposition speed v_r are given by

$$v_e = \frac{I}{n_0 A_t}(Y_m\theta_m + Y_c\theta_c + Y_r\theta_r) \tag{4.19a}$$

$$v_r = \varepsilon_t \frac{I_{ion}}{n_0 A_t}(Y_m\overline{\theta_m} + Y_c\overline{\theta_c} + Y_r\overline{\theta_r}) \tag{4.19b}$$

The erosion speed v_e only depends on the local condition of a target cell and its local ion current density $I/A_t(= j)$. The redeposition speed v_r however is determined by the average condition of the target (see eq. 4.8 for the definition) and the local fraction ε_t of the redeposited material. The sum of these local fractions ε_t equals the total fraction of material E_t that is redeposited on the target. This surface speed v_s describes the rate of transport. Besides transport, the chemical reaction between reactive atoms and metal particles decreases both the metal and the reactive concentration (second term in eq. 4.17). This chemical reaction is modeled as a second order reaction mechanism with the reaction coefficient k.

The two sources of reactive atoms in the subsurface region are direct and knock-on implantation. For direct implantation (third term in eq. 4.17b), it is assumed that only diatomic reactive gas ions are implanted. Such an ion breaks up when hitting the target surface, explaining the factor two. Its constituents will be implanted according to a certain implantation profile $p(x)$ in the subsurface region where x represents the depth coordinate. The ion fraction f (eq. 4.7) defines the reactive ion current density from the total ion current density. The knock-on implantation (fourth term in eq. 4.17b) is the second source of reactive atoms. Ions hitting the surface where chemisorbed reactive atoms reside, have a chance to be knocked into the subsurface region according to the yield β. These reactive atoms are as such knock-on. An estimate for this yield can be calculated with SRIM as explained in section 3.3.2. In a first approximation, the same implantation profile $p(x)$ is assumed for direct and knock-on implantation.

An additional constraint applies to the concentration of reactive atoms in a subsurface cell. When the surface speed v_s is small compared to the local ion current density, a build-up of reactive atoms due to implantation would occur. As such the model defines a saturation function $s(n_M, n_R)$ (Fig. 4.5) which limits the implantation of reactive atoms in a subsurface cell. This function constraints the enrichment of the subsurface around a critical concentration $n_{R,max}$ of reactive atoms. This saturation function is given as

$$s(n_M, n_R) = \frac{1}{2} - \frac{1}{2}\mathrm{erf}\left(\frac{z(n_0 - n_M) + n_R - n_{R,max}}{\Delta n_R}\right) \tag{4.20}$$

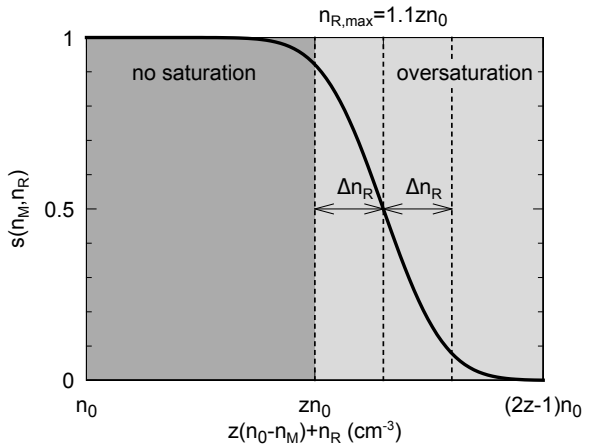

Figure 4.5: *Illustration of the saturation function $s(n_M, n_R)$ where the critical concentration $n_{R,max} = 1.1zn_0$ and the statistical spread $\Delta n_R = 0.1zn_0$. In the limit of $\Delta n_R \to 0$ this becomes a step function.*

where Δn_R defines a statistical spread around the critical concentration $n_{R,max}$ [33]. In the limit of Δn_R going to zero, this saturation function becomes a step function. The concentration $n_{R,max}$ accounts for all the reactive atoms, bounded in a compound particle and unbounded. The excess of implanted reactive atoms, determined by the complementary of the saturation function $s(n_M, n_R)$, is assumed to diffuse directly back into the vacuum chamber. This is a crude approximation, but introducing a sensible physical diffusion mechanism increases the complexity of the model.

The PDEs (eq. 4.17) are constrained by the following time-dependent boundary condition

$$\begin{aligned}\frac{\mathrm{d}}{\mathrm{d}t}n_M(0,t) &= -\frac{v_e(t)}{\Delta x}n_M(0,t) + \frac{v_r(t)}{\Delta x}n_0\theta_m(t) + \frac{v_s(t)}{\Delta x}n'_M(t) \\ &\quad -kn_M(0,t)n_R(0,t) \qquad (4.21a)\\ \frac{\mathrm{d}}{\mathrm{d}t}n_R(0,t) &= -\frac{v_e(t)}{\Delta x}n_R(0,t) + \frac{v_s(t)}{\Delta x}n'_R(t) \\ &\quad -kzn_M(0,t)n_R(0,t) \\ &\quad +j[2f(t) + \beta\theta_c(t)]p(x)s(n_M(0,t), n_R(0,t)) \qquad (4.21b)\end{aligned}$$

where

$$n'_i(t) = \begin{cases} n_i(1,t) & \text{if } v_s(t) > 0 \\ n_i(0,t) & \text{if } v_s(t) < 0 \end{cases}, \text{with } i = M, R \qquad (4.22)$$

This boundary condition describes the first subsurface cell (defined by $n_M(0,t)$ and $n_R(0,t)$) connected to the target surface as a layer with a thickness of one

monolayer $\Delta x (= n_0^{-1/3})$. Equation 4.22 distinguishes between the case of target erosion ($v_s > 0$) and of growth ($v_s < 0$). Surface erosion transports metal particles/reactive atoms out of the subsurface cell (first term of eq. 4.21). Redeposition transports metal particles from the surface into the subsurface cell (second term of eq. 4.21a). As no free reactive atoms are considered in the surface, this term drops out of eq. 4.21b. To preserve the particle/atom density in this subsurface cell, particles/atoms are transported into the subsurface cell from the cell underneath in the case of erosion. In the case of growth, particles/atoms are transported in the reversed way (third term in eq. 4.21a and second term in eq. 4.21b). The reaction and implantation terms are unchanged compared to eq. 4.17. These boundary conditions effectively connect the surface description with the subsurface description. Recall that $n_M(0,t)$ is related to $\theta_b(t)$ as defined in eq. 4.11, acting as a coupling variable between the ODEs of the surface and the PDEs of the subsurface.

The target effectively consumes reactive gas by its reaction mechanisms. This reactive gas is extracted from the vacuum chamber. The reactive gas consumption q_t of a target cell is defined as

$$q_t = \begin{cases} \alpha_t F_r \theta_m A_t + fI - q_d - v_s \frac{n_R(0)}{2} A_t & \text{if } v_s > 0 \\ \alpha_t F_r \theta_m A_t + fI - q_d & \text{if } v_s < 0 \end{cases} \tag{4.23}$$

Reactive gas is incorporated in the target by chemisorption (first term eq. 4.23) forming chemisorbed particles. Additionally, reactive gas can become ionized and be implanted into the target cell (second term eq. 4.23). If the state of the subsurface region allows it, these implanted reactive atoms can react and form compound particles. The flow q_d accounts for the amount of out-diffused reactive gas, due to saturation of the subsurface. This term q_d is given as

$$q_d = I(f + \frac{\beta}{2}\theta_c) \int_0^D [1 - s(n_M(x), n_R(x))] p(x) \mathrm{d}x \tag{4.24}$$

The integration extends over the whole implantation depth D. When there is an effective erosion ($v_s > 0$), some amount of non-reacted implanted reactive atoms (third term eq. 4.23) can reach the surface where they are transported back into the vacuum chamber. This latter mechanism is not applicable when there is effective growth ($v_s < 0$). The sum of the local gas consumptions q_t equals then the total reactive gas flow Q_t consumed by the target.

4.3.1.3 Substrate

The substrate is the other boundary that encloses the vacuum chamber. It is defined as all the surfaces where sputtered material has been deposited with the exclusion of the target. The reactive gas of the vacuum chamber can be incorporated in the non-reacted deposited material. The description of the substrate is maximally

two dimensional in space, as only the evolution of its surface is considered. This two-dimensionality is adopted in order to account for the nonuniform deposition profile of the sputtered material. It is in the same way modelled as the target surface by subdividing the substrate in surface cells. The state of each surface cell is characterized by a local particle fraction θ_s which represents the fraction of compound particles. The fraction $1 - \theta_s$ then evidently represents the fraction of metal particles. The surface state of a substrate cell is modified by the following processes which the model accounts for:

- Chemisorption of reactive gas with surface metal particles, converting them to compound particles.
- Deposition of sputtered compound and metal particles, effectively transporting the underlying material deeper into the layer.

This implicitly assumes that no other (plasma)wall interactions besides deposition and chemisorption are included. Note that no distinction is made between chemisorbed and compound particles (due to deposition), in contrast to the target description. They are collectively called compound particles, in the case of the substrate. The need for a distinction between them is less critical as for the target because the chemisorption process is actually an incorporation process [34]. The reactive gas atoms which stick on the substrate are simultaneously deposited with sputtered metal and compound. This contrasts with the usual picture of a metal surface where a reactive gas molecule can chemisorb on. During deposition the reactive atoms are build-in or incorporated in the deposited layer, and a sort of co-deposition of metal and reactive gas atoms exists. The reaction products of this process should then not necessarily be considered in a chemisorbed state. The state of a substrate cell is determined by its corresponding ODE which defines the time evolution of the fraction θ_s. The idea behind its derivation is identical to the treatment of the fractions defined for a target surface cell. Figure 4.6 assists in the derivation of this ODE, given as

$$n_{0,s}\frac{\mathrm{d}\theta_s(t)}{\mathrm{d}t} = F_{r,s}(1-\theta_s) - F_{m,s}\theta_s + \frac{2}{z}\alpha_s F_r(1-\theta_s) \tag{4.25}$$

where $F_{m,s}$ and $F_{r,s}$ here represent the flux density of respectively metal and compound material deposited on the substrate cell. Similar definitions for $F_{m,s}$ and $F_{r,s}$ apply as for the target case (eq. 4.10), namely

$$F_{m,s} = \varepsilon_s \frac{I_{ion}}{A_s} Y_m \overline{\theta_m} \tag{4.26a}$$

$$F_{c,s} = \varepsilon_s \frac{I_{ion}}{A_s} (Y_r \overline{\theta_r} + Y_c \overline{\theta_c}) \tag{4.26b}$$

with the understanding that A_s is the area of a substrate cell and ε_s is the deposition fraction on this substrate cell. Summing of these fractions ε_s equals the

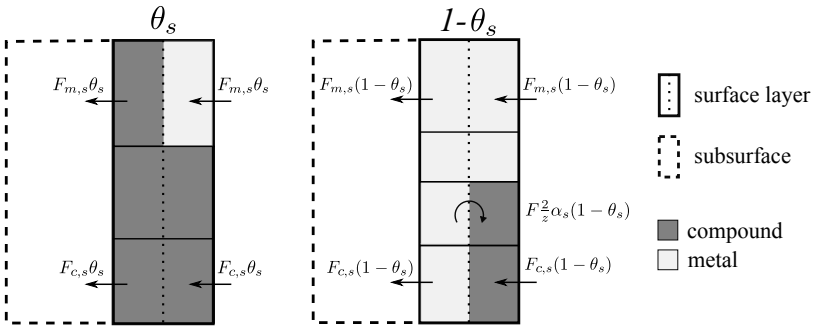

Figure 4.6: *A similar representation of the modeling of a substrate surface cell as for the case of a target surface cell (Fig. 4.4) with the fraction θ_s (dark gray) and the fraction $1-\theta_s$ (light gray).*

total fraction of material E_s that is deposited on all the substrates. Recalling the definition of E_t, it is evident that E_s and E_t add to one, where it is assumed that the pumping of sputtered material is negligible.

As sputtering and implantation are minimal for a substrate cell compared to the target, the evolution of its compound fraction θ_s is less involved. The fraction is increased due to the transport of metal particles out of the surface cell into the deposited layer by the covering of sputtered compound material (first term in eq. 4.25). Reversely, the fraction is decreased due to the transport of compound particles out of the surface cell into the layer by the deposition of sputtered metal material (second term in eq. 4.25). Finally, the fraction increases by the chemisorption reaction of reactive gas with metal particles on the substrate (third term in eq. 4.25). It converts metal particles into compound particles. The affinity for chemisorption is characterized by the sticking probability α_s, while the stated factor two again originates from the assumption of a diatomic reactive gas.

Similar as for a target cell, a reactive gas consumption of a substrate cell q_s can be defined. It is given as

$$q_s = \alpha_s F_r (1-\theta_s) A_s \tag{4.27}$$

This gas consumption is solely determined by the chemisorption process which effectively incorporates reactive gas molecules into the deposited layer. It depends on the availability of metal particles, the sticking probability and the flux of reactive gas. Summation of these individual q_s results in the total reactive gas flow Q_s consumed by the substrate.

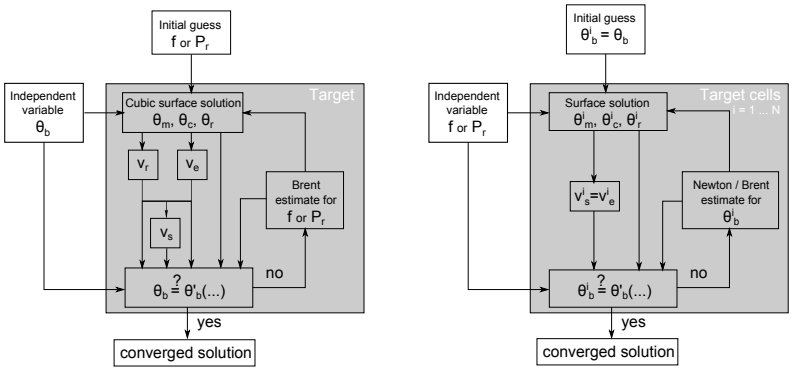

Figure 4.7: *Schematic representation of the steady state solution strategy for (a) a one-cell target with redeposition and for (b) a multi-cell target without redeposition. In case (a), the variable f (or P_r) is iteratively solved for while in case (b) a loop over the N target cells individually solves for each cell the subsurface fraction θ^i_b. The function $\theta'_b(\dots)$ gives a value for θ_b based on the equation of the boundary layer (eq. B.7).*

4.3.2 Steady state solver

The time dependent RSD2013 model can be formulated into a steady state model by setting all the time derivatives to zero. The ODE for the reactive pressure (eq. 4.4) becomes a balance equation for the reactive flows. The ODEs for the substrate (eq. 4.25) become balance equations for the compound fractions. These equations are similary solved as in the Berg model and as in the previous RSD model, once a solution for the target is obtained. However the model extensions compared to the previous steady state RSD model (section 3.2.1) complicate the steady state solution for the target. Especially the introduction of a current profile and redeposition prevent the direct application of the strategy explained in section 3.2.2. First two special cases are discussed: the case of redeposition for a one-cell target and the case of no redeposition for a multi-cell target. After which a general solution strategy for a multi-cell target with redeposition is proposed. The general steady state equations for the target of the RSD2013 model are presented in Appendix B.

4.3.2.1 Redeposition/one-cell target

If redeposition is considered for a one-cell target, the target is specified by a single subsurface compound fraction θ_b with a corresponding reactive mole fraction

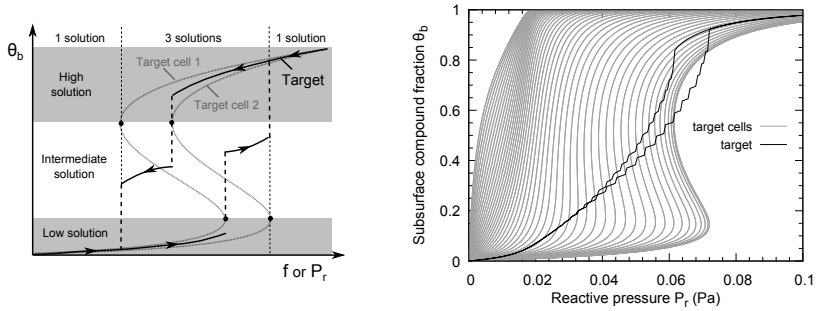

(a) ***(b)***

Figure 4.8: *(a) Schematic representation of how the steady state solution of two individual target cells is combined into one solution for the target. (b) The individual target cell solutions and the combined target solution for a simulation of a 100-cell target without redeposition. The simulated system corresponds with the 100-cell solution of Fig. 4.10a.*

f. The same solution method as in section 3.2.2 for this $\theta_b - f$ relation can be applied. However the determination of the surface fractions (θ_m, θ_c and θ_r) necessary to solve eq. 3.33 are now not a linear system. Indeed based on eq. B.1 and the definitions in eq. B.3, these balance equations can be written as

$$jY_m\theta_m + [F_m(\theta_m) + F_c(\theta_c,\theta_r)]\theta_m + \frac{2}{z}\alpha_t F_r\theta_m = jY_{av}(\theta_m,\theta_c,\theta_r)(1-\theta_b) + F_m(\theta_m) + j\frac{\beta}{z}\theta_c \quad (4.28a)$$

$$jY_r\theta_r + [F_m(\theta_m) + F_c(\theta_c,\theta_r)]\theta_r = jY_{av}(\theta_m,\theta_c,\theta_r)\theta_b + F_c(\theta_c,\theta_r) \quad (4.28b)$$

$$jY_c\theta_c + [F_m(\theta_m) + F_c(\theta_c,\theta_r)]\theta_c + j\frac{\beta}{z}\theta_c = \frac{2}{z}\alpha_t F_r\theta_m \quad (4.28c)$$

recalling that $\overline{\theta} \equiv \theta$ for a one-cell target. This shows that the balance equations will contain quadratic terms in the surface fractions due to the redeposition contributions $F_m(\theta_m)$ and $F_c(\theta_c,\theta_r)$. This quadratic system can be analytically solved for a given θ_b and f under the assumption that sputter yields $Y_r = Y_c$. Then these three equations can be rewritten into a single cubic equation with one of the surface fraction as unknown. A derivation of this cubic equation is outlined in Appendix B. A schematic representation of the solution strategy is given in Fig. 4.7a.

4.3.2.2 No redeposition/multi-cell target

If only a current profile is considered and no redeposition, namely $\varepsilon_t = 0$, there is no coupling between the different target surface cells. The dependency of the

model on F_m and F_c (eq. 4.10) cancels out and the individual cells do not depend on the average condition of the target. The balance equations for the surface fractions and the ODEs for the subsurface region can be individually solved for each target cell. The total solution for the target boils then down to separately solving the RSD model for the N targets cells with different current densities and areas. However the solution method of section 3.2.2 will result in a solution for $f(\theta_b)$ as function of θ_b for each target cell. When these solutions have to be combined in a solution for the entire target, a problem may arise. The reactive pressure P_r or equivalent f is assumed to be the same across the entire target in the model. As such only one reactive pressure value is connected to the target for given conditions. To find the target state for a given pressure, the inverse solution $\theta_b(f)$ as function of f(or P_r) is needed. This solution strategy is schematically represented in Fig. 4.7b.

Figure 4.8a shows however that this inverse solution is possibly not single valued but can have at most three solutions. This raises the question for each target cell which of these three solutions have to be combined with the solutions of the remaining target cells for a given f. For relatively low and high f there is normally only one solution θ_b^i for each target cell and the problem does not exist. This solution is then a single root of $\theta_b^i - \theta_b'(\ldots)$ where $\theta_b'(\ldots)$ is the solution for the boundary layer. Numerically, a Brent method [35] can be used to find this single root. For an intermediate f, there can be three θ_b^i solutions per target cell: a high, a low and an intermediate valued solution. The high valued solution will correspond to a more poisoned mode while the low valued solution corresponds to a more metallic mode. The intermediate solutions can be identified with a transition mode. A solution strategy now consists of first combining all the low valued θ_b^i solution of the target cell for a given f, and subsequently combining the high valued θ_b^i solutions (Fig. 4.8a). These low and high valued θ_b^i solutions are the lowest and highest root of $\theta_b^i - \theta_b'(\ldots)$. These two roots are found by using the Newton method [35] with initial guess $\theta_b^i = 0$ for the low valued solution and with $\theta_b^i = 1$ for the high valued solution.

The multiple solutions makes that the typical S-shaped $P_r - Q_{in}$ hysteresis curve can split up in two S-shapes as shown in Fig. 4.10. The smoothness of this hysteresis as function of P_r will depend on the number of target cells used in the model (Fig. 4.10a). The two values for the target fraction for a given P_r result in two values for the reactive flow Q_{in}. The region in between the two S-branches will consist of the transition operation points. Experimental operation curves by feedback control are now assumed to follow a trajectory in between or on these two S-branches. The exact position of such curve will depend on how the operation curve is dynamically stabilized in time.

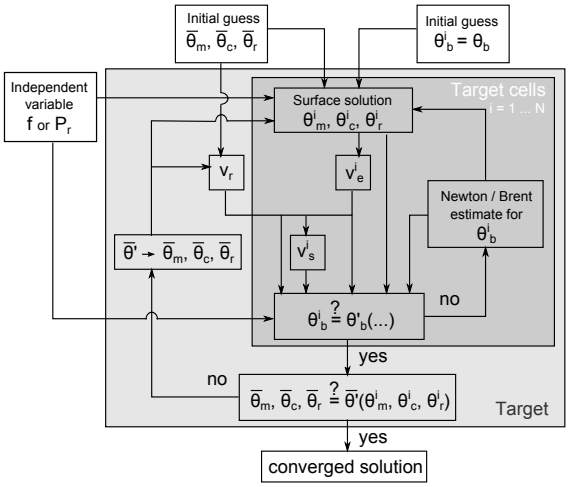

Figure 4.9: *Schematic representation of the general solution strategy for the steady state description of the RSD2013 model. An inner loop (dark gray) individually solves the N target cells based on an estimate for the average fractions ($\overline{\theta_m}$, $\overline{\theta_c}$,$\overline{\theta_r}$) and the subsurface fraction θ_b^i. The outer loop (light gray) iteratively updates these average fractions until convergence is achieved. The function $\theta_b'(\dots)$ are the solutions θ_b^i obtained from the boundary layers (eq. B.7). The function $\overline{\theta'}(\theta_m^i, \theta_c^i, \theta_r^i)$ calculates the three average fractions.*

4.3.2.3 Redeposition/multi-cell target

For the general case of a multi-cell target with a redeposition profile, an extended version of the previous solution strategy for a multi-cell target is used. The balance equations for the surface fractions across the different target cells are now coupled through their redeposition fluxes (eq. 4.10). These redeposition fluxes depend on the average target surface fractions . In order to decouple the equations for a target cell from the other target cells, an estimate for these average surface fractions is initially given. In this way, each target cell can be solved independently with the average surface fractions as constant parameter. After solving all the target cells, the average surface fractions are recalculated based on the individual solutions of the target cells. With this updated estimate, the calculation is repeated until convergence is retrieved in the average surface fraction. It is this strategy that is implemented in the current RSD2013 software and is schematically represented in Fig. 4.9. Recall that this solution method only reproduces the most metallic and the most poisoned process curves. Intermediate process curves where some target cells are in transition mode are not reproduced. However they will be bounded by the two simulated process curves. An illustration of a hysteresis curve for a 100-cell target with redeposition (4%) is given in Fig. 4.10b.

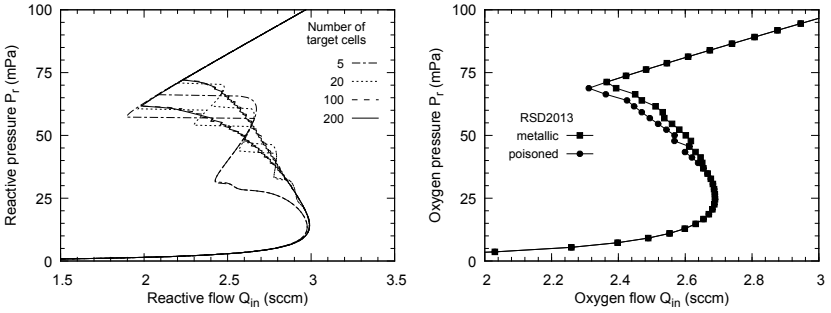

Figure 4.10: *Illustration of the steady state solver for a multi-cell target without redeposition (a) and with redeposition (b). (a) The dependency on the number of target cells is shown. (b) The open symbols correspond to the most metallic state while the full symbols corresponds with the most poisoned state for a given reactive pressure. The region between the curves contains the transition points. Simulation parameters are taken from Table 4.2 for the system B (a) and for the system E (b) as defined in section 4.4.*

4.3.3 Implementation

The presented RSD2013 model is implemented in a publicly available [36] and user-friendly software program equally entitled RSD2013. This software is currently closed source but a compiled version for the Windows platform can be downloaded from the DRAFT website together with a full body manual. The entire software is coded in the object oriented C++ language with some C dependencies. The software consists out of two separated binaries: `RSD2013_GUI.exe` and `RSD2013.exe` (Fig. 4.11). The first binary is the Graphical User Interface (GUI) which purpose is twofold. It generates in a user-friendly way the necessary input text files for the second binary, the effective simulation program. Its second purpose is the managing and creation of multiple simulations. The GUI is implemented with the `wxWidgets` C++ library [37], a cross-platform GUI library. As the GUI is completely separated from the effective simulation program, the simulation program can be directly executed from the command line if appropriate input files are provided.

In Fig. 4.11 the names and the structure of the most important C++ classes of the simulation program `RSD2013.exe` are given. At the top level there are the classes `InputParam` and `Simulation`. An instance of the class `InputParam` embodies all the input provided by the input text files. Within an instance of `InputParam`, the (re)deposition profiles will be saved within an instance of `Simtra`. A `Simtra` instance will contain one or more `SimtraSurf` instances which represent each an individual deposition surface. The redeposition on the tar-

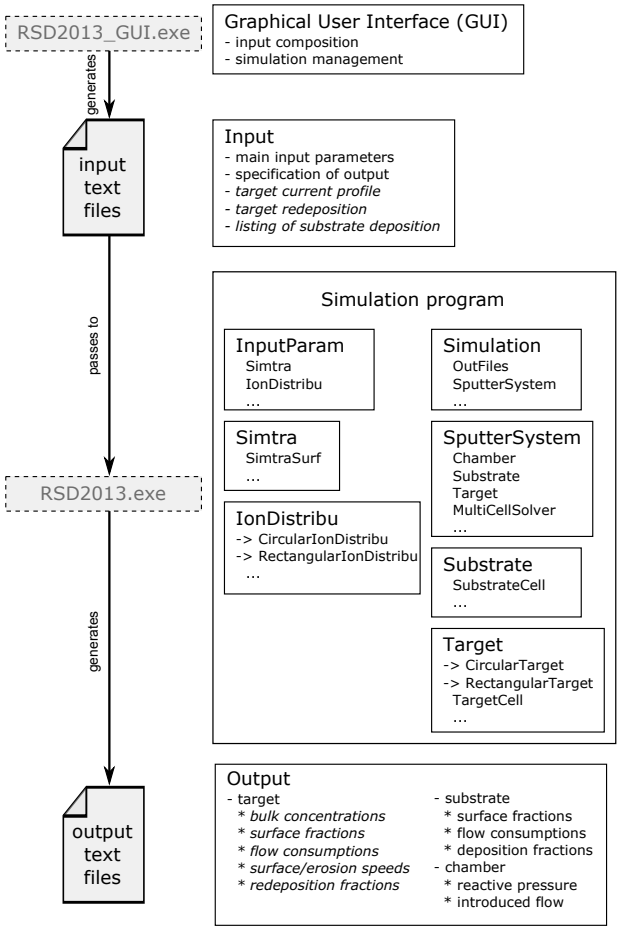

Figure 4.11: *Schematic representation of the RSD2013 software with the general work flow of the software. The two separated binaries* `RSD2013_GUI.exe` *and* `RSD2013.exe` *are interconnected with plain input text files. The general class structure of the* `RSD2013.exe` *binary representing the effective simulation program is given in addition to the expected input and output.*

get will be represented by a single `SimtraSurf` instance within a single `Simtra` instance while for the substrate typical multiple `SimtraSurf` instances are contained within a single `Simtra` instance. The class `IonDistribu` saves the possible ion current profile on the target. Two specializations of this class, `CircularIonDistribu` and `RectangularIonDistribu` are defined to distinguish between a circular target with an axial symmetric current profile and a general rectangular target. All other input is stored in basic C/C++ types or simple C `struct`'s.

An instance of `InputParam` is passed to the class `Simulation`. This class represents the actual simulation. Based on this input, `Simulation` constructs an appropriate instance of the class `OutFiles` which manages the output that will be generated. The modeled system is represented by an instance of the class `SputterSystem` constructed in `Simulation`. The main attributes of `SputterSystem` namely `Chamber`, `Substrate` and `Target` represent the three entities defined in the RSD model (section 4.3). These instances embody the governing equations of the model inside them. As the RSD2013 model allows to spatial resolve the target and the substrate, their classes contain one or multiple instance of respectively the classes `TargetCell` and `SubstrateCell`. For the class `Target`, two specializations exist namely `CircularTarget` and `RectangularTarget`. This allows the simulation with an axial symmetric circular target and a general rectangular target. Finally the class `SputterSystem` will contain an instance of `MultiCellSolver`. This class defines the machinery and numerical algorithms for solving either the time dependent or the steady state model.

The RSD2013 software has several simulation facilities. Figure 4.12 summarizes the principal choices to be made when setting up a RSD simulation. The first choice is the solution method: a (direct) steady-state solution or a time dependent solution. Secondly the user can opt for a multi-cell description of the target and/or of the substrate. Consequently an ion current profile for the target and/or a deposition profile for the substrate has to be provided. Furthermore, when including redeposition and choosing for a multi-cell target description, a redeposition profile on the target should also be provided. A final choice is to limit the amount of reactive species in the subsurface. This limitation can be sharp (=step function), smooth (=error function) or absent (=constant function). An additional restriction currently applies. The sputter yields of the chemisorbed and the compound fraction are taken to be the same, because exact knowledge of specific sputter yields of chemisorbed material is limited [38].

Some numeric and mathematical aspects for solving the time dependent and steady state model are given. The time dependent model numerically boils down to a solution of a set of $3N + M$ ODEs coupled to a set of $2N$ PDEs. N represent the number of target surface cells, while M is the number of substrate cells.

These equations are solved by the use of finite difference methods. These $3N+M$ ODEs are integrated in time with an own implementation of a 4^{th} order explicit RungeKutta algorithm [35]. The dependencies of the ODEs on the subsurface fraction θ_b (eq. 4.11) is treated as a time dependent function. This θ_b function has then to be evaluated at every half time step, meaning solving the corresponding PDEs. The solution scheme of the PDEs is based on a first order upwind differencing [35], which distinguishes between forward and backward transport. The prime concern here is the stability of the solution. To obtain stability, the spatial integration step Δz has to fulfill the Courant condition [35]

$$\max(|v_s|)\Delta t \leq \Delta z \tag{4.29}$$

where Δt is the time step. The equality in eq. 4.29 is adopted to maximize numerical accuracy, while $\max(|v_s|)$ is the highest absolute value of the surface speed v_s. The definition of a time step (typically $1\,\text{ms}$) specifies in this way the spatial integration step and as such the partition of the subsurface region of a target surface cell in subsurface cells.

The target part of the steady-state model is numerical solved with the aid of C routines of the GNU Scientific Library v1.15 or 1.16 (GSL) [39]. The determination of θ_b^i (see Fig. 4.9) numerically translates into root finding problems. For this an own implemented Newton method is combined with a Brent-Dekker method from the GSL. The decoupled $2N$ ODEs describing the steady state condition of the subsurface region of the N target surface cells are solved with an explicit 4^{th} order embedded Runge-Kutta-Fehlberg method with a 5^{th} order error estimator of the GSL. This error estimation allows the use of an adaptive step control.

4.4 RSD2013 examples

The RSD2013 software is used to illustrate the impact of the most important model choices on the simulation outcome. The reactive magnetron sputtering system which is modeled consists out of a circular, planar Al target in an Ar/O_2 atmosphere. The aluminum target is a $2\,\text{inch}$ diameter disk, partially covered by a conic anode shield. This setup reduces the effective sputter zone of the target to a diameter of $1.63\,\text{inch}$ ($4.13\,\text{cm}$). In total five different simulations A, B, C, D and E are formulated. The simulations differ in the used simulation options, schematically reproduced in Fig. 4.12. When moving forward in the series of simulations (e.g. from A to B), all the options of the previous simulation are kept fixed with the exception of one. By this, an increase in detail of the simulations is realized. All simulations are simulated with the time dependent formulation of the RSD2013 model.

The first simulation A describes the target and the substrate in a one-cell approach excluding any redeposition effect or a saturation limit of the subsurface.

Time model	A,B,C, D,E		Steady state model
Deposition profile	C,D,E	A,B	Uniform deposition
Redeposition	D,E	A,B,C	No redeposition
Current profile	B,C,D, E	A	Uniform current
Saturation limit	E	A,B,C, D	No saturation limit

Figure 4.12: *Schematic representation of the most essential simulation options in RSD2013. The five simulation configurations of the system are indicated by the letters A, B, C, D and E. The scheme defines the used simulation options for each simulation.*

The second simulation B contrasts with the first one by describing the target in a multicell approach. The sputter zone of the target is here modelled by 100 equidistant, concentric target cells, exploiting the axial symmetry of the circular magnetron. As such the area of these target cells scale as $\pi\Delta r^2(2i-1)$ where Δr $(0.02\,\mathrm{cm})$ represent the width of a concentric cell and $i = 1 \ldots 100$, the cell index counted from the center to the edge of the target. The associated radial current profile is assumed to be Gaussian with a mean of $1.03\,\mathrm{cm}$ and a deviation of $0.28\,\mathrm{cm}$ which fairly agrees with a realistic erosion profile obtained in non-reactive operation.

For the third simulation C, the substrate is also modeled in a multi-cell approach. This modeling approach was already briefly discussed in chapter 3. The substrate geometry is similar to in section 3.3.1. The target is inserted at the top of a cylindrical container which acts as the substrate of the system. This container fully encloses the sputtering side of the target. The cylinder has a diameter of $25\,\mathrm{cm}$ and a height of $51\,\mathrm{cm}$. The substrate cells are defined to have an area of $2\,\mathrm{cm}^2$ for the cylinder mantle and $1\,\mathrm{cm}^2$ for the top and the bottom of the cylinder, as for the anode shield. The deposition fractions ε_s of the substrate cells were obtained with SiMTra [24, 25]. These transport simulations were performed in an Ar atmosphere of uniform pressure $(0.4\,\mathrm{Pa})$ and temperature $(300\,\mathrm{K})$ with Al as the transported element. An erosion profile is needed to define the starting positions of the transported particles in the racetrack. For this, the same Gaussian distribution is used as for the current profile. A SRIM [40] simulation of Ar^+ $(320\,\mathrm{eV})$ bombardment on an Al target, defines the initial emission angles and energies of the sputtered Al particles in the SiMTra simulation. The Ar^+ energy corresponds to 80% of the discharge voltage $(400\,\mathrm{V})$ [41]. The resulting deposition profiles can then readily be used as input in RSD2013.

Global parameters	Value
Y_m, Y_c, Y_r ($M[R_z]\,ion^{-1}$)	0.65, 0.052, 0.052
α_t, α_s	0.08, 0.107
k ($cm^3 s^{-1} R^{-1}$)	5.4×10^{-23}
β ($R\,ion^{-1}$)	0.2
p(x) (cm^{-1})	Gaussian profile $R_p = 1.2\,nm$, $\Delta R_p = 0.8\,nm$
n_0 ($M[R_z] cm^{-3}$)	6.03×10^{22}
$n_{0,s}$ ($M[R_z]) cm^{-3}$)	1.54×10^{15}
Δx (cm)	2.55×10^{-8}
z	1.5
I_{ion} ($ion\,s^{-1}$)	3.12×10^{18}
P_i (Pa)	0.4
T (K)	300
V (cm^3)	12500
S ($cm^3 s^{-1}$)	50000

Table 4.2: *Overview of the global simulation parameters for the reference system.*

The fourth simulation D considers the effect of redeposition. The SiMTra simulation also gives the redeposition fractions ε_t on the target cells. For the chosen working conditions, the total redeposition fraction E_t appears to be 0.04. This is rather low due to the low working pressure ($0.4\,Pa$).

The last simulation E includes a saturation limit on the reactive species in the subsurface as modelled by eq. 4.20. A smooth saturation limit is adapted with a critical concentration $n_{R,max} = 1.1 z n_0$ and a spread $\Delta n_R = 0.1 z n_0$.

Besides the local, cell-specific parameters, the sputter system is further specified by global parameters as defined in Table 4.1 and specified in Table 4.2. The reactive implantation profile $p(x)$ is assumed to be Gaussian, where its mean R_p and deviation ΔR_p are determined by a SRIM simulation of O^+ ($160\,eV$) bombardment of the target. The impingement energy of O^+ corresponds to half the energy the ion acquires in the electrical field, as it is assumed that the bombarding $O_2{}^+$ breaks up at incident and its energy is equally divided.

The remaining parameters are taken from section 3.3. It is important to mention that those fitted parameters are for an implementation of the RSD2009 model. The model specifications were a one-cell description for the target and a multi-cell description for the substrate without considering a redeposition fraction or a saturation limit.

For the five defined simulation configurations, a hysteresis experiment is simulated. The reactive oxygen flow is stepwise increased up to $4\,sccm$ and subsequently decreased to $0.5\,sccm$. The step sizes are $0.25\,sccm$ at the start, but are

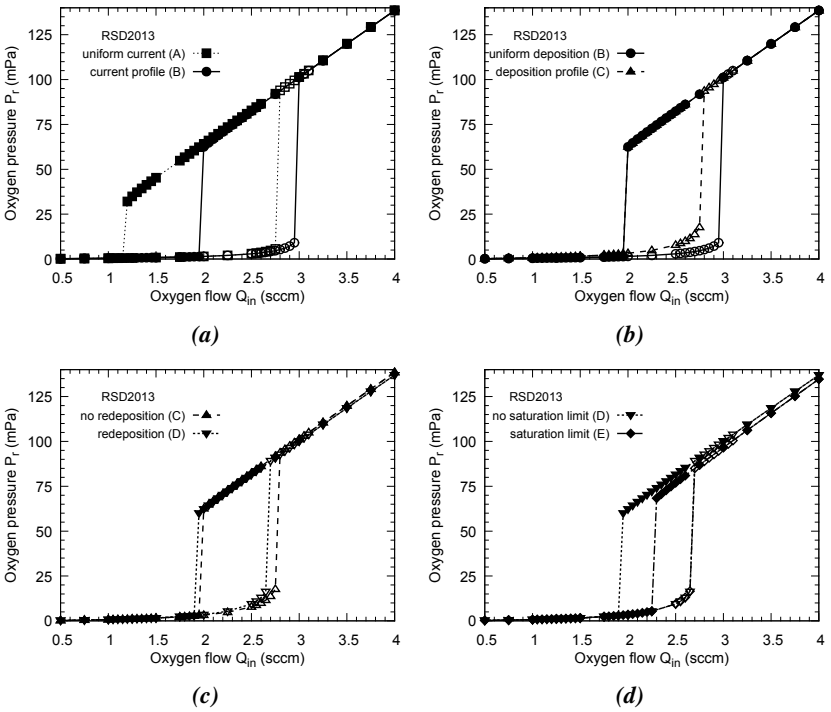

Figure 4.13: *The flow-controlled hysteresis curves of the oxygen partial pressure for the five simulation configurations of Fig. 4.12 with the simulation parameters in Table 4.2. The open markers represent the variation by an increase in oxygen flow, while the solid markers represent the variation by a decrease in oxygen flow.*

reduced to $0.05\,\mathrm{sccm}$ in the regions around the critical points. The maximum time between every step was $120\,\mathrm{s}$. This time interval was long enough to evolve the system into a steady state. The five simulated reactive pressure hystereses are shown in Fig. 4.13. A clear impact of the modified simulation options on the positions of the two critical points is observed, with the biggest change in the second critical point. In the following sections, some interesting differences between the successive simulations are elucidated.

4.4.1 Target

For the first simulation A, the target and substrate are described in a one-cell approach excluding redeposition on the target or a saturation limit in the targets subsurface. The simulation B differs in the description of the target where a multi-cell approach is applied with a corresponding Gaussian current profile. Figure 4.14

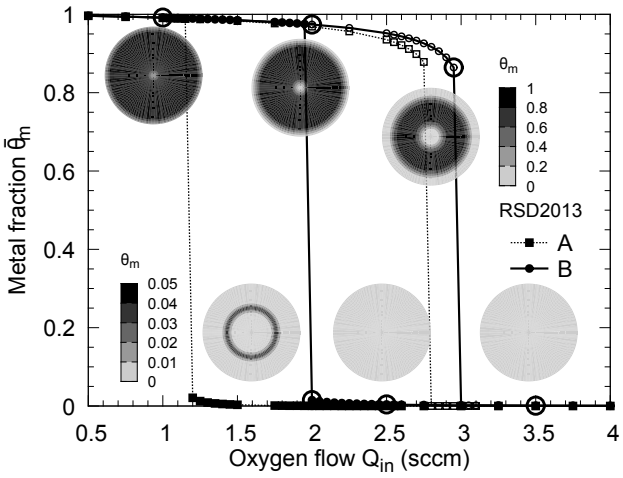

Figure 4.14: *The flow-controlled hystereses of the current-weighted average metal fraction on the target for the simulation A (one-cell description of the target) and B (multi-cell description of the target). The spatially resolved target profiles of the simulation B are shown at the indicated points (○). The open markers represent the variation by an increase in oxygen flow, while the solid markers represent the variation by a decrease in oxygen flow.*

shows the target surface state, characterized by the current-weighted average metal fraction (eq. 4.8), as a function of the reactive flow. The same hysteresis phenomena pops up as for the reactive partial pressure. This hysteresis of the target state can be directly linked to a hysteresis in the discharge voltage of the system. The variation in the discharge voltage at fixed current during a hysteresis experiment is for the most part determined by the changing effective secondary electron yield of the target surface [42]. The shift of the first and second critical point to higher reactive flows in simulation B can be understood from the applied non-uniform current profile. This current profile results in a gradual oxidation of the target surface as illustrated by the six insets in Fig. 4.14. They show the non-reacted metal fractions across the target. Be aware that a perfect axial symmetry of the target is imposed.

When increasing the reactive flow, the target zones with the lowest current density will be the first which fully oxidize. These zones are the center and the edges of the target. The zone with a higher current density, namely the inner racetrack ring, is kept longer in the metallic state due to the higher sputter cleaning of the surface. For the same reason, on the return from the poisoned regime to the metal regime, the center of the racetrack will more quickly transform back into the metallic state. This non-uniform oxidation of the target keeps the system longer in the metal regime due to a longer lasting source of non-reacted metal in the

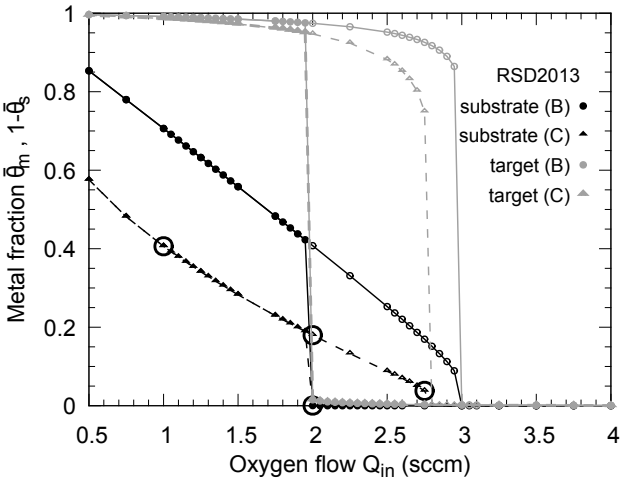

Figure 4.15: *The flow-controlled hystereses of the average metal fraction on the target (gray color) and the substrate (black color) for the simulations B (one-cell description of the substrate) and C (multi-cell description of the substrate). The additional markers (○) refer to the substrate configurations shown in Fig. 4.16. The open markers represent the variation by increasing the oxygen flow, while the solid markers represent the variation by decreasing the oxygen flow.*

center of the racetrack, explaining the shift of the first critical point towards higher oxygen flows. As the sputter rate in the center of the racetrack will be higher than the average, this zone will be more easily transformed back into a source of metal particles, explaining the shift of the second critical point to a higher oxygen flow. Further, notice that the change of the target state for the second critical point is much more abrupt than for the first critical point, i.e. for the first critical point some significant oxide is seen before the transition to the poisoned regime. This effect seems to be irrespective of applying a current profile or not. However, the average metal fraction at the critical points for the simulation A and B are comparable. As this fraction quantifies the amount of sputtered metal, the system does avalanche into metallic (poisoned) mode at the same deposition fluxes. This indicates that these transitions are driven by the capacity of the substrate to (un)successfully getter most of the reactive gas.

4.4.2 Substrate

Simulation C differs from simulation B by the addition of a simulated SiMTrA deposition profile on the substrates. So in the simulation the one-cell description of the substrate is replaced by a multi-cell description. When looking at the sub-

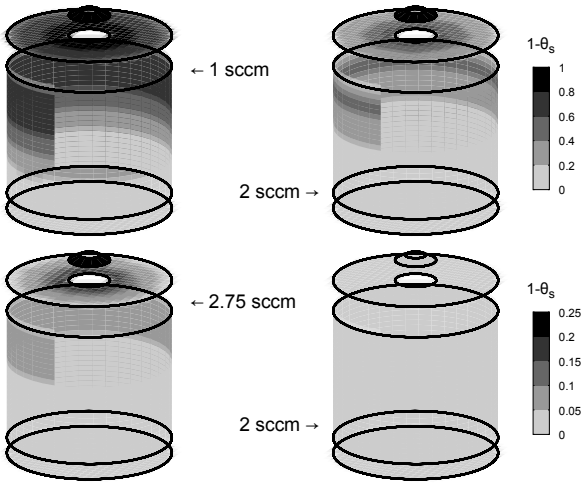

Figure 4.16: *The substrate profiles of the metal fraction for the simulation C. The bottom-right substrate configuration in the figure gives the state just before the second critical point at* $2\,\mathrm{sccm}$*, while the three other substrate configurations give the state in the metal regime (*$1\,\mathrm{sccm}$ *and* $2\,\mathrm{sccm}$*) and just before the first critical point (*$2.75\,\mathrm{sccm}$*).*

strate state, characterized by the average non-reacted metal fraction, the hysteresis behavior is also observed but appears to be less abrupt in comparison with the target state. Both average variations of the substrate and target state are shown in Fig. 4.15 for simulation B and C. The average state of the spatially resolved substrate (simulation C) is systematically less metallic than the non-resolved substrate (simulation B) during the metal regime.

The non-uniformity of the deposition profile can explain this observation. The substrate areas that receive a low flux of sputtered metal particles, will already fully oxidize at very low oxygen pressures. This decreases the average metal state of the substrate. This is illustrated by Fig. 4.16, which shows the detailed substrate state in the metal regime at 1 and $2\,\mathrm{sccm}$, just before the first critical point at $2.75\,\mathrm{sccm}$ and just before the second critical point at $2\,\mathrm{sccm}$. As this reduces the substrate area which acts as an efficient gettering pump, the first critical point will be shifted to a lower value compared to the simulation B.

4.4.3 Redeposition

The effect of redeposition is included in simulation D. Besides the deposition profiles on the substrates, SiMTra also gives a deposition profile of the target, the redeposition profile. Under the chosen working conditions, the fraction of redeposited material only amounts to 4% of the total sputtered flux. Nevertheless the

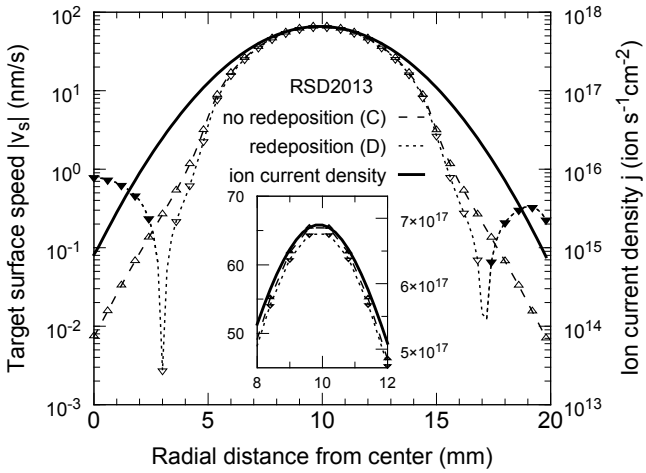

Figure 4.17: *The target surface speed profile for the simulation C (without redeposition) and D (with redeposition) just before the first critical point on a logarithmic scale. The open markers represent erosion ($v_s > 0$), while the closed markers represent growth ($v_s < 0$). For comparison, the normalized current profile is added. The inset shows the region around the maximum of the profiles on a linear scale.*

impact on the target state is considerable, while the overall effect on the hysteresis shape is small (Fig. 4.13c). As a result the substrate condition before and after the critical points is nearly equal, when comparing simulation C and D. In contrast to the previous simulations, there will be areas on the target where no net erosion takes place but the target surface grows. These zones are located at the center and edges of the target, where the sputter rate is at its lowest. Figure 4.17 compares the surface speed of the simulation C without redeposition, with the simulation D with redeposition, both just before their first critical points. For comparison, the current profile is added to the figure, which is normalized with the maximal surface speed of simulation C. Due to the redeposition, it is obvious that the surface speed of simulation D is overall lower than the surface speed of simulation C. The growth zones on the target are located in the center ($< 3\,\mathrm{mm}$) and at the edges ($> 17\,\mathrm{mm}$) which are indicated with closed markers. An additional observation for both simulation C and D is the faster decreasing erosion speed further away from the center of the racetrack compared with the current profile. This effect is due to the already mentioned non-uniform oxidation of the target. This non-uniformity is maximal just before the first critical point, the situation of Fig. 4.17. The edges and the center of the target will be more oxidized (refer to Fig. 4.14), and the lower sputter yield of the oxide results in the lower erosion speeds. The existence of growth zones causes a significant difference in the target subsurface condition.

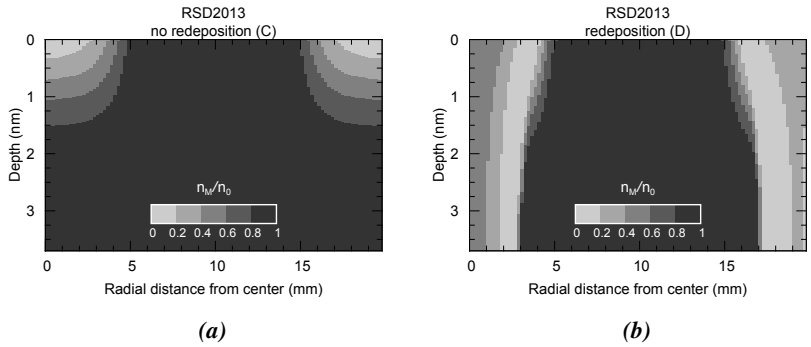

Figure 4.18: *The in-depth profiles of the non-reacted metal fraction in the implantation zone of the subsurface. Results are given for the simulation C (without redeposition) and D (with redeposition), just before their first critical points.*

The depth profiles of the non-reacted metal fraction just before their first critical point is given in Fig. 4.18 for the simulations C and D. The shown depth range of the subsurface stretches over the implantation zone. At this reactive flow, the in-depth oxide formation is primarily present at the center and the edges of the target for both simulations. While the oxide is limited to a range of $\sim 1.5\,\mathrm{nm}$ for the simulation C without redeposition, the oxide for the simulation D with redeposition extends over the whole implantation zone. This is a direct consequence of target "growth" (in contrast to "erosion") at those places. The oxide formed at the surface and subsurface is transported deeper into the target.

4.4.4 Saturation limit

While the former simulations were not limited by the reactive atom concentration in the subsurface, a saturation limit was applied for the last simulation E. This saturation limit is taken to be smooth as explained in section 4.4. The necessity of such a saturation limit is illustrated by Fig. 4.19 and Fig. 4.20, which respectively show the subsurface state just before the first and the second critical point for the simulation D and E. It compares the depth profiles of the ratios of unbounded reactive atom concentrations to the total metal density, which is a constant. These results are represented on a logarithmic scale for Fig. 4.19 while a linear scale is used for Fig. 4.20. For the simulation D without saturation limit, there are small regions where reactive concentrations take unphysical high values just before the first critical point. These regions correspond with small absolute surface speeds, around the locations where the target erosion turns into growth. The in- or outward transport of reactive atoms is here too low compared to the reactive implantation which builds up the excessively high concentrations. Nevertheless, this is a minor

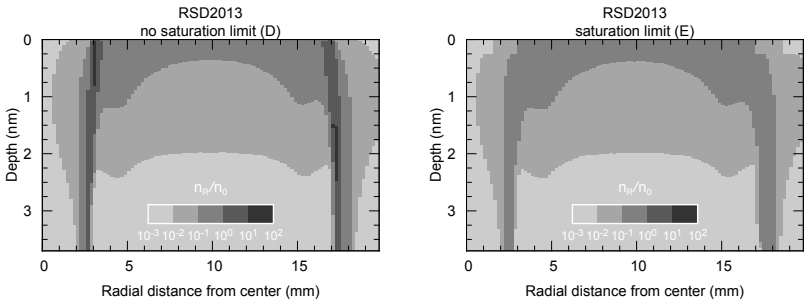

Figure 4.19: *The in-depth profiles of the unbounded reactive concentrations relative to the metal particle density on a logarithmic scale. The profile stretches over the implantation zone of the targets subsurface. Results are given for the simulations D and E, just before their first critical points.*

problem for the determination of the first critical point as the build-up of these extreme concentrations occurs only in a limited region in the metal regime. Indeed, the first critical points of simulations D and E do coincide (see Fig. 4.13d). The situation for the second critical point is different. Because of the excessive build-up of unbounded reactive atoms in the poisoned regime for simulation D (Fig. 4.20a), the subsurface oxide formation is much more enhanced. As such the return from the poisoned to the metal regime does happen at a lower reactive flow in this simulation compared to the simulation E with a saturation limit. Figure 4.20b further shows that the concentration of unbounded reactive gas just before the second critical point is the highest in the center region of the racetrack. As the current density is the highest in the racetrack center, the highest reactive implantation rate and the highest erosion rate is located there. The latter results in a shorter reaction time which in combination with the former can explain this behavior. Also note that the target surface will be the most metallic in this region which further enhances the erosion rate. Although these processes are important at target level, they have little impact on the description of the substrate condition when comparing similar points along the hysteresis.

4.5 Case study : redeposition fraction

The RSD2013 model enables to study the influence of the reactive sputter conditions on the process. A case study for the Al/O_2 DC reactive sputter system is now presented. More specifically, the Ar pressure influence through a changing redeposition fraction is investigated along a direct controlled hysteresis in oxygen flow. In section 4.2 the relevance of the redeposition fraction, i.e. the fraction of

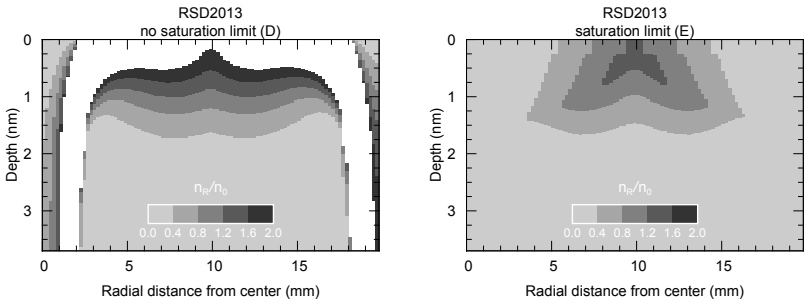

Figure 4.20: *The in-depth profiles of the unbounded reactive concentrations relative to the metal particle density on a linear scale. The white region corresponds to concentration $n_R > 2n_0$. The profile stretches over the implantation zone of the targets subsurface. Results are compared for the simulations D and E, just before their second critical points.*

sputtered material deposited back on the target, was touched on. The reference system is defined in section 4.5.1. The impact of the redeposition fraction on the hysteresis is examined in section 4.5.3. However, the focus in this study will be the change in the formed racetrack, i.e. the erosion depth profile (section 4.5.4), and the sputter profile which defines the distribution of the sputtered atoms in the vacuum chamber (section 4.5.5). Both profiles are defined by the target condition (section 4.5.2) through the sputter yield. It is for this target condition that the RSD2013 model gives a spatial description.

In view of the results the definitions of the net transport speed v_s and the erosion speed v_e are important. The net transport speed v_s (eq. 4.18) defines the receding or the progressing of the target surface, and as such the racetrack profile of the target. On the other hand, the erosion speed v_e (eq. 4.19a) quantifies the flux of sputtered material, and as such the sputter profile of the target.

4.5.1 Reference system

A reference system has been composed to simulate the behavior of a reactive magnetron sputter system with a circular, planar target. This modeled system is the same as previously defined in section 4.4. Some key aspects about the target are here repeated. The target is an Al disk with a sputter area of $41.3\,\mathrm{mm}$ in diameter. As the target is simulated in a multi-cell approach, a spatially resolved current profile has been defined. This current profile is axial symmetric and considered to have a Gaussian shape (mean $10.3\,\mathrm{mm}$ and deviation $2.8\,\mathrm{mm}$) in the radial direction. The target is partitioned in 100 concentric surface cells. These cells have a fixed radial dimension of $0.2\,\mathrm{mm}$. The redeposition fractions ε_t were simulated

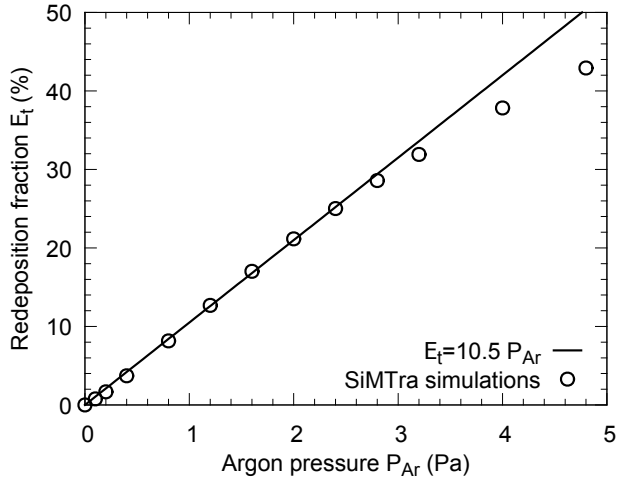

Figure 4.21: *Simulated redeposition fraction as function of the Ar pressure. A linear behavior for pressures* $< 3.2\,\mathrm{Pa}$ *is obtained.*

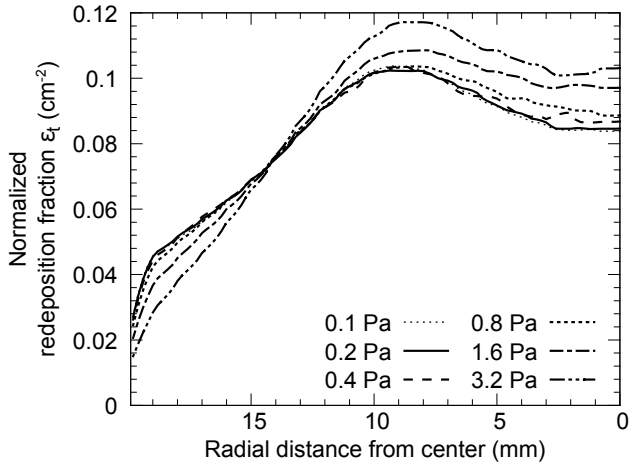

Figure 4.22: *The normalized redeposition profiles simulated with SiMTra for different Ar pressures. The shape of the redeposition profile at* $0.4\,\mathrm{Pa}$ *is used for the simulations in section 4.5.*

with the SiMTra program for a uniform Ar pressure of $0.4\,\mathrm{Pa}$ with the previously defined Gaussian current profile as starting distribution. This pressure is a typical working value during thin film deposition, and as can be seen in Fig. 4.21 the redeposition fraction will be limited (4%). This simulation fixes the distribution of the redeposited flux for all the simulations in section 4.5 where only the total redeposition fraction E_t is varied and thus not how it is distributed. As can be seen in Fig. 4.22, the weight of the distribution is shifted towards the center of the target. This is understandable from the circular geometry of the target and the axial symmetry of the racetrack with its deepest point halfway the target radius. The emission angle distribution of the sputtered particles is symmetric. Thus the probability for a sputtered particle to move in the direction of the target center or the edge is equal. Because of the smaller area for redeposition around the target center compared to the target edge, will the redeposition be more intense around the target center. Nevertheless some atoms will be able to travel from one edge to the other over the center of the target which results in a more smooth distribution at low pressure. At higher pressures the mean free path of a sputtered particle will become smaller, meaning that it is harder to escape from its original sputter location. This results in a stronger non-uniformity.

A further remark is that by taking a single, fixed redeposition profile for each hysteresis, another dependency is left out. As the composition of the target surface changes along the hysteresis, the emission profiles of the reacted and non-reacted particles will also change. The RSD2013 model currently does not include this dependency, but a small influence is expected as in the presented simulations, the transition region is not accessed. In metallic mode, compound is preferentially formed at the racetrack edges, and due to the low current density, it will in a minor way contribute to the overall deposition profile. Toward the second critical point, the target oxidation is quite uniform, and hence this dependency is of minor importance. A same implantation profile is used as in section 4.4 for the oxygen reactive atoms. The oxygen implantation is limited by the saturation function with the saturation concentration $n_{R,max}$ set to $1.1zn_0$ and a spread $\Delta n_R = 0.1zn_0$.

As before, the substrate consists of an almost closed cylindrical container where the target is mounted at top of it. The target is as such fully enclosed by the cylindrical substrate. Like the target, the substrate is described by a multi-cell approach with the deposition profile obtained from the SiMTra simulation as input. Similarly to the redeposition profile, this deposition profile is fixed for all shown simulations in this section. However the total deposition fraction E_s is complementary varied with the total redeposition fraction E_t as their sum should always equal one.

4.5.2 Target condition

The change of the target condition as function of the redeposition fraction and as function of the reactive flow is investigated in this section. The hysteresis of the just discussed reference system (section 4.5.1) is simulated. Figure 4.23 compares the reference system without redeposition ($E_t = 0\%$) with the system with redeposition ($E_t = 4\%$). A typical direct controlled hysteresis is observed in both cases, where the effect of redeposition shifts the two critical points of the hysteresis to lower flow values. The insets in Fig. 4.23a and Fig. 4.23b show the fraction of non-reacted metal (= n_M/n_0) in the subsurface region just before and after each critical flow point. The depth ($3.5\,\mathrm{nm}$) of these radial cross-sections corresponds with the zone where reactive implantation is significant. In both cases the formation of the oxide ($n_M/n_0 = 0$, light gray color) is the strongest at the edges of the racetrack zone. However the oxidation profiles look significantly different. In the case without redeposition the oxide skin thickness decreases from the edges toward the center of the racetrack, while a different behavior is observed when including redeposition.

Firstly, when distinguishing between the target operating in metal mode (bottom insets of Fig. 4.23b) and in poisoned mode (top insets of Fig. 4.23b), a stoichiometric oxide skin in poisoned mode spans the whole implantation zone at the edges, in contrary to a substoichiometric oxide skin in metal mode. Nevertheless the formed oxide penetrates in both these modes much deeper into the target at these edges than in the non-redeposition case. Secondly, the locations, where full in-depth oxidation occurs first as function of the oxygen flow, are located at radial positions $\sim 2\,\mathrm{mm}$ and $\sim 18\,\mathrm{mm}$ for the redeposition case. This is clearly seen just before the first and just after the second critical point (bottom insets on Fig. 4.23b).

Figure 4.24a and Fig. 4.24b can help explain these two observations. The subsurface states of the target just before the first critical point of respectively the non-redeposition (Fig. 4.24a) and the redeposition (Fig. 4.24b) case are shown, together with the surface speed v_s. The differences in the oxidation profile can be traced back to the locations where effective growth occurs. When still operating in metal mode, the substoichiometric edges are enriched with redeposited metal, sputtered from the center of the racetrack. This protects the edges of a complete oxidation together with the low implantation rate of reactive species. Nevertheless, when increasing the average poisoning of the target, the edges get deeply oxidized. For this the redeposition of mainly oxidized particles and the transport of oxide into the subsurface are responsible. The radial positions $\sim 2\,\mathrm{mm}$ and $\sim 18\,\mathrm{mm}$, where full in-depth oxidation occurs first as function of the oxygen flow, correspond to locations where the growth speed is extremely low. Nevertheless the reactive implantation rate ($\sim$ current) is still substantial. Here, the slow growth speed compared to the reaction rate of implanted species causes the full oxidation of the implantation zone.

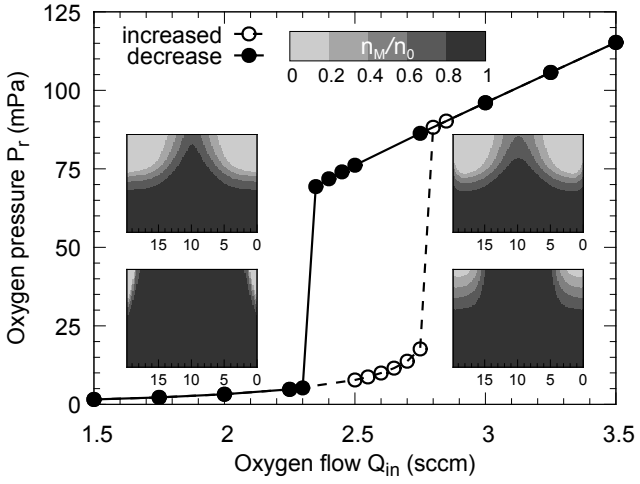

(a)

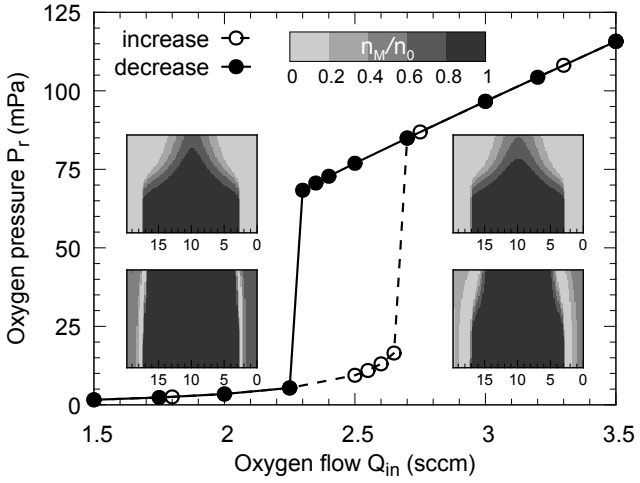

(b)

Figure 4.23: *Simulated direct flow controlled hysteresis of the reference system excluding redeposition ($E_t = 0\%$) (a) and including redeposition ($E_t = 4\%$) (b). The insets in (a) and (b) show the steady state non-reacted metal fraction in the implantation zone of the target, just before and after each critical point. The light gray color corresponds with oxide while the darker gray colors indicate more metal. The width of the inset corresponds to half the target, i.e.* $20.7\,\mathrm{mm}$*, while the height is equal to* $3.5\,\mathrm{nm}$*.*

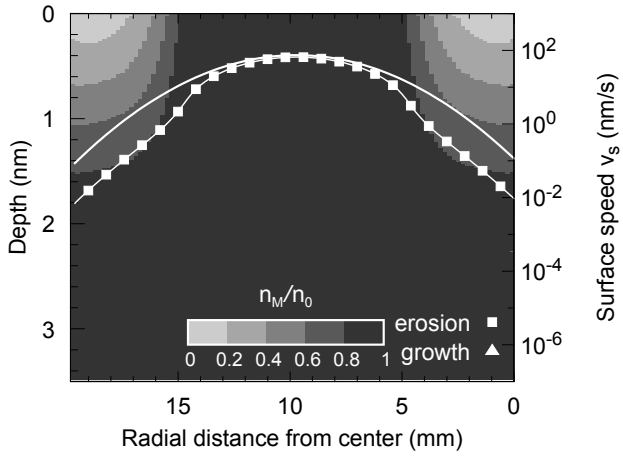

(a)

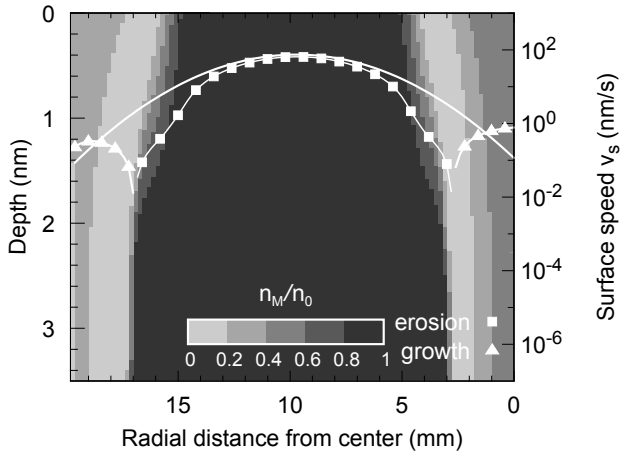

(b)

Figure 4.24: *A detailed view of the target state just before the first critical point, excluding redeposition (a) and including redeposition (b), with the steady state surface speed profile (log scale) which distinguishes between netto erosion (square markers) or growth (triangle markers). As reference, the ion current profile is included (white line without markers).*

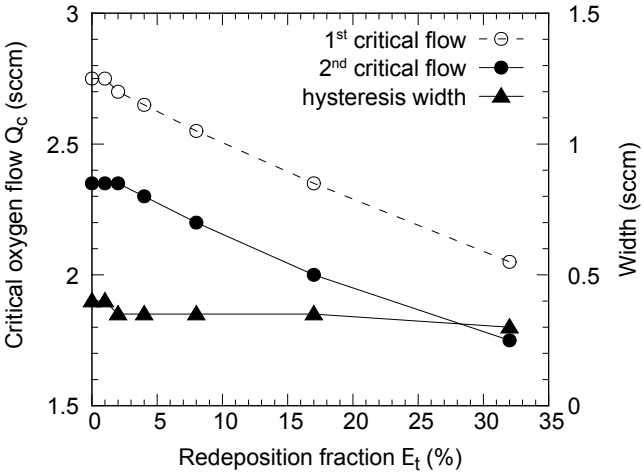

Figure 4.25: *The critical oxygen flows and the hysteresis width of direct flow controlled hysteresis curves as function of the redeposition fraction. The critical points shift to lower flow values, while the hysteresis width remains almost constant.*

4.5.3 Hysteresis

The hysteresis as function of the redeposition fraction is examined. The redeposition fraction in a reactive sputter system is varied by changing the Ar pressure. Indeed, SiMTra simulations showed a linear relationship between the redeposition fraction and the operating pressure for pressures below $3.2\,\mathrm{Pa}$ (Fig. 4.21). Given this linearity and the fact that the operating pressure is in practice an easily controllable parameter, why not just use this parameter? Changing the operating pressure would not only result in a changing redeposition fraction, but also modifies the (re)deposition profile on the target and on the substrate, the discharge voltage [43, 44], the discharge current profile [45] and the reactive mole fraction. The benefit of a model is that a direct correlation between the redeposition fraction and the observed trends can be investigated. The other influences that an increased Ar pressure brings along can as such gradually be investigated. In this way the variation in the redeposition fraction originates from SiMTra simulations by subsequently doubling (halving) the Ar pressure.

The influence of the redeposition fraction on the hysteresis curve is shown in Fig. 4.25. Both critical points are shifted toward lower oxygen flows when increasing the redeposition fraction while the hysteresis width hardly changes. The shift at the lowest redeposition fractions ($E_t < 4\%$) falls within the resolution ($0.05\,\mathrm{sccm}$) of the simulation. This behavior can be understood from the redeposition fraction. For the first critical point where the system moves from the metal regime into the poisoned regime, the reduction in deposited metal causes

the shift. As the redeposition fraction increases, less material gets deposited onto the substrate surfaces. This material flux is mainly metallic in the metal regime. When reducing it, the gettering capacity of the substrate is decreased. As such the reactive gas flow to fully oxidize the substrate will be lower, which ignites the transition to the poisoned regime.

The shift of the second critical point where the system moves back from the poisoned regime to the metal regime can be understood as follows. In poisoned mode, the redeposited material flux is mainly composed of oxide particles. As the redeposition fraction increases, more of these oxide particles are returning to the target. This effect keeps the target in an oxidized state. As a consequence the reactive gas flow, at which the target operates again in metal regime, will have to be subsequently lower.

The width of the hysteresis hardly changes as function of the redeposition fraction (Fig. 4.25). This indicates that the observed disappearing of the hysteresis as a function of the Ar pressure studied in section 3.1.1.2 can not be explained due to an increased redeposition fraction. This further sustains the statement that reactive ion implantation should be considered in a reactive sputtering model.

4.5.4 Racetrack profile

The shape of the racetrack during reactive sputtering is defined by the spatial target condition as this determines the local erosion speed, and by the redeposition profile as this reduces or even locally surpasses the target erosion. Figure 4.26 shows the racetrack profile for three different target conditions (metallic mode, first critical flow and poisoned mode) and for a relatively low ($E_t = 4\%$) and high ($E_t = 17\%$) redeposition fraction. The reactive sputter time was such that a similar erosion depth below the original target surface was obtained for each simulation. The racetrack profiles clearly differ under these different operation conditions. At the low redeposition fraction $E_t = 4\%$, the racetrack seems to become more narrow when moving from metallic into poisoned mode. At the high redeposition fraction $E_t = 17\%$, a similar behavior is noted but the shape at the first critical point is less smooth, and the asymmetry of the profile is increased.

To study in detail the shape dependency of the racetrack profiles for long time sputtering, the procedure goes as follows. The racetrack profile in steady state will be defined by the surface speed profile v_s (eq. 4.18). When sputtering a fresh target under the same conditions, these two profiles are identical after normalization. Therefore, referring to the surface speed profile is the same as referring to the racetrack profile. The normalization is performed such that the full integration of the profile is one, after shifting the profiles minimum to zero. In non-reactive operation excluding redeposition, the normalized ion current profile corresponds to the racetrack profile. During reactive operation the oxidation grade of the tar-

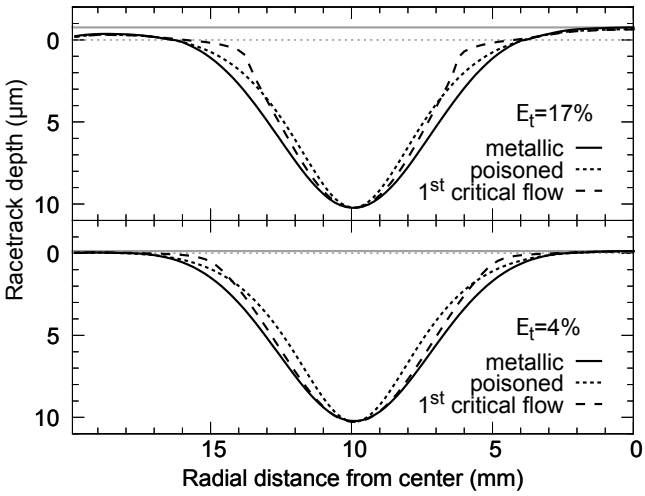

Figure 4.26: *Comparison of the formed racetrack shapes after reactive sputtering at the first critical oxygen flow Q_c, in metallic mode $(Q_c - 1\,\mathrm{sccm})$ and in poisoned mode $(Q_c + 1\,\mathrm{sccm})$. The sputtering times were set as such that the same depth was obtained. The top figure shows the case with a redeposition fraction $E_t = 17\%$ with $Q_c = 2.35\,\mathrm{sccm}$. An equal depth of $10\,\mu\mathrm{m}$ was reached after $149\,\mathrm{s}$ for the metallic mode, after $179\,\mathrm{s}$ for the first critical point and after $1102\,\mathrm{s}$ for the poisoned mode. The bottom figure shows the case $E_t = 4\%$ with $Q_c = 2.65\,\mathrm{sccm}$ after respectively a time of $139\,\mathrm{s}$ for metallic mode, $154\,\mathrm{s}$ for the first critical point and $978\,\mathrm{s}$ for the poisoned mode. The dotted horizontal gray line presents the original target surface before sputtering, while the solid gray horizontal is the highest surface level after sputtering in metallic mode.*

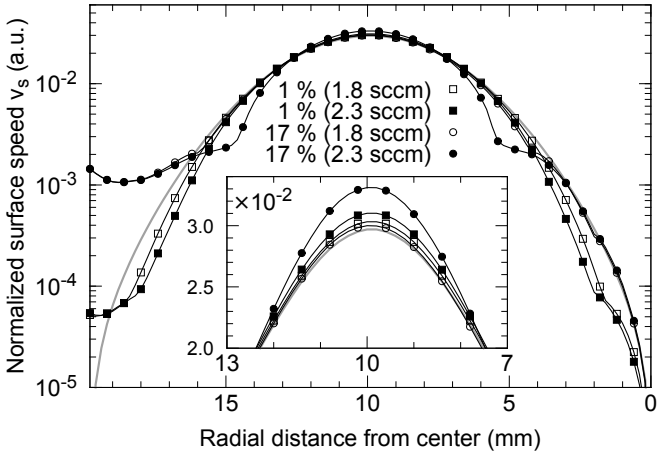

Figure 4.27: *Comparison of the normalized surface speed profiles on a log scale for a low redeposition ($E_t = 1\%$, square markers) and for a high redeposition ($E_t = 17\%$, circle markers) case at low ($1.8\,\mathrm{sccm}$, open markers) and high ($2.3\,\mathrm{sccm}$, solid markers) oxygen flow in the metal regime. The inset shows the maximum of the profiles on a linear scale. The profile normalization includes a shift such that the profile minimum becomes zero. This is equivalent with the shift in Fig. 4.26 of the dotted horizontal toward the solid horizontal, as shown for the metallic mode case.*

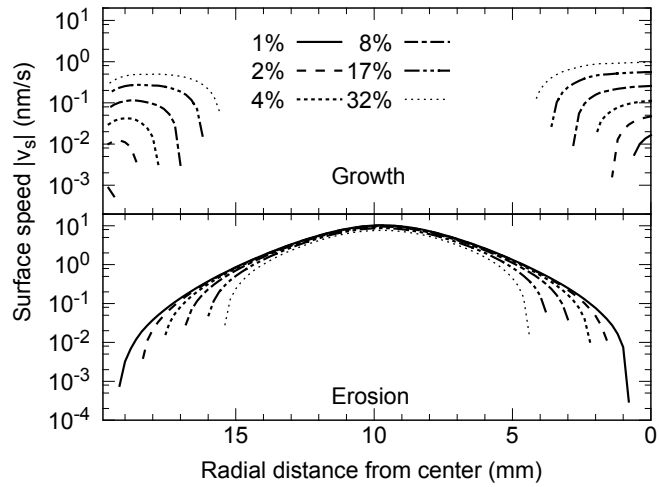

Figure 4.28: *Erosion (bottom graph) and growth (top graph) speeds across the radius of the target as function of the redeposition fraction in the poisoned regime ($4\,\mathrm{sccm}$).*

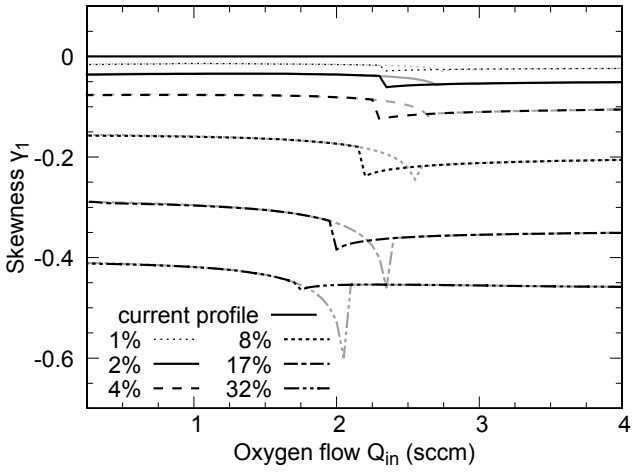

Figure 4.29: *Skewness of the racetrack profiles as function of the redeposition fraction along the hysteresis curve. Gray lines indicate increasing oxygen flow, while black lines indicate decreasing oxygen flow.*

get surface will, depending on the reactive gas flow, be non-uniform. Therefore a changing racetrack profile as function of the reactive gas flow is expected. Including redeposition will also modify the racetrack profile. The high asymmetry of the redeposition profile induces an asymmetric [1] racetrack profile on the one hand, while an increasing redeposition fraction narrows the effective erosion zone. The increased asymmetry of the racetrack profile from low ($E_t = 1\%$) towards high redeposition ($E_t = 17\%$) is shown on Fig. 4.27. The surface speed profile is shown for two different flows, situated in the metal regime ($1.8\,\mathrm{sccm}$ and $2.3\,\mathrm{sccm}$). The (Gaussian) ion current profile is used as reference profile (gray line) which is in the same way normalized as the surface speed profiles. A narrowing of the profile with increased redeposition fraction is noted for the higher oxygen flow in Fig. 4.27. The narrowing of the effective erosion zone with increasing redeposition fraction is given by Fig. 4.28. It shows the surface speeds for the different redeposition fractions at a flow ($4\,\mathrm{sccm}$) for which all systems operate in poisoned mode. Besides this increased narrowing, the growth at the edges also increases.

To quantify the asymmetry of these racetrack profiles as function of the reactive flow and of the redeposition fraction, the skewness of the profiles is calculated. The skewness γ_1 of a racetrack profile is defined as

$$\gamma_1 = \frac{\mu_3}{\sigma^3} \tag{4.30}$$

[1] Notwithstanding the description of the circular target is here assumed fully axial symmetric, the mentioned asymmetry is with respect to the radial racetrack center. Symmetry would mean that this center acts as a reflection point.

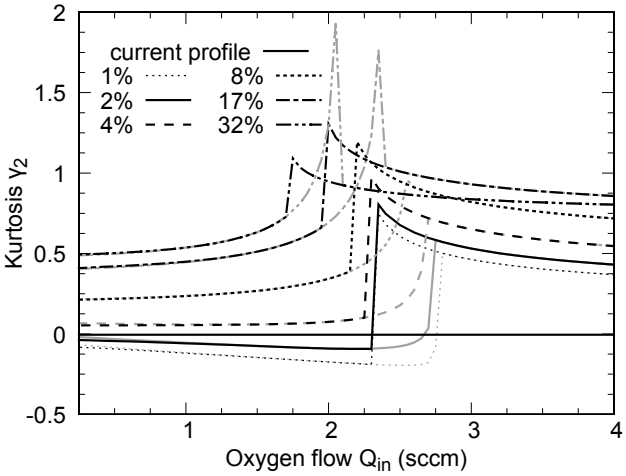

Figure 4.30: *Kurtosis of the racetrack profiles as function of the redeposition fraction along the hysteresis curve. Gray lines indicate increasing oxygen flow, while black lines indicate decreasing oxygen flow.*

where μ_3 is the third central moment and σ is the standard deviation of the profile. A negative skewness means that the mass of the profile is more concentrated toward the edge of the target. A positive skewness would mean a mass shift more toward the center of the target. To illustrate, the skewness in Fig. 4.26 for the case of low redeposition ($E_t = 1\%$) is -0.015 (1.8 sccm) and -0.018 (2.3 sccm), while -0.317 (1.8 sccm) and -0.400 (2.3 sccm) for the case of high redeposition ($E_t = 17\%$). As a reference, the expected skewness of the Gaussian ion current profile should be zero, while the calculated skewness equals 0.00023. Figure 4.29 summarizes the results. Indeed, a higher skewness is observed when increasing the redeposition fraction. The skewness also increases as function of the reactive flow toward the first critical point. This effect is stronger for a higher redeposition fraction. The same behavior is observed when moving to the second critical point, although this effect seems less pronounced with increasing redeposition fraction.

A further descriptor of the racetrack profiles is the excess kurtosis. The excess kurtosis γ_2 of a profile is defined as

$$\gamma_2 = \frac{\mu_4}{\sigma^4} - 3 \tag{4.31}$$

where μ_4 is the fourth central moment and σ is the standard deviation of the profile. The kurtosis can be interpreted as a quantifier of the peakedness of the profile and as a weight for the tails. Higher peaks and heavier tails result in a higher kurtosis. To illustrate, the kurtosis in Fig. 4.26 for the case of low redeposition ($E_t = 1\%$) is -0.16 (1.8 sccm) and -0.19 (2.3 sccm), while 0.59 (1.8 sccm) and

1.23 (2.3 sccm) for the case of high redeposition ($E_t = 17\%$). As a reference, the expected kurtosis of the Gaussian ion current profile should be zero, while the calculated kurtosis equals -0.0045.

Figure 4.30 presents the kurtosis as function of the redeposition fraction and of the oxygen flow. The increased kurtosis with increasing redeposition fraction can be attributed to the heavier tails of the high redeposition profiles. The comparison in Fig. 4.27 between low and high redeposition fraction for both flows supports this conclusion. The left tail of the high redeposition profile is heavier compared to the Gaussian current profile. The right tail of the high redeposition profiles grossly matches the Gaussian, while the right tail of the low redeposition profiles are lighter. The small negative kurtosis for the low redeposition profiles and its slight decrease with the oxygen flow can also be explained in terms of the profile tails. The smaller tails of these profiles ($E_t = 1 - 2\%$), compared to the Gaussian profile, result in negative values. The further diminishing of these tails with increasing flow slightly decreases the kurtosis. The diminishing of the tails for the profiles with a higher redeposition fraction ($E_t = 4 - 32\%$) is small or non-existing. Here the shoulders of the profile decreases, which is attributed to its peakedness. Nevertheless the peak of all profiles does grow with increasing flow before the first critical point. This effect is stronger in the case of a higher redeposition fraction as it reaches its first critical point at a lower flow. This is also illustrated by the inset in Fig. 4.27.

Finally, the non-return to the original kurtosis (Fig. 4.30), and in a lower degree to the original skewness, (Fig. 4.29) after the transition to poisoned mode indicates that the target surface is not yet fully oxidized. A fully oxidized target would have the same racetrack shape as a pure metallic target, as the deviations in the surface speed profile originate from the non uniform state of the target surface. If the surface state of the target at very low oxygen flow (Fig. 4.31a) is compared with the surface state at high oxygen flow (Fig. 4.31b), it is seen that in both cases the state is non uniform. However the stronger this non uniformity occurs near the racetrack center, the larger its impact on the racetrack shape. This is because of the scaling with the Gaussian current profile which is maximum in the racetrack center. As for the metallic case (Fig. 4.31a) the uniformity around the racetrack center is much better approached then in the poisoned case (Fig. 4.31b), the racetrack shape can not be similar. Further more this indicates that the racetrack center, even in full poisoned mode, retains a certain substoichiometry.

4.5.5 Sputter profile

What the (re)deposition profile looks like is partially determined by the sputter profile. The shape of the sputter profile is similar to the shape of the erosion speed profile v_e (eq. 4.19a) after normalization. Its deviation from the Gaussian current

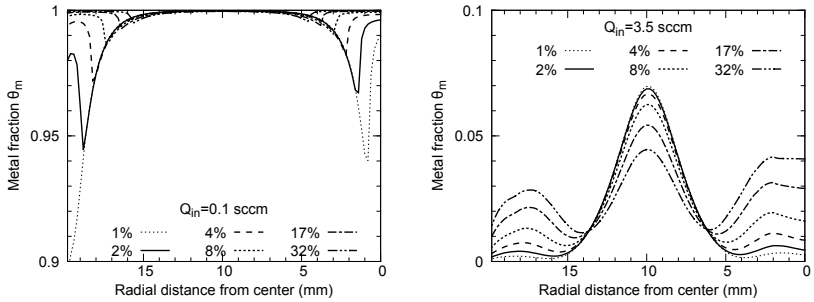

Figure 4.31: *The state of the target surface in (a) metallic mode and in (b) poisoned mode for different redeposition fractions.*

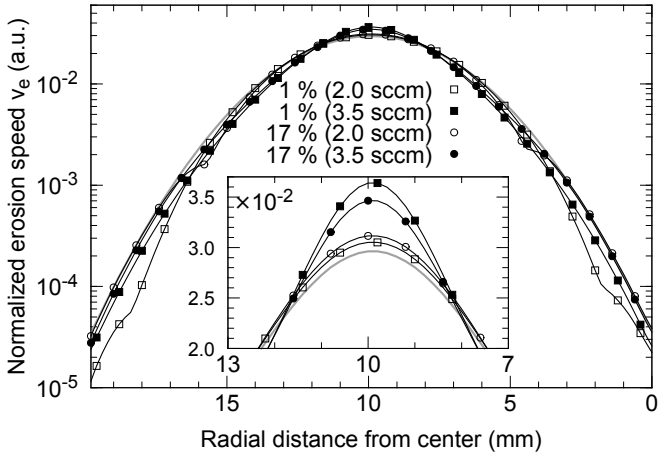

Figure 4.32: *Comparison of the normalized sputter profiles for a low redeposition ($E_t = 1\%$, square marker) and for a high redeposition ($E_t = 17\%$, circle marker) case in the metal regime ($2\,\mathrm{sccm}$, open markers) and in the poisoned regime ($3.5\,\mathrm{sccm}$, solid markers). The inset shows the maximum of the profiles on a linear scale.*

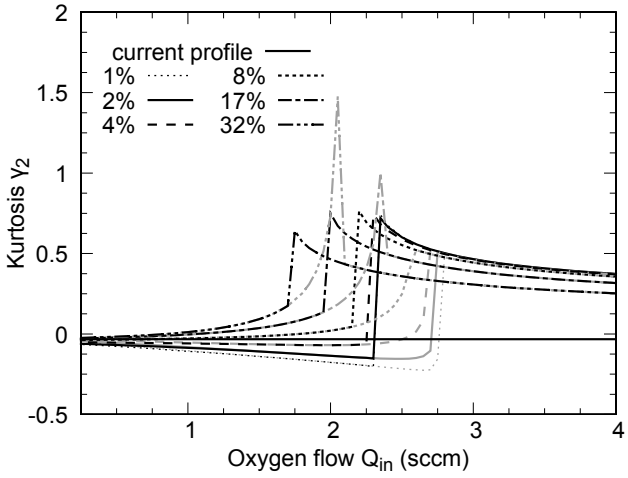

Figure 4.33: *Kurtosis of the sputter profiles as function of the redeposition fraction along the hysteresis curve. The gray lines represent an increasing flow, while black lines a decreasing flow.*

profile is only determined by the average sputter yield Y_{av} (eq. 4.9). This average sputter yield only depends on the metal fraction θ_m, as the sputter yields Y_c and Y_r respectively of the chemisorbed and the compound fraction are taken the same.

When applying the same profile descriptors, namely the skewness and the excess kurtosis, as with the racetrack profiles, some important differences are noted. As the asymmetry of the sputter profiles is small (Fig. 4.32), the same conclusion can be drawn for the skewness. This small skewness remains in all circumstances positive and reaches its maximum (~ 0.012) at the first critical point. This positive skewness corresponds to a weight shift of the profile to the center of the target. This commensurates with the (much larger) positive skewness of the redeposition profile. From this, it turns out that redeposition slightly increases the metal fraction on the target.

The evolution of the excess kurtosis as function of the redeposition fraction and along the hysteresis curve is shown in Fig. 4.33. The kurtosis for the different redeposition fractions all converge to zero, when the system approaches the non-reactive mode ($0\,\mathrm{sccm}$). This is expected as the state of the target surface in non-reactive mode will be uniform, and the sputter profile will equal the Gaussian current profile. The negative kurtosis at low flows ($< 1\,\mathrm{sccm}$) can be attributed to the light-weighted tails compared to the Gaussian, as in the case of the racetrack profiles. The higher kurtosis for increasing redeposition fraction before the first critical point is also due to the increasing weight of the tails. Higher redeposition keeps the tails more heavy as they are enriched with more metal compared to

low redeposition where they oxidize faster. This is also supported by Fig. 4.32, when comparing the low and high redeposition situation for the low oxygen flow (2 sccm). In the poisoned regime, the kurtosis increases as the redeposition fraction decreases. As the weight of the tails become comparable between low and high redeposition, this trend can be assigned to the increasing peakedness for lower redeposition. Figure 4.32 illustrates this finding by comparing a low and high redeposition situation for a flow (3.5 sccm) in the poisoned regime. The non-uniformity of the target surface state in full poisoned regime (Fig. 4.31b) results, similar as for the racetrack profiles, in a non-return to the original zero kurtosis of a fresh target.

4.6 Summary

The RSD2009 model is critically reviewed and enhanced to the new RSD2013 model. It is a step forward in the direction of a genuine model of the process. The following processes that modify the state of the target are modelled: the chemisorption of reactive gas, the direct and knock-on implantation of reactive atoms, the subsurface compound formation and the transport of target material due to erosion or growth. The most important enhancement is how redeposition is integrated within the model. The combination of RSD2013 with the Monte-Carlo transport code SiMTra results in a great tool to investigate the impact of redeposition on reactive sputtering.

The redeposition probability of a sputtered particle is studied with SiMTra simulations by varying the metal, the sputtering gas, the target-substrate distance, the angular sputtering distribution and the gas density. Once the metal-gas combination is chosen, the largest impact on the redeposition probability originates from the gas density. Increasing the gas pressure or decreasing the gas temperature can result in substantial more redeposition, especially if the gas-metal mass ratio is high. During reactive sputtering, this redeposition will impact the poisoning behavior of the target and as such influence the hysteresis, the racetrack shape and the sputtering profile.

The RSD2013 model is derived including a redeposition mechanism. The model is implemented in a user-friendly, publicly available C++ software package equally called RSD2013. The Graphical User Interface (GUI) and a provided manual allow third party users exploit the benefits of the model. The model is modularly implemented to allow switching on and off different subprocesses or, spatial and temporal details. This modularity is illustrated with a series of simulation examples where an increasing degree of detail of the modeled system is realized. Their individual impact on the hysteresis, the target condition and/or the substrate condition are presented and shortly discussed. These comparisons show the impact of the model features on the simulated results and the output power of

RSD2013.

A more detailed case study about the effect of the redeposition fraction on the reactive sputtering system for an aluminum/oxygen system is performed. The RSD2013 model shows that increasing the redeposition fraction shifts the critical points of the hysteresis toward lower reactive flows. Including redeposition clearly changes the evolution of the in-depth oxidation of the target. The cause of this, is the existence of growth zones on the target edges and center. The size of these growth zones increases with increasing redeposition fraction. The racetrack and sputter profiles are calculated as function of the redeposition fraction and of the reactive flow. The changing shapes of racetrack and sputter profile are interesting as they respectively determine how the target erosion groove is formed and how the deposition profile will look like. By making use of the shape parameters skewness and kurtosis, a quantitative analysis of these profile changes was possible. An absolute increase of the skewness was observed for the racetrack profiles while the skewness for the sputter profiles remained small when the redeposition fraction is increased. This indicator of asymmetry also increases when the critical reactive flows were approached. The kurtosis which was used for quantifying the peakedness and the weight of the profile tails increased with increasing redeposition fraction, which could be assigned to heavier profile tails. The kurtosis increases as function of the reactive flow toward the critical points which can be attributed to a higher peaking of the profile. For the sputter profiles, the trend of the kurtosis as function of the redeposition fraction seems to be reversed when comparing them at reactive flows in metal or in poisoned mode. In metal mode the tails are heavier for higher redeposition, while in poisoned mode the peakedness is higher for lower redeposition. These differences between the racetrack and the sputter profiles show that they cannot be considered as synonyms during reactive sputtering. This is an important difference with non-reactive sputtering.

References

[1] Heller, J. *Thin Solid Films* **7**(2), 163–176 (1973).

[2] Abe, T. and Yamashina, T. *Thin Solid Films* **30**(1), 19–27 (1975).

[3] Shinoki, F. and Itoh, A. *Journal of Applied Physics* **46**(8), 3381–3384 (1975).

[4] Castellano, R. N. *Thin Solid Films* **46**(2), 213–221 (1977).

[5] Hrbek, J. *Thin Solid Films* **42**(2), 185–191 (1977).

[6] Berg, S., Blom, H. O., Larsson, T., and Nender, C. *Journal of Vacuum Science & Technology a-Vacuum Surfaces and Films* **5**(2), 202–207 (1987).

[7] Berg, S. and Nyberg, T. *Thin Solid Films* **476**(2), 215–230 (2005).

[8] Affinito, J. and Parsons, R. R. *Journal of Vacuum Science & Technology A* **2**(3), 1275–1284 (1984).

[9] Kubart, T., Kappertz, O., Nyberg, T., and Berg, S. *Thin Solid Films* **515**(2), 421–424 (2006).

[10] Depla, D., Heirwegh, S., Mahieu, S., and De Gryse, R. *Journal of Physics D-Applied Physics* **40**(7), 1957–1965 (2007).

[11] Chen, Z. Y., Bogaerts, A., Depla, D., and Ignatova, V. *Nuclear Instruments & Methods in Physics Research Section B-Beam Interactions with Materials and Atoms* **207**(4), 415–423 (2003).

[12] Guttler, D., Abendroth, B., Grotzschel, R., Moller, W., and Depla, D. *Applied Physics Letters* **85**(25), 6134–6136 (2004).

[13] Depla, D. and De Gryse, R. *Surface & Coatings Technology* **183**(2-3), 184–189 (2004).

[14] Depla, D., Chen, Z. Y., Bogaerts, A., Ignatova, V., De Gryse, R., and Gijbels, R. *Journal of Vacuum Science & Technology A* **22**(4), 1524–1529 (2004).

[15] Depla, D. and De Gryse, R. *Surface & Coatings Technology* **183**(2-3), 190–195 (2004).

[16] Depla, D. and De Gryse, R. *Surface & Coatings Technology* **183**(2-3), 196–203 (2004).

[17] Strijckmans, K., Leroy, W. P., De Gryse, R., and Depla, D. *Surface & Coatings Technology* **206**(17), 3666–3675 (2012).

[18] Depla, D., Mahieu, S., and De Gryse, R. *Reactive Sputter Deposition*, chapter 5, 153–197. Springer Berlin Heidelberg (2008).

[19] Depla, D., Li, X. Y., Mahieu, S., Van Aeken, K., Leroy, W. P., Haemers, J., De Gryse, R., and Bogaerts, A. *Journal of Applied Physics* **107**(11), 113307 (2010).

[20] Rossnagel, S. M. *Journal of Vacuum Science & Technology a-Vacuum Surfaces and Films* **6**(6), 3049–3054 (1988).

[21] Boydens, F. *Key aspects of sputter ing illustrated by the use of multi-element powder mixtures*. PhD thesis, (2013).

[22] Segers, A., Bekaert, N., Depla, D., Eufinger, K., Haemers, J., and De Gryse, R. *45th Annual Technical Conference Proceedings*. Society of Vacuum Coaters.

[23] Li, X. Y., Depla, D., Leroy, W. P., Haemers, J., and De Gryse, R. *Journal of Physics D-Applied Physics* **41**(3), 035203 (2008).

[24] Van Aeken, K., Mahieu, S., and Depla, D. *Journal of Physics D-Applied Physics* **41**(20), 205307 (2008).

[25] Depla, D. and Leroy, W. P. *Thin Solid Films* **520**(20), 6337–6354 (2012).

[26] Chambers, A. *Modern Vacuum Physics*, chapter 5. Chapman & Hall/CRC (2005).

[27] Bogaerts, A., Bultinck, E., Kolev, I., Schwaederle, L., Van Aeken, K., Buyle, G., and Depla, D. *Journal of Physics D-Applied Physics* **42**(19), 194018 (2009).

[28] Bultinck, E. *Numerical simulation of a magnetron discharge utilized for the reactive sputter deposition of titanium nitride and oxide layers*. PhD thesis, (2009).

[29] Pekker, L. *Thin Solid Films* **312**(1-2), 341–347 (1998).

[30] Li, C., Hsieh, J. H., and Huang, W. M. *Surface & Coatings Technology* **198**(1-3), 372–378 (2005).

[31] Depla, D. and De Gryse, R. *Plasma Sources Science & Technology* **10**(4), 547–555 (2001).

[32] Depla, D., Heirwegh, S., Mahieu, S., Haemers, J., and De Gryse, R. *Journal of Applied Physics* **101**(1), 013301 (2007).

[33] Vandervorst, W., Janssens, T., Huyghebaert, C., and Berghmans, B. *Applied Surface Science* **255**(4), 1206–1214 (2008).

[34] Leroy, W. P., Mahieu, S., Persoons, R., and Depla, D. *Thin Solid Films* **518**(5), 1527–1531 (2009).

[35] Press, W. H., Teukolsky, S. A., Vetterling, W. T., and Flannery, B. P. *Numerical Recipes: The Art of Scientific Computing*. Cambridge University Press, 3rd edition, (2007).

[36] Strijckmans, K. *RSD2013*. www.draft.ugent.be. (2013).

[37] Smart, J. *wxWidgets*. www.wxwidgets.org. (1992).

[38] Depla, D. and De Gryse, R. *Journal of Vacuum Science & Technology a-Vacuum Surfaces and Films* **20**(2), 521–525 (2002).

[39] Jungman, G. and Gough, B. *GNU Scientific Library*. www.gnu.org/software/gsl. (2013).

[40] Ziegler J.F., Biersack J.P., Z. M. *SRIM - The Stopping and Range of Ions in Matter*. www.srim.org. (2012).

[41] Czekaj, D., Hollman, E. K., Volpyas, V. A., Zaitsev, A. G., Chernakova, A., and Goranchev, B. *Bulgarian Journal of Physics* **18**(1), 63–67 (1991).

[42] Depla, D., Haemers, J., and De Gryse, R. *Thin Solid Films* **515**(2), 468–471 (2006).

[43] Chang, S. A., Skolnik, M. B., and Altman, C. *Journal of Vacuum Science & Technology a-Vacuum Surfaces and Films* **4**(3), 413–416 (1986).

[44] Depla, D., Strijckmans, K., and De Gryse, R. *Surface & Coatings Technology* **258**, 1011–1015 (2014).

[45] Buyle, G., Depla, D., Eufinger, K., Haemers, J., De Gryse, R., and De Bosscher, W. *Journal of Vacuum Science & Technology A* **21**(4), 1218–1224 (2003).

5
Future models

Reactive magnetron sputtering is a mature technique for the deposition of thin films, both at laboratory and industrial level. The basics of the technique are conceptually quite simple and can be summarized in a few lines. However, behind this apparent simplicity a complex interplay between the different physical and chemical subprocesses is hidden. Most of these subprocesses are already modeled in great detail and a growing number of models become available. Each of these models typically employ specific methods suitable at very specific scales. These models range from simulations of the magnetic field and the plasma, over the particle-solid interactions to the transport of sputtered particles in the gas phase and the gas dynamics, up to models for the thin film growth. While often the quantitative strength of these models lies in the fact that they simulate their specific aspect very thoroughly, for describing the reactive sputtering as a whole it forms one of the most important drawbacks. The combination of any or all of these models to a global model for reactive sputtering is hardly feasible due to the strong difference in temporal and spatial scale. The problem originates from the huge discrepancy between the physical time scale of some processes and the simulation time needed to quantitatively describe these process. Despite the many attempts, the so-called "virtual sputtering magnetron" and especially the "virtual reactive sputtering magnetron" is therefore still far from realization. Notwithstanding the exponentially strong increase in computational power, a complete simulation of the reactive sputtering process would take too long to have a sufficiently fast feedback loop between the obtained results and their interpretation. Therefore, the link between the different models is weak and most researchers focus on a small as-

pect of the whole process using crude boundary conditions. An integrated global model for reactive sputtering would however shorten the time-to-market of thin film products, as well as save experimental time and costs. Moreover, it would give insight in the interplay between different subprocesses.

To achieve this goal, this work presented an other way of modeling. Here the development of such a global model starts with the most crude approximations but grabs at the same time as much as possible the most essential features of the reactive sputtering process. Starting from this, the RSD models which originates out of the Berg model are gradually extended. However the need to further integrate different mechanisms and effects drives the future development of the RSD model and resulted in the presented RSD2013. In a nutshell, the RSD2013 model models the reactive sputtering deposition of a stationary planar target which is DC powered. The surface state of the substrate and the in-depth state of the target is described besides the reactive pressure. The processes of chemisorption, reactive implantation (direct and knock-on), subsurface reaction, deposition and redeposition, and pumping of the reactive gas are described. The combination of RSD2013, SiMTra and a ion-solid simulation package as SRIM form already a strong tool for studying reactive sputtering deposition. Yet, the road towards a genuine RSD model is still long and interesting improvements, even to existing mechanisms, can be given. Work has been done on some of these milestones, while others are, at least for the RSD model developers, unknown territory.

A first improvement would be the formulation of an atomic RSD model compared to the present molecular model. It would mean an increase in particle species but on the other hand it opens up the way to the description of non-congruently sputtering materials. Also the mostly atomic nature of sputtering would be better described. To see it broader, a multi-species RSD model would be desirable. It not only allows to consider multiple oxidation states of the compound but also to model multiple targets with different materials. This would result in the simulation of more complex thin films. In a same way it is desirable to allow multiple reactive gases. An other improvement would be the introduction of density effects. In all RSD models the metal species are assumed to occupy the same volume irrespective if they form a compound with reactive gas atoms or not. As a consequence the reactive (gas) atoms are considered to be volumeless. In the model they do not take extra volume when implanted for example. A third improvement or concern is the spatial description of the target. The first two top layers are modeled discrete, while the subsurface is modeled in a continuous way. A more clean way would be to have a same spatial description for the entire target. This should be either discrete in monolayers or continuous. A fourth improvement could be the mixing of the species in target by ion bombardment, namely collisional mixing. In RSD2013 the knock-on of chemisorbed reactive gas is implemented which is an example of this collisional mixing. However also other species are susceptible

to this effect. To integrate this in the RSD model, the link with ion-solid models will have to be tightened. Current work by the author tries to tackle these four issues. However such kind of RSD model does not fit within the framework of the RSD2013 model. A more broader framework is used which is based on continuous transport equations provided with relaxation terms. Within this framework it is even possible to formulate a similar model as the RSD2013 model. The biggest problem on the long term for this kind of models will not be their implementation but the desparate need for more and more input parameters.

An other critical issue in modeling of reactive sputtering deposition is the compound formation at the substrate. The reaction between the reactive gas with the deposited material is described by chemisorption where a simple Langmuir model is used. Other researchers have investigated this topic using more advanced models, and experimental work by DRAFT have shown the need for more advanced modeling. The implementation of these more advanced models will enable to check the impact of the compound formation on the overall reactive process, and to investigate the need for further improvement.

A final suggestion for improvement is the introduction of a non-uniform reactive gas distribution. The distribution of the reactive gas in the vacuum chamber has an important technological impact, especially for large area coaters where the distribution of the reactive gas within the chamber must be carefully controlled with multiple gas inlet zones. However, also at laboratory scale the gas distribution is important. Deposition of fully oxidized thin films in metallic mode can be achieved by a local gas distribution, and the hysteresis behavior can be modified by a separate sputter gas injection at the target level. As the Knudsen number of a sputtering system is in the order of 0.1 to 10, rarefied gas flow conditions must be considered. Direct Simulation Monte Carlo (DMSC) seems therefore the most appropriate approach to tackle this problem. The development of a stand-alone package designed to couple to an RSD model would be interesting. Such a package could produce a meshed gas density distribution which would not only serve an RSD model from input but could also be used within a future modified SiMTra model. A feedback between this kind of DMSC model and the RSD model would be the extraction of reactive gas out of the chamber by the gettering effect of the substrate and the target.

With the RSD2013 model and software at hand, some preliminary improvements are under construction within the research group DRAFT. The first is the ability to rotate and move some substrate surfaces, while the second improvement consists out of multiple target sputtering under the assumption of no deposition of one target on the other. Plans are made to improve the deposition and redeposition description by linking the sputter position and particle type to the location where it is (re)deposited instead of using an average value. This would result in a deeper integration of SiMTra in the RSD model.

To conclude : “RSD2013 is not the end, it is just the beginning!”

Appendices

A

Solutions Berg model

The basic Berg model (see section 2.2.1) is summarized into a set of seven equations, namely

$$Q_{in} = Q_p + Q_s + Q_t \tag{A.1}$$

$$Q_p = \frac{P_r S}{k_B T} \tag{A.2}$$

$$Q_s = \alpha_s F_r (1 - \theta_s) A_s \tag{A.3}$$

$$Q_t = \alpha_t F_r (1 - \theta_t) A_t \tag{A.4}$$

$$F_r = \kappa P_r \tag{A.5}$$

$$\frac{2}{z} \alpha_t F_r A_t (1 - \theta_t) = J_{ion} A_t Y_c \theta_t \tag{A.6}$$

$$\frac{2}{z} \alpha_s F_r A_s (1 - \theta_s) + J_{ion} A_t Y_c \theta_t (1 - \theta_s) = J_{ion} A_t Y_m (1 - \theta_t) \theta_s \tag{A.7}$$

with the conversion factor κ defined as

$$\kappa = \frac{1}{\sqrt{2\pi m_r k_B T}} \tag{A.8}$$

This set equations involves nineteen possible variables. For the definition of these variables we refer to section 2.2.1. By taking eleven of them as parameters (=constant variables), the model can be solved as function of an independent twelfth variable solving the seven remaining variables.

Four solution methods are here presented, reproducing respectively the $J_{ion} - \theta_t -$, the $S - \theta_t$, the $A_s - \theta_t$ and the $A_t - \theta_t$ process curve. All solution meth-

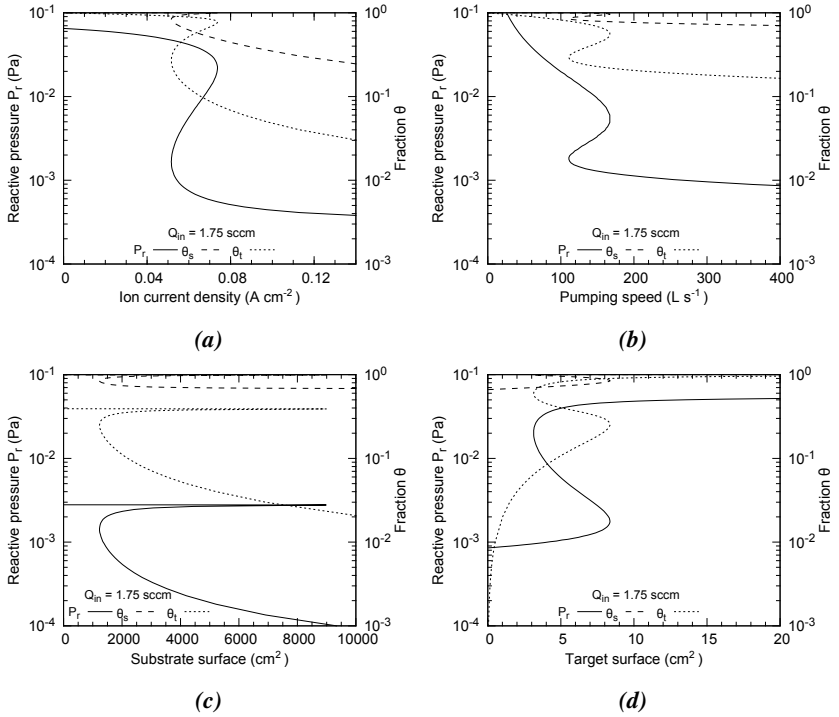

Figure A.1: *Illustration of the solution for the (a) $J_{ion} - \theta_t$ curve, (b) the $S - \theta_t$ curve, (c) the $A_s - \theta_t$ curve and (d) the $A_t - \theta_t$ curve under standard conditions (Table 2.1) for $Q_{in} = 1.75 sccm$.*

ods solve the six dependent variables Q_p, Q_s, Q_t, F_r, P_r and θ_s as function of the independent variable θ_t. The seventh dependent variable is then respectively J_{ion}, S, A_s and A_t. The remaining variables are considered each time as constant parameters.

The four solution methods are illustrated in Fig. A.1 for the "standard" system defined by Table 2.1 where $Q_{in} = 1.75\,\mathrm{sccm}$. Under these conditions, a hysteresis in the variables P_r, θ_s and θ_t as function of the chosen independent variable is obtained.

$J_{ion} - \theta_t$ curve

Solving eq. A.6 towards J_{ion} with substitution of F_r by eq. A.5 gives

$$J_{ion}(P_r, \theta_t) = \frac{\frac{2}{z}\alpha_t \kappa P_r (1 - \theta_t)}{Y_c \theta_t} \tag{A.9}$$

This sets J_{ion} as a function of the independent variable θ_t and the dependent variable P_r. An expression for the latter is obtained by substitution of eq. A.2, eq. A.4, eq. A.3 and eq. A.5 in eq. A.1, and solving towards P_r which results in

$$P_r(\theta_s, \theta_t) = \frac{Q_{in}}{\frac{S}{k_B T} + \kappa \left(\alpha_t(1-\theta_t)A_t + \alpha_s(1-\theta_s)A_s\right)} \tag{A.10}$$

A relation between θ_s and θ_t is obtained by substitution of eq. A.9 and eq. A.5 into eq. A.7 and solving towards θ_s, gives

$$\theta_s(\theta_t) = \frac{Y_c\theta_t(\alpha_s A_s + \alpha_t(1-\theta_t)A_t)}{Y_c\theta_t(\alpha_s A_s + \alpha_t(1-\theta_t)A_t) + \alpha_t Y_m(1-\theta_t)^2 A_t} \tag{A.11}$$

This gives an one-to-one relation between the variable θ_t on the one hand and the dependent variable J_{ion} on the other hand.

$S-\theta_t$ curve

By substitution of eq. A.2, eq. A.4, eq. A.3 and eq. A.5 into eq. A.1, and solving towards S gives

$$S(P_r, \theta_s, \theta_t) = k_B T \left[\frac{Q_{in}}{P} - \kappa(\alpha_t(1-\theta_t)A_t + \alpha_s(1-\theta_s)A_s)\right] \tag{A.12}$$

The dependent variable S is now a function of θ_t, θ_s and P_r. The latter can be obtained as function of θ_t by substitution of eq. A.5 into eq. A.6 and solving towards P_r, which gives

$$P_r(\theta_t) = \frac{J_{ion}Y_c\theta_t}{\frac{2}{z}\alpha_t\kappa(1-\theta_t)} \tag{A.13}$$

The dependency of θ_s on θ_t is obtained by substitution of eq. A.13 and eq. A.5 into eq. A.7, and solving towards θ_s. This results in the same expression $\theta_s(\theta_t)$ as eq. A.11. Again an one-to-one relation between the variable θ_t and S is obtained.

$A_s-\theta_t$ curve

Solving eq. A.1 towards A_s gives it as a function of θ_t and θ_s, namely

$$\begin{aligned} A_s(\theta_s, \theta_t) &= \frac{1}{\kappa\alpha_s(1-\theta_s)}\left[\frac{Q_{in}}{P_r(\theta_t)} - \frac{S}{k_B T} - \kappa\alpha_t(1-\theta_t)A_t\right] \\ &= \frac{1}{\kappa\alpha_s(1-\theta_s)}\mathcal{C}(\theta_t) \end{aligned} \tag{A.14}$$

where the dependency of P_r on θ_t is given by eq. A.13.

The functional dependency of A_s on θ_s can be eliminated by substitution of eq. A.11 under the form of

$$\begin{aligned} 1-\theta_s(A_s,\theta_t) &= \frac{\alpha_t Y_m(1-\theta_t)^2 A_t}{Y_c\theta_t(\alpha_s A_s+\alpha_t(1-\theta_t)A_t)+\alpha_t Y_m(1-\theta_t)^2 A_t} \\ &= \frac{\mathcal{A}(\theta_t)}{\mathcal{B}(A_s,\theta_t)+\mathcal{A}(\theta_t)} \end{aligned} \tag{A.15}$$

into eq. A.14. This gives an equation which only depends on A_s and θ_t, namely

$$A_s = \frac{\mathcal{B}(A_s,\theta_t)+\mathcal{A}(\theta_t)}{\kappa\alpha_s\mathcal{A}(\theta_t)}\mathcal{C}(\theta_t) \tag{A.16}$$

If this is solved towards A_s with θ_t as independent variable, the following dependency

$$A_s(\theta_t) = \frac{\mathcal{A}(\theta_t)+Y_c\alpha_t\theta_t(1-\theta_t)A_t}{\kappa\alpha_s\mathcal{A}(\theta_t)-Y_c\alpha_s\theta_t\mathcal{C}(\theta_t)}\mathcal{C}(\theta_t) \tag{A.17}$$

is obtained. This shows a one-to-one relation between the variable θ_t and A_s.

$A_t-\theta_t$ curve

The derivation of the $A_t-\theta_t$ curve start similar as for the $A_s-\theta_t$ curve. Now eq. A.1 is rewritten as

$$A_t(A_t,\theta_s,\theta_t) = \frac{1}{\kappa\alpha_t(1-\theta_t)}\left[\frac{Q_{in}}{\mathcal{P}_r(\theta_t)}A_t - \frac{S}{k_BT} - \kappa\alpha_s(1-\theta_s)A_s\right] \tag{A.18}$$

where a dependency on A_t through P_r (eq. A.13) remains. This dependency is factorized out in eq. A.18 by defining

$$\mathcal{P}_r(\theta_t) = P_r(A_t,\theta_t)A_t \tag{A.19}$$

Recall that $J_{ion}=I_{ion}/A_t$ and that I_{ion} is here treated as a constant.

The functionality of θ_s on θ_t and A_t is similarly as in eq. A.15. It is stated as

$$\begin{aligned} 1-\theta_s(A_t,\theta_t) &= \frac{\alpha_t Y_m(1-\theta_t)^2 A_t}{Y_c\theta_t(\alpha_s A_s+\alpha_t(1-\theta_t)A_t)+\alpha_t Y_m(1-\theta_t)^2 A_t} \\ &= \frac{\mathcal{A}'(A_t,\theta_t)}{\mathcal{B}'(A_t,\theta_t)+\mathcal{A}'(A_t,\theta_t)} \end{aligned} \tag{A.20}$$

Substitution of eq. A.20 into eq. A.18 finally gives a relation between the variables A_t and θ_t stated as

$$\begin{aligned} &\kappa\alpha_s A_s\mathcal{A}'(A_t,\theta_t)+[\mathcal{A}'(A_t,\theta_t)+\mathcal{B}'(A_t,\theta_t)] \\ &\qquad\left[\frac{S}{k_BT}+\left(\kappa\alpha_t(1-\theta_t)-\frac{Q_{in}}{\mathcal{P}_r(\theta_t)}\right)A_t\right]=0 \end{aligned} \tag{A.21}$$

This is a quadratic equation in A_t for a given θ_t which means that a mathematical one-to-two relation exists between the variable θ_t and A_t. However one of the two solutions is always physical not real.

B

RSD2013
Steady state target solution

The steady state formulation of the RSD2013 model for the target (see section 4.3.1.2) is retrieved by setting all time derivatives to zero. This gives three balance equations per target cell i for the surface fractions θ_m, θ_r and θ_c, namely

$$jY_m\theta_m + [F_m(\overline{\theta_m}) + F_c(\overline{\theta_c}, \overline{\theta_r})]\theta_m + \frac{2}{z}\alpha_t F_r \theta_m = jY_{av}(\theta_m, \theta_c, \theta_r)(1-\theta_b) + F_m(\overline{\theta_m}) + j\frac{\beta}{z}\theta_c \quad \text{(B.1a)}$$

$$jY_r\theta_r + [F_m(\overline{\theta_m}) + F_c(\overline{\theta_c}, \overline{\theta_r})]\theta_r = jY_{av}(\theta_m, \theta_c, \theta_r)\theta_b + F_c(\overline{\theta_c}, \overline{\theta_r}) \quad \text{(B.1b)}$$

$$jY_c\theta_c + [F_m(\overline{\theta_m}) + F_c(\overline{\theta_c}, \overline{\theta_r})]\theta_c + j\frac{\beta}{z}\theta_c = \frac{2}{z}\alpha_t F_r \theta_m \quad \text{(B.1c)}$$

The index i numbering the target cells is omitted for brevity. The average sputter yield $Y_{av}(\theta_m, \theta_c, \theta_r)$ is defined as

$$Y_{av}(\theta_m, \theta_c, \theta_r) = Y_m\theta_m + Y_c\theta_c + Y_r\theta_r \quad \text{(B.2)}$$

and the redeposition fluxes $F_m(\overline{\theta_m})$ and $F_c(\overline{\theta_c}, \overline{\theta_r})$ are defined as

$$F_m(\overline{\theta_m}) = \varepsilon_t \frac{I_{ion}}{A_t} Y_m \overline{\theta_m} \quad \text{(B.3a)}$$

$$F_c(\overline{\theta_c}, \overline{\theta_r}) = \varepsilon_t \frac{I_{ion}}{A_t} (Y_r\overline{\theta_r} + Y_c\overline{\theta_c}) \quad \text{(B.3b)}$$

The current weighted average fraction $\overline{\theta}$ occurring in eq. B.3 is stated as

$$\overline{\theta} = \frac{1}{I_{ion}} \sum_i I^i \theta^i \tag{B.4}$$

The involved parameters are described in section 4.3.1 and summarized in Table 4.1.

The steady state equations for the subsurface region of each target cell (eq. 4.17) reduce to two ODEs describing the bulk in terms of a non-reacted metal concentrations $n_M(x)$ and a concentration of unbounded implanted reactive gas atoms $n_R(x)$. These ODEs are stated as

$$\begin{aligned} -v_s \frac{\mathrm{d}}{\mathrm{d}x} n_M(x) &= -k n_M(x) n_R(x) && \text{(B.5a)} \\ -v_s \frac{\mathrm{d}}{\mathrm{d}x} n_R(x) &= -z k n_M(x) n_R(x) + j[2f + \beta\theta_c] p(x) s(n_M, n_R) && \end{aligned}$$

with the effective surface speed v_s, the erosion speed v_e and the growth speed v_r defined as

$$\begin{aligned} v_s &= v_e - v_r && \text{(B.6a)} \\ v_e &= \frac{I}{n_0 A_t} Y_{av}(\theta_m, \theta_c, \theta_r) && \text{(B.6b)} \\ v_r &= \frac{1}{n_0} [F_m(\overline{\theta_m}) + F_c(\overline{\theta_c}, \overline{\theta_r})] && \text{(B.6c)} \end{aligned}$$

These ODEs are connected to the surface layer by a boundary layer where the concentrations $n_M(0)$ and $n_R(0)$ are defined by the balance equations

$$\frac{v_r}{\Delta x} n_0 \theta_m + \frac{v_s}{\Delta x} n'_M = \frac{v_e}{\Delta x} n_M(0) + k n_M(0) n_R(0) \tag{B.7a}$$

$$\frac{v_s}{\Delta x} n'_R + j[2f + \beta\theta_c] p(x) s(n_M(0), n_R(0)) = \frac{v_e}{\Delta x} n_R(0) + k z n_M(0) n_R(0) \tag{B.7b}$$

where

$$n'_i = \begin{cases} n_i(1) & \text{if } v_s > 0 \\ n_i(0) & \text{if } v_s < 0 \end{cases}, \text{with } i = M, R \tag{B.8}$$

The connection of this boundary layer to the surface layer is by θ_b given as

$$\theta_b = 1 - \frac{n_M(0)}{n_0} \tag{B.9}$$

The boundary layer interfacing the surface and the subsurface region can be omitted in the case of no redeposition ($v_r = 0$) as $v_s = v_e$. In that case eq. B.7 become a discretized version of the ODEs (eq. B.5) for the most upper layer of the subsurface region.

One-cell target redeposition

If a one-cell target with redeposition is considered in the RSD2013 model, the steady state solution for the surface layer of the target can be analytical retrieved for a given reactive mole fraction f and a subsurface fraction θ_b. The is only true if the sputter yields for the chemisorbed Y_c and the compound Y_r particles are set equal, namely

$$Y_r = Y_c \tag{B.10}$$

In that case the average sputter yield Y_{av} (eq. B.2) and the redeposition fluxes F_m and F_c (eq. B.3) depend only on the metal fraction θ_m as

$$\begin{aligned} Y_{av}(\theta_m) &= Y_m\theta_m + Y_c(1-\theta_m) && \text{(B.11a)} \\ F_m(\theta_m) &= \varepsilon_t j Y_m \theta_m && \text{(B.11b)} \\ F_c(\theta_m) &= \varepsilon_t j Y_c (1-\theta_m) && \text{(B.11c)} \end{aligned}$$

recalling that for a one-cell target $\overline{\theta_m} \equiv \theta_m$ and the relation $\theta_m + \theta_c + \theta_r = 1$. This reduces eq. B.1 for the surface layer to

$$jY_m\theta_m + [F_m(\theta_m) + F_c(\theta_m)]\theta_m + \frac{2}{z}\alpha_t F_r \theta_m = jY_{av}(\theta_m)(1-\theta_b) + F_m(\theta_m) + j\frac{\beta}{z}\theta_c \tag{B.12a}$$

$$jY_c\theta_r + [F_m(\theta_m) + F_c(\theta_m)]\theta_r = jY_{av}(\theta_m)\theta_b + F_c(\theta_m) \tag{B.12b}$$

$$jY_c\theta_c + [F_m(\theta_m) + F_c(\theta_m)]\theta_c + j\frac{\beta}{z}\theta_c = \frac{2}{z}\alpha_t F_r \theta_m \tag{B.12c}$$

where only quadratic terms involving θ_m occur. The easiest way to solve this system is written it as a single equation in the variable θ_m. Solving eq. B.12b and eq. B.12c respectively towards θ_r and θ_c as a function of θ_m gives

$$\begin{aligned} \theta_r(\theta_m) &= \frac{jY_{av}(\theta_m)\theta_b + F_c(\theta_m)}{jY_c + [F_m(\theta_m) + F_c(\theta_m)]} && \text{(B.13a)} \\ \theta_c(\theta_m) &= \frac{\frac{2}{z}\alpha_t F_r \theta_m}{jY_c + [F_m(\theta_m) + F_c(\theta_m)] + j\frac{\beta}{z}} && \text{(B.13b)} \end{aligned}$$

An analytical solvable cubic equation in θ_m is now obtained by substitution of eq. B.13 into

$$\theta_m = 1 - \theta_r(\theta_m) - \theta_c(\theta_m) \tag{B.14}$$

If the knock-on yield $\beta = 0$, this even reduces to a quadratic equation. Back substitution of the physical solution for θ_m into eq. B.13 solves the surface layer of the one-cell target.

C

Publications and Conference Contributions

Publications

- K. Strijckmans, W.P. Leroy, D. Depla, *Corrigendum to Modeling reactive magnetron sputtering: Fixing the parameter set Surf. Coat. Technol. 206(17) (2012) 36663675*, *Surface & Coatings Technology* **278**, 126 (2015)
- R. Schelfhout, K. Strijckmans, F. Boydens, D. Depla, *On the target surface cleanness during magnetron sputtering*, *Applied Surface Science* **355**, 743-747 (2015)
- K. Strijckmans, D. Depla, *Modeling target erosion during reactive sputtering*, *Applied Surface Science* **331**, 185-192 (2015)
- D. Depla, K. Strijckmans, R. De Gryse, *The role of the erosion groove during reactive sputter deposition*, *Surface & Coatings Technology* **258**, 1011-1015 (2014)
- K. Strijckmans, D. Depla, *A time-dependent model for reactive sputter deposition*, *Journal of Physics D Applied Physics* **47** (23), 235302 (2014)

- E. Särhammar, K. Strijckmans, T. Nyberg, S. Van Steenberge, S. Berg, D. Depla, *A study of the process pressure influence in reactive sputtering aiming at hysteresis elimination*, *Surface & Coatings Technology* **232**, 357-361 (2013)

- K. Strijckmans, W.P. Leroy, D. Depla, *Modeling reactive magnetron sputtering: fixing the parameter set*, *Surface & Coatings Technology* **206** (17), 3666-3675 (2012)

Conference contributions

- K. Strijckmans, D. Depla, *The modelling of the reactive magnetron sputter process by RSD2013*, 16th International Conference on Thin Films, 2014, Dubrovnik, Croatia (oral)

- K. Strijckmans, D. Depla, *The reactive sputter model RSD2013*, Reactive Sputter Deposition, 13th International symposium, 2014, Ghent, Belgium (oral)

- K. Strijckmans, W.P. Leroy, D. Depla, *How does redeposition influence reactive sputtering?*, 19th International Vacuum Congress, 2013, Paris, France (oral)

- K. Strijckmans, W.P. Leroy, D. Depla, *A dynamic simulation tool for reactive sputtering*, Reactive Sputter Deposition, 11th International symposium, 2012, Ghent, Belgium (oral)

- K. Strijckmans, W.P. Leroy, D. Depla, *Modeling the time dependency of the reactive sputter process*, Plasma Surface Engineering, 13th International conference, 2012, Garmisch-Partenkirchen, Germany (poster)

- K. Strijckmans, W.P. Leroy, D. Depla, *Reactive sputtering in 5D*, Reactive Sputter Deposition, 10th International symposium, 2011, Linköping, Sweden (oral)

- K. Strijckmans, W.P. Leroy, D. Depla, *In search for the ultimate model parameters of reactive magnetron sputtering*, 18th International Colloquium on plasma processes, 2011, Nantes, France (oral)

- K. Strijckmans, W.P. Leroy, A. Bogaerts, D. Depla, *Fixing the parameter set for reactive sputtering modelling*, Plasma Surface Engineering, 12th International conference, 2010, Garmisch-Partenkirchen, Germany (poster)